creative commons
COMMONS DEED

저작자표시-비영리-변경금지 2.0 대한민국

이용자는 아래의 조건을 따르는 경우에 한하여 자유롭게

- 이 저작물을 복제, 배포, 전송, 전시, 공연 및 방송할 수 있습니다.

다음과 같은 조건을 따라야 합니다:

저작자표시. 귀하는 원저작자를 표시하여야 합니다.

비영리. 귀하는 이 저작물을 영리 목적으로 이용할 수 없습니다.

변경금지. 귀하는 이 저작물을 개작, 변형 또는 가공할 수 없습니다.

- 귀하는, 이 저작물의 재이용이나 배포의 경우, 이 저작물에 적용된 이용허락조건을 명확하게 나타내어야 합니다.
- 저작권자로부터 별도의 허가를 받으면 이러한 조건들은 적용되지 않습니다.

저작권법에 따른 이용자의 권리는 위의 내용에 의하여 영향을 받지 않습니다.

이것은 이용허락규약(Legal Code)을 이해하기 쉽게 요약한 것입니다.

Disclaimer

dCollection

공학박사학위논문

가솔린 엔진에서 현상학적 유사차원 연소 모델링에 관한 연구

A Study on Phenomenological Quasi-Dimensional Combustion Modeling of Spark-Ignited Engine

2016 년 8 월

서울대학교 대학원

기계항공공학부

김 남 호

가솔린 엔진에서 현상학적 유사차원 연소 모델링에 관한 연구

A Study on Phenomenological Quasi-Dimensional Combustion Modeling of Spark-Ignited Engine

지도교수 민 경 덕

이 논문을 공학박사 학위논문으로 제출함

2016 년 4 월

서울대학교 대학원

기계항공공학부

김 남 호

김남호의 공학박사 학위논문을 인준함

2016 년 6 월

위 원 장 고 상 근 (인)

부위원장 민 경 덕 (인)

위 원 송 한 호 (인)

위 원 도 형 록 (인)

위 원 이 진 욱 (인)

Abstract

A Study on Phenomenological Quasi-Dimensional Combustion Modeling of Spark-Ignited Engine

Namho Kim
Department of Mechanical and Aerospace Engineering
The Graduate School
Seoul National University

The efficiency improvement of the SI engine is still an important task even though tremendous enhancement has been realized over past decades. To address the requirement to meet the stringent regulation on fuel economy, newly developed engines are being equipped with technologies such as variable valve actuation (VVA) system. As a result, the engine is becoming more complex system. Thus, for the hardware optimization, and optimal calibration of the engine, the aid of 1D simulation is necessary. The combustion model implemented in 1D simulation tools, however, lacks the accuracy when it is to be applied to variety of engine operating conditions, and designs. Therefore, in this study, zero-dimensional (0D) turbulence model and phenomenological quasi-dimensional (QD) combustion model were developed to improve the accuracy of the combustion model close to three-dimensional computational fluid dynamics (3D CFD).

The 0D turbulence model was developed based on the energy cascade model with several revisions so that the model can predict the mean flow velocity and turbulence intensity close to those of 3D CFD. Correlations for integral length scale, loss in kinetic energy during intake process, and the production rate of turbulent

kinetic energy were derived. An adjustable constant was added to incorporate the effect of engine design affecting tumble strength.

The phenomenological QD combustion model was developed based on the QD turbulence model. The QD turbulence model is an extended version of the 0D turbulence model which can estimate the turbulence intensity of burned and unburned zone during combustion. It was assumed that the combustion processes can be divided into three steps: initial flame kernel development, transition from laminar to turbulent flame propagation, and fully-developed turbulent flame propagation. The transition phase and fully-developed turbulent flame propagation phase were described using a correlation derived in former study with several modifications. The heat transfer model was also modified from Woschni's correlation to improve the accuracy of the estimation of the heat loss.

The developed models implemented in 1D simulation tool, GT-Power, were verified over various engine operating conditions by comparing the turbulence intensity, and combustion characteristics with those of 3D CFD. The mean flow velocity and the turbulence intensity predicted by the 0D turbulence model closely resembled those of 3D CFD. It was also confirmed that the model can predict the turbulence intensity of the engine designed for stronger tumble strength by tuning only one adjustable constant. The phenomenological QD combustion model was successful in reproducing the burn rate, in-cylinder pressure, turbulence intensity of burned and unburned zone, and heat transfer rate obtained from 3D CFD. Except for the cases with late spark timing at 6000 rpm, the combustion phase (MFB 50), and burn duration (MFB 10-80) were predicted with the error less than 0.5 CA, and 2 CA, respectively under part load, and full load with the engine speed varied from 1500 rpm to 6000 rpm.

The phenomenological QD combustion model was also verified with the experimental data obtained from single cylinder engine. By introducing the correlation of initial flame kernel size with the amount of residual gas fraction (RGF),

the model was able to predict the in-cylinder pressure sufficiently accurate without changing the adjustable constant over wide operating range. The combustion phase (MFB 50) was predicted with the error less than 1 CA for 20 simulation cases out of 24 cases.

Finally, the developed model was utilized to observe the energy flow in the engine, and the effect of VVA function on engine performance. By comparing the energy balance of various spark timing, it was possible to gain insight to the tendency in changes of heat loss to the piston, head, and liner. With the cycle simulation using short-duration valve profile, reduction in pumping loss was observed as pump mean effective pressure (PMEP) decreased by 27.8% at the given condition. The simulation result also showed that the gain in indicated mean effective pressure (IMEP) is larger than the reduction in PMEP. It was found that the reduction of effective compression ratio, and the faster combustion due to reduction in RGF were responsible for such result.

The 0D turbulence model, and the phenomenological QD combustion model developed in this study contain very small number of the adjustable constants including a constant to incorporate the effect of engine design related to tumble strength, and do not require changes to the values of the constants over wide range of engine operating conditions. Thus, it is expected that the developed models would contribute to the assessment of various engine designs, and system configurations at the initial phase of the engine development with better accuracy.

Keywords: SI engine, 0D (zero-dimensional), QD (quasi-dimensional), Turbulence intensity, Combustion model

Student Number: 2010-20652

Contents

Abstract i

List of Figures viii

List of Tables xviii

Nomenclature xix

Chapter 1. Introduction 1

1.1 Background and Motivation 1

1.1.1 Internal combustion engine and its outlook 1

1.1.2 Issues in the internal combustion engine 2

1.1.3 Factors affecting efficiency of SI engines 4

1.1.4 Technological developments for efficiency improvement of SI engines 6

1.2 Literature Review 17

1.3 Objectives 26

Chapter 2. Development of zero-dimensional turbulence model under motored condition 27

2.1 Necessity of model development 27

2.2 Modeling approach 29

2.3 Integral length scale for energy cascade model 31

2.3.1 Modeling approach 31
2.3.2 Comparison of multi-cycle simulation results to the single cycle simulation results 32
2.3.3 Sensitivity analysis on integral length scale 32
2.3.4 Fitting model of the integral length scale 35

2.4 Analysis on the kinetic energy of in-cylinder flow 53

2.5 Modeling of the production rate of turbulent kinetic energy 63
2.5.1 Assessment of the original energy cascade model in enclosed system 63
2.5.2 Production rate of turbulent kinetic energy 66
2.5.3 Derivation of geometric length scale for production rate 67
2.5.4 Phenomenological model of production term dependent on tumble strength 70

2.6 Verification of the developed model 78
2.6.1 Assessment of the developed model to base engine 78
2.6.2 Assessment of the developed model to engine with intensified tumble strength 80

Chapter 3. Development of phenomenological quasi-dimensional combustion model 103

3.1 Necessity of model development 103

3.2 Modeling approach 104

3.3 Standard for dividing zones in 3D CFD 107

3.4 Turbulence intensity prediction during combustion 109

3.5 Flame propagation mode during combustion processes 124
3.5.1 Initial flame kernel development 124
3.5.2 Transition from laminar to turbulent flame propagation 126
3.5.3 Fully-developed turbulent flame propagation 127

3.6 Modifications of the heat transfer model 129

3.7 Verification of the developed model..... 135

3.8 Sensitivity analysis of the developed model 153

Chapter 4. Verification of the developed model with experimental results 159

4.1 Experimental setup 159

4.2 Experimental conditions..... 164

4.3 Verification of the developed model..... 166

4.3.1 GT-Power model verification..... 166

4.3.2 Calibration of the developed model at reference conditions 166

4.3.3 Comparison of the in-cylinder pressure at various test conditions..... 167

Chapter 5. Application of the developed model for engine performance prediction 180

5.1 Energy flow analysis within engine cylinder..... 180

5.2 Effect of VVA function on engine performance 182

Chapter 6. Conclusions 187

Bibliography..... 191

국 문 초 록..... 201

List of Figures

Figure 1.1 Outlook on the market shares of power source of propulsion in 2004 [3] 11

Figure 1.2 Outlook on the market shares of power source of propulsion in 2015 [4] 12

Figure 1.3 Trend in world-wide regulation on CO_2 emission [6].....13

Figure 1.4 Comparison of the engine operating range corresponding to various driving cycles 14

Figure 1.5 Energy flow in a typical gasoline engine [7] 14

Figure 1.6 Losses in engine cycle [9].....15

Figure 2.1 Engine mesh generated at BDC of test engine 1.....38

Figure 2.2 Comparison of profiles of the integral length scale obtained from 0D models to 3D simulation result.....39

Figure 2.3 Comparison of profiles of the integral length scale of two consecutive cycles.....39

Figure 2.4 Valve profiles of various valve timing 40

Figure 2.5 Valve profiles of various lift and duration.....40

Figure 2.6 Geometry of (a) conventional, and (b) extruded piston 41

Figure 2.7 Profiles of the integral length scale of various intake pressure.....42

Figure 2.8 Profiles of the integral length scale of various engine speed 42

Figure 2.9 Profiles of the integral length scale of various valve timings 43

Figure 2.10 Profiles of the integral length scale of various valve profiles 43

Figure 2.11 Profiles of the integral length scale of different compression ratio.....44

Figure 2.12 Profiles of the integral length scale of different piston under CR 9.5....44

Figure 2.13 Profiles of the integral length scale of different SB ratio with constant bore.....45

Figure 2.14 Profiles of the integral length scale of different SB ratio with constant cylinder volume.....45

Figure 2.15 Profiles of the integral length scale of different engines.....46

Figure 2.16 Definition of local maximum and minimum points.....46

Figure 2.17 Location and magnitude of local maximum and minimum points.....47

Figure 2.18 Correlation between aspect ratio of clearance volume and magnitude of second local minimum point 48

Figure 2.19 Comparison of profiles of the integral length scale reproduced with developed model for the case with nominal valve profiles 49

Figure 2.20 Comparison of profiles of the integral length scale reproduced with developed model for the case with short duration valve profiles 49

Figure 2.21 Comparison of the total kinetic energy to cumulative kinetic energy....57

Figure 2.22 Velocity field during intake stroke at (a) 405 CA and, (b) 430 CA.....58

Figure 2.23 Ratio of total kinetic energy to cumulative kinetic energy 59

Figure 2.24 The effect of correlation of loss factor on prediction of total kinetic energy for (a) case 1, (b) case 8, (c) case 9, (d) case 10, (e) case 11, and (f) case 12 60

Figure 2.25 Comparison of total kinetic energy of test engine at (a) 1500 rpm, IVO 336 CA, (b) 2000 rpm, IVO 336 CA, (c) 4000 rpm, IVO 352 CA, and (d) 6000 rpm, IVO 365 CA 61

Figure 2.26 Mean flow velocity magnitude and turbulent kinetic energy at 1500 rpm 73

Figure 2.27 Comparison of mean flow velocity magnitude at (a) 1500 rpm, (b) 3000 rpm, and (c) 6000 rpm 74

Figure 2.28 Comparison of the rate of change of turbulent kinetic energy (a) without limitation on RDT term, and (b) with limitation on RDT term 75

Figure 2.29 Comparison of the turbulent kinetic energy under (a) 1500 rpm, (b) 3000 rpm, and (c) 6000 rpm 76

Figure 2.30 Comparison of profiles of the geometric length scale 77

Figure 2.31 Comparison of (a) mean flow velocity magnitude and (b) turbulence intensity of case 1 81

Figure 2.32 Comparison of (a) mean flow velocity magnitude and (b) turbulence intensity of case 2 82

Figure 2.33 Comparison of (a) mean flow velocity magnitude and (b) turbulence intensity of case 3 83

Figure 2.34 Comparison of (a) mean flow velocity magnitude and (b) turbulence intensity of case 4 84

Figure 2.35 Comparison of (a) mean flow velocity magnitude and (b) turbulence intensity of case 5 85

Figure 2.36 Comparison of (a) mean flow velocity magnitude and (b) turbulence intensity of case 6 86

Figure 2.37 Comparison of (a) mean flow velocity magnitude and (b) turbulence intensity of case 7 87

Figure 2.38 Comparison of (a) mean flow velocity magnitude and (b) turbulence intensity of case 8 88

Figure 2.39 Comparison of (a) mean flow velocity magnitude and (b) turbulence intensity of case 9 89

Figure 2.40 Comparison of (a) mean flow velocity magnitude and (b) turbulence intensity of case 10 90

Figure 2.41 Comparison of (a) mean flow velocity magnitude and (b) turbulence intensity of case 11 91

Figure 2.42 Comparison of (a) mean flow velocity magnitude and (b) turbulence intensity of case 12 92

Figure 2.43 Comparison of (a) mean flow velocity magnitude and (b) turbulence intensity of case 13 93

Figure 2.44 Comparison of (a) mean flow velocity magnitude and (b) turbulence intensity of case 15 94

Figure 2.45 Comparison of (a) mean flow velocity magnitude and (b) turbulence intensity of case 16 95

Figure 2.46 Comparison of (a) mean flow velocity magnitude and (b) turbulence intensity of case 17 96

Figure 2.47 Comparison of (a) mean flow velocity magnitude and (b) turbulence intensity of case 18 97

Figure 2.48 Comparison of (a) mean flow velocity magnitude and (b) turbulence intensity of case 19 98

Figure 2.49 Comparison of (a) mean flow velocity magnitude and (b) turbulence intensity of case 20 99

Figure 2.50 Comparison of (a) mean flow velocity magnitude and (b) turbulence intensity of high tumble engine at 1500 rpm 100

Figure 2.51 Comparison of (a) mean flow velocity magnitude and (b) turbulence intensity of high tumble engine at 3000 rpm 101

Figure 2.52 Comparison of (a) mean flow velocity magnitude and (b) turbulence intensity of high tumble engine at 6000 rpm 102

Figure 3.1 Comparison of the turbulence intensity of unburned zone calculated with 0D model and 3D CFD 106

Figure 3.2 Comparison of the burned zone mass fraction according to the zoning strategy under the condition of 1500 rpm, P_i 0.6 bar, and spark timing of 35º bTDC 108

Figure 3.3 Rate of change of turbulent kinetic energy in (a) unburned, and (b) burned zone under 1500 rpm, P_i = 0.6 bar, and spark timing of 45º bTDC 114

Figure 3.4 Rate of change of turbulent kinetic energy in (a) unburned, and (b) burned zone under 1500 rpm, P_i = 0.6 bar, and spark timing of 35º bTDC 115

Figure 3.5 Rate of change of turbulent kinetic energy in (a) unburned, and (b) burned zone under 1500 rpm, P_i = 0.6 bar, and spark timing of 25º bTDC 116

Figure 3.6 Rate of change of turbulent kinetic energy in (a) unburned, and (b) burned zone under 1500 rpm, P_i = 0.6 bar, and spark timing of 15º bTDC 117

Figure 3.7 Comparison of integral length scale of unburned zone predicted by QD model and 3D CFD for spark timing of (a) 45º bTDC, (b) 35º bTDC, (c) 25º bTDC, and (d) 15º bTDC 118

Figure 3.8 Comparison of integral length scale of burned zone predicted by QD model and 3D CFD for spark timing of (a) 45º bTDC, (b) 35º bTDC, (c) 25º bTDC, and (d) 15º bTDC 119

Figure 3.9 Rate of change of turbulent kinetic energy in (a) unburned, and (b) burned zone calculated with modified governing equations under 1500 rpm, P_i = 0.6 bar, and spark timing of 45º bTDC.....120

Figure 3.10 Rate of change of turbulent kinetic energy in (a) unburned, and (b) burned zone with modified governing equations under 1500 rpm, P_i = 0.6 bar, and spark timing of 35º bTDC 121

Figure 3.11 Rate of change of turbulent kinetic energy in (a) unburned, and (b) burned zone with modified governing equations under 1500 rpm, P_i = 0.6 bar, and spark timing of 25º bTDC 122

Figure 3.12 Rate of change of turbulent kinetic energy in (a) unburned, and (b) burned zone with modified governing equations under 1500 rpm, P_i = 0.6 bar, and spark timing of 15º bTDC 123

Figure 3.13 Comparison of damping factors in correlation of turbulent flame speed 128

Figure 3.14 Comparison of the effect of exponent of temperature term in the correlation of heat transfer rate for (a) unburned and (b) burned zones.....133

Figure 3.15 Comparison of the effect of exponent of temperature term in the correlation of heat transfer rate for (a) unburned and (b) burned zones after normalization.....133

Figure 3.16 Comparison of (a) burned mass fraction profile, (b) in-cylinder pressure, (c) unburned zone turbulence intensity, and (d) burned zone turbulence intensity of QD model and 3D CFD results under 3000 rpm, P_i = 0.6 bar condition at spark timing of 35º bTDC.....140

Figure 3.17 Comparison of total heat transfer rate under 3000 rpm, P_i = 0.6 bar condition at spark timing of 35º bTDC 141

Figure 3.18 Comparison of burned mass fraction profile with spark timing of (a) 45º bTDC, (b) 35º bTDC, (c) 25º bTDC, and (d) 15º bTDC under 3000 rpm, P_i = 0.6 bar 142

Figure 3.19 Comparison of (a) combustion phase (MFB 50), and (b) combustion duration (MFB 10-90) for various spark timing under 3000 rpm, P_i = 0.6 bar condition.....143

Figure 3.20 Comparison of (a) combustion phase (MFB 50) , and (b) combustion duration (MFB 10-90) for various spark timing under 3000 rpm, P_i = 0.6 bar after modification of turbulent flame speed correlation 144

Figure 3.21 Comparison of total heat transfer rate with spark timing of (a) 45º bTDC, (b) 35º bTDC, (c) 25º bTDC, and (d) 15º bTDC under 3000 rpm, P_i = 0.6 bar after modification of turbulent flame speed correlation.....145

Figure 3.22 Comparison of combustion phase (MFB 50) for various spark timing under P_i = 0.6 bar, (a) 1500 rpm, and (b) 6000 rpm 146

Figure 3.23 Comparison of combustion duration (MFB 10-90) for various spark timing under P_i = 0.6 bar, (a) 1500 rpm, and (b) 6000 rpm.....147

Figure 3.24 Comparison of combustion phase (MFB 50) for various spark timing under P_i = 1.0 bar, (a) 1500 rpm, (b) 3000 rpm and (c) 6000 rpm 148

Figure 3.25 Comparison of combustion duration (MFB 10-90) for various spark timing under P_i = 1.0 bar, (a) 1500 rpm, (b) 3000 rpm and (c) 6000 rpm.....149

Figure 3.26 Comparison of burn duration (MFB 10-80) for various spark timing under P_i = 0.6 bar, (a) 1500 rpm, (b) 3000 rpm and (c) 6000 rpm 150

Figure 3.27 Comparison of burn duration (MFB 10-80) for various spark timing under P_i = 1.0 bar, (a) 1500 rpm, (b) 3000 rpm and (c) 6000 rpm conditions.....151

Figure 3.28 Comparison of (a) combustion phase (MFB 50) , and (b) combustion duration (MFB 10-90) for various spark timing under 3000 rpm, P_i = 0.6 bar according to the variation in constant C_{engine} 155

Figure 3.29 Comparison of (a) combustion phase (MFB 50) , and (b) combustion duration (MFB 10-90) for various spark timing under 3000 rpm, P_i = 0.6 bar according to the variation in constant C_{ψ}.....156

Figure 3.30 Comparison of (a) combustion phase (MFB 50) , and (b) combustion duration (MFB 10-90) for various spark timing under 3000 rpm, P_i = 0.6 bar according to the variation in constant A 157

Figure 4.1 Schematic diagram of experimental apparatus 161

Figure 4.2 Comparison of intake manifold pressure at WOT condition at (a) 1500 rpm, (b) 2000 rpm, and (c) 2500 rpm.....169

Figure 4.3 Comparison of in-cylinder pressure curve at 1500 rpm (a) P_i = 0.6 bar, and (b) P_i = 1.0 bar predicted with the correlation 1-2.1x_b for laminar flame speed correction factor 170

Figure 4.4 Comparison of in-cylinder pressure curve at 1500 rpm (a) P_i = 0.6 bar, and (b) P_i = 1.0 bar predicted with the correlation 1-2.06$y_b^{0.77}$ for laminar flame speed correction factor 171

Figure 4.5 Comparison of in-cylinder pressure curve at 1500 rpm, P_i = 0.6 bar with spark timing of (a) 45º bTDC, (b) 40º bTDC, (c) 35º bTDC, (d) 30º bTDC, and (e) 25º bTDC.....172

Figure 4.6 Comparison of in-cylinder pressure curve at 1500 rpm, P_i = 1.0 bar with spark timing of (a) 10º bTDC, (b) 5º bTDC, and (c) 0º bTDC 173

Figure 4.7 Comparison of in-cylinder pressure curve at 2000 rpm, P_i = 0.6 bar with spark timing of (a) 45º bTDC, (b) 40º bTDC, (c) 35º bTDC, (d) 30º bTDC, and (e) 25º bTDC.....174

Figure 4.8 Comparison of in-cylinder pressure curve at 2000 rpm, P_i = 1.0 bar with spark timing of (a) 15º bTDC, (b) 10º bTDC, and (c) 5º bTDC 175

Figure 4.9 Comparison of in-cylinder pressure curve at 2500 rpm, P_i = 0.6 bar with spark timing of (a) 45º bTDC, (b) 40º bTDC, (c) 35º bTDC, (d) 30º bTDC, and (e) 25º bTDC.....176

Figure 4.10 Comparison of in-cylinder pressure curve at 2500 rpm, P_i = 1.0 bar with spark timing of (a) 25º bTDC, (b) 20º bTDC, and (c) 15º bTDC 177

Figure 4.11 Comparison of combustion phase (MFB 50) for various spark timing under P_i = 0.6 bar, (a) 1500 rpm, (b) 2000 rpm and (c) 2500 rpm 178

Figure 4.12 Comparison of combustion phase (MFB 50) for various spark timing under P_i = 1.0 bar, (a) 1500 rpm, (b) 2000 rpm and (c) 2500 rpm 179

Figure 5.1 Comparison of the heat balance for various spark timings under 1500 rpm, and P_i = 0.6 bar condition 181

Figure 5.2 Valve profiles used for cycle simulation 184

Figure 5.3 Comparison of the PV diagram of base and short duration valve profile 184

Figure 5.4 Comparison of the pressure loop of negative work of base and short duration valve profile 185

Figure 5.5 Comparison of the turbulence intensity of base and short duration valve profile 185

List of Tables

Table 1.1 European regulation standards on the passenger car emission 16

Table 1.2 Equations of zero-dimensional turbulence models 24

Table 1.3 Equations of quasi-dimensional combustion models 25

Table 2.1 Simulation conditions for sensitivity analysis of integral length scale 50

Table 2.2 Specifications of engines used for comparison of integral length scale 52

Table 2.3 Specifications of engines used for verification of correlation of loss factor 62

Table 3.1 Exponent of the temperature term for convective heat transfer coefficient 134

Table 3.2 Simulation conditions 152

Table 3.3 Values of adjustable constants used in sensitivity analysis 158

Table 4.1 Specifications of the test engine 162

Table 4.2 Specifications of the piezoresistive sensor 163

Table 4.3 Specifications of the piezoelectric sensor 163

Table 4.4 Experimental conditions 165

Table 5.1 Simulation conditions for VVA function assessment 186

Table 5.2 Cycle simulation results 186

Nomenclature

A	area [m^2]
C_d	discharge coefficient [-]
h	Specific enthalpy [J kg^{-1}]
h_c	convective heat transfer coefficient [W m^{-2} K^{-1}]
h_{cyl}	instantaneous cylinder height [m]
k	turbulent kinetic energy [J]
K	mean kinetic energy [J]
l	integral length scale [m]
$\bar{L}$	geometric length scale [m]
m	mass [kg]
P	In-cylinder pressure [Pa]
Re	Reynold's number [-]
r_f	flame radius [m]
S_L	laminar flame speed [m s^{-1}]
S_T	turbulent flame speed [m s^{-1}]
t	time [s]
T	temperature [K]
$\bar{U}$	mean flow velocity [m s^{-1}]
u'	turbulence intensity [m s^{-1}]
V	volume [m^3]
x_b	mass fraction of burned species [-]
y_b	mole fraction of burned species [-]

Greek letters

ε	dissipation rate of turbulent kinetic energy [-]
λ	Taylor microscale [m]
μ	dynamic viscosity [m^2 s^{-1}]

ψ	production rate of turbulent kinetic energy [W]
ρ	density [kg m^{-3}]
τ	characteristic time constant [s]

Subscripts

b	burned zone
c	clearance volume
cyl	cylinder
d	displacement volume
u	unburned zone

Acronym

0D	zero-dimensional
aTDC	after top dead center
bTDC	before top dead center
CA	crank angle
CR	compression ratio
EVC	exhaust valve closing
EVO	exhaust valve opening
IMEP	indicated mean effective pressure
IVC	intake valve closing
IVO	intake valve opening
MBT	maximum brake torque
PMEP	pumping mean effective pressure
QD	quasi-dimensional
RDT	rapid distortion theory
RGF	residual gas fraction
SB	stroke-to-bore
SI	spark-ignition

Chapter 1. Introduction

1.1 Background and Motivation

1.1.1 Internal combustion engine and its outlook

Internal combustion engine is defined as the heat engine that converts chemical energy into mechanical energy [1]. The internal combustion has been the major power source of the propulsion system as the automobiles became available widely in 20th century due to its high power density and reliable supply of the fuel.

The types of internal combustion engine which can be classified by basic engine design, working cycle, valve design and location, types of fuel used, method of mixture preparation, method of ignition, combustion chamber design, method of load control, and method of cooling [2]. Among these categories, the mainstream of the internal combustion engine has become four stroke reciprocating engine with double head overcame (DOHC) and water cooling for transport application.

The state-of-the-art engine designs enabled the great improvement in efficiency of internal combustion engine while keeping the harmful emissions as low as possible. The depletion of fossil fuels and environmental issues, however, led to increased demand on renewable power source for propulsion to replace the former internal combustion engines. According to the outlook on the market share of power sources for propulsion in early 2000's, it is estimated that market share of the internal combustion engine would be diminished by up to 30% in 2015, and replaced by renewable power sources such as fuel-cell, electricity, or internal combustion engines hybridized with electricity [3]. The recent statistics, however, shows that the former

outlook on the power source of propulsion was incorrect. The new outlook announced in 2015 shows that the most of the power source of the propulsion will rely on the internal combustion engine even in 2050 [4].

1.1.2 Issues in the internal combustion engine

As the CO_2, generally known as the greenhouse gas, emitted from transport application consists of the 23% of the total CO_2 production, the world-wide regulation on fuel economy is becoming more stringent than ever [5]. This paradigm in regulation is facilitated by the depletion of fossil fuels, and concerns with energy security as well. The regulation in EU requires CO_2 emission to be reduced to 130 g/km, and 95 g/km by 2015, and 2021 respectively [6]. Further reduction of CO_2 emission to 70 g/km is currently under debate. Recently announced regulations in US requires passenger vehicles to satisfy fuel economies of 35.5 mpg, and 54.5 mpg by 2016, and 2025 respectively. The goal in 2025 is a 53.5% improvement from that in 2016, which requires approximately 4.9% improvement annually. The CO_2 regulations in other nations have similar tendency as in EU and US.

Environmental concerns are also driving emission regulations to become harsher. EURO regulation on emissions has been strengthened to reduce NOx and PM emission by 64% and 90% respectively through 2000 to 2011. From 2014, EURO 6 has been enacted which requires NOx level below 80 mg/km for diesel engines. The new standard on NOx level is extremely difficult to be met without the aid of after-treatment system. Furthermore, EURO 6 regulation imposes particulate number regulation not only on diesel engines, but also on SI engines as well. The details about the EURO standards are summarized in Table 1.1.

California ARB (CARB) and federal regulation of the US is becoming very stringent as well. CARB LEV III standards which begins to phase-in from 2015 through 2025, is categorized into 6 emission standard bins based on the emission level of sum of non-methane organic gas (NMOG) and NOx. More stringent bin requires additional reduction of carbon monoxide (CO) as well. On the other hand, the PM emission standard is applied regardless of the bins, and will be tightened from 10 mg/mile to 1 mg/mile gradually from 2017 to 2028. EPA Tier 3 standards which will begin to phase in from 2017 through 2025 have the same stringency with the CARB LEV III standards. Both LEV III and Tier 3 limits the fleet average level of NMOG and NOx combined below 100 g/mile, and the level is tightened continuously during the phase-in period up to 30 g/mile by 2025.

Despite of the harsher regulations and tremendous efforts to satisfy the regulations, the air pollutant level of present days remains similar to that in past few decades. This led to concerns that the former methods for measuring emission characteristics fails to convey the real emission characteristics on the road. Consequently, there is an attempt to propose new test driving cycles which can reflect actual driving conditions more realistically, and one such new driving cycle is called world harmonized light-duty vehicle test cycle (WLTC). WLTC will be applied to phase 2 of EURO 6 regulation in 2017. In addition, another test method named real driving emission (RDE) will be applied from September of 2017, with a conformity factor of 2.1. Fig. 1.4 shows that the new test cycles uses much broader engine operating conditions compared to the former driving cycle, NEDC. The engine operation under higher load is unfavorable in terms of particulate, NOx, and other gaseous emissions and it would be more challenging for auto-makers to meet both fuel economy and emission regulations. Thus, it can be concluded that it is becoming

more difficult to meet the stringent regulation on fuel economy and emission despite of the tremendous advancement in engine technologies.

As the SI engines comprise the larger market share compared to the diesel engines, it is crucial to improve the fuel economy of the propulsion systems equipped with SI engines [4]. The state-of-the-art SI engines are mostly equipped with gasoline direct injection (GDI) system, which has the positive effect in fuel economy enhancement also may increase particulate emission. Therefore, SI engines are no longer free from particulate emission regulation, and it has become more challenging for SI engines to meet the reinforced regulations.

1.1.3 Factors affecting efficiency of SI engines

To improve the fuel conversion efficiency of the SI engines, it is prerequisite to understand energy flow in the engine, the factors that affect efficiency, and the causes of the energy losses in the engines.

The analysis on the energy flow in the engine shows that only 20 % of the chemical energy of the fuel is used for propulsion and rest of the energy is used to overcome friction or lost due to heat transfer and exhaust enthalpy [7]. From this result, it can be conceived that reducing the energy lost to the environment would contribute to the engine efficiency improvement.

The fuel conversion efficiency of internal combustion engine is defined as the combustion efficiency multiplied by thermal efficiency [2]. The theoretical thermodynamic cycle of SI engine can be described by the Otto cycle. Thus, the Otto cycle yields the ideal thermal efficiency. The efficiency of the Otto cycle can be expressed as the follows:

$$\eta_{th} = 1 - \frac{1}{r_c^{\gamma-1}} \quad (1.1)$$

This indicates that the higher compression ratio and specific heat ratio are the major factors affecting the efficiency of the Otto cycle. Increasing compression ratio of SI engine is limited by the abnormal combustion phenomenon known as engine knock. This abnormal phenomenon is caused by the auto-ignition of the air-fuel mixture before it is consumed by the propagating flame.

Specific heat ratio depends on the species present in the combustion chamber, and the temperature of the mixture. In the SI engine, adoption of exhaust gas recirculation (EGR) system can reduce temperature during combustion. However, adoption of EGR not only changes the temperature, but also result in change in species. The water vapor and carbon dioxides, however, which are the main compositions of the EGR gas, has lower specific ratio compared to nitrogen or oxygen. Thus, the increment of specific heat ratio may not be realized simply by addition of EGR. Also, in an SI engine, unless the fuel is changed from gasoline to alternative fuels, increment in specific heat ratio is difficult to be realized [8]. Thus, compression ratio of the SI engine is the factor that has the greater importance which affects the theoretical thermal efficiency, and requires more attention.

In addition to the compression ratio, the real-world SI engine efficiency deviate from that of the ideal cycle. The first reason is that the actual combustion takes place under finite time. While the Otto cycle assumes that the all the chemical energy of the fuel is released when the air-fuel mixture is compressed into minimum cylinder volume, the combustion duration in real world SI engine is in the order of milli-seconds. Due to the finite duration of combustion, the air-fuel mixture must be ignited before the end of compression stage to achieve the maximum work output. This causes

the in-cylinder pressure to rise during the compression stage which increases the negative work done by piston, and lower peak pressure than that of Otto cycle which decreases the positive work done by piston. This phenomenon is also expressed as combustion time loss [9].

Second reason is the heat loss to the wall. The Otto cycle assumes that the expansion stage is an adiabatic process, but this is not true in the real world. In SI engine, adequate cooling of combustion chamber and subsequent components must be done to protect them from overheating. During this process, significant amount of the heat energy is transferred to the engine coolant, and cannot be utilized to produce meaningful work.

Third reason is the pumping loss. The load control in SI engine is done by using throttle. When the required load is low, the opening of the throttle is very small and causes intake pressure to be much lower than exhaust pressure. This lead to negative work done by the piston. The amount of the negative work due to throttling becomes very significant when the engine load is very low.

It can be concluded that the main factor affecting efficiency of SI engines is compression ratio, combustion time loss, heat loss, and pumping loss.

1.1.4 Technological developments for efficiency improvement of SI engines

A great variety of new technologies to achieve higher compression ratio and reduced losses have been developed over decades. The technologies can be distinguished into two large categories depending on how they contribute to the efficiency improvement.

Variable mechanism

Variable valve timing (VVT) system enables to adjust the valve opening and closing timing within certain range according to the engine operating conditions. VVT has positive effect on reducing residual gas of which the temperature is very high compared to that of the fresh charge. Lower residual gas helps suppression of knock and compression ratio may be increased [10-12]. VVT can also increase the amount of residual gas under the low load conditions so that throttle opening must be increased to induct adequate amount of fresh charge into the cylinder. This helps to reduce the pumping loss under the low load conditions [12-16].

In addition to VVT system, variable valve lift (VVL) system is another variable mechanism for improving efficiency of the engine. With the adoption of VVL system, it is possible to restrict the amount of fresh charge inducted to the cylinder by altering the valve profile to that with advanced or retarded valve closing timing, and reduce pumping loss. With such valve profiles, it is also possible to reduce the effective compression ratio which contributes in lower in-cylinder temperature at the end of compression stage and enables increment in compression ratio[15]. Also, by altering the valve profiles asymmetrically, the in-cylinder turbulence can be enhanced which may reduce combustion duration [17-21]. The first generation of the VVL systems had two or three distinct valve lifts, and the valve lifts were shifted according to the engine operating conditions [22, 23]. To further improve the merits of VVL system, continuously variable valve lift (CVVL) system has been introduced so that the number of valve profiles realizable would not be limited [24, 25]. The variable mechanism with combination of VVT and VVL systems are also simply termed as the variable valve actuation (VVA) system.

Cylinder deactivation (CDA) is another variable mechanism which can contribute in reduction of pumping loss. The concept of CDA is to run the engine with some of the cylinders only, and leave other cylinders turned-off instead of using all of the cylinders [26-28]. By deactivating part of the cylinders under the same operating engine condition makes each active cylinders to perform more work. This shifts the operating condition of the working cylinders to higher load where pumping loss becomes much lower. CDA can also be implemented dynamically by switching the deactivated cylinder from one another to further reduce power output and shift operating engine load to the higher load [29]. When the calibration is optimized, the efficiency gain can be up to 27% [30].

Use of variable compression ratio (VCR) system is an alternative way to increase compression ratio. High compression ratio can be used under the condition free of knock, and the compression ratio can be lowered when knock must be avoided. VCR system may be realized by altering connecting rod length, combustion head height, eccentric piston pin, or complex linkage system for crank shaft [31-35]. It is reported that adoption of VCR system has potential of 6.5% improvement in fuel economy [34].

Combustion system

The fuel injection system in SI engine which have become very common recently is the GDI (gasoline direct injection) system. Over the processes of fuel injection to the fuel vaporization, in-cylinder temperature decreases due to latent heat of vaporization of the fuel. From this benefit, knock tolerance can be improved and hence the compression ratio can be increased [36-38]. GDI system also has potential to achieve stratified combustion which reduces the dependency of the throttle on the load control, and heat loss to the combustion chamber wall [39, 40].

Combined with GDI system, Engine downsizing is among the most interested technology nowadays. The concept is to reduce the engine displacement in order to shift the engine operating conditions to the higher engine loads where the efficiency of the engine is higher. The reduction in the maximum engine output due to reduction of the engine displacement is then recovered by adding turbocharger/supercharger. One of the example of downsizing is to reduce engine displacement from 3.3L to 2.0L [41]. It is reported that the fuel consumption under the FTP city cycle can be reduced more than 17% [41].

Utilization of external cooled EGR has a positive effect in reduction of pumping loss as the EGR gas replaces some of the fresh charge which would require increased throttle opening to maintain the same amount of the demanded fresh charge [42]. Cooled EGR also helps to mitigate the knock phenomena and compression ratio may be increased. This effect is very important especially for downsized engines where knock phenomena becomes more severe. Improvement in knock tolerance in downsized engine using cooled EGR may gain additional improvement in fuel consumptions [43-45]. Cooled EGR, however, is limited in the quantity that can be supplied as the combustion stability deteriorates severely when the amount of EGR exceeds certain level.

Dedicated exhaust gas recirculation (D-EGR) is a new concept of EGR supplement system which uses one of the cylinders of engine solely to produce incomplete combustion product such as carbon monoxide and hydrogen under the fuel rich condition. The product of fuel rich combustion is then supplied to the other cylinders. D-EGR concept has potential for high EGR operation under high compression ratio compared to that of conventional engines, improve knock tolerance at higher loads, and reduce fuel consumption at lower loads [46].

Homogeneous charge compression ignition (HCCI) also known as controlled auto-ignition (CAI) [47-49], and jet ignition [50-52] combustion technologies have been introduced for reduction of combustion duration. These novel combustion method also enables the lean-limit of the fuel-air charge which has positive effect in reduction of heat lost to the combustion chamber wall as well. Within CAI operating range, it is reported that fuel consumption can be 30% lower than conventional SI engine [48, 49].

The dual fuel combustion is another method for the compression ratio increment. The dual fuel combustion can be realized with the dual injection system where the fuel with higher octane rating, such as ethanol, is used in addition to gasoline when knock mitigation is needed. Previous researches show that the optimum spark timing can be maintained under higher engine load with boosting and under higher compression ratio as well [53-55].

As introduced above, various technologies have been and are being developed for efficiency improvement. The design and operating strategy optimization are prerequisite for maximizing their advantages. However, it is very difficult to address all of the development and optimization of design and operating strategies with experimental approach as it consumes extremely large sum of cost and time. For example, valve profile optimization of fully VVA system with external cooled EGR system under entire engine operating condition would require countless number of experimental conditions, and conducting optimization by means of engine experiment would be almost impossible. To keep the cost and time minimal, the aid of simulation tools is crucial.

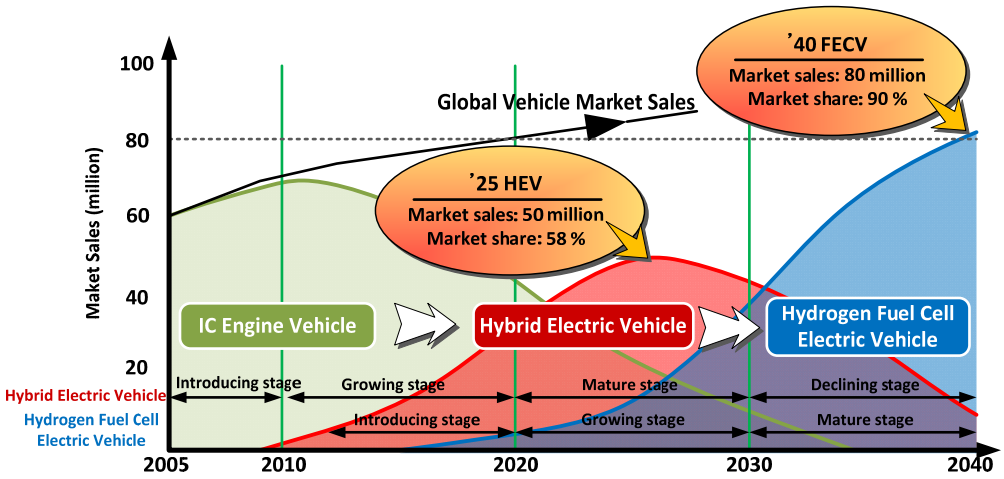

Figure 1.1 Outlook on the market shares of power source of propulsion in 2004 [3]

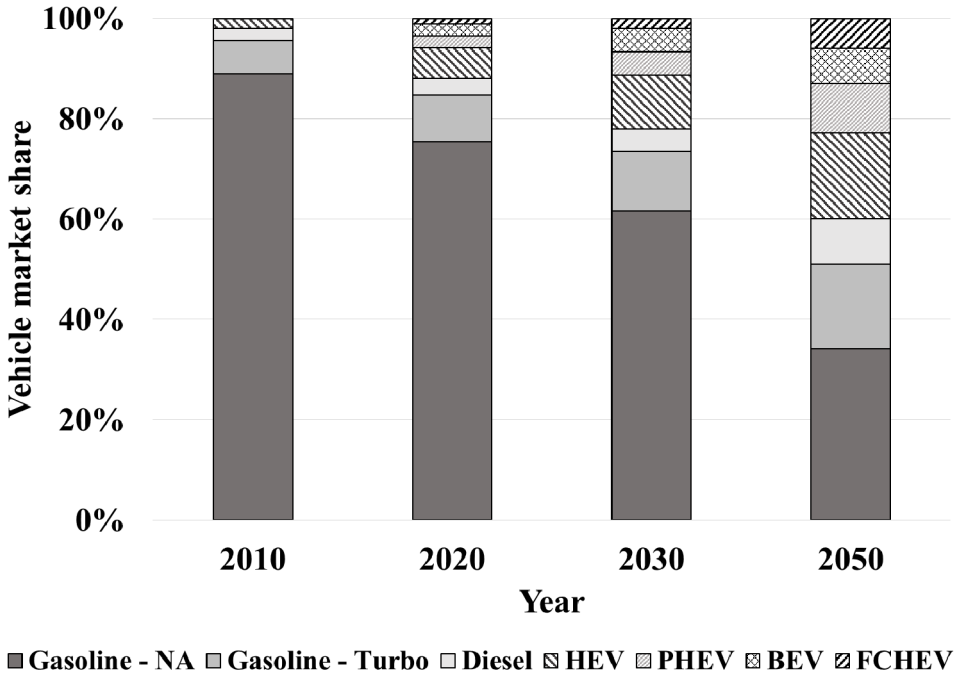

Figure 1.2 Outlook on the market shares of power source of propulsion in 2015 [4]

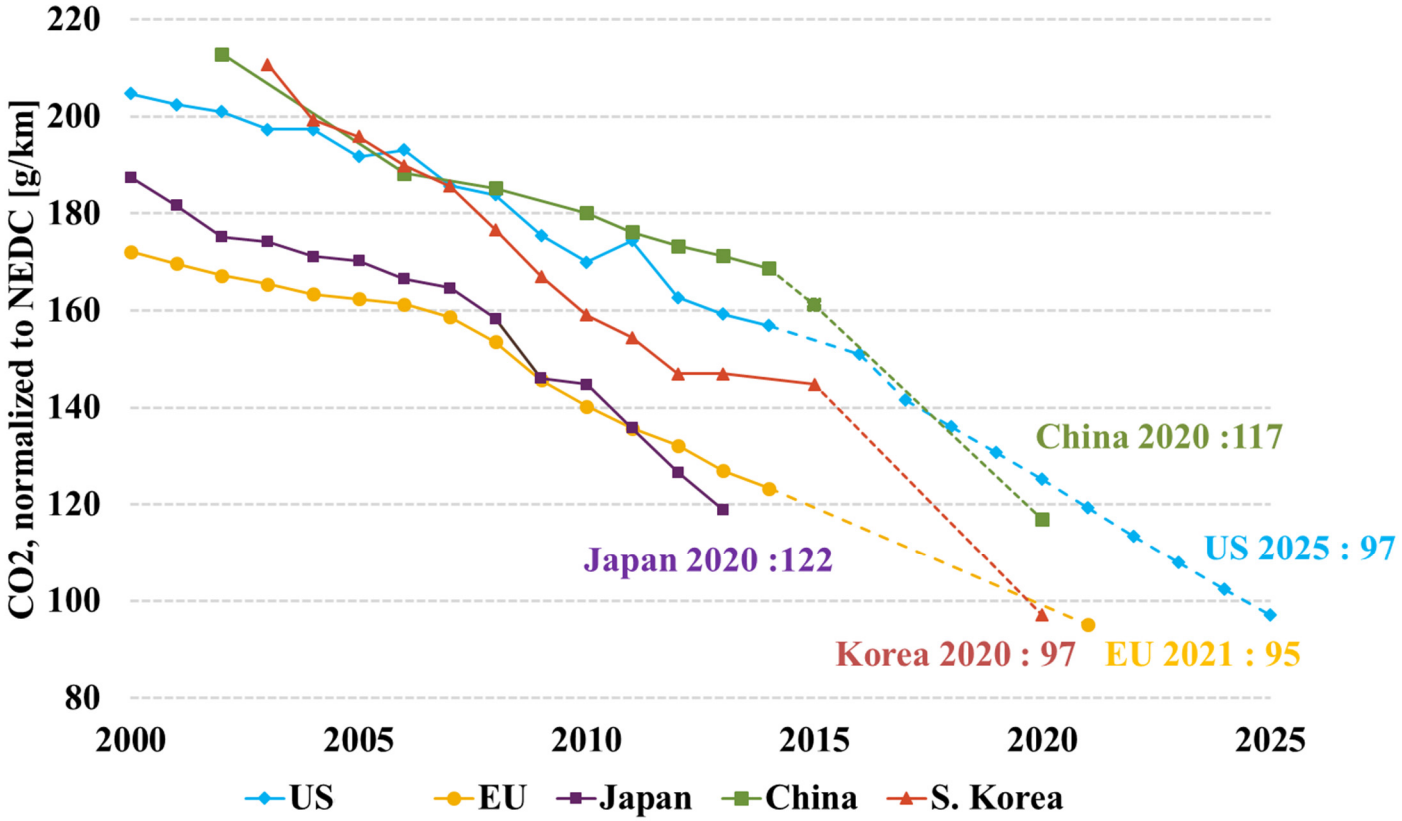

Figure 1.3 Trend in world-wide regulation on CO_2 emission [6]

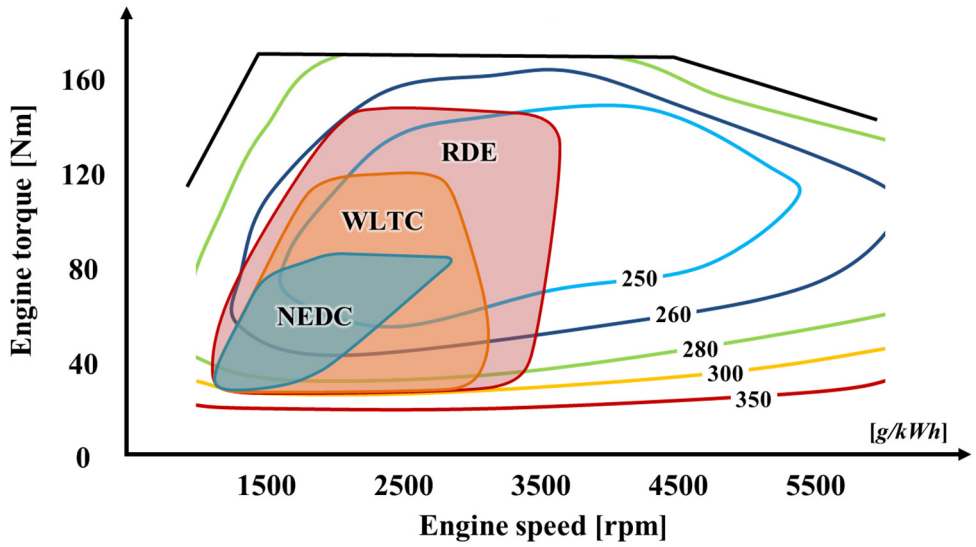

Figure 1.4 Comparison of the engine operating range corresponding to various driving cycles

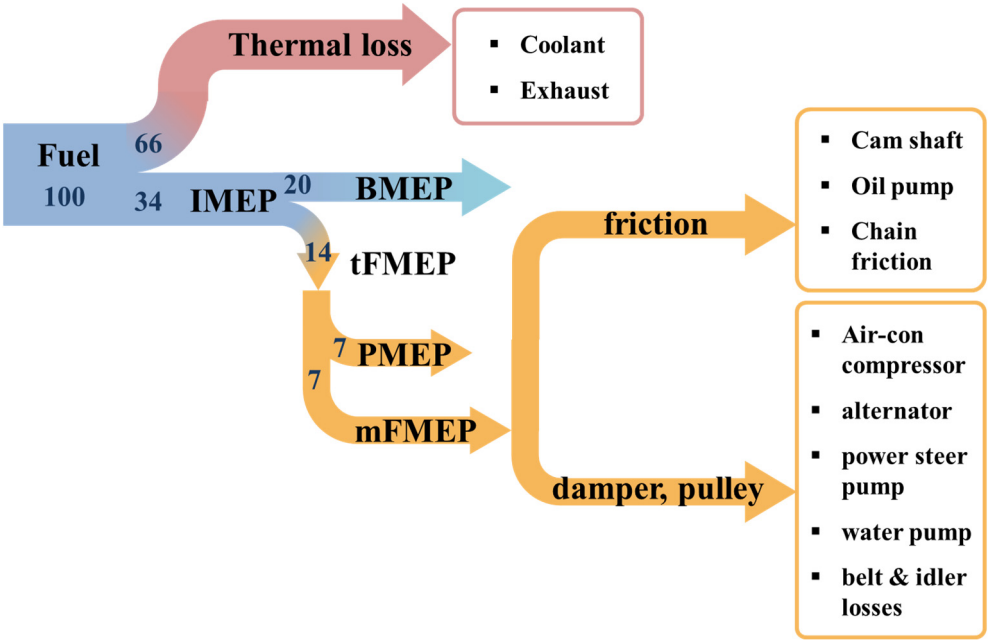

Figure 1.5 Energy flow in a typical gasoline engine [7]

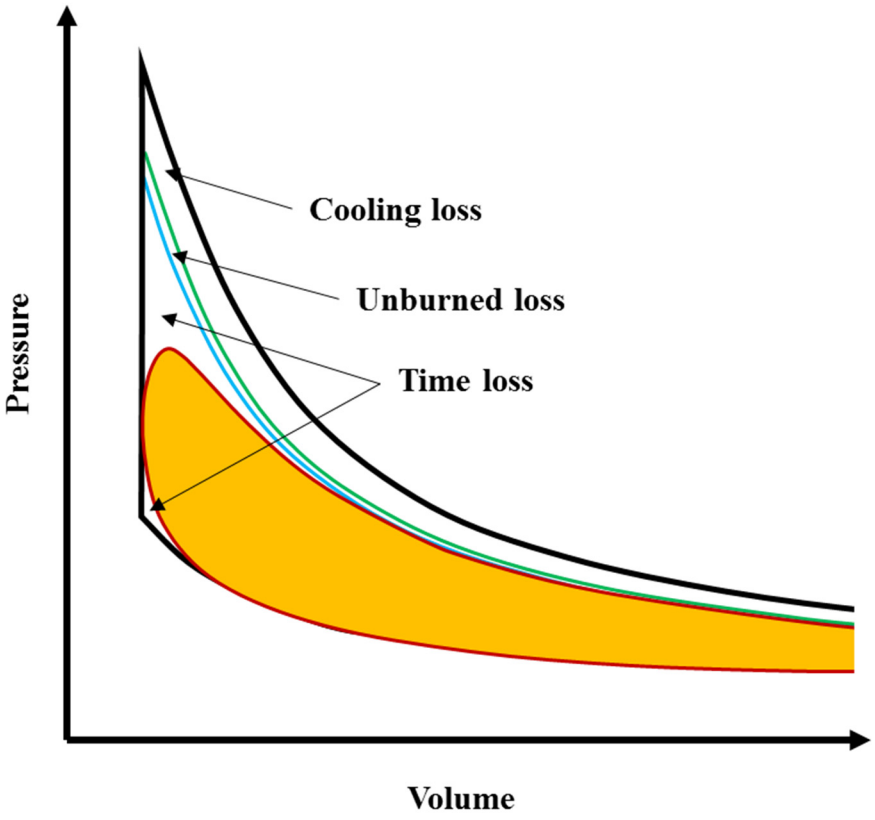

Figure 1.6 Losses in engine cycle [9]

Table 1.1 European regulation standards on the passenger car emission

	Euro 4 (2005)	Euro 5a (2008)	Euro 5b (2011)	Euro 6b (2014)	Euro 6C (2017)
CO	1	1	1	1	1
THC	0.1	0.1	0.1	0.1	0.1
NMHC	-	0.068	0.068	0.068	0.068
NOx	0.08	0.06	0.06	0.06	0.06
PM[1)]	-	0.005	0.045	0.045	0.045
PN[1)]	-	-	-	$6.0 * 10^{12}$	$6.0 * 10^{11}$

1) Applicable to GDI engines only

[units : #/km for PN, g/km for others]

1.2 Literature Review

A tremendous advancement in 3D CFD has been achieved over decades. 3D CFD not only enables to understand the flow field characteristics of the intake and exhaust ports, and combustion chamber, but also can emission formation quantitatively. With the aid of 3D CFD, numerous works have benefited in optimization of engine design [9, 56-60]. So far, Reynolds-averaged models were the most commonly used model in the 3D CFD software tool for internal combustion engine application. Recently, thanks to the improvement in computation power, the large-eddy simulation (LES) is gaining more attention. With the introduction of LES, it is expected that the nature of the cyclic variation in engine combustion would be possible to be understood more deeply [61-65].

Although it is undeniable that the 3D CFD is extremely powerful, computational cost is still very high compared to simpler codes such as 1D simulation tool, or combination of quasi-dimensional (QD) models with 1D simulation tool when the simulation tool is to be used for aiding optimization of engine calibration over wide operating range [66]. The 1D simulation tools for SI engine combustion usually use the Wiebe function which prescribes the burn rate. Wiebe function is capable of producing S-shaped burn rate curve similar to the ones typically observed in the experimental results. However, it is not a predictive model as the constants in the Wiebe function cannot be adjusted automatically according to the engine operating conditions. Therefore, predictive models are being incorporated into the 1D simulation tools. The predictive models are based on the QD models which have been developed for long time. The QD models differ from zero-dimensional models as the in-cylinder mass is separated into two zones by fictitious flame surface, and the thermodynamic properties of each zones are calculated.

The original form of the QD models was developed to work stand alone. Even though QD models may seem primitive, some studies using QD models were successful in predicting the effect of engine design variables and chamber geometry on performance to some extent. The QD models are comprised of in-cylinder turbulence model and burn-rate model. This is because the combustion in the SI engine is governed by the turbulent flame propagation which is largely determined by the turbulence intensity.

Blizard and Keck [67] proposed so-called entrainment model for prediction of the burn rate of engine combustion. The concept of the entrainment model is to assume that the combustion takes place at two separate stages. At the first stage, the turbulent eddies in the unburned gas is engulfed by the flame at the entrainment speed u_e described by the sum of turbulent intensity and laminar flame speed. At the subsequent stage, the entrained turbulent eddies burns at the characteristic time determined from the ratio of the characteristic eddy radius and the laminar flame speed as it is presumed that the combustion process is proceeded by turbulent eddies burning inwards from the peripherals of them. Although it is among the oldest model, it is treated as the most popular representative model among QD combustion model [68].

Tabaczynski et al. [69] made some modifications to the original entrainment model as the previous model was not successful in predicting variation in combustion duration according to the equivalence ratio, and latter part of the combustion processes when flame contacts the combustion chamber wall. To address the issue, the authors revised the turbulence characteristics, and the characteristic time scale for eddy to burn. The evolution of turbulent intensity was described by the conservation of angular momentum of individual eddies. This concept is also known as the rapid distortion theory. The initial value of the turbulent intensity was assumed to be proportional to the mean piston speed and independent of the spark timing. The new

characteristic time for eddy burn-up was described by the sum of chemical reaction time and entrainment time for eddy of size of integral length scale. The chemical reaction time was defined as the time in which laminar flame takes to travel over reaction sites where the average spacing between the sites is described by the Taylor microscale. This concept was derived from the turbulence structure proposed by Tennekes [70]. The modified model was capable of capturing the typical trends in effect of equivalence ratio, amount of external EGR supplied, and spark timing on the combustion duration. Tabaczynski et al. [71] made further amendments into their former model by modifying the characteristic time of eddy burn-up to be the ratio of Taylor microscale and the laminar flame speed instead. This refinement was made in order to allow the smooth transition from ignition processes to flame development processes. This model is still utilized as the basis of the QD simulations [72].

Borgnakke et al. [73] postulated a set of simplified k-ε equations, also known as a two-zone k-ε model, to calculate the evolution of turbulence intensity of burned and unburned zones respectively. A flux term is included to consider the transport of turbulent kinetic energy across the boundary of burned and unburned zone. Also, the authors accounted for the anisotropy of the turbulence to improve the accuracy of the model. Borgnakke et al. [74] upgraded the previous model to predict the swirl velocity and its effect on turbulence by introducing the tangential velocity profile and the production term due to shear of the swirling flow. Later, Davis and Borgnakke [75] added a new term to consider the turbulent kinetic energy production due to the flow motion caused by squish. The authors utilized the developed model to observe the effect of position and number of spark plug on burn rate. Here, the burn rate was calculated by the entrainment model extended by Tabaczynski et al [71]. They drew out the conclusion that even though the dual wall spark sources speeds up the burn rate, the use of single spark located on the center of the combustion chamber would

be more advantageous which is similar to the results yielded by the 3D CFD results [76].

Mansouri et al. [77] introduced the concept of energy cascade to account for the mean and turbulent kinetic energy evolution over the entire engine cycle. The processes of the turbulent kinetic energy was divided into two stages where the kinetic energy of the intake flow is first converted into the mean kinetic energy within the cylinder, and then the turbulent kinetic energy is extracted from the mean kinetic energy at the rate described by production term. The integral length scale necessary for the calculation of the dissipation of the turbulent kinetic energy was assumed to be equal to the instantaneous height of the cylinder with the upper limit set as the half of the bore size. The turbulent kinetic energy during combustion was calculated using the conservation of angular momentum of a turbulent eddy. The initial energy cascade model, however, did not include the term accounting for compressibility explained by rapid distortion theory.

Poulous [78] utilized the energy cascade model initially developed by Mansouri el al. to observe the effect of combustion chamber geometry on the combustion characteristics. For the burn rate prediction, the extended version of entrainment model was used. To consider the characteristics of the flame geometry within the combustion chamber, the QD flame geometry generating code was applied to tabulate the information on the flame area of burned gas volume and piston position.

Santavicca et al. [79] proposed a model for turbulent flame kernel growth based on the Gouldin's [80] interpretation on premixed turbulent flame speed. This model is one of the so-called fractal model. The fractal model assumes that the flame structure is the result of the competing effects of wrinkling due to the turbulence, and smoothing due to laminar burning. This effect is expressed as fractal dimension which

can be obtained from turbulence intensity, and laminar flame speed. The fractal dimension is used for calculating turbulent flame speed by calculating the ratio of the turbulent and laminar flame area. Later, Wu et al. [81] attempted to ameliorate the overshoot in the peak pressure near the end of combustion when fractal model was used for engine cycle simulation. This was done by considering the characteristics of the turbulence intensity being exponentially decaying near the wall.

Recently, it has become more common to incorporate the QD models into the 1D simulation tool rather than using the QD model alone. The general trend of the studies are to improve the former QD models based on the results of 3D CFD so that integration of QD and 1D simulation tools may gain enough fidelity.

Lafossas et al. [82] attempted to reduce the 3D CFD combustion model into the physical 0D model which has better predictability for the transient engine applications. The authors introduced the wrinkling factor based on the classical Damköhler's formulation for calculating the flame propagation speed and hence the burn rate. The model is then implemented in AMESim 1D simulation tool and validated under the transient operating condition. Later, Richard et al. [83] further extended the previous model to include the emission formation predictability by incorporating simple chemical mechanism.

Bozza et al. [84] evolved the energy cascade model from the original from in [77] to reproduce the turbulence evolution characteristics closer to that of 3D CFD. To match the mean kinetic energy and turbulent kinetic energy simultaneously, constants are multiplied to reduce the mean kinetic energy flux to the cylinder from the incoming flow across the intake and exhaust valves. The production rate of the turbulent kinetic energy, and subsequent energy extraction rate from mean kinetic energy is calculated independently. With these modification, the authors successfully

reproduced the 3D CFD results to some extent. The authors also attempted to observe the predictability of engine knock by implementing the reduced chemical mechanism with the combustion model and the developed turbulence model.

Sjeric et al. [85] made a modification to the production term in the equation of dissipation rate of single zone k-ε model. For the burn rate prediction, weighted mean of fractal and entrainment model was used. The model was compared with the 3D CFD simulation results conducted under two different engine design. Even though the developed model could not capture the difference in turbulence characteristics due to different engine design as the 3D CFD did, the model was successful in predicting the evolution of turbulent kinetic energy similar to the results yielded by 3D CFD for one engine design.

Grasreiner [86] attempted to model the evolution of swirl and tumble strength of the in-cylinder flow and their contribution to the turbulent kinetic energy flow using the relationship between angular momentum and turbulent kinetic energy. The authors used the assumption that the tumble and swirl motion of the flow are independent. The production of the turbulent kinetic energy was calculated from the change rate in rotational energy of tumble or swirl direction respectively during open valve and closed valve phase separately. During the closed valve phase, a time decay term was introduced to consider the decay in tumble motion due to piston movement during the compression stage. This term was calculated from the 3D CFD results obtained under simplified condition where the piston was fixed at a given position. With the appropriate tuning, the developed model was successful in reproducing angular momentum of tumble and swirl, and turbulent kinetic energy simultaneously. The turbulence model was then combined with the entrainment model and implemented in GT-Power. After the integrated model was validated under several engine operating conditions, virtual calibration of the given engine was conducted.

Bellis et al. [87] evolved the energy cascade model to reproduce the results closer to the results yielded by state-of-the-art 3D CFD tools. Several new modifications are made from the former model described in [84]. The integral length scale is fitted to the 3D CFD results instead of calculating it from geometrical information of the engine. An additional term is added to account for the mean flow generated due to piston motion. Based on the developed turbulence model, Bellis et al. [88] postulated a new phenomenological combustion model which extends the combustion model with weighted mean of fractal and entrainment model. The developed model was implemented in 1D simulation tool, GT-Power, and with the appropriate values for tuning constants, the authors successfully validated the model over engine speed from 1800 to 5100.

The previous works have been quite successful in reproducing the results obtained in either experiment or 3D CFD even though the QD modeling of the turbulence and combustion are based on rather simple concepts. The basic form of widely used turbulence and combustion models can be found in Tables 1.2 and 1.3 for comparison between one another.

Table 1.2 Equations of zero-dimensional turbulence models

Model name	Relevant equations	Descriptions
Simplified k-ε [73]	$dk = \frac{2}{3}(1+a)k\frac{d\rho}{\rho} - \varepsilon + F_k$ (1.1)	Rate of change in turbulent kinetic energy
	$d\varepsilon = \frac{4}{3}\varepsilon\frac{d\rho}{\rho} - 1.44\frac{\varepsilon^2}{k} + F_\varepsilon$ (1.2)	Rate of change in turbulence energy dissipation
	$F_k = \frac{\dot{m}}{m}(k_i{}^* - k)$ (1.3)	Flux of turbulent kinetic energy
	$F_\varepsilon = \frac{\dot{m}}{m}(\varepsilon_i{}^* - \varepsilon)$ (1.4)	Flux of dissipation rate
	$k_i{}^* = \begin{cases} 0 & (unburned\ zone) \\ k_u\left(\rho_b/\rho_u\right)^{0.66} & (burne\ zone) \end{cases}$ (1.5)	
	$\varepsilon_i{}^* = \begin{cases} 0 & (unburned\ zone) \\ \varepsilon_u\left(\rho_b/\rho_u\right)^{1.33} & (burne\ zone) \end{cases}$ (1.6)	
Energy cascade [77]	$\frac{dK}{dt} = \frac{1}{2}\dot{m}_i V_i{}^2 - K\frac{\dot{m}_{ex}}{m} - P$ (1.7)	Rate of change in mean kinetic energy
	$\frac{dk}{dt} = P - \varepsilon - k\frac{\dot{m}_{ex}}{m}$ (1.8)	Rate of change in turbulent kinetic energy
	$P = 0.3307\frac{k^2}{\varepsilon}\frac{U^2}{l_t{}^2}$ (1.9)	Production rate of turbulent kinetic energy
	$\varepsilon = 0.5443\frac{u'^3}{l_t}$ (1.10)	Dissipation rate of turbulent kinetic energy

Table 1.3 Equations of quasi-dimensional combustion models

Model name	Relevant equations	Descriptions
Entrainment (Eddy burning)	$\dot{m}_e = \rho_u \mathrm{A}_f u_e$ (1.11)	Rate of entrainment of unburned gas
	$\dot{m}_b = \frac{m_e - m_b}{\tau}$ (1.12)	Rate of burning
	$\tau = \frac{\lambda}{S_L}$ (1.13)	Characteristic time scale of burning entrained mass
Fractal	$\dot{m}_b = \rho_u A_f \left(\frac{A_T}{A_f}\right) \mathrm{S_L}$ (1.14)	Rate of combustion
	$\frac{A_T}{A_f} = \left(\frac{\eta}{L}\right)^{2-D}$ (1.15)	Ratio of turbulent flame area to projected area
	$\mathrm{D} = 2.0 \frac{S_L}{u' + S_L} + 2.35 \frac{u'}{u' + S_L}$ (1.16)	Fractal dimension

1.3 Objectives

It is evident that the engines will become more complex system as increased number of variable mechanisms such as VVA system will be applied in near future for efficiency improvement. Due to the high computational cost of 3D CFD tools, it would be infeasible to utilize the 3D CFD tool for optimization of engine calibration under full range of engine operating conditions. The 1D simulation tools with QD combustion model can take an important role in engine calibration optimization, but the applicability of the previous models are limited as many of the models were validated under fewer number of operating conditions. For the QD combustion model to be utilized for optimization of engine calibration and assessment of a new technology before the engine development, models have to be more physically intuitive, and applicable to various engine designs without excessive tuning of adjustable constants. Therefore, the objectives of this study are:

1. Development of 0D turbulence model which has better applicability under the various engine designs and operating conditions, including VVA function, to provide the turbulence intensity at spark timings.

2. Development of the phenomenological QD combustion model which predicts similar results to those of 3D CFD with small number of adjustable constants to enhance the reliability of 1D simulation tool.

3. Assessment of the developed model with analysis on the energy flow in the engine, and the effect of new technologies such as VVA function on engine performance.

Chapter 2. Development of zero-dimensional turbulence model under motored condition

2.1 Necessity of model development

There has been numerous attempts to develop model to predict the turbulence intensity under various conditions. Recently, a new model developed by De Bellis et al. [89] can be considered as the state-of-the-art model since this model can predict the evolution of both turbulence intensity and mean flow velocity close to those of 3D CFD. It was also confirmed that the model can be applied to the engine equipped with VVA system. This model consists of equations shown below:

$$\frac{dK}{dt} = \dot{K}_{in} - \dot{K}_{ex} + \dot{K}_{tum} - \Psi - D \tag{2.1}$$

$$\frac{dk}{dt} = \dot{k}_{in} - \dot{k}_{ex} + \Psi - d \tag{2.2}$$

$$\dot{K}_{in} = \left[\frac{1}{2}\dot{m}_{in,f}\left(c_{in}v_{in,f}\right)^2 + \frac{1}{2}\dot{m}_{ex,b}\left(c_{ex}v_{ex,b}\right)^2\right] \tag{2.3}$$

$$\dot{K}_{tum} = c_{tum}K\left(\frac{\dot{\rho}}{\rho} - \frac{\dot{V}}{V}\right)\left(w_h\frac{h_{max,PL}}{h_{max,\,FL}} + (1 - w_h)\frac{\theta_{IVC} - 360}{180}\right) \tag{2.4}$$

$$\Psi = c_P\frac{K}{k}d + 0.5\,\frac{\dot{K}_{tum}}{K}\left(1 - \frac{x_p}{S}\right)k \tag{2.5}$$

$$D = c_D\frac{K}{k}d + 0.5\,\frac{\dot{K}_{tum}}{K}\left(1 - \frac{x_p}{S}\right)(2K - k) \tag{2.6}$$

$$d = 0.09^{0.75}\frac{k^{1.5}}{L_I m^{0.5}} \tag{2.7}$$

where C_D, C_{ex}, C_{in}, C_P, C_{tum}, and, W_h are adjustable constants, K is the mean kinetic energy, k is the turbulent kintetic energy, m is the trapped mass, ρ is the in-cylinder density, S is the stroke, v is the velocity of fluid across the valve during intake stroke, V is the cylinder volume. The subscripts in, and ex indicate that the properties are from intake and exhaust ports, respectively [89].

Although the model has very high accuracy in prediction of turbulence intensity, the model contains 6 adjustable constants as shown in the Eqs. 2.1 to 2.7. The large number of adjustable constant is unfavorable when considering the applicability of the model. This is because the model constants used in the former study are not universal, and additional calibration of constants would be necessary if the design of the engine is altered. Also, the large number of adjustable constants would require excessive effort in tuning the constants. Another issue of this model is that only the peak in the profile of mean flow velocity appearing at the end of compression stroke was reproduced even though there is another peak in the profile at the beginning of expansion stroke. It is thought that the source of the peaks in the mean flow velocity was not identified correctly. This would reduce the physical consistency of the model.

For a model to be utilized for various applications, and conditions with high reliability, the model with less number of adjustable constants with physical background is needed. Therefore, in this study, a new 0D turbulence model with minimum number of adjustable constants with physical background was developed.

2.2 Modeling approach

Before proceeding with the development of the model, former models widely used in 0D sense are reviewed. The well-known models are simplified k-ε model, angular momentum model, and energy cascade model. The characteristics of each models are explained in the following paragraphs.

Simplified k-ε model is capable of predicting the turbulent kinetic energy and its dissipation rate when initial values for turbulent kinetic energy and its dissipation rate, and evolution in density are given. The advantage of using this model is that the information on the integral length scale is not required as the dissipation rate of turbulent kinetic energy is obtained from the governing equation. The integral length scale is computed from the Eq. 1.11 given in Table 1.2. When the flux terms are considered correctly, it is reported that the turbulent kinetic energy during combustion can also be predicted with relatively high accuracy [85]. Simplified k- ε model, however, can be accurate only if the initial values are correctly given. Therefore, it is a general approach that the simplified k-ε model is usually coupled with angular momentum model or energy cascade model.

Angular momentum model is capable of predicting evolution the tumble strength in addition to the turbulence intensity [86, 90-92]. This model assumes that the intake generated flow is converted into tumble flow. The characteristics of the tumble flow can be expressed with the change in angular momentum of the in-cylinder fluid. The production of turbulent kinetic energy is obtained from the shear due to rotational flow. For the calculation of the angular momentum, loss due to wall friction needs to be predicted precisely. The loss due to wall friction was calculated from the wall friction coefficient [90-92], or characteristic decay function obtained from 3D CFD [86].

Although tumble strength can be predicted with relatively high accuracy, this model tends to overpredict the turbulent kinetic energy at the end of compression stroke.

Energy cascade model is capable of calculating mean and turbulent kinetic energy. The concept of this model is that the kinetic energy flux due to intake and exhaust gas flow is first converted into the mean kinetic energy, and some portion of the mean kinetic energy is extracted as turbulent kinetic energy. Then, a portion of turbulent kinetic energy is converted into heat due to viscous dissipation. The advantage of this model is that evolution of turbulent kinetic energy can be estimated by itself and not necessarily coupled with other models. However, as shown in Table 1.2, the information on integral length scale must be supplied to the model to calculate production and dissipation rate of the turbulent kinetic energy. Thus, one of the key factor in enhancing the accuracy of the simulation results using this model is to find an appropriate description of the integral length scale.

As introduced above, the 0D turbulence models have distinct characteristics, and inherent advantages and disadvantages. Since the purpose of developing turbulence model is to reproduce the 3D CFD results, the model which can be consistent with 3D CFD models as much as possible has to be selected as a starting point. In this sense, the disadvantage of the energy cascade model that the integral length scale is required in advance may be overcome as the integral length scale can be obtained from 3D CFD. Also, energy cascade model is capable of calculating the mean kinetic energy which is also a relevant value for the turbulence generation. From these points, energy cascade model would be more consistent to 3D CFD. Therefore, in this study, 0D turbulence model was developed based on the energy cascade model.

2.3 Integral length scale for energy cascade model

2.3.1 Modeling approach

There have been numerous attempts to model the integral length scale of the in-cylinder turbulence characteristics. In a former study, it is postulated that the integral length scale is in the order of intake valve lift as the turbulent eddy generated while the flow passes the aperture between intake valve and engine head should be smaller than intake valve lift [67]. Later, the integral length scale was calculated from the instantaneous height of the cylinder (h_{cyl}) with the limitation that it cannot exceed the half the size of bore [77, 78, 93]. With the supplement of 3D CFD calculation, it was found that integral length scale may scale well when the volume to the power of one third ($\sqrt[3]{V_{cyl}}$) is used [84].

However, when comparing the integral length scale calculated from 3D CFD with the former models, it can be found that there are still some discrepancies as shown in Fig. 2.2. To compensate the difference, the former study attempted to reproduce the integral length scale using Wiebe function which is usually used for expressing S-shaped burn rate of engine [87]. The latter approach can enhance the accuracy of the dissipation rate estimation as integral length scale close to that of 3D CFD is supplied. Nevertheless, the dependency of the integral length scale on engine design parameters, and operating conditions have not been clarified yet. In order to constitute the model which is less specific to the engine under study, the characteristics of the integral length scale must be analyzed more thoroughly.

As the direct measurement of temporal characteristics of in-cylinder turbulence is difficult, the characteristics of the integral length scale were analyzed with 3D CFD

results instead. In this study, STAR-CD ver. 4.22 was used for 3-D CFD calculation. The number of the mesh for given engine geometry was approximately 850,000 at BDC. For the calculation of in-cylinder turbulence, k-ε RNG model was used.

2.3.2 Comparison of multi-cycle simulation results to the single cycle simulation results

Before proceeding with calculation of turbulence characteristics for various computing conditions, the effect of simulation duration must be identified. The multi-cycle simulation was performed under the condition given in Table 2.1. The results in Fig. 2.3 show that the integral length scale show very small discrepancies over two consecutive cycles. Similar results were also reported in the previous work which used a different CFD software [84]. From this result, it can be concluded that single cycle simulation is adequate. Therefore, the calculation of the in-cylinder turbulence was performed over single cycle only.

2.3.3 Sensitivity analysis on integral length scale

The sensitivity analysis on the integral length scale was carried out to investigate how it changes according to the engine speed, engine load, valve timing, valve profiles, and engine designs such as stroke-to-bore ratio (SB ratio), and compression ratio. The simulation conditions, engine specifications, valve profiles, and piston geometries can be found in Table 2.1, Figs. 2.4, 2.5, and 2.6, respectively. To obtain higher compression ratio with the given engine, extruded piston was utilized to reduce clearance volume (V_c) at the end of compression. To observe the effect of the piston geometry on the profile of the integral length scale, the position of the extruded piston

at TDC was descended to obtain the same compression ratio as the cases with conventional piston.

When changing SB ratio, two possible choices exist. First, the bore and V_c were kept constant. However, this method changes the compression ratio in order to exclude the effect of the change in geometry of V_c and intake port. Next, the displaced volume (V_d) and compression ratio were kept constant, and bore and stroke were altered. With this method, the changes in the geometry of the intake port as well as the flow characteristics were inevitable. When increasing SB ratio while maintaining the constant V_d and compression ratio, the combustion chamber and piston geometry were scaled down in isometric way. For the case with lower SB ratio, it was impossible to maintain the compression ratio by simply scaling up the combustion chamber and piston geometry. In this case, extruded piston was used to achieve the identical compression ratio. A case with conventional piston is observed in addition to check the effect of piston geometry although the compression ratio would be lower.

The profiles of the integral length scale of each conditions are grouped into several categories to compare the influence of the factors listed above. Observing the results displayed in Figs. 2.7 to 2.14, the valve profile seems to have the greatest impact on the profile of the integral length compared to the others. Nevertheless, most of the cases shared very similar shape during the compression and first part of the expansion stage regardless of the changes in parameters. Fig. 2.15 shows the profiles of integral length scale two different engine geometries also share many similarities.

To quantify the similarities of the profiles of the integral length scale, locations and magnitudes of local maximum and minimum points of the profiles of the integral length scale were defined as shown in Fig. 2.16, and summarized in Fig. 2.17. Fig. 2.17 shows that the location and magnitude of local minimum point near firing TDC,

denoted as the second local minimum point, is almost invariant unless compression ratio, or geometry of V_c is altered. When observing Fig. 2.11, it can be postulated that the compression ratio is the main factor that affects the magnitude of the minimum point. However, Fig. 2.13 suggests that the compression ratio is not a dominant factor affecting the magnitude of the minimum point. This is because Fig. 2.13 shows that the cases with compression ratio of 6.95, 12.0, and 14.6 have the magnitude of local minimum point very similar to one another. In addition, Fig. 2.15 shows that the magnitude of local minimum point for two different engines are similar to one another even if the size of V_c are different. From these results, it is crudely deduced that the characteristics of the local minimum point are affected by both the size and geometry of V_c.

The location and magnitude of local maximum point are scattered more widely compared to the second local minimum point. It is presumable that the flow velocity across the intake valve has a dominant effect on the location and magnitude of the local maximum point. However, the result in Fig. 2.8 suggests that the change in valve flow velocity cannot describe it properly as the change in engine speed did not show notable influence. The dependency of local maximum point magnitude on V_d may be crudely deduced as V_d of case 15 is decreased from the base case while those of case 16, and 17 is increased from the base case. Correlating the integral length scale to the characteristics of the size of the cylinder volume is feasible as the previous measurements report the dependency of the integral length scale on the size of the confinement [69].

The first local minimum points also show widely scattered distribution compared to the second local minimum points. In case of the first local minimum points, the deviation of the local minimum location is larger compared to that of the magnitude. The dominant factor affecting the characteristics of the first local minimum point may

be the valve timing and profile since they are major factors affecting flow characteristics near intake TDC. However, result shown in Fig. 2. 17 does not show clear dependency on the valve timing, and profile.

The result of the sensitivity analysis can be summarized as below:

1. The overall profile of integral length scale stays unchanged regardless of engine operating conditions, valve timing, and engine designs unless the valve profile is shortened to a certain limit.

2. The second local minimum point is almost invariant unless the size and geometry of V_c is changed.

3. The location of the local maximum point is less likely to be altered while the magnitude is changed according to V_d.

4. The first local minimum point also shows widely scattered distribution. The clear dependency of the characteristics of the local minimum point, however, is not observed.

2.3.4 Fitting model of the integral length scale

To formulate the expression for the integral length scale, the profile of the integral length scale was fragmented into three parts. The locations for fragmentation were determined with the location of local maximum and minimum points. Up to this point, the methodology is the same as the former study [87]. After the fragmentation, former study used the Wiebe function to reproduce the integral length scale of each part. In this study, however, an expression with physical connection to the engine geometry was used instead. The length scales related to the engine cylinder are bore,

h_{cyl}, or $\sqrt[3]{V_{cyl}}$. Since the bore is constant, and does not vary with time, expression for h_{cyl}, and $\sqrt[3]{V_{cyl}}$ were used for fitting the fragmented parts of the profile of the integral length scale.

The magnitude and location of the local maximum and minimum points have been deduced based on the sensitivity analysis. The second local minimum point was almost invariant, so the magnitude and location of this point was simply taken from average values which are 731.8 CA, and 0.00134 m, respectively. The result from the cases with different sizes and geometry of V_c were excluded when computing the average values. To incorporate the effect of size and geometry of V_c, it is postulated that the magnitude of the second local minimum point is dependent on the aspect ratio of V_c which is defined as the volumetric size of V_c divided by the surface area of V_c. For variety of simulation cases, the magnitude of this local minimum point shows nearly linear dependency on the aspect ratio as shown in Fig. 2.18. From this tendency, the correlation for the magnitude of the second local minimum point was deduced as below:

$$l_{2nd\ local\ minimum} = a\ (V_c/A_c) + b \tag{2.8}$$

where a, and b are model constants.

As for the location of the local maximum point, it may be described by the average value as the deviation in location was marginal. The average value for the location was calculated to be 606 CA. For describing the magnitude of this point, average value is calculated first, and correlated to the V_d as shown below:

$$l_{local\ maximum} = c\ V_d + d \tag{2.9}$$

where c, and d are model constants.

In case of the first local minimum point, clear dependency on the relevant parameters was not observed. Thus, the averaged values for location and magnitude are used similar to the second local minimum point. The average values of the location and magnitude of this point is 396.7 CA, and 0.00043 m, respectively.

The fitted integral length scale based on the above description is shown in Figs. 2.19 and 2.20. This is the result obtained when the expression for h_{cyl} was used for the first and second parts, and $\sqrt[3]{V_{cyl}}$ for the third part, respectively. For the case with very short valve opening duration, the expression for $\sqrt[3]{V_{cyl}}$ is used instead of h_{cyl} for the first part of the fragments to account for the difference in profile. The physical meaning of using h_{cyl} can be thought that the main driving source of the in-cylinder flow is piston motion which directs the flow to the direction of piston motion. On the other hand, the physical meaning of using $\sqrt[3]{V_{cyl}}$ can be considered as the flow is less likely to be directed strongly in one specific direction but rather closer to isotropic manner.

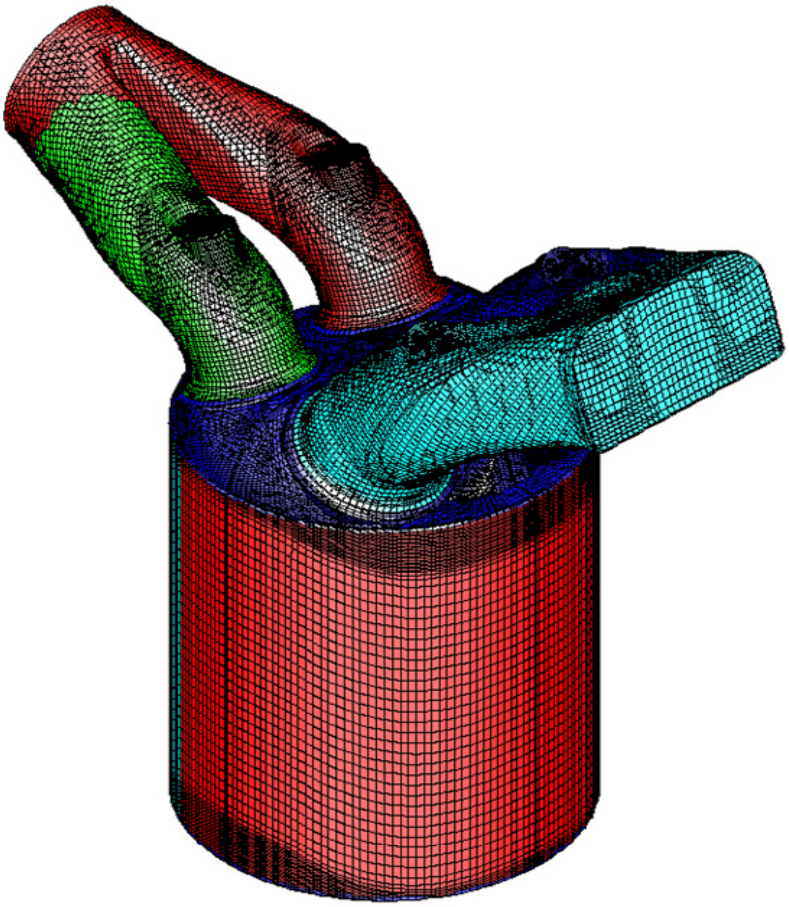

Figure 2.1 Engine mesh generated at BDC of test engine 1

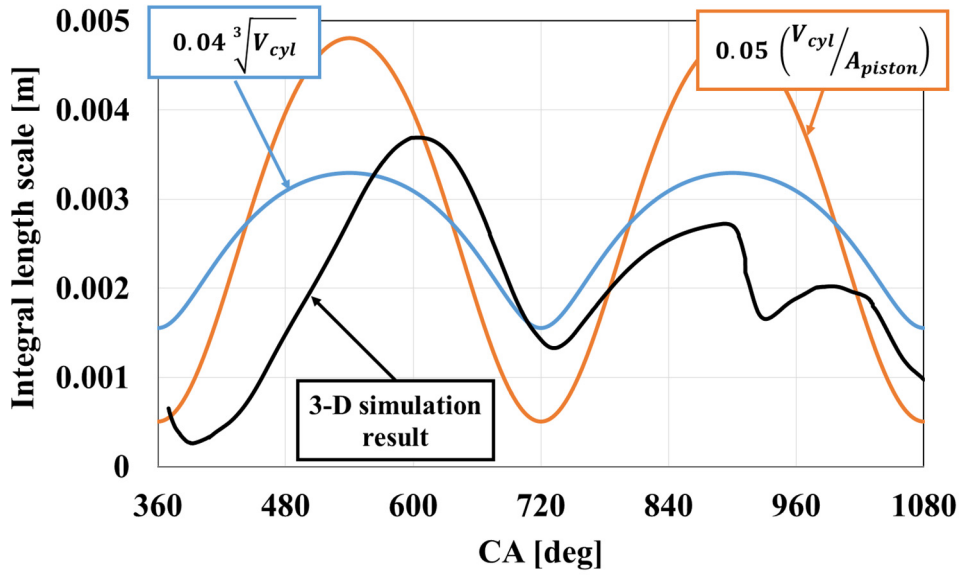

Figure 2.2 Comparison of profiles of the integral length scale obtained from 0D models to 3D simulation result

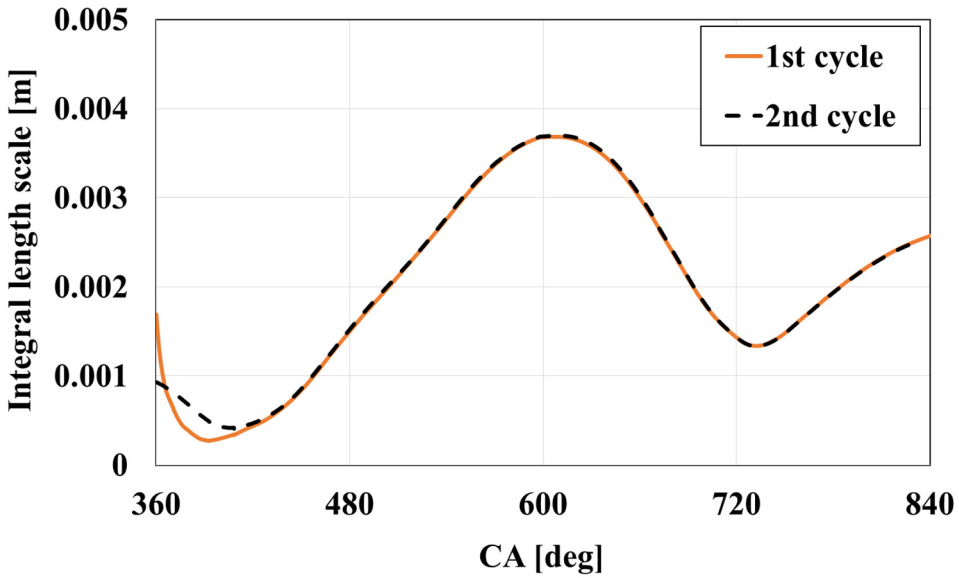

Figure 2.3 Comparison of profiles of the integral length scale of two consecutive cycles

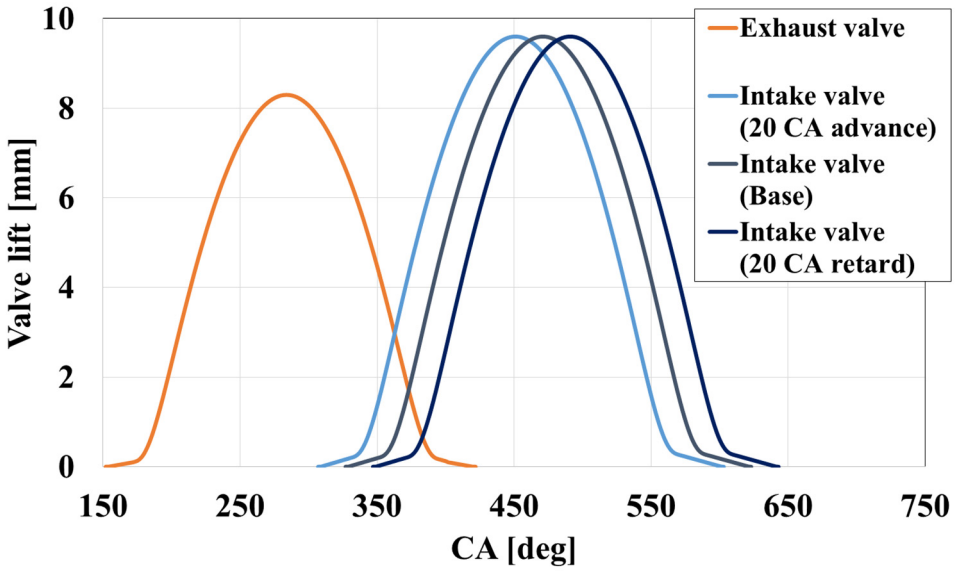

Figure 2.4 Valve profiles of various valve timing

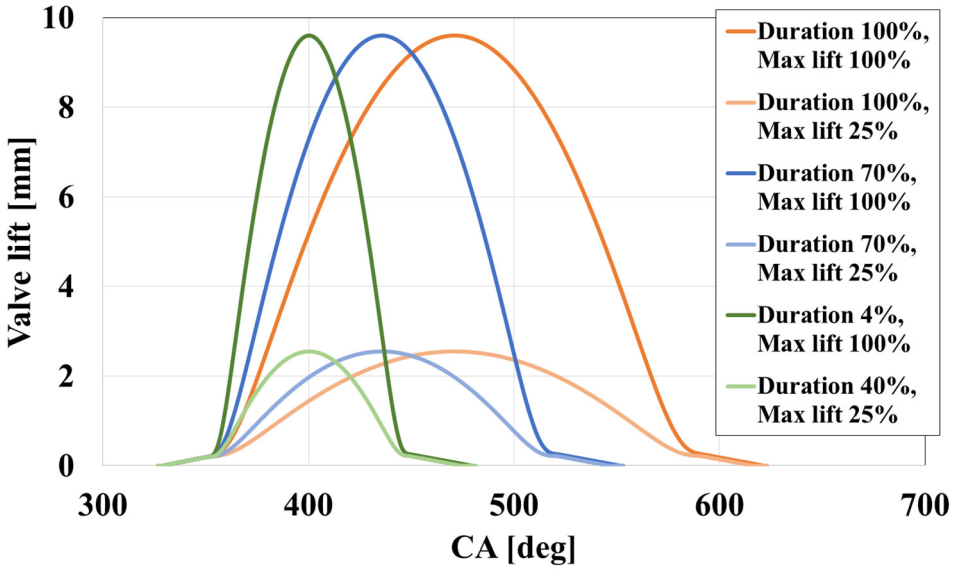

Figure 2.5 Valve profiles of various lift and duration

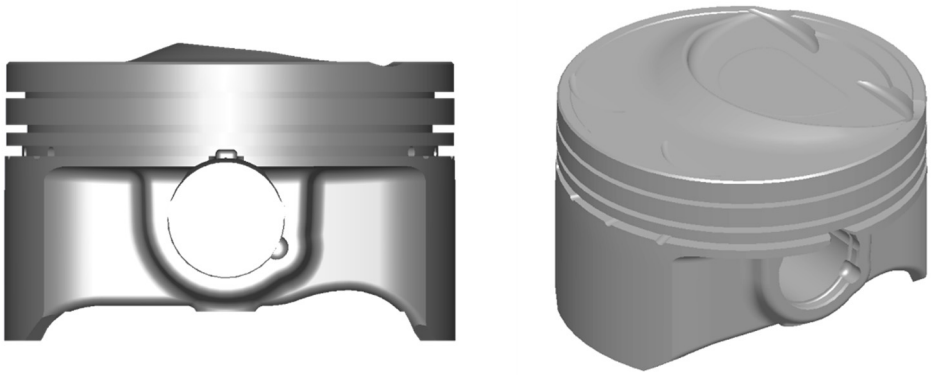

(a)

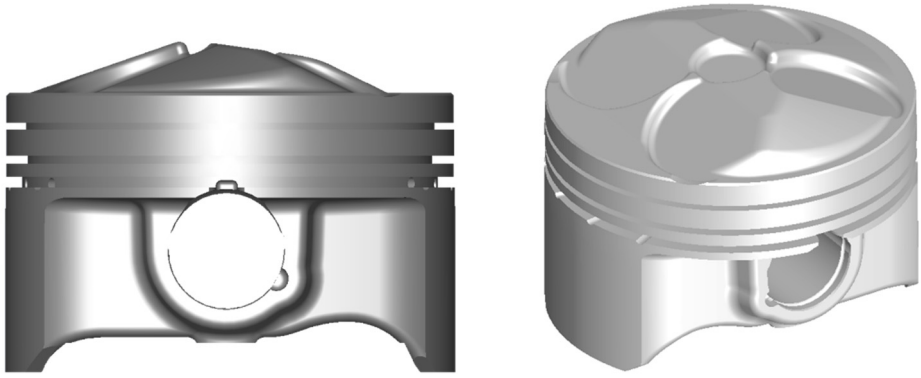

(b)

Figure 2.6 Geometry of (a) conventional, and (b) extruded piston

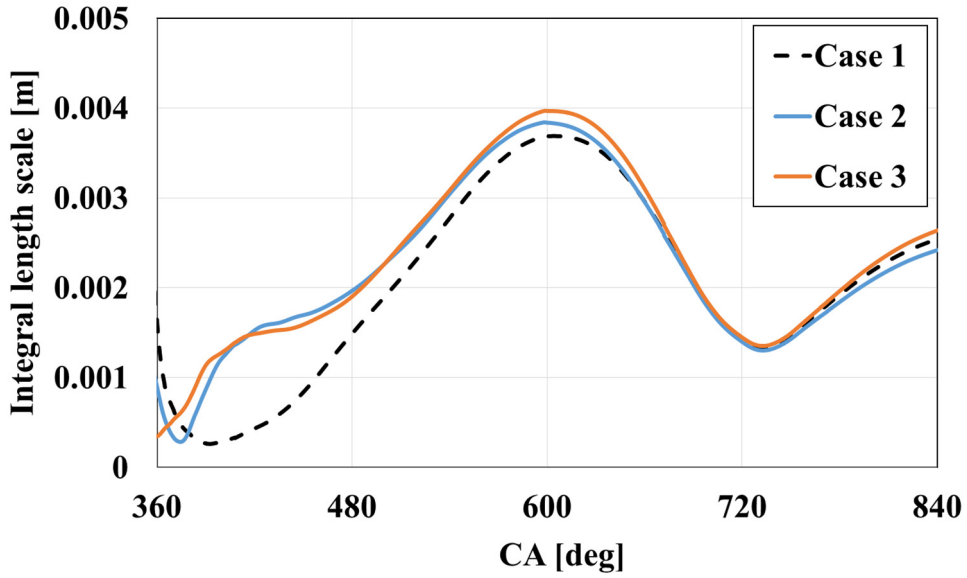

Figure 2.7 Profiles of the integral length scale of various intake pressure

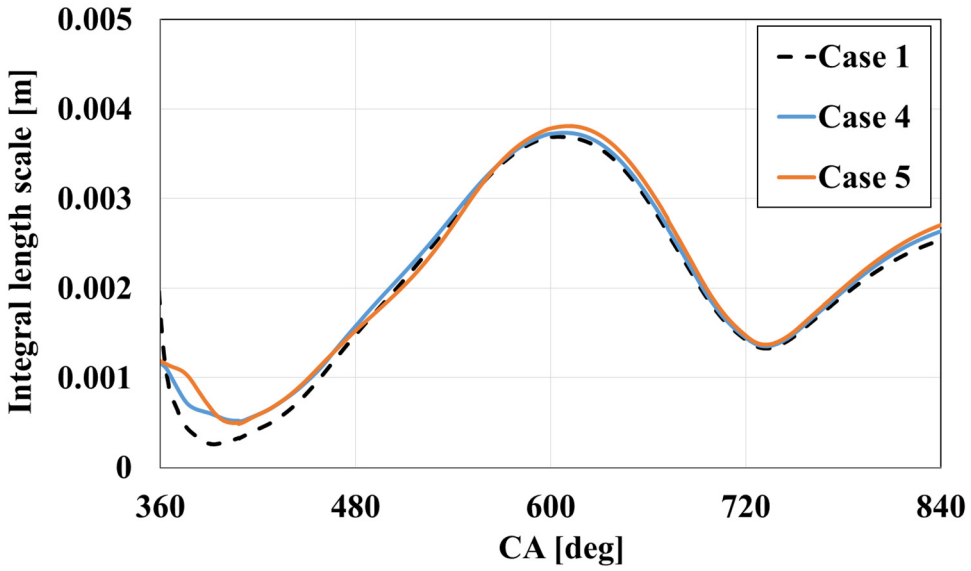

Figure 2.8 Profiles of the integral length scale of various engine speed

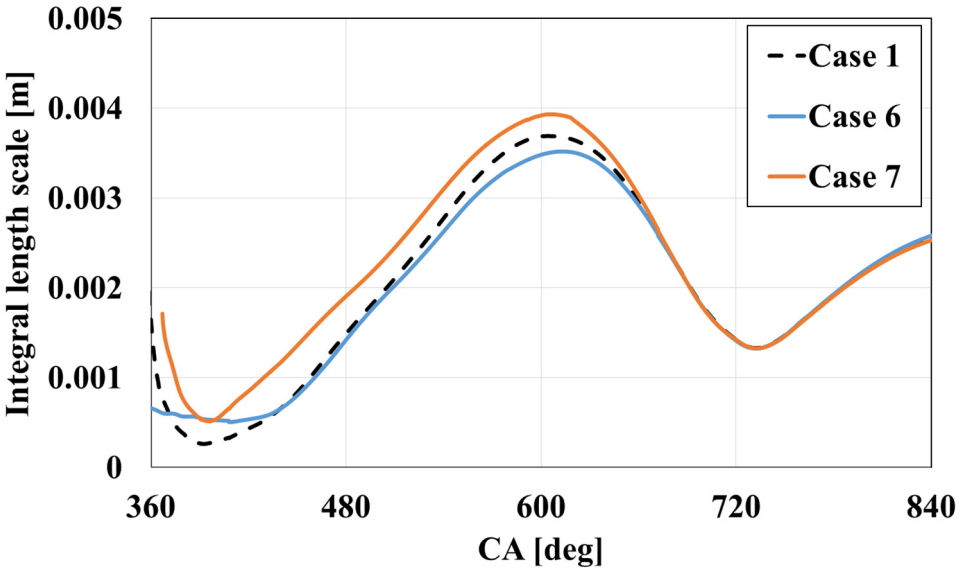

Figure 2.9 Profiles of the integral length scale of various valve timings

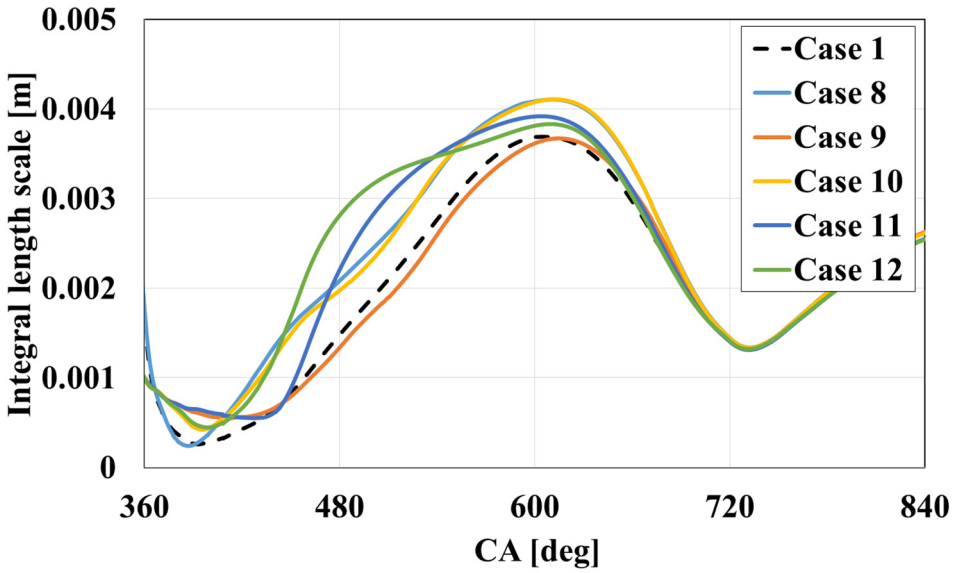

Figure 2.10 Profiles of the integral length scale of various valve profiles

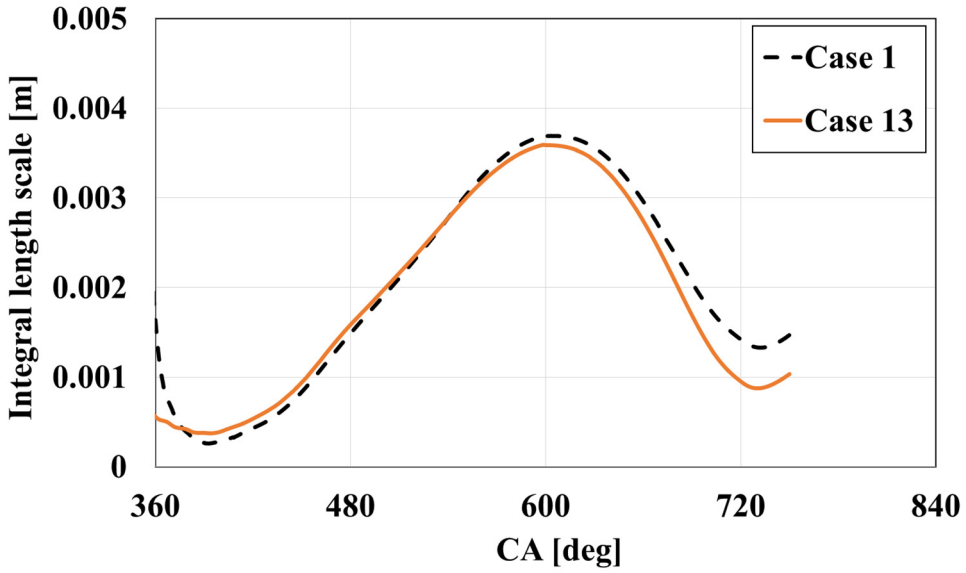

Figure 2.11 Profiles of the integral length scale of different compression ratio

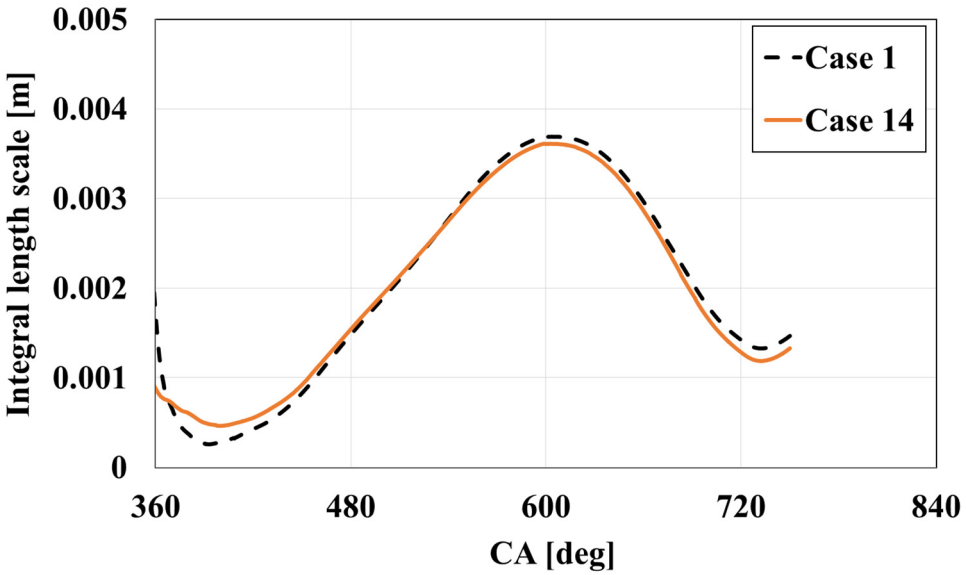

Figure 2.12 Profiles of the integral length scale of different piston under CR 9.5

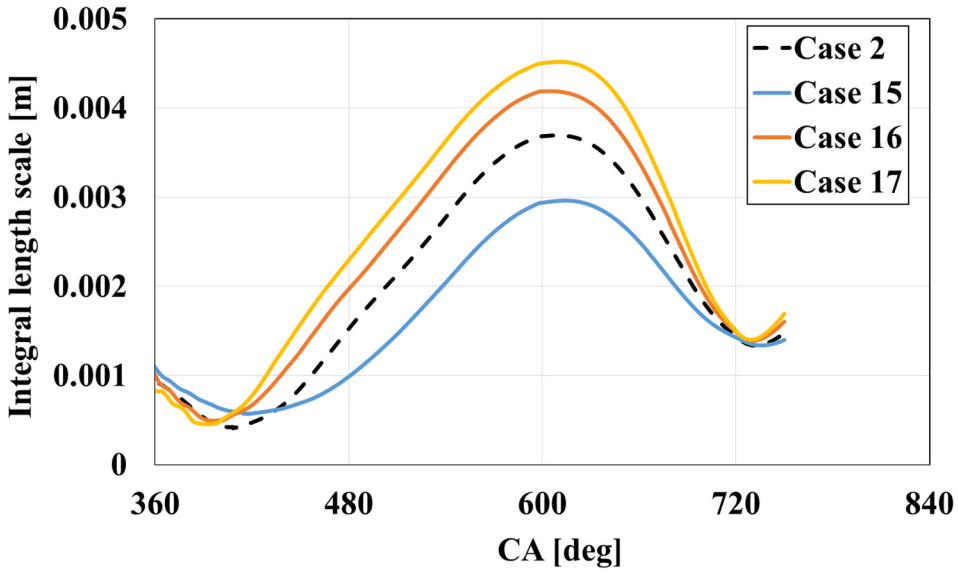

Figure 2.13 Profiles of the integral length scale of different SB ratio with constant bore

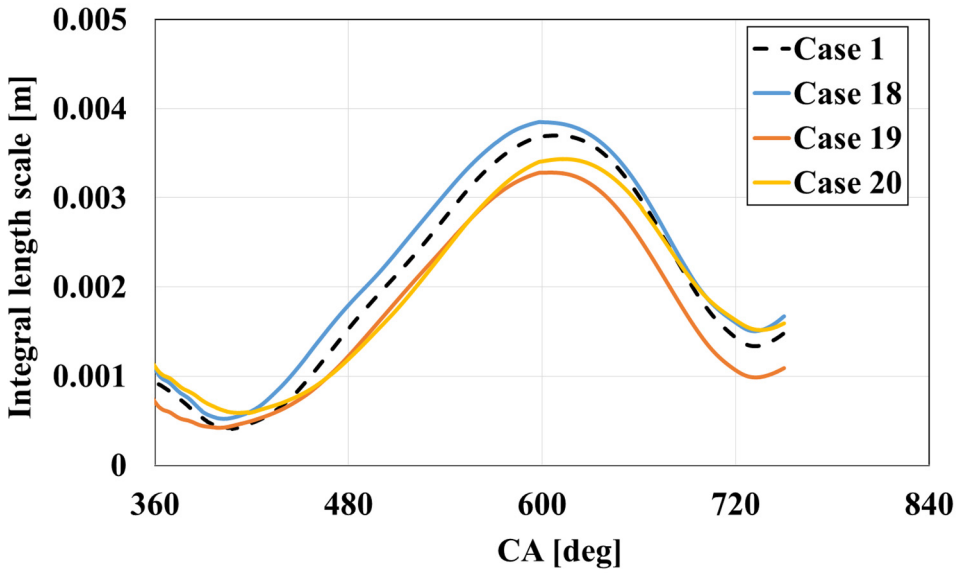

Figure 2.14 Profiles of the integral length scale of different SB ratio with constant cylinder volume

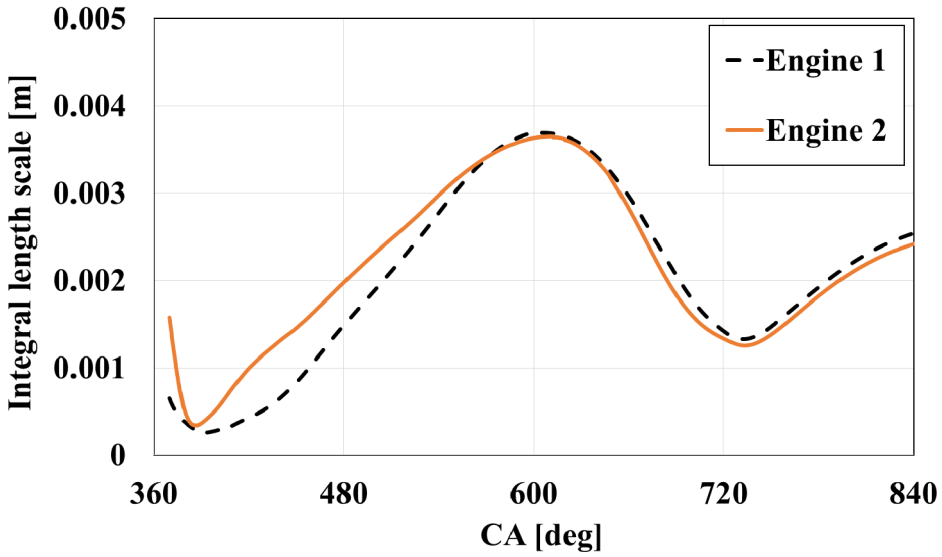

Figure 2.15 Profiles of the integral length scale of different engines

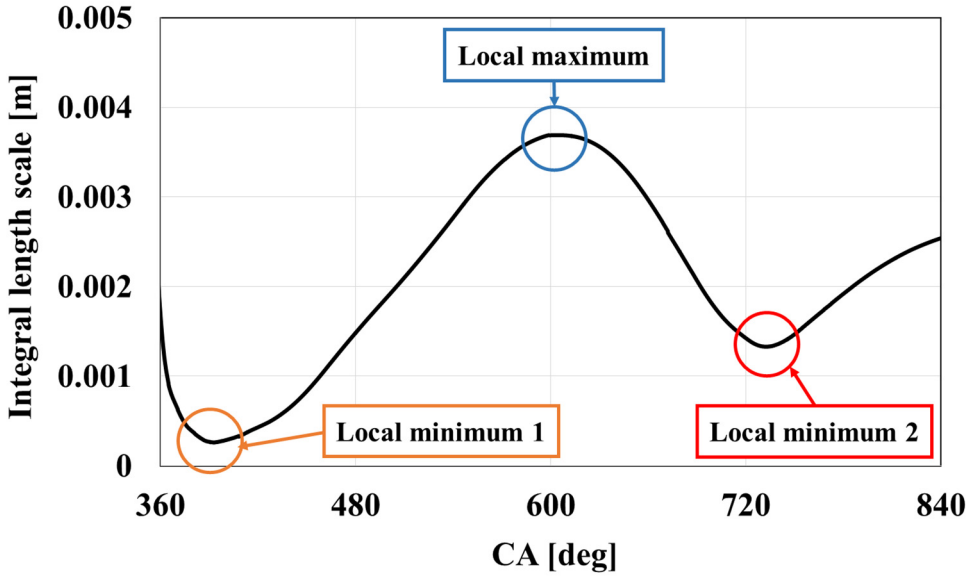

Figure 2.16 Definition of local maximum and minimum points

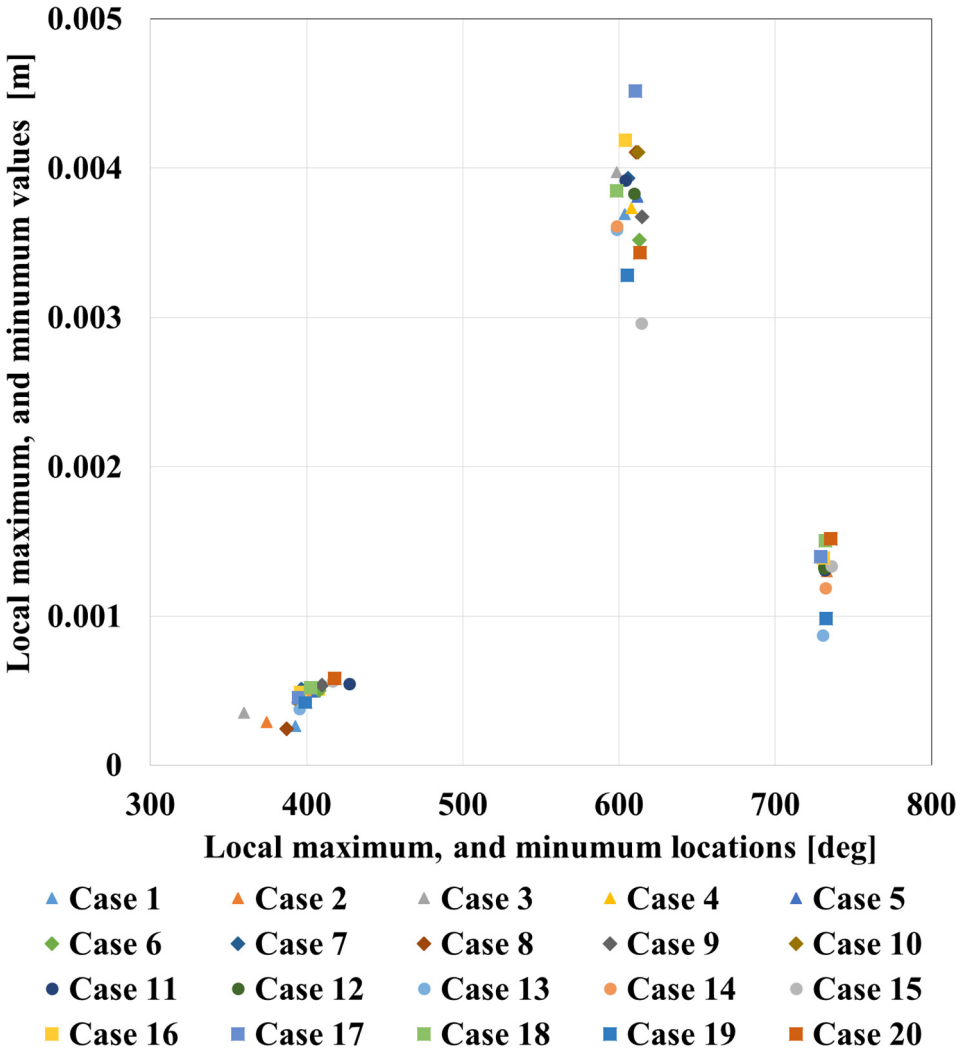

Figure 2.17 Location and magnitude of local maximum and minimum points

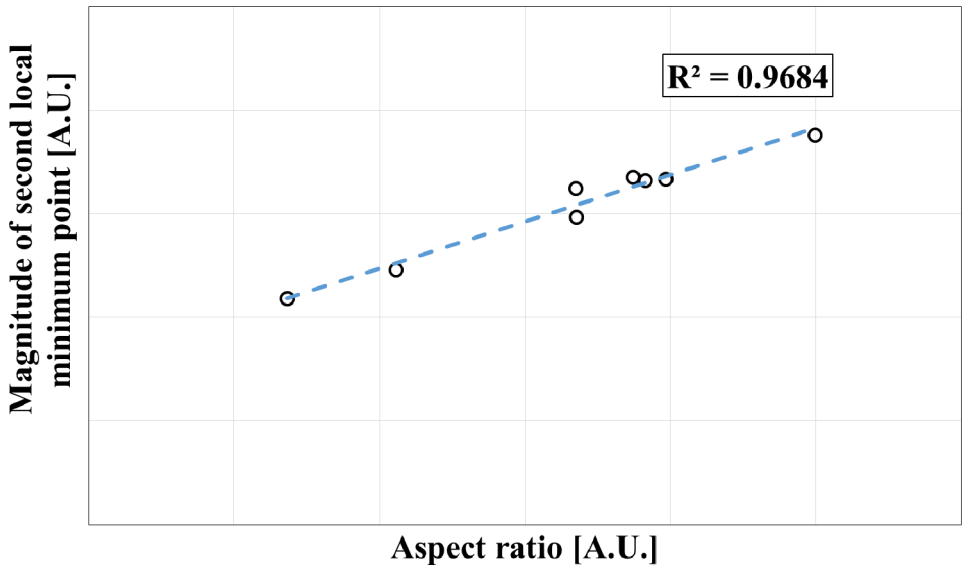

Figure 2.18 Correlation between aspect ratio of clearance volume and magnitude of second local minimum point

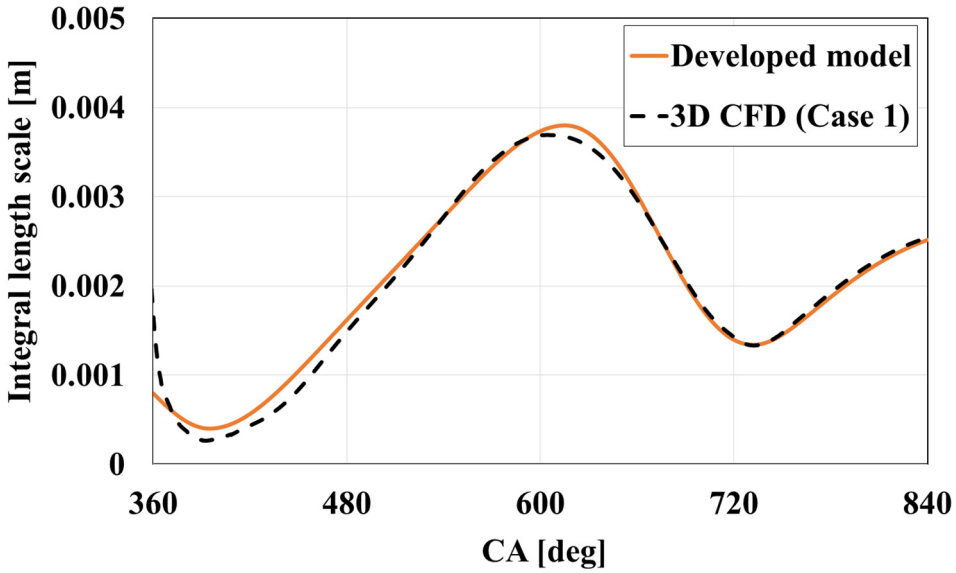

Figure 2.19 Comparison of profiles of the integral length scale reproduced with developed model for the case with nominal valve profiles

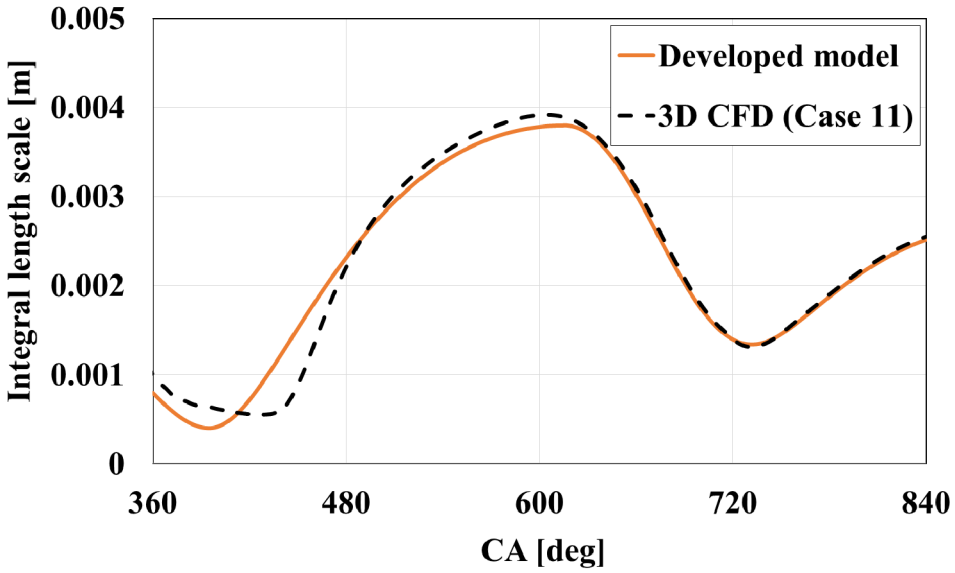

Figure 2.20 Comparison of profiles of the integral length scale reproduced with developed model for the case with short duration valve profiles

Table 2.1 Simulation conditions for sensitivity analysis of integral length scale

Case	Engine speed	Engine load	Valve timing	Valve profile	Bore/ Stroke	Compression ratio
1	1500	WOT (P_i = 1 bar)	Base (IVO 351 CA)	Base	86 / 86	9.5 (conv. Piston)
2	↑	Part (P_i = 0.6 bar)	↑	↑	↑	↑
2	↑	Boosted (P_i = 2 bar)	↑	↑	↑	↑
4	3000	WOT (P_i = 1 bar)	↑	↑	↑	↑
5	6000	↑	↑	↑	↑	↑
6	1500	↑	IVO 20 CA advance	↑	↑	↑
7	↑	↑	IVO 20 CA retard	↑	↑	↑
8	↑	↑	Base (IVO 351 CA)	Duration 100% Max lift 25%	↑	↑
9	↑	↑	↑	Duration 70% Max lift 100%	↑	↑
10	↑	↑	↑	Duration 70% Max lift 25%	↑	↑
11	↑	↑	↑	Duration 40% Max lift 100%	↑	↑
12	↑	↑	↑	Duration 40% Max lift 25%	↑	↑

13	↑	↑	↑	Base	↑	13.3 (ext. piston)
14	↑	↑	↑	↑	↑	9.5 (ext. piston)
15	↑	↑	↑	↑	86 / 60.2	6.95 (conv. Piston)
16	↑	↑	↑	↑	86 / 111.8	12.0 (conv. Piston)
17	↑	↑	↑	↑	86 / 137.6	14.6 (conv. Piston)
18	↑	↑	↑	↑	78.8 / 102.5	9.5 (conv. Piston)
19	↑	↑	↑	↑	96.8 / 67.8	9.5 (ext. piston)
20	↑	↑	↑	↑	96.8 / 67.8	7.95 (conv. piston)

Table 2.2 Specifications of engines used for comparison of integral length scale

Parameter	Specification	
	Engine 1	Engine 2
Bore / stroke	86 / 86	77.2 / 84
Connecting rod	146.25	140
Intake port type	Tumble	Swirl
Piston geometry	Flat bowl type	Bath tub type

2.4 Analysis on the kinetic energy of in-cylinder flow

The 0D turbulence models introduced in previous literatures incorporate a constant smaller than 1 multiplied to the kinetic energy flux term during intake processes [84, 87]. The purpose of introducing such constant is considered to be an effort to match both the magnitude of the mean and turbulent kinetic energy to those of 3D CFD. The physical meaning of the constant, however, is not well established in the literatures. Therefore, in this study, the necessity of the constant and relevant parameters to quantify the magnitude of the constant were analyzed.

To analyze the characteristics of total mean kinetic energy of in-cylinder flow, it was assumed that the total kinetic energy in the cylinder can be expressed by sum of mean kinetic energy, turbulent kinetic energy, and energy converted to heat due to viscous dissipation. The total kinetic energy calculated with the assumption above was then compared with the cumulative kinetic energy calculated from kinetic energy flux integrated from IVO to IVC. There is a large discrepancy between the total kinetic energy and the cumulative kinetic energy shown in Fig. 2.21. The reason for such phenomenon can be found from the characteristics of the flow field in Fig. 2.22. The flow passing through the intake valve is not perfectly coherent, and wakes occur near the intake valves. The wakes generated after the flow restrictions are considered as a contributing factor to loss in the kinetic energy. Thus, it can be deduced that the constant multiplied to the kinetic energy flux term accounts for the loss in the kinetic energy due to incoherent flows formed when fluid passes the valve.

From the result above, it is postulated that the three step mechanism of the original energy cascade model which consist of kinetic energy flux during intake process, mean kinetic energy accumulated in cylinder due to intake flow, and turbulent kinetic energy generated due to shear in mean flow, is to be modified into four step

mechanism to account for the loss in kinetic energy during the intake process. To account for the loss in kinetic energy during the intake process, an appropriate correlation to describe the phenomenon is needed. There are several correlation introduced to quantify the losses in the fluid flow components [94]. The correlation are mostly expressed with the geometrical characteristics of the given fluid flow component. It is, however, difficult to apply the existing correlation to the in-cylinder flow as the geometry of engine is quite different from those of fluid flow components. Thus, this study attempted to seek a correlation to find the appropriate loss term which can incorporate the characteristics of the given engine geometry.

As a first step, the ratio between the total kinetic energy to the cumulative kinetic energy was calculated for the cases 1, 8~12 listed in Table 2.1. The selected cases have distinct flow velocity across the intake valves when compared to one another as the flow velocity changes drastically with valve profiles. Fig. 2.23 suggests that the ratio the total kinetic energy to the cumulative kinetic energy is close to constant except for a particular incidence with short duration valve profile. Therefore, for the most of the cases, it would be possible to quantify the magnitude of the loss in kinetic energy flux with an appropriate constant. It is, however, less significant to use constant value when the correlation is to be applied to various engine operating conditions, and engine designs as the temporal evolution of the loss in kinetic energy flux is not truly constant, and the value of the constants would not be universal. To improve the generality of the correlation for kinetic energy loss phenomena, another assumption is introduced that the loss in kinetic energy flux is related to the ratio of piston speed and flow velocity across the valve.

$$C_{loss} \approx 1 - \left(\frac{V_{piston}}{V_{valve}}\right)^{n} \tag{2.10}$$

This assumption is deduced from Fig. 2.23 which indicates that the loss increases with the increase in the flow velocity across the valve while the piston speed of the selected cases are the same as the engine speed was held constant. This expression can also be interpreted in a sense that the loss in kinetic energy flux is governed by the degree of the amplification in the flow velocity since the flow across the valve is driven by the piston movement, and the magnitude of the flow velocity is a resultant of piston speed amplified by factor of the ratio between the cross-sectional area of the cylinder, and the valve flow area. The exponent *n* in Eq. 2.10 was empirically determined to be 0.5. Using a simple continuity equation, this expression can be simplified as follows:

$$C_{loss} = 1 - \left(\frac{V_{piston}}{V_{valve}}\right)^{0.5} \tag{2.11a}$$

$$= 1 - \left(\frac{\rho_{cyl} A_{valve}}{\rho_{cyl} A_{piston}}\right)^{0.5} \quad \left(\dot{m} = \rho_{cyl} A_{valve} V_{valve} = \rho_{cyl} A_{piston} V_{piston}\right) \tag{2.11b}$$

$$= 1 - \frac{D_{valve}}{Bore}(nC_d)^{0.5} \quad \left(A_{valve} = \frac{\pi}{4} n {D_{valve}}^2, A_{piston} = \frac{\pi}{4} Bore^2\right) \tag{2.11c}$$

where *n* is the number of valves, C_d is the discharge coefficient of the intake port, and D_{valve} is the reference diameter used for calculating discharge coefficient. The discharge coefficient of intake port is defined as the ratio between the actual flow area between the head and valve to the reference area [2]. In this study, the discharge coefficient of the given engine was obtained from 3D port flow analysis using STAR-CCM+.

For the verification of the derived correlation above, the cumulative kinetic energy with correction factor was obtained from the equation below, and compared with the total kinetic energy.

$$\dot{E}_{total} = \frac{1}{2}\dot{m}_i V_i^2 \times \frac{D_{valve}}{Bore}(nC_d)^{0.5} \quad (2.12)$$

The results plotted in Fig. 2.24 shows that the developed correlation can sufficiently predict the total amount of in-cylinder kinetic energy with the use of geometrical information of the given engine. To confirm the generality of the correlation, it was also applied to the engine with different intake port and combustion chamber design. The specifications of the engine are shown in Table 2.3. Even though the engine speed, valve timing, and engine geometry are different, Fig. 2.25 shows that the predictability is preserved.

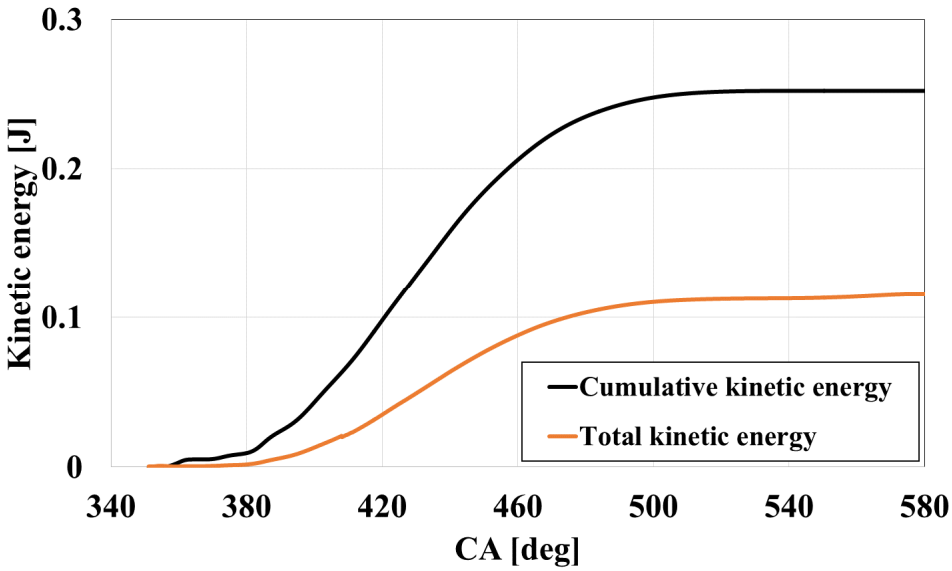

Figure 2.21 Comparison of the total kinetic energy to cumulative kinetic energy

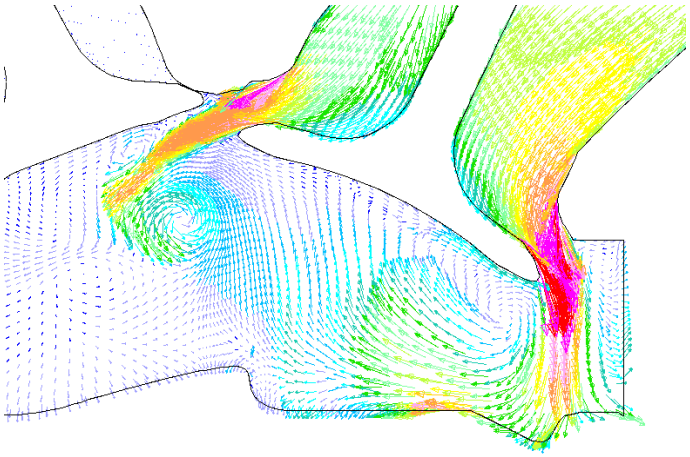

(a)

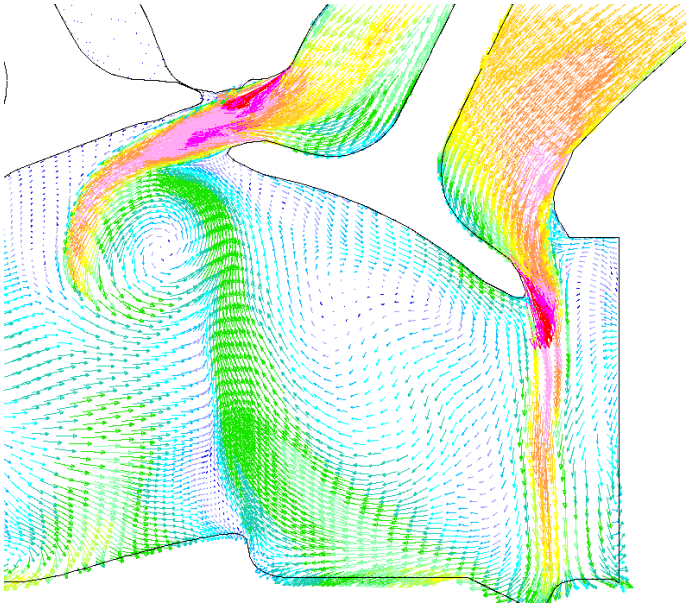

(b)

Figure 2.22 Velocity field during intake stroke at (a) 405 CA and, (b) 430 CA

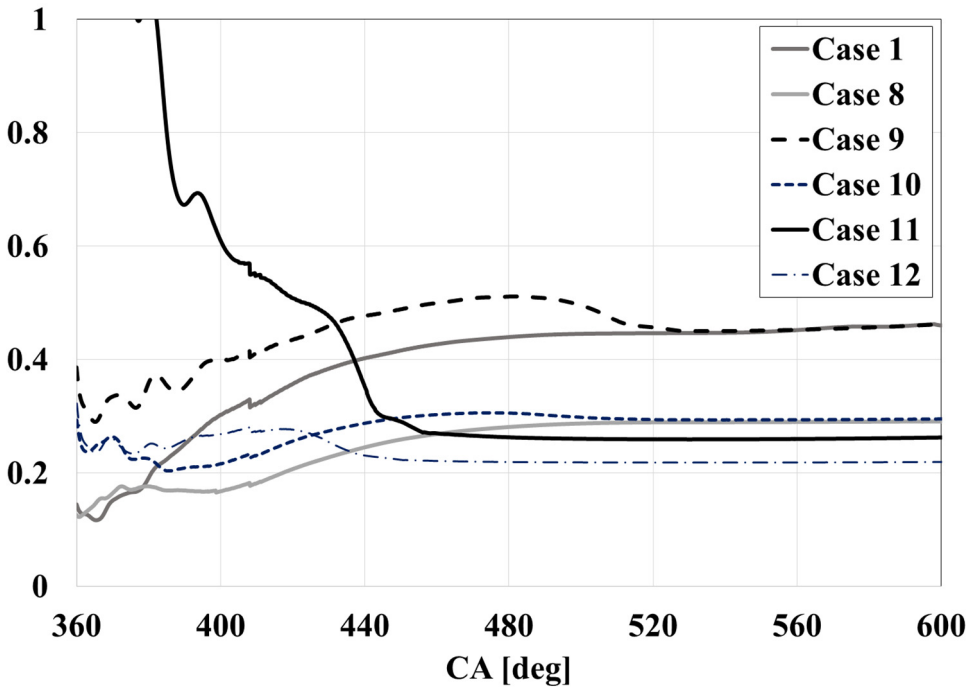

Figure 2.23 Ratio of total kinetic energy to cumulative kinetic energy

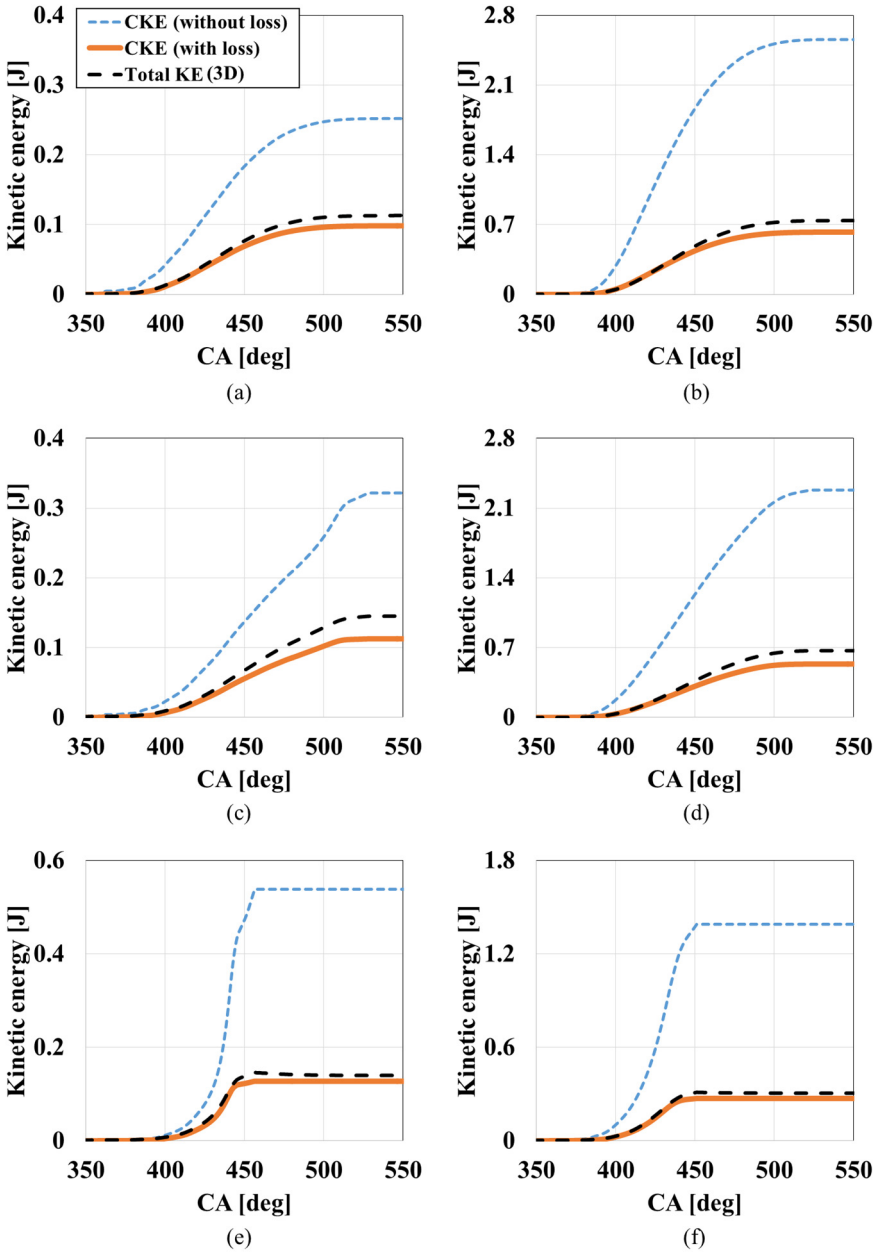

Figure 2.24 The effect of correlation of loss factor on prediction of total kinetic energy for (a) case 1, (b) case 8, (c) case 9, (d) case 10, (e) case 11, and (f) case 12

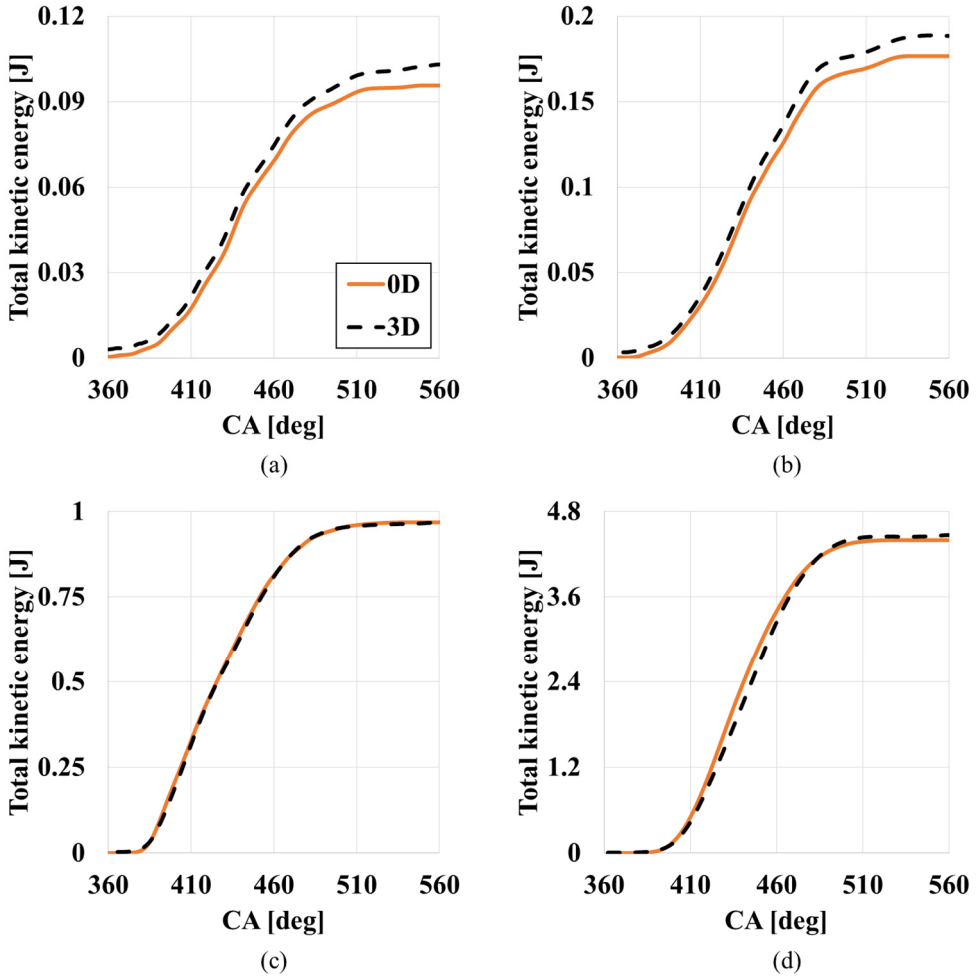

Figure 2.25 Comparison of total kinetic energy of test engine at (a) 1500 rpm, IVO 336 CA, (b) 2000 rpm, IVO 336 CA, (c) 4000 rpm, IVO 352 CA, and (d) 6000 rpm, IVO 365 CA

Table 2.3 Specifications of engines used for verification of correlation of loss factor

Parameter	Specification	
	Engine 1	Engine 3
Bore / stroke	86 / 86	86 / 86
Connecting rod	146.25	149
Intake port type	Tumble	Tumble
Combustion chamber pentroof angle	133	146
Injection type	GDI	MPI

2.5 Modeling of the production rate of turbulent kinetic energy

Accurate prediction of the production rate of turbulent kinetic energy is crucial for correct estimation of both mean and turbulent kinetic energy. Thus, an appropriate description on the production rate must be sought so that mean and turbulent kinetic energy can be matched simultaneously with those of 3D CFD. The processes of the derivation of the production term was carried out in three steps.

2.5.1 Assessment of the original energy cascade model in enclosed system

As a first step, the original energy cascade model was assessed to check the consistency under an extreme case where all the valves were closed, while piston kept moving as in a normal engine cycle. The 3D CFD results in Fig. 2.26 are taken from the second cycle even though simulation was carried out more than three cycles so that the flow within the cylinder would have been stabilized. Here, the mean kinetic energy is expressed in the form of velocity magnitude of mean flow for the purpose to make the comparison of the 0D and 3D results easier. From Fig. 2.26, it can be seen that the mean flow velocity profile does not change noticeably over the cycles. For such results to be obtained, the source and sink of the mean kinetic energy must be equal for every cycles. Since the valves are closed, the kinetic energy flux does not exist and the only possible source of the kinetic energy is the piston motion. A simple approximate velocity profile of the in-cylinder flow due to piston motion can be expressed as below:

$$V_z(z,t) = S_P(t)\left(1 - \frac{z}{h_{cyl}}\right) \tag{2.13}$$

where the z represents the distance from piston in z direction, assuming that the piston surface is located at z = 0, and S_p and h_{cyl} are the instantaneous piston speed and cylinder height, respectively.

Assuming that the density in the cylinder is uniform, the mean flow velocity can be calculated from averaging $V_z(z,t)$. This yields that the mean flow velocity magnitude is $\left|S_p(t)/2\right|$ which is the half the magnitude of the instantaneous piston speed. When comparing this result to the mean flow velocity obtained from 3D CFD, it can be confirmed that the piston motion is the factor responsible for the repetitive shape in the mean flow velocity. This result suggests that the mean kinetic energy, or mean flow velocity, can stay unaltered and self-sustaining only if the energy extracted from the mean kinetic energy to the turbulent kinetic energy, i.e. production rate, equals zero. According to the definition of the original energy cascade model, the production rate is only related to the shear of the mean flow. In this case, shear effect due to the velocity profile given in Eq. 2.13 eventually becomes zero as the velocity profile does not vary in radial direction of the cylinder.

On the other hand, the turbulence intensity in Fig. 2.26 shows the profile which continues to decrease over the cycles with some spikes in equidistance. Since the production rate due to mean flow shear is determined to be zero, the turbulent kinetic energy must keep decreasing due to dissipation. It is, however, partially true as overall magnitude keeps decreasing. Referring to the energy cascade models which have been amended from the original form in [84, 87, 93], a term related to rapid distortion theory (RDT) has been added. The RDT term can be expressed as follows:

$$\text{RDT} = -k\frac{\partial U_i}{\partial x_i} = \frac{k}{\rho}\frac{d\rho}{dt} \tag{2.14}$$

where k is the turbulent kinetic energy, U_i is the mean flow velocity in x, y, or z direction, and ρ is the cylinder gas density.

To confirm the contribution of this term, the profile of the turbulent kinetic energy was attempted to be reproduced based on the Eq. 1.1 using mean values from 3D CFD with zero boundary flux. With appropriate selection of constant a in Eq. 1.1, it was possible to match the positive peak values of rate of change of turbulent kinetic energy very closely. However, huge underestimation occurs when the RDT term became negative. This problem was resolved when the RDT term is considered only when its value is positive, and neglected when it is negative. This process would cause discontinuity in rate of change of turbulent kinetic energy. However, discontinuous point was also observed in 3D CFD result. Thus, this assumption can be presumed consistent. It is thought that the dissipation rate term already includes the reduction in the turbulent kinetic energy due to negative effect of the RDT term. The final result of turbulent kinetic energy estimated using Eq. 1.1 shown in Fig. 2.28 indicates that using the RDT term is the only way to explain the spikes in the turbulent kinetic energy, and this term must be added to the original form of energy cascade model as in recent studies.

From the analysis on the extreme case, it is possible to confirm that the mean kinetic energy is driven solely by the piston motion when valves are closed, and the production of turbulent kinetic energy due to piston-driven flow is zero as the shear in the mean flow is zero. Also, a term related to the RDT must be added to the energy cascade model to reproduce the 3D CFD results as in the former studies, but the increase in the turbulent kinetic energy due to compressibility effect does not give change in mean kinetic energy. Thus, it can be postulated that the mean kinetic energy due to kinetic energy flux across the valves may be superimposed with the mean

kinetic energy due to piston motion when valves are closed, as the latter mean kinetic energy does not contribute directly to increase in the turbulent kinetic energy.

2.5.2 Production rate of turbulent kinetic energy

In this section, equation for describing production rate of turbulent kinetic energy is discussed. In the original energy cascade model, the production rate was expressed using a simple equation for the flow over a flat plate with velocity in one direction. In reality, the in-cylinder flow is very complex, and less likely to be expressed adequately using the equation for the flow over a flat plate. Although it is limited for 0D models to be able to describe such sophisticated phenomena, it is necessary to find appropriate expression to incorporate the complex phenomena. Thus, the production term used in 3D CFD turbulence models is analyzed first. The analytical equation for the production rate can be expressed as below:

$$\Psi_{3D} = \tau_{ij} \frac{\partial U_j}{\partial x_i} \tag{2.15a}$$

$$= \mu_t \frac{\partial U_j}{\partial x_i} \left(\frac{\partial U_i}{\partial x_j} + \frac{\partial U_j}{\partial x_i} \right) - \frac{2}{3} \rho k \frac{\partial U_i}{\partial x_i} - \frac{2}{3} \mu_t \frac{\partial U_j}{\partial x_j} \frac{\partial U_k}{\partial x_k} \tag{2.15b}$$

where τ_{ij} is the stress tensor, μ_t is the turbulent viscosity, k is the turbulent kinetic energy, U_i is the mean flow velocity in x, y, or z direction, and ρ is the in-cylinder gas density.

Each terms in the above equation represents the turbulent kinetic energy produced due to shear in mean flow, dilatation of the flow field, and square of the dilation of the flow field. Comparing Eqs. 1.9 and 2.15, the term related to shear in mean flow is considered solely as a contributing factor in production rate and other

two terms are not considered. The second term has been confirmed that it should be added to the Eq. 1.9 to explain the increase in the turbulent kinetic energy during compression stroke in the previous section as in other literatures. The third term, however, has not been included in the models. The third term is always a negative value, and it would reduce the contribution of the first term when there is a change in in-cylinder density.

In 0D model, the first term in Eq. 2.15b is simply expressed using the ratio of mean flow velocity and relevant geometric length scale. This term cannot distinguish whether the direction of deformation of a fluid element is in normal direction or shear direction as the direction of mean flow velocity is not prescribed. Since the 0D model is attempting to express the production of turbulent kinetic energy due to shear in mean flow, deformation in normal direction must be excluded. This is similar to the role of the third term in Eq. 2.15b. Thus, in this study, addition of the square of the dilation of the flow field to the equation for turbulent kinetic energy production rate is proposed. The new form of the production rate of turbulent kinetic energy deduced in this study can be expressed as in Eq. 2.16, where C_{shear} is a tunable constant to match the mean and turbulent kinetic energy comparable to the results of 3D CFD.

$$\Psi_{QD} = \mu_t C_{shear} \left(\frac{\bar{U}}{\bar{L}}\right)^2 - \frac{2}{3}\mu_t \left(\frac{1}{\rho}\frac{d\rho}{dt}\right)^2 \tag{2.16}$$

2.5.3 Derivation of geometric length scale for production rate

Lastly, the relevant geometric length scale for production rate is discussed. The geometric length scale in the denominator of the production term in energy cascade model is usually assumed to be the same as the integral length scale of turbulence. This assumption may hold if the integral length scale is modelled from the geometry

of engine cylinder. In this study, however, the integral length scale is fitted to the 3D CFD results instead of simply calculating from the geometry of the cylinder. Thus, the former assumption that the geometric length scale and integral length scale are identical would be inappropriate, and another expression for the geometric length scale must be found.

The geometric length scale introduced in former studies utilized h_{cyl} or $\sqrt[3]{V_{cyl}}$. These choices would contain the assumption that the gradient of the velocity profile is in radial direction of the cylinder, or in an isotropic way, respectively. However, the shear in the mean flow in 3D CFD may not be precisely reproduced by the assumptions above. This is because in 3D CFD, the shear in the flow is calculated for x, y, and z directions, and the shear in three directions are not assumed to be the same, i.e. isotropic. To find the appropriate definition of the geometric lengths scale for the 0D model, the methods for calculating the mean values in 3D CFD was revised. Since all of the mesh in 3D geometry carries information on physical quantities, the process of averaging is required to obtain one mean value representative for in-cylinder condition. This procedure is done in two steps: averaging the quantities expressed in three dimensions for each mesh, and then taking mass or volume weighted averaging over the total mesh. In this study, the averaged value for mean flow velocity magnitude was obtained using the volume averaging as shown in the Eq. 2.17.

$$\overline{U} = \frac{\int U_{average,i-th\ mesh} dV_{i-th\ mesh}}{\int dV_{i-th\ mesh}} \tag{2.17}$$

$$U_{average,i-th\ mesh} = \sqrt{{U_{x,i-th}}^2 + {U_{y,i-th}}^2 + {U_{z,i-th}}^2} \tag{2.18}$$

Since the magnitude of the mean flow velocity is obtained from volume-averaged geometrical mean value of the flow velocity of each mesh, it would be analogous to use the geometrically averaged length scale when considering the geometric length scale for the production term in Eq. 2.18. This geometric length scale differs from the previous expressions in a way that it is not unidirectional, nor isotropic.

$$\bar{L} = \sqrt{{L_x}^2 + {L_y}^2 + {L_z}^2} \tag{2.19}$$

The expression now requires which physical length scale is relevant. The z-direction length scale can be expressed with h_{cyl}. Although the combustion chamber is not strictly symmetric due to the geometry of V_c of the engine head, the volume displaced by piston which is exactly symmetric comprises most of the cylinder volume. Thus, the length scale in x and y direction is assumed to be identical. The length scale of x, and y direction cannot be simply be represented with the cylinder bore as the cylinder bore is a quantity of cylindrical coordinate while the velocity magnitude is expressed in the Cartesian coordinate. Thus, spatially averaged value was used for obtaining average length scales in x, and y direction.

$$\mathrm{L_x} = \frac{\int_0^h \int_{-R}^{R} \int_{-\sqrt{R^2-x^2}}^{\sqrt{R^2-x^2}} \sqrt{R^2-y^2}\, dx dy dz}{\int_0^h \int_{-R}^{R} \int_{-\sqrt{R^2-x^2}}^{\sqrt{R^2-x^2}} dx dy dz} \tag{2.20a}$$

$$= \frac{\frac{8}{3}R^3}{\pi R^2} \tag{2.20b}$$

$$= \frac{4 * bore}{3\pi} \tag{2.20c}$$

The expression for the length scale of each direction can be summarized as in Eq. 2.21.

$$\bar{L} = \sqrt{(V_{cyl}/A_{piston})^2 + 2 * (4/(3\pi) * bore)^2} \quad (2.21)$$

The profile of the newly derived geometric length scale is compared with the former geometric length scales in Fig. 2.30.

The newly introduced geometric length scale, however, still needs a modification. Consider a case of which the SB ratio is changed while the displaced volume is changed. Subsequent change in bore and stroke will differ by a factor of 2 as the cylinder volume is calculated from multiplication of stroke and bore squared. For instance, when displaced volume is 500 cc, and SB ratio is changed from 1 to 0.7, the bore would increase by 12% while the stroke will be shortened to 78% of the original stroke. To account for the difference in the sensitivity of the bore and stroke due to change in SB ratio, h_{cyl} is divided with the square root of the SB ratio. The final form of the geometric length scale can be expressed as in Eq. 2.22.

$$\bar{L} = \sqrt{((V_{cyl}/A_{piston})^2) \,/\, (SB\ ratio) + 2 * (4/(3\pi) * bore)^2} \quad (2.22)$$

2.5.4 Phenomenological model of production term dependent on tumble strength

As the tumble strength of the SI engine is being increased to enhance turbulence intensity recently, it is important to incorporate the effect of tumble strength in the model. The characteristics of tumble motion in the cylinder can be represented with

vorticity. Former study reported that the relationship between the vorticity and density can be related by Cauchy's vorticity equation as expressed below [95].

$$\frac{\omega}{\rho} = \frac{\omega_0}{\rho_0} \frac{l_{vortex\ tube}}{l_{vortex\ tube,0}} \tag{2.23}$$

where ω is the vorticity of a flow, ρ is the density of the fluid, $l_{vortex\ tube}$ is the length of the vortex tube, and the subscript 0 indicates that the properties are from some reference state.

For tumble motion, the axis of the vortex is aligned with the radial direction of the cylinder. During compression and expansion of the cycle, the length of the vortex tube does not change as the deformation in radial direction does not occur [96]. Thus, vorticity of the tumble motion is dependent on the density ratio only during the compression stage.

In this study, it is postulated that the characteristics of the vorticity of turbulent eddies due to tumble flow can be expressed with Eq. 2.23. Turbulent vorticity can be expressed with turbulence intensity multiplied by characteristic size of turbulent eddy. Thus, above equation can be rearranged as Eq. 2.24.

$$u'_{tumble} = u'_{tumble,0} \frac{l_{eddy,0}}{l_{eddy}} \frac{\rho}{\rho_0} \tag{2.24}$$

If it is assumed that the mass of the individual eddy is conserved, then the ratio of the characteristic size of turbulent eddy can be expressed with density ratio [78]. Then the evolution of the turbulence intensity related to tumble motion can be expressed only with density ratio. This is in similar form to that of RDT term shown in the previous section. Although it is not strictly based on the physics of the turbulent

kinetic energy production due to tumble motion, it is crudely postulated that the tumble strength contributes to the production of turbulent kinetic energy in the form similar to that of RDT term. Therefore, in the final model, a constant which is related to the tumble strength is added to incorporate the effect of tumble strength on the production of turbulent kinetic energy. The constant introduced above is named as C_{engine}. This is because the concept of the model developed in this study is to incorporate the characteristics of engine designs which determines the tumble strength instead of the characteristics of the evolution tumble strength which changes according to the engine operating conditions.

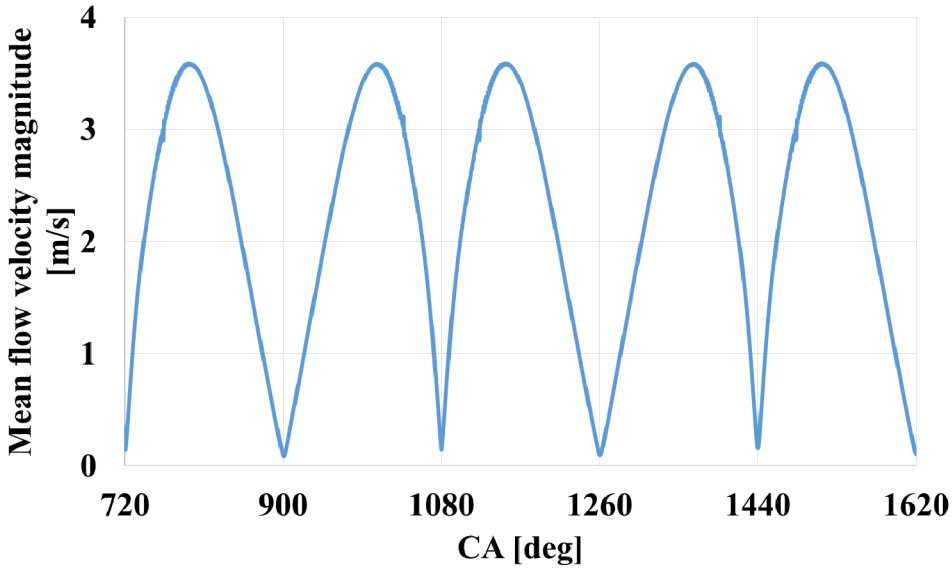

(a)

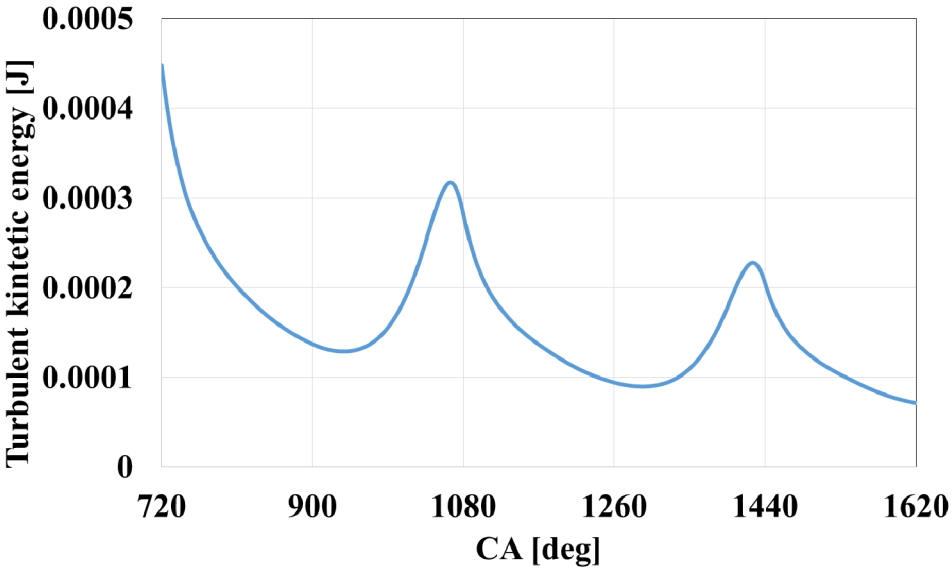

(b)

Figure 2.26 Mean flow velocity magnitude and turbulent kinetic energy at 1500 rpm

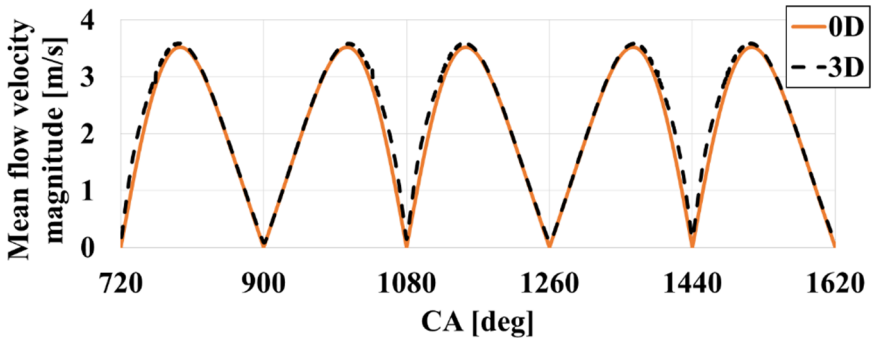

(a)

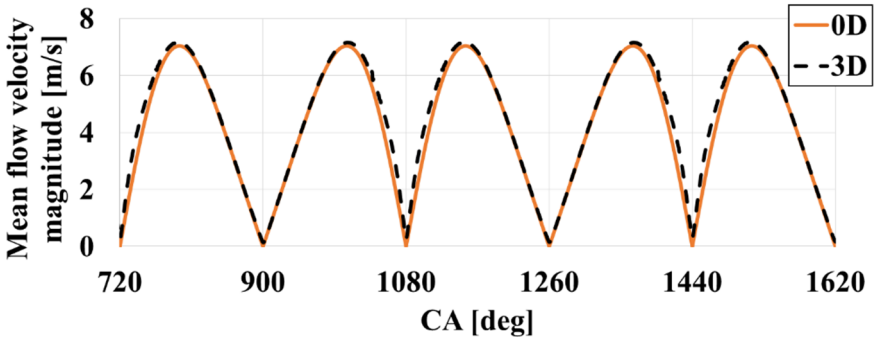

(b)

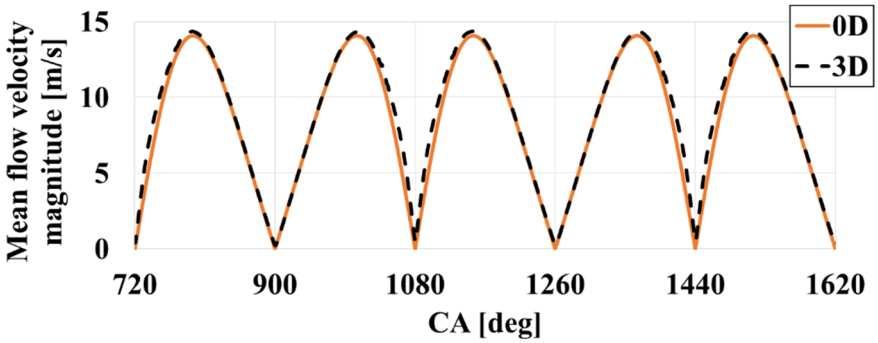

(c)

Figure 2.27 Comparison of mean flow velocity magnitude at (a) 1500 rpm, (b) 3000 rpm, and (c) 6000 rpm

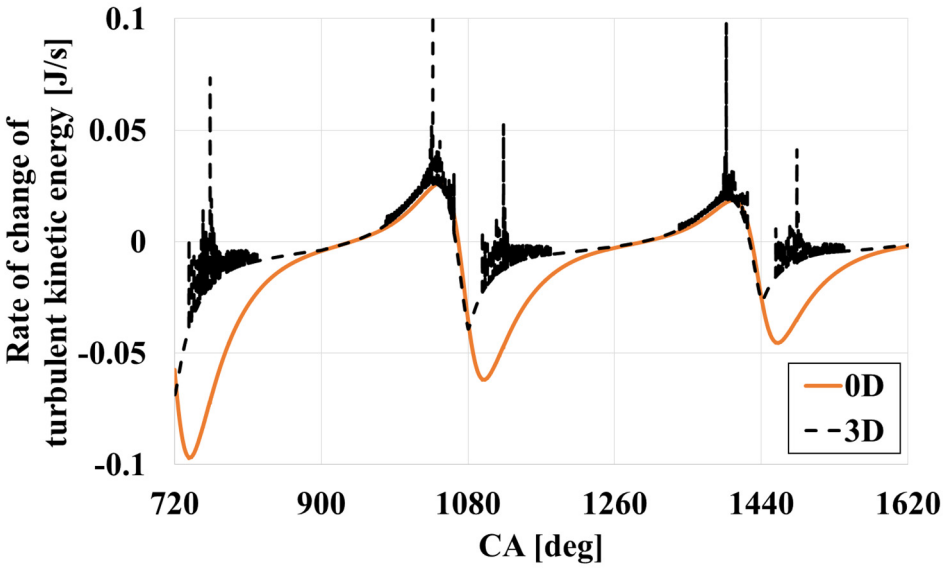

(a)

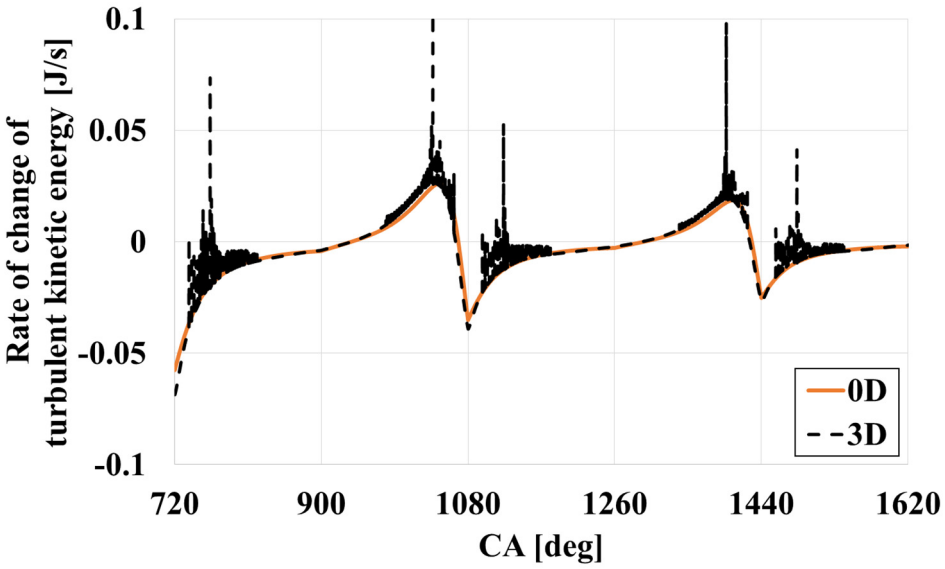

(b)

Figure 2.28 Comparison of the rate of change of turbulent kinetic energy (a) without limitation on RDT term, and (b) with limitation on RDT term

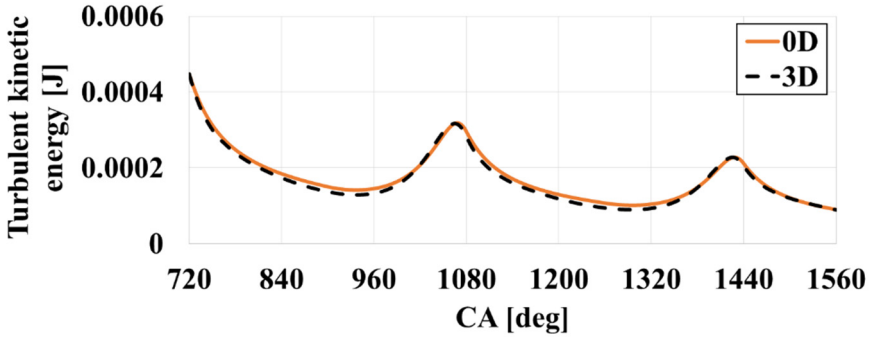

(a)

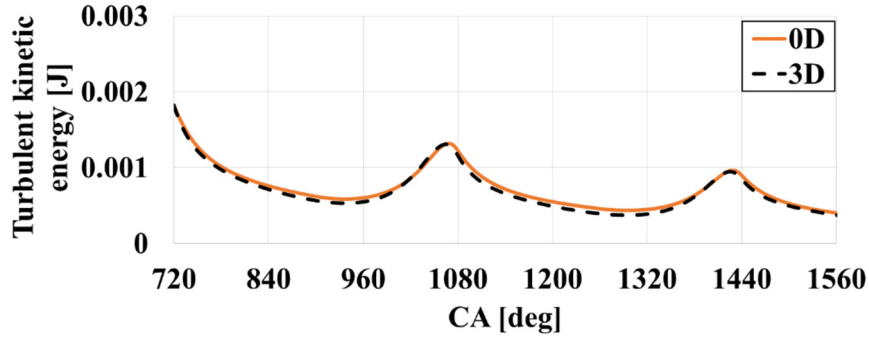

(b)

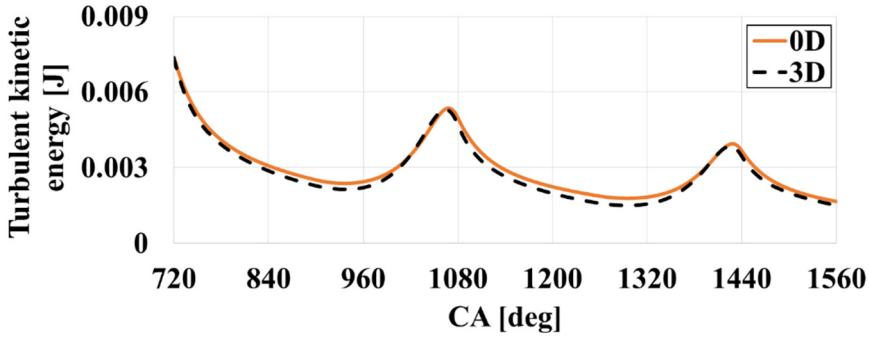

(c)

Figure 2.29 Comparison of the turbulent kinetic energy under (a) 1500 rpm, (b) 3000 rpm, and (c) 6000 rpm

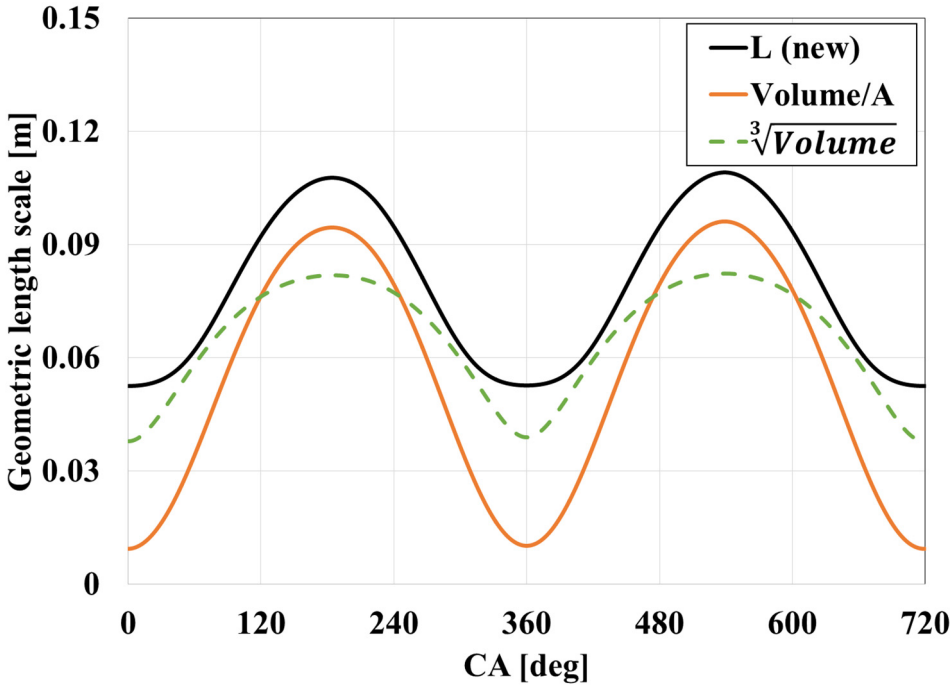

Figure 2.30 Comparison of profiles of the geometric length scale

2.6 Verification of the developed model

2.6.1 Assessment of the developed model to base engine

The final form of the developed 0D turbulence model can be expressed in the equations below:

$$\frac{dK}{dt} = \frac{1}{2}\left(\sqrt{2C_f}\frac{D_{valve}}{Bore}\right)\dot{m}_i {V_i}^2 - K\frac{\dot{m}_e}{m_{cyl}} - m_{cyl}\Psi_{\mathrm{QD}} \tag{2.25}$$

$$\frac{dk}{dt} = m_{cyl}\Psi_{\mathrm{QD}} + \left(C_{rho} + C_{engine}\right)m_{cyl}\mathrm{RDT} - m_{cyl}\varepsilon - k\frac{\dot{m}_e}{m_{cyl}} \tag{2.26}$$

$$RDT = \begin{cases} \frac{k}{\rho}\frac{d\rho}{dt} & \left(\frac{d\rho}{dt} > 0\right) \\ 0 & \left(\frac{d\rho}{dt} < 0\right) \end{cases} \tag{2.27}$$

$$\Psi_{QD} = C_{shear}\left(0.09\frac{k^2}{\varepsilon}\right)\left(\frac{\overline{U_{flow}}}{\bar{L}}\right)^2 - 0.66\left(0.09\frac{k^2}{\varepsilon}\right)\left(\frac{1}{\rho}\frac{d\rho}{dt}\right)^2 \tag{2.28}$$

$$\varepsilon = C_{dissipation}\frac{u'^3}{l_t} \tag{2.29}$$

$$u' = \sqrt{\frac{2}{3}\frac{k}{m_{cyl}}} \tag{2.30}$$

$$\overline{U_{flow}} = \sqrt{2\frac{K}{m_{cyl}}} \tag{2.31}$$

$$\bar{U} = \begin{cases} \overline{U_{flow}} & \text{(if valves are oepn)} \\ \overline{U_{flow}} + 0.5 * V_{pist} & \text{(if valves are closed)} \end{cases} \tag{2.32}$$

where $\overline{U_{flow}}$ is the mean flow velocity due to flow generated during intake process, $\bar{U}$ is the mean flow velocity, and u' is the turbulence intensity.

The constants in above equations C_{engine}, C_{shear}, and $C_{dissipation}$ are found by matching a mean flow velocity and turbulent intensity of 3D CFD in one selected case, and kept constant over other conditions. In this study, the base case for finding values for adjustable constants was selected to be case 4 in Table 2.1. Such choice was made as it is the case with engine speed of 3000 rpm which is the intermediate value between 1500 rpm and 6000 rpm.

The verification of the model was conducted by implementing the set of equations in GT-Power user subroutine. Fig. 2.31 shows that the evolution of the mean flow velocity magnitude and turbulence intensity predicted by 0D model agree well with those of 3D CFD. The value for C_{engine}, C_{shear}, and $C_{dissipation}$ were set to be 0.08, 300, and 0.33, respectively. For C_{rho}, the value which has been found in section 2.4.1 was used. The verification of the developed model was also conducted for various cases listed in Table 2.1 and compared with the results of 3D CFD. Except for some discrepancies observed during the early part of the intake stroke, it can be confirmed that the developed model can predict the evolution of both mean flow velocity magnitude and turbulence intensity fairly accurate without additional tuning of adjustable constants. The accuracy of the prediction of turbulence intensity over the range of 670 CA to 720 CA, which is the typical range for the ignition timing, was within 6 % error for most of the cases, except for the case 12, and 19. The reason for higher error in particular cases can be attributed to the differences in characteristics of flow field compared to that of the base case.

The mean flow velocity magnitude for the cases with intake pressures different from atmospheric pressure, and valve profiles with low lift were overestimated during intake stroke. This may be attributed to the inaccuracy in the correlation of loss factor. When the induction of intake flow changes drastically compared the nominal cases where the correlation for the loss factor was derived, the loss factor should be changed

accordingly. Although the correlation for loss factor was derived to incorporate the effect of changes in flow characteristics according to engine operating conditions, the 0D model could not capture all of the details in the flow characteristics.

As discussed above, the error in the predicted mean flow velocity magnitude and turbulence intensity, especially during the intake stroke, are attributable to the limitation of the 0D models compared to the 3D CFD. Yet, the 0D model can correctly predict the mean flow velocity and the turbulence intensity according to the engine operating conditions and design parameters after IVC timing. This is adequate enough for predicting the effect of engine operating conditions and design parameters on engine combustion characteristics.

2.6.2 Assessment of the developed model to engine with intensified tumble strength

The assessment of the developed model was conducted with test engine which has much stronger tumble strength compared to the base engine. The constants in the sets of equation introduced previously were kept unchanged except for the constant related to the engine design determining tumble strength. For this case, the value for C_{engine} was increased from 0.08 to 0.68. The results in Figs. 2.50, 2.51 and 2.52 show that the turbulence intensity can be predicted well with tuning one constant only. However, the model predictability for the mean flow velocity was found to be not as high as that for the turbulence intensity. It is thought that the model has difficulty in predicting the evolution of the mean flow velocity when the degree of the coherence in the flow field increases during intake process. Nevertheless, the developed model can be utilized for turbulence intensity prediction which has direct impact on the combustion characteristics.

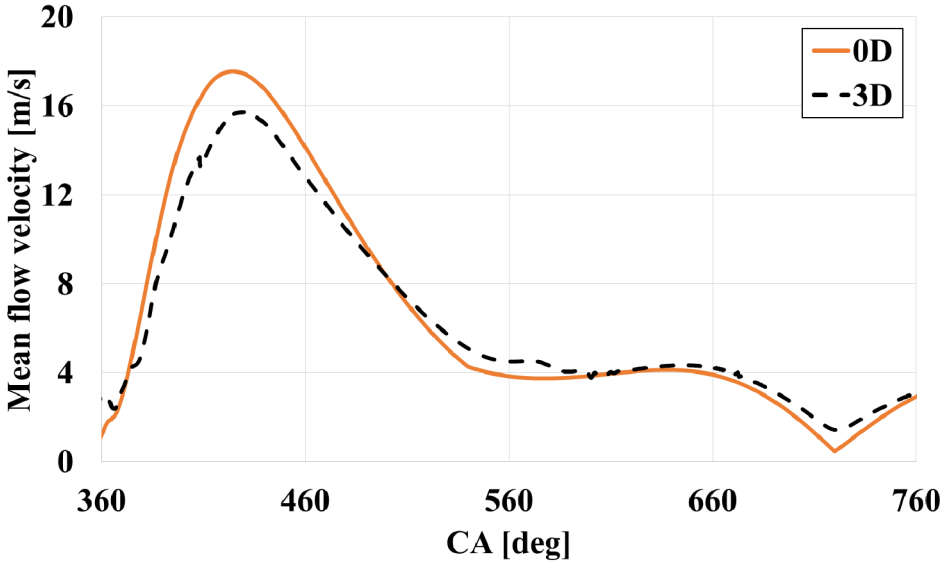

(a)

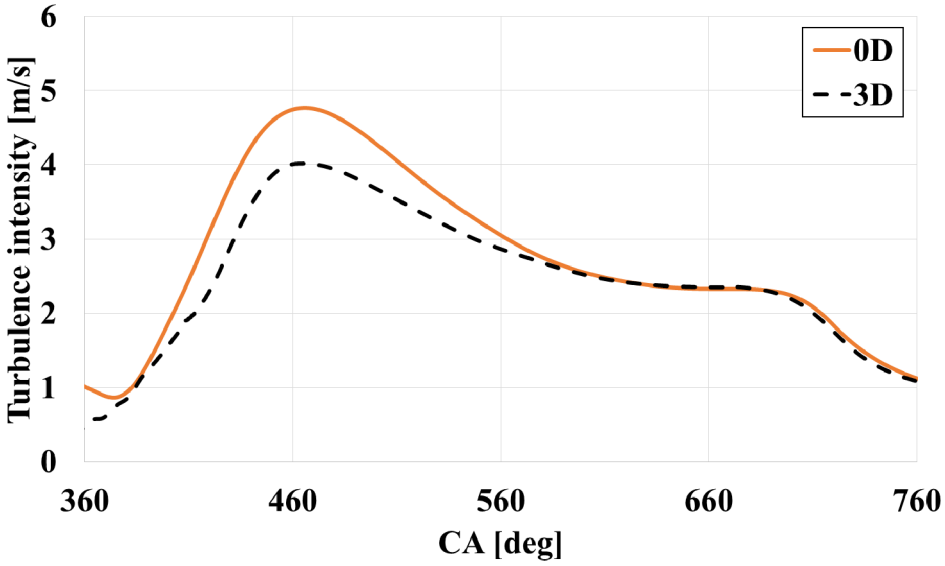

(b)

Figure 2.31 Comparison of (a) mean flow velocity magnitude and (b) turbulence intensity of case 1

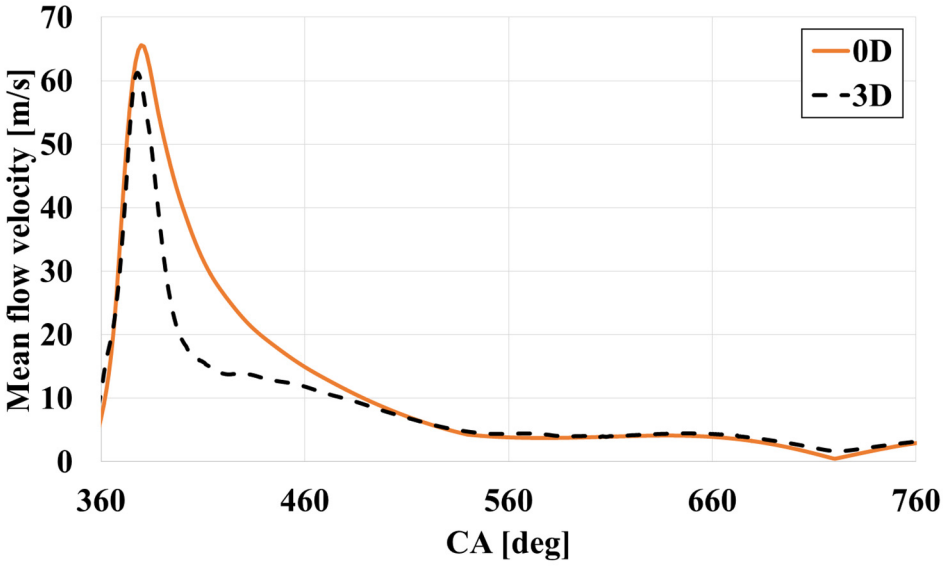

(a)

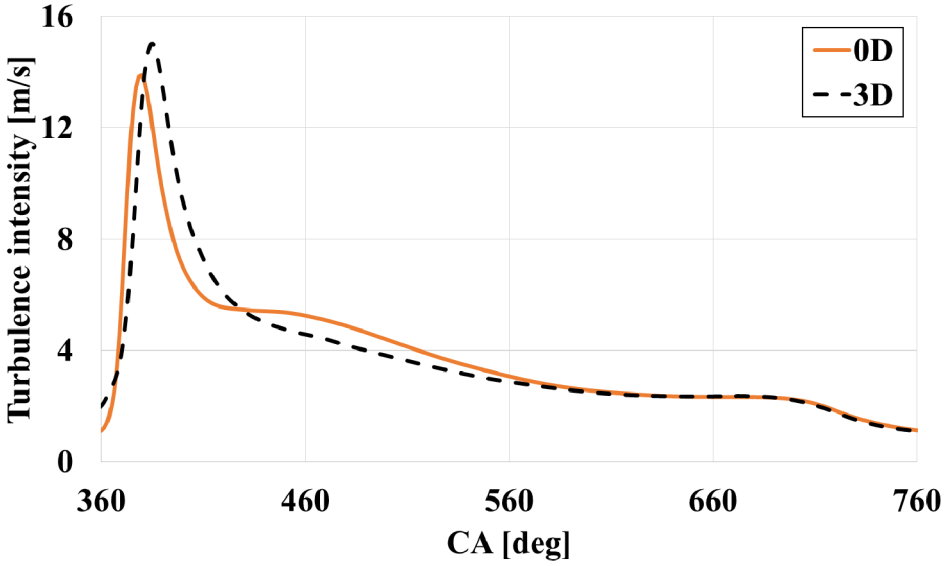

(b)

Figure 2.32 Comparison of (a) mean flow velocity magnitude and (b) turbulence intensity of case 2

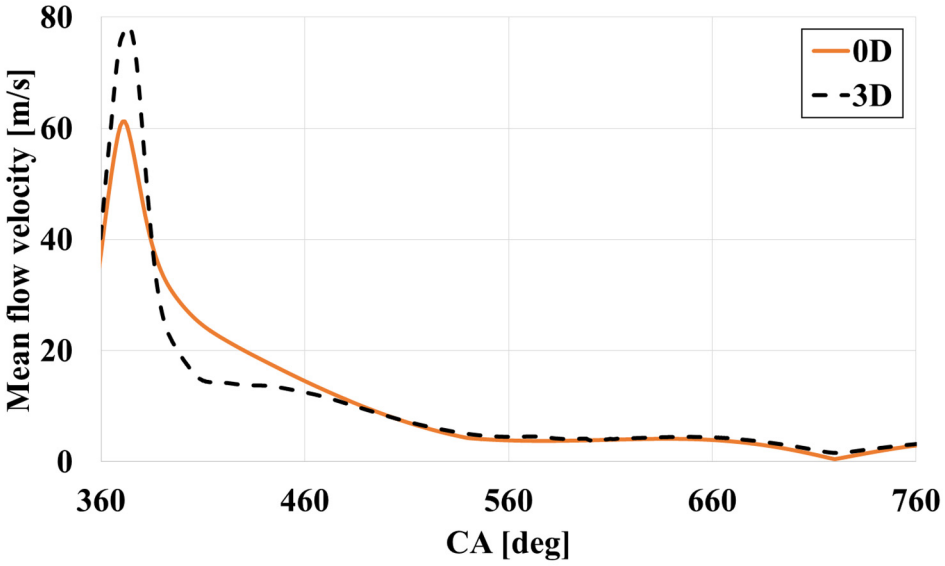

(a)

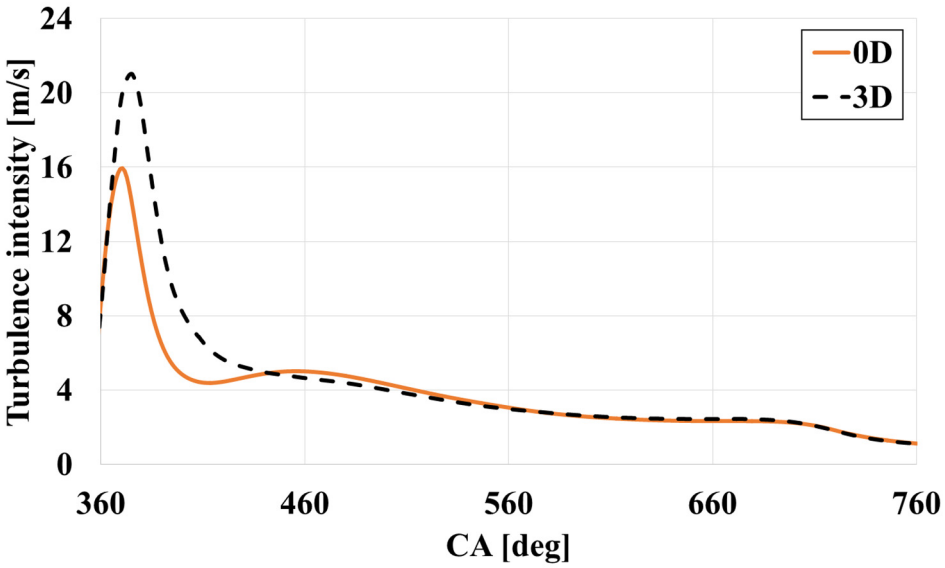

(b)

Figure 2.33 Comparison of (a) mean flow velocity magnitude and (b) turbulence intensity of case 3

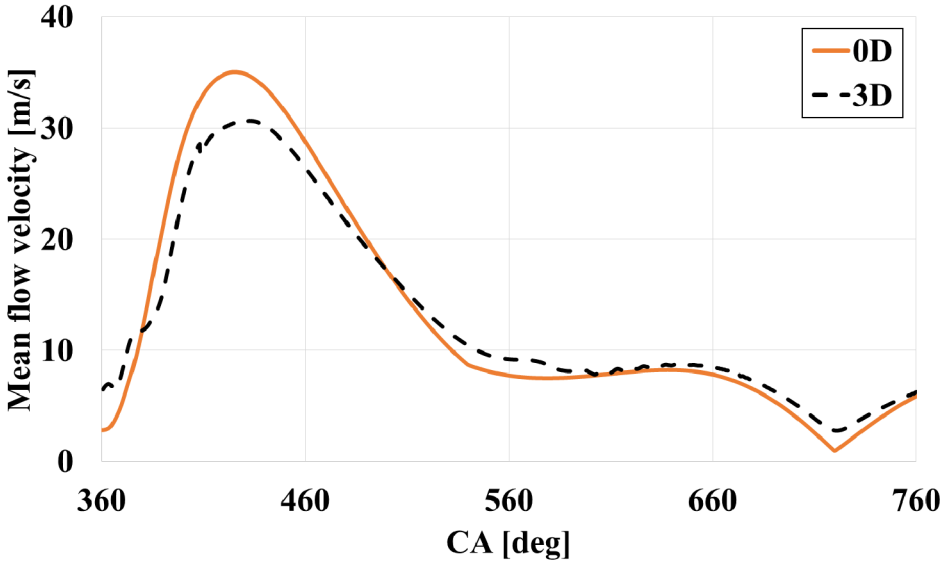

(a)

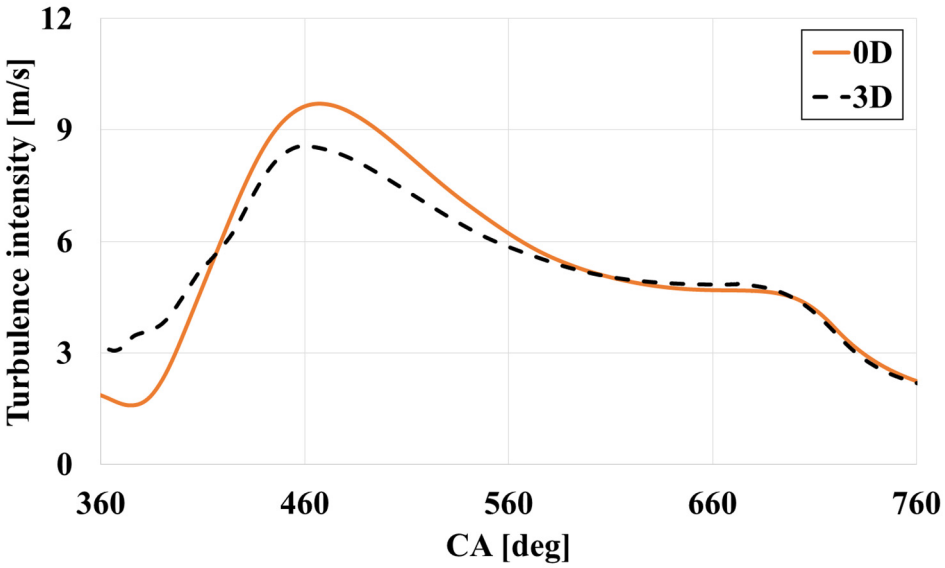

(b)

Figure 2.34 Comparison of (a) mean flow velocity magnitude and (b) turbulence intensity of case 4

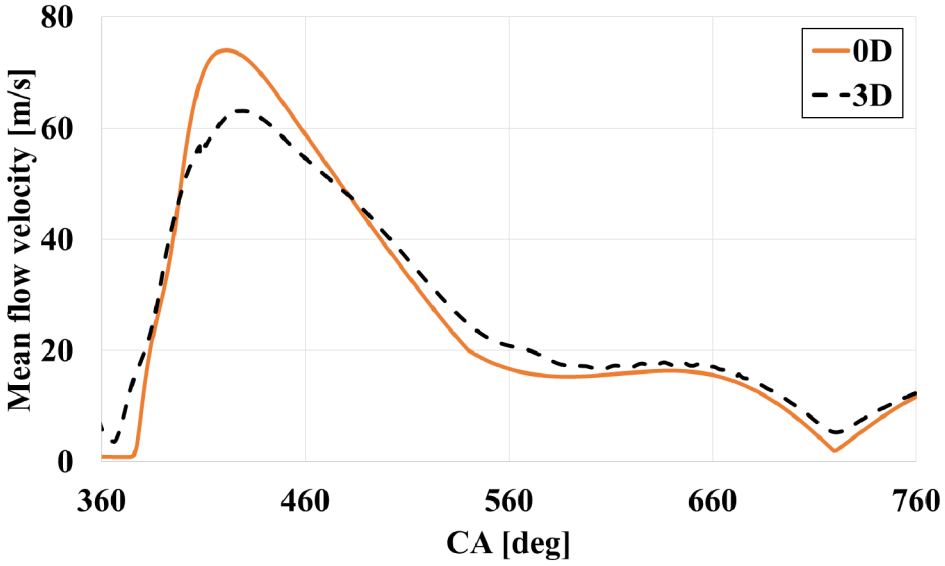

(a)

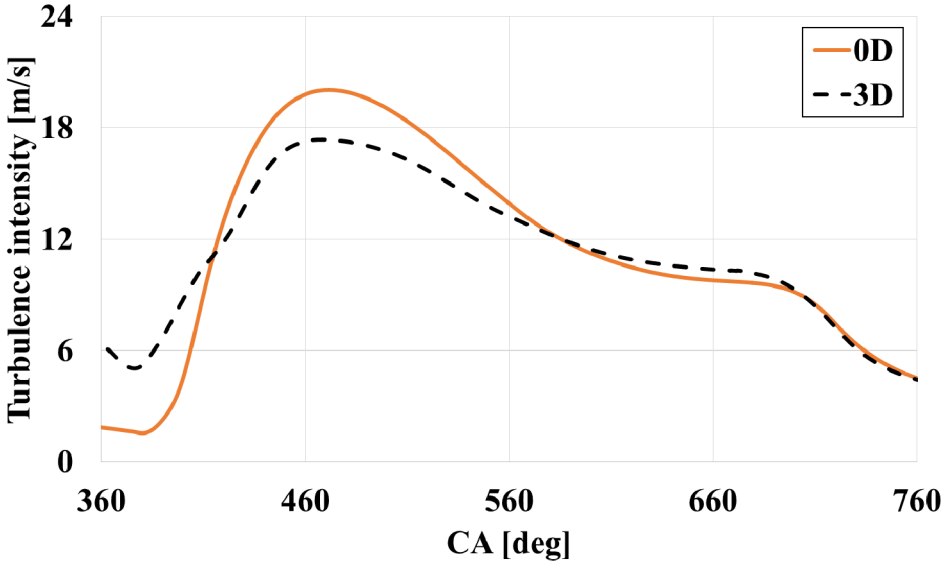

(b)

Figure 2.35 Comparison of (a) mean flow velocity magnitude and (b) turbulence intensity of case 5

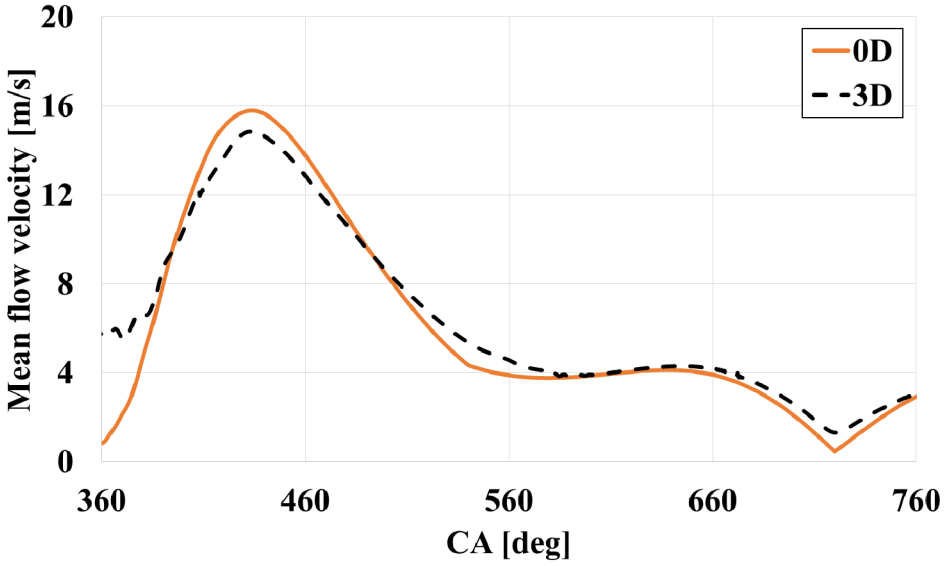

(a)

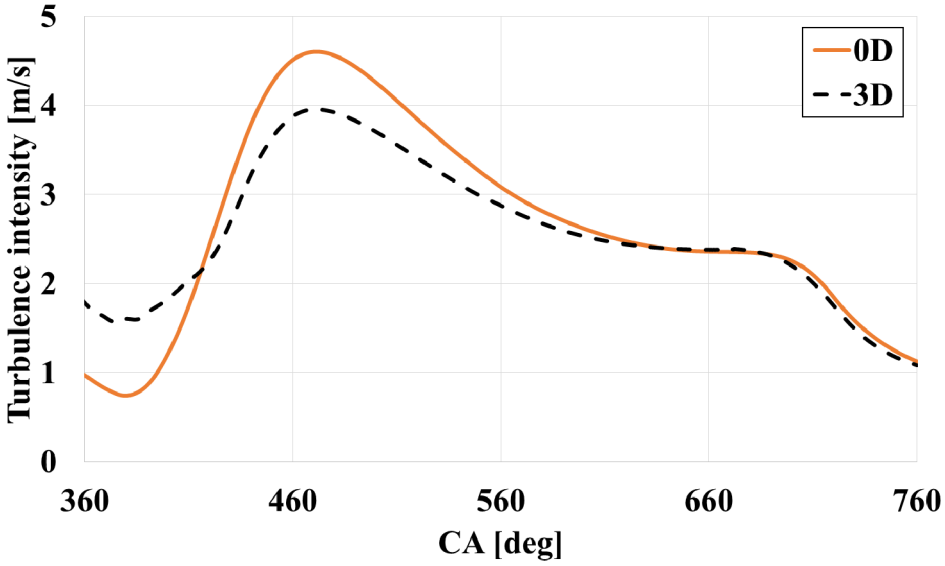

(b)

Figure 2.36 Comparison of (a) mean flow velocity magnitude and (b) turbulence intensity of case 6

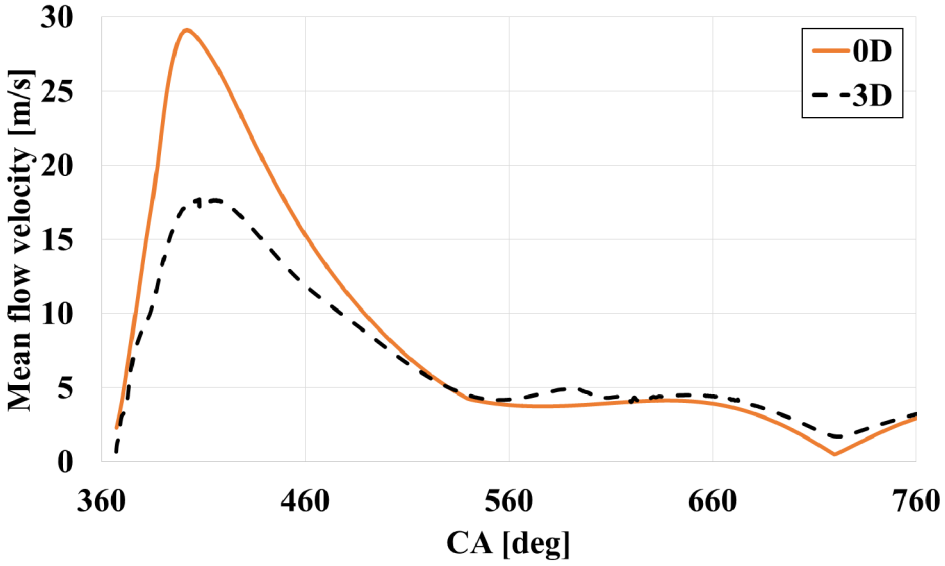

(a)

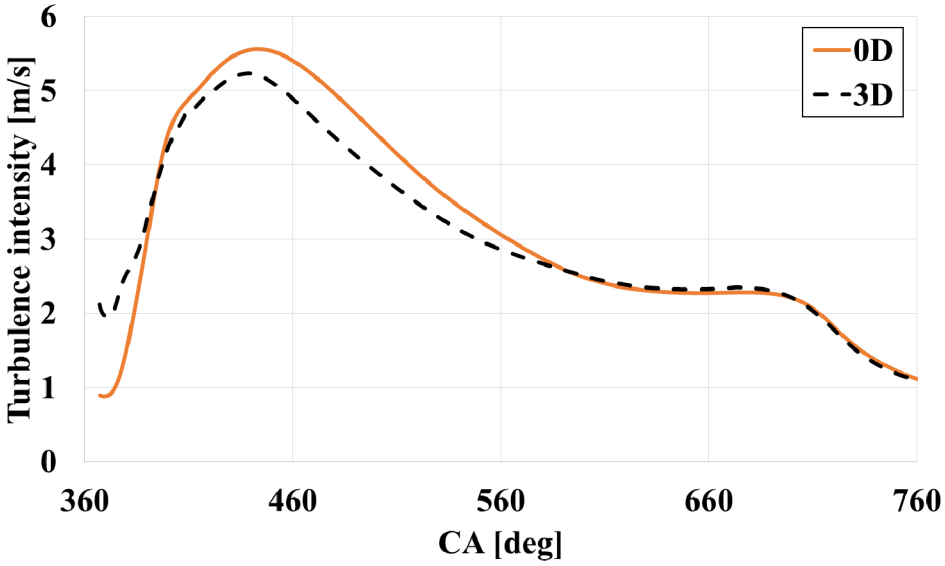

(b)

Figure 2.37 Comparison of (a) mean flow velocity magnitude and (b) turbulence intensity of case 7

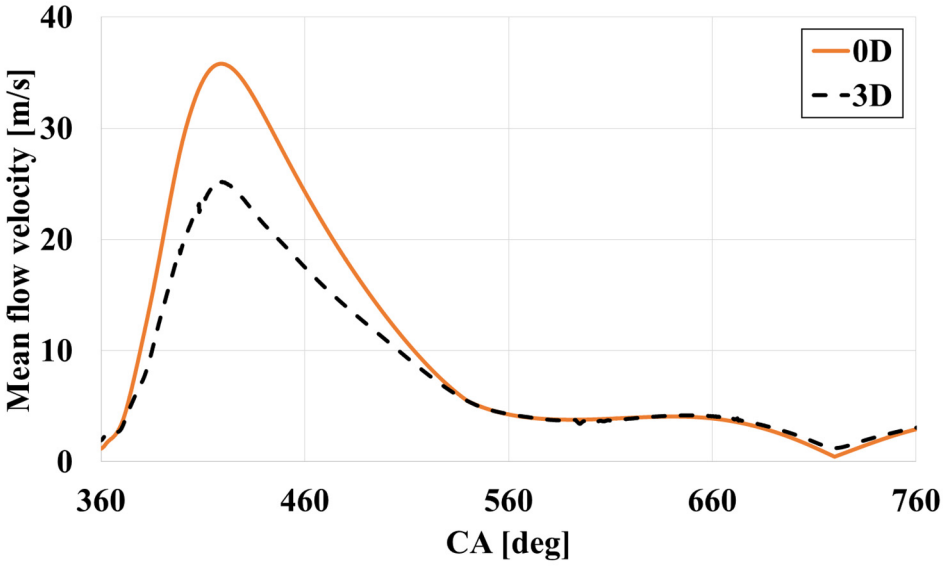

(a)

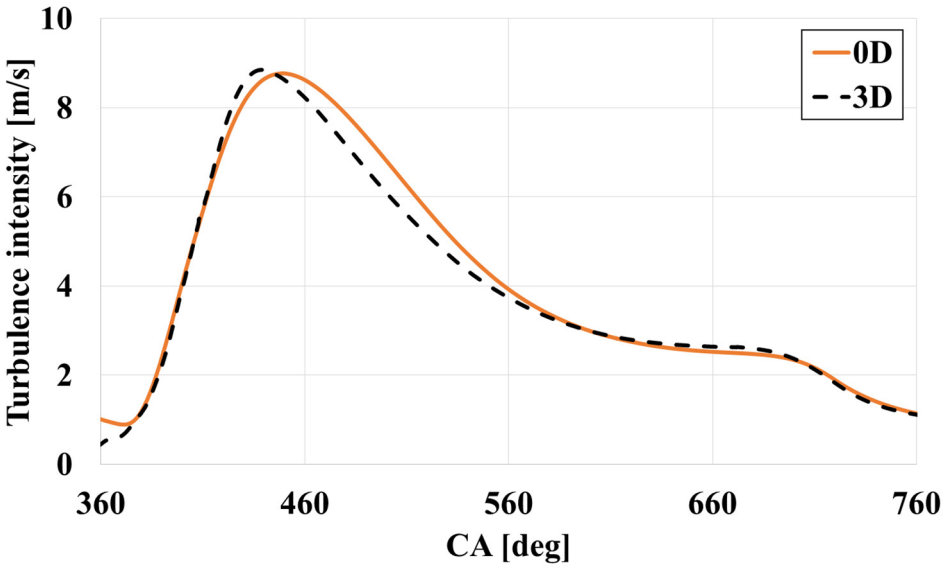

(b)

Figure 2.38 Comparison of (a) mean flow velocity magnitude and (b) turbulence intensity of case 8

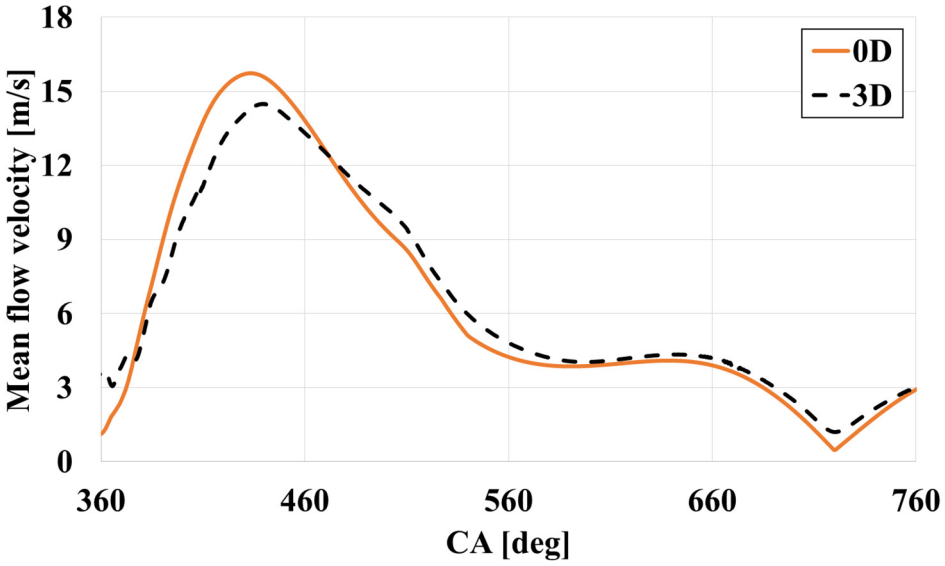

(a)

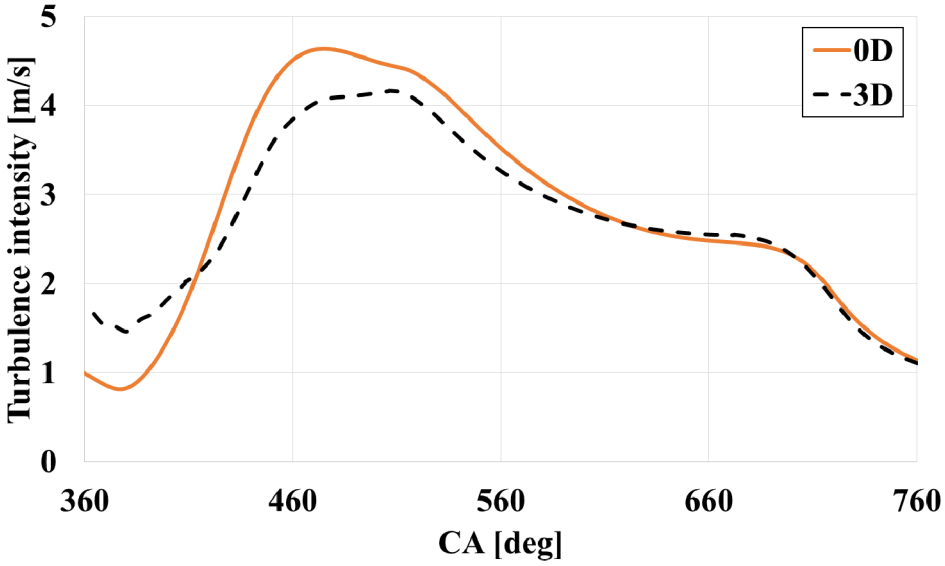

(b)

Figure 2.39 Comparison of (a) mean flow velocity magnitude and (b) turbulence intensity of case 9

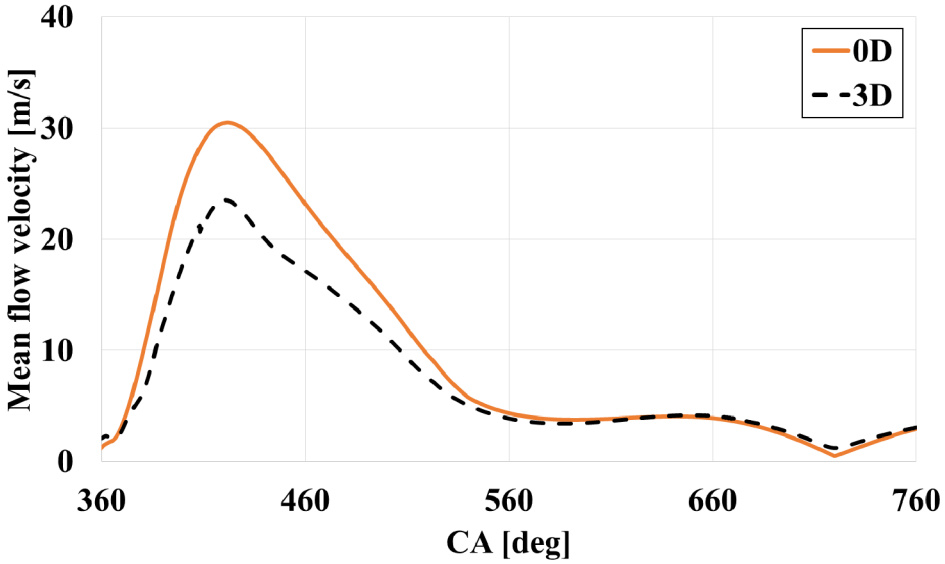

(a)

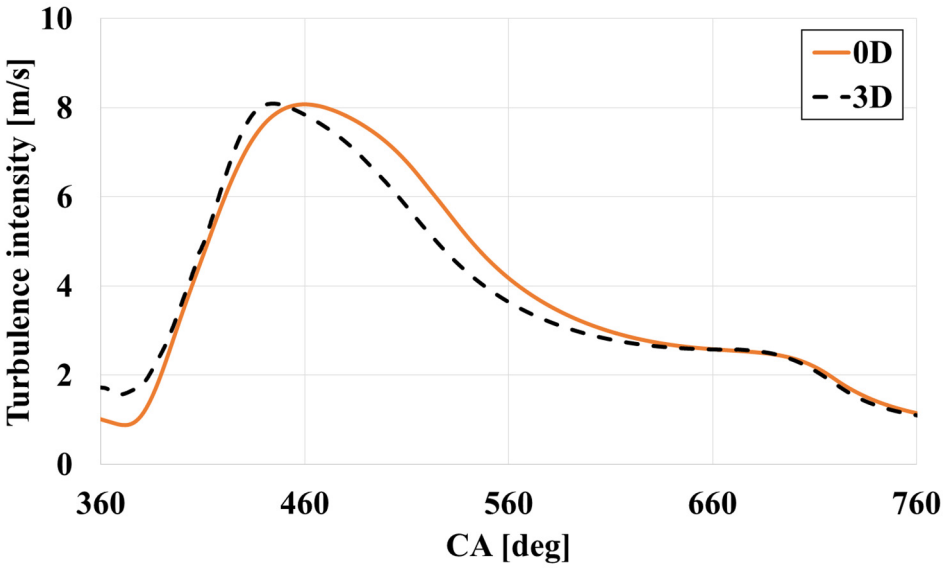

(b)

Figure 2.40 Comparison of (a) mean flow velocity magnitude and (b) turbulence intensity of case 10

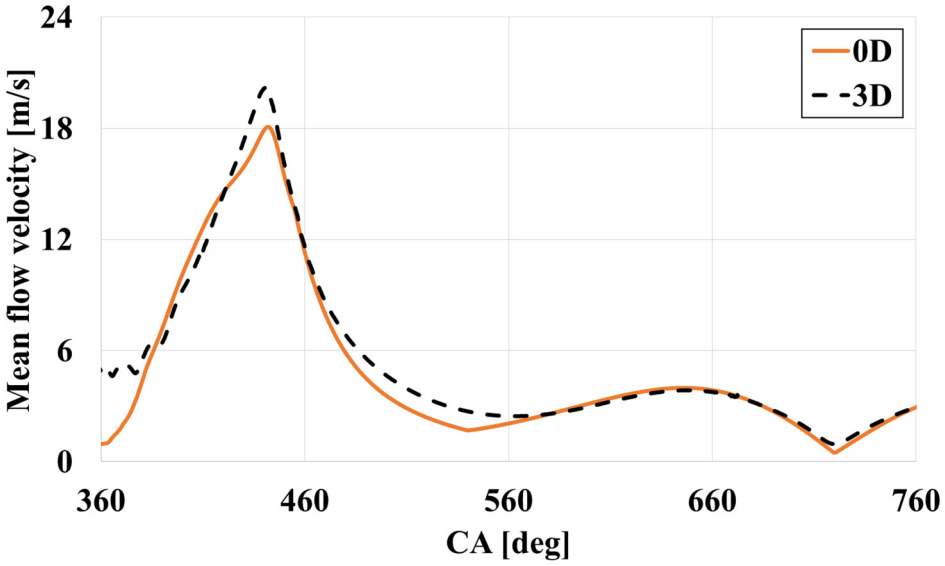

(a)

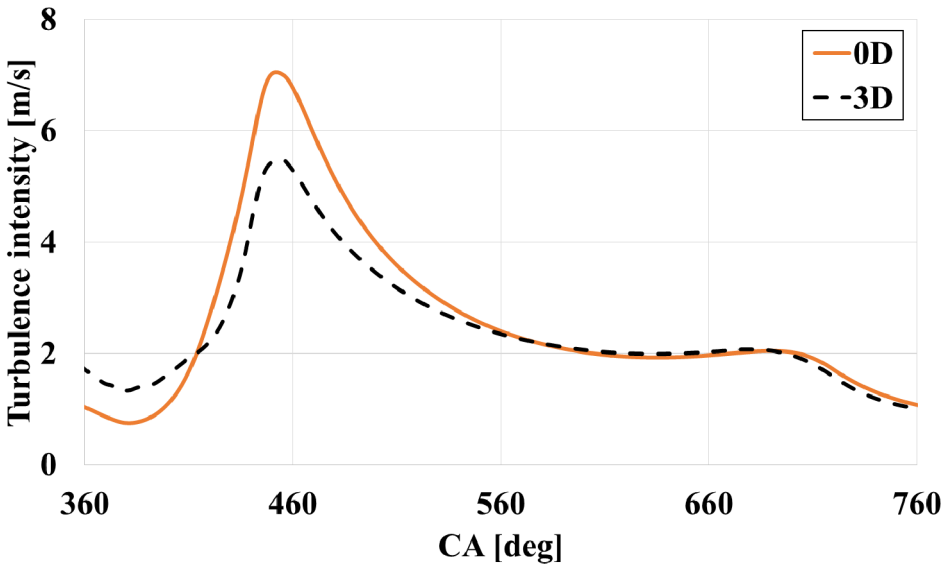

(b)

Figure 2.41 Comparison of (a) mean flow velocity magnitude and (b) turbulence intensity of case 11

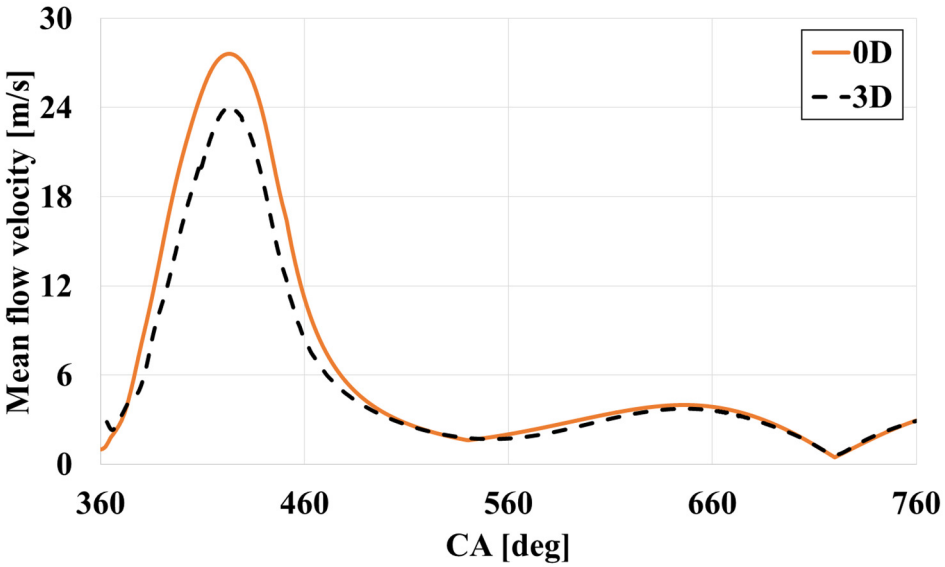

(a)

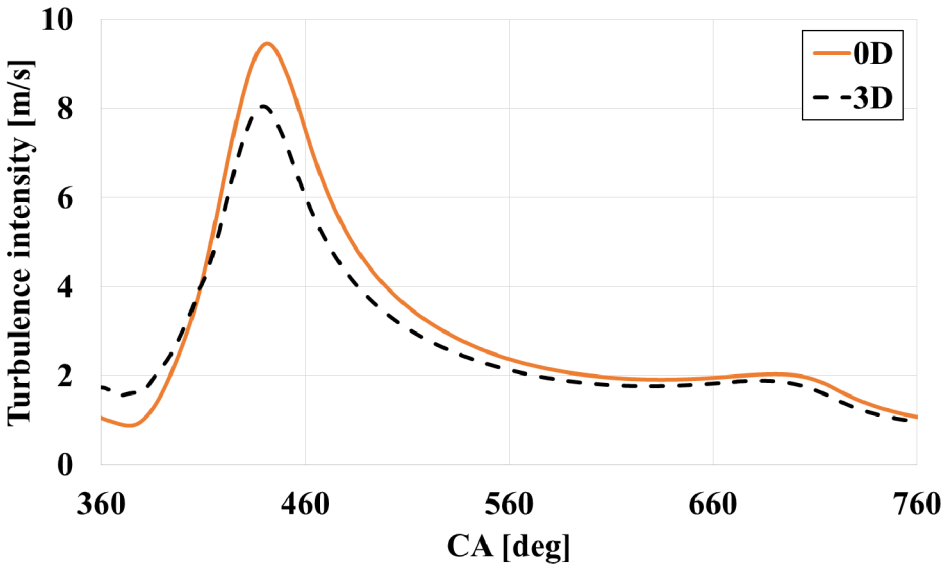

(b)

Figure 2.42 Comparison of (a) mean flow velocity magnitude and (b) turbulence intensity of case 12

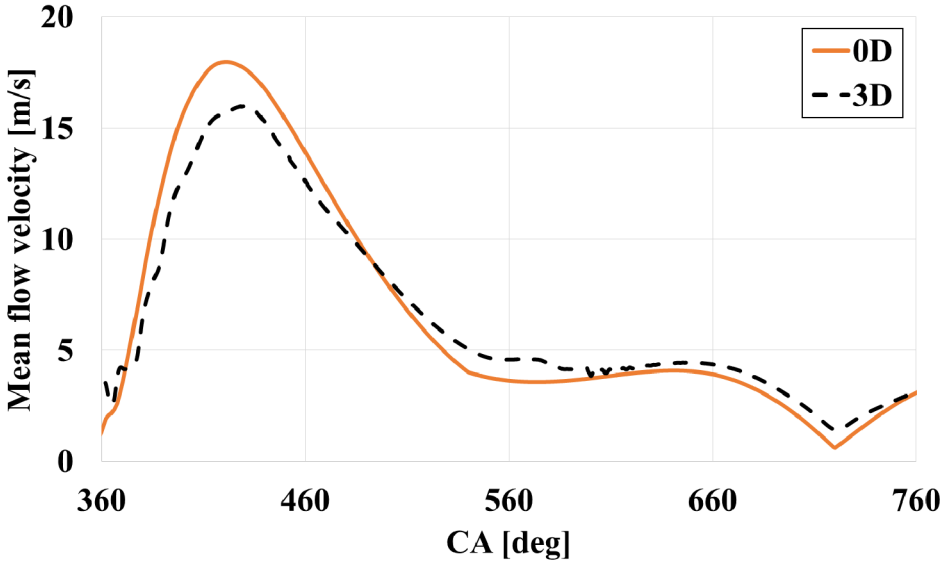

(a)

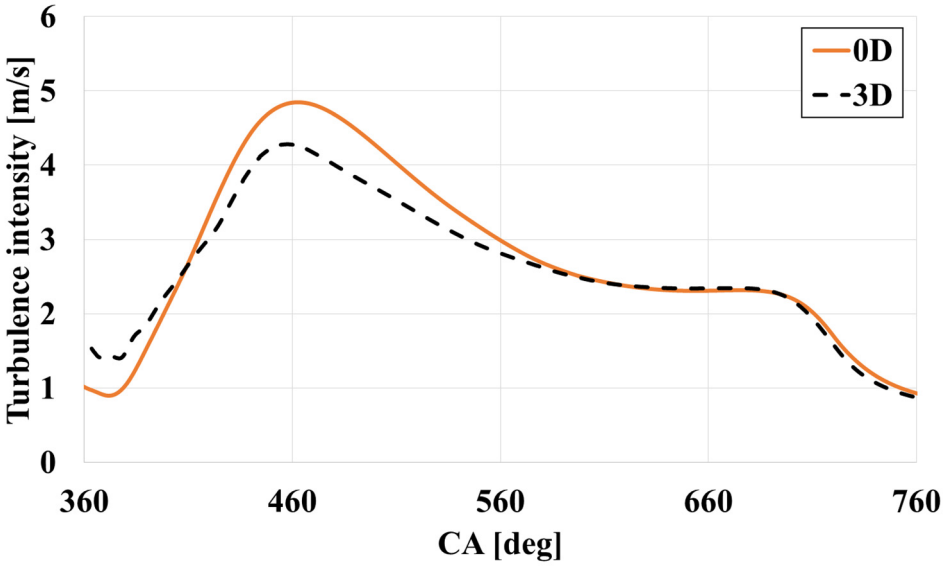

(b)

Figure 2.43 Comparison of (a) mean flow velocity magnitude and (b) turbulence intensity of case 13

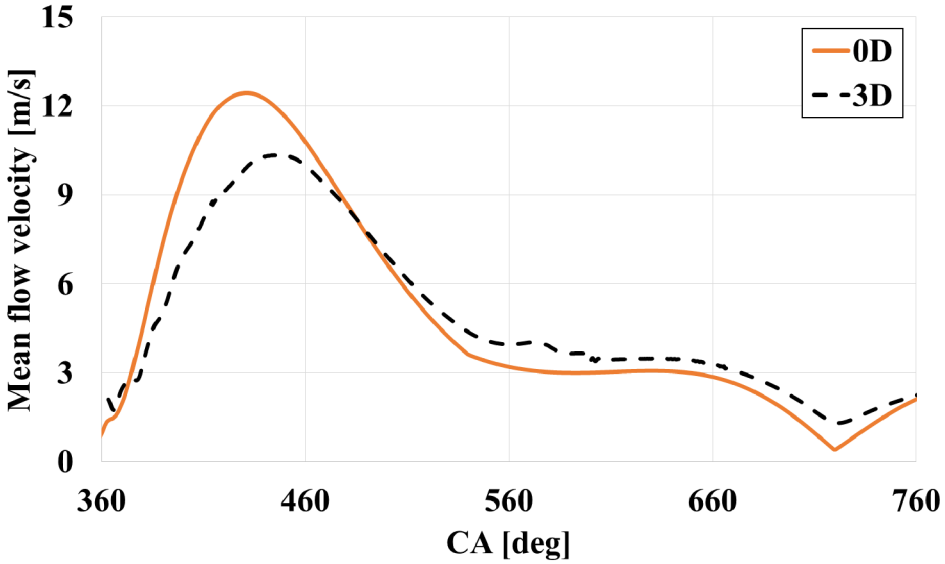

(a)

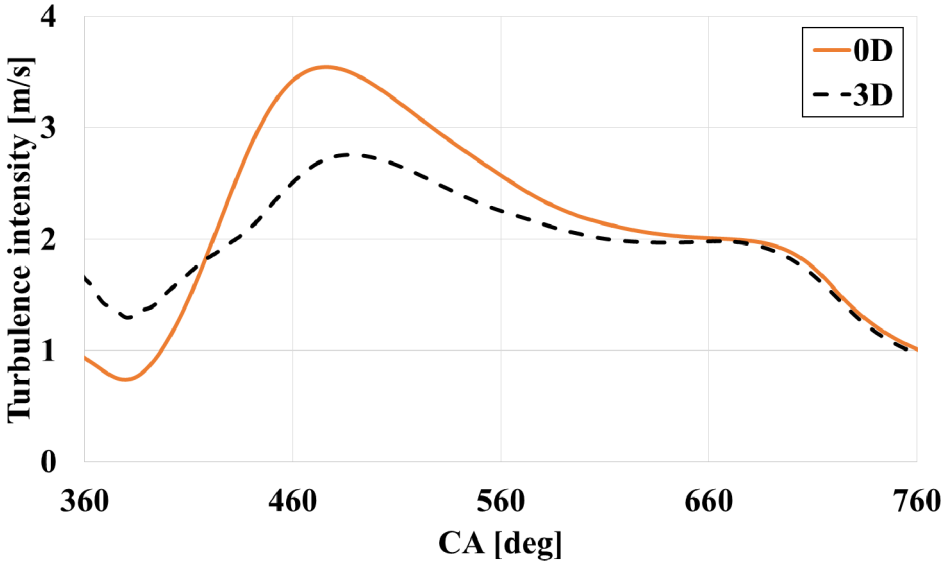

(b)

Figure 2.44 Comparison of (a) mean flow velocity magnitude and (b) turbulence intensity of case 15

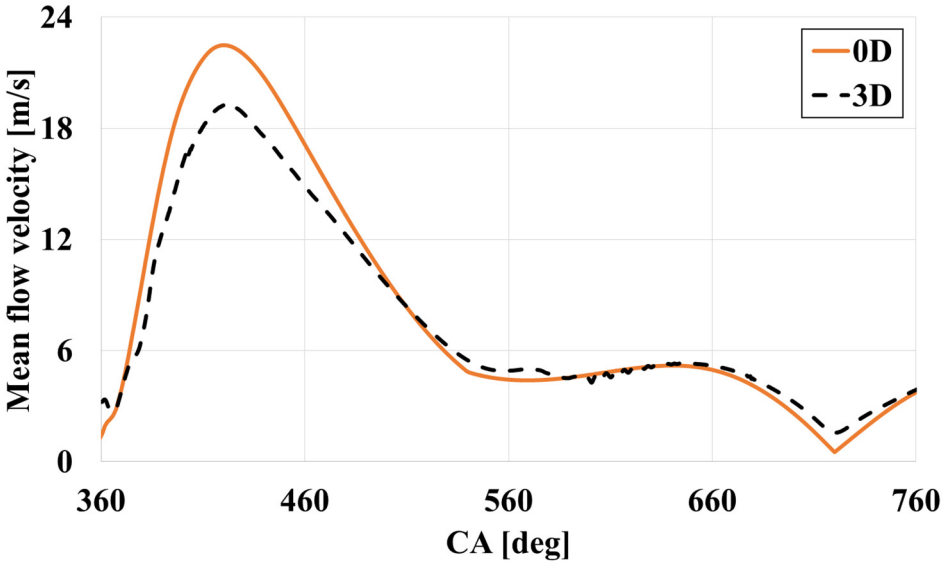

(a)

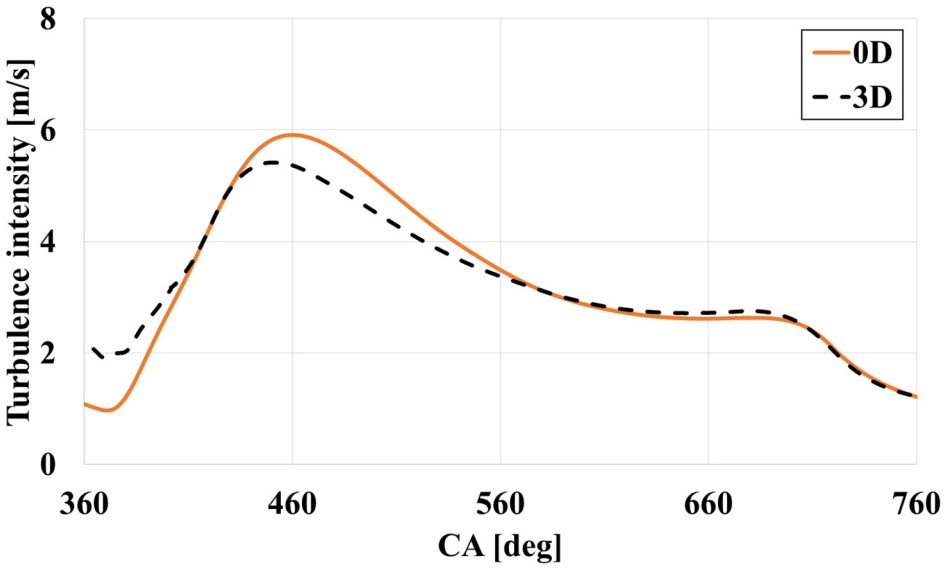

(b)

Figure 2.45 Comparison of (a) mean flow velocity magnitude and (b) turbulence intensity of case 16

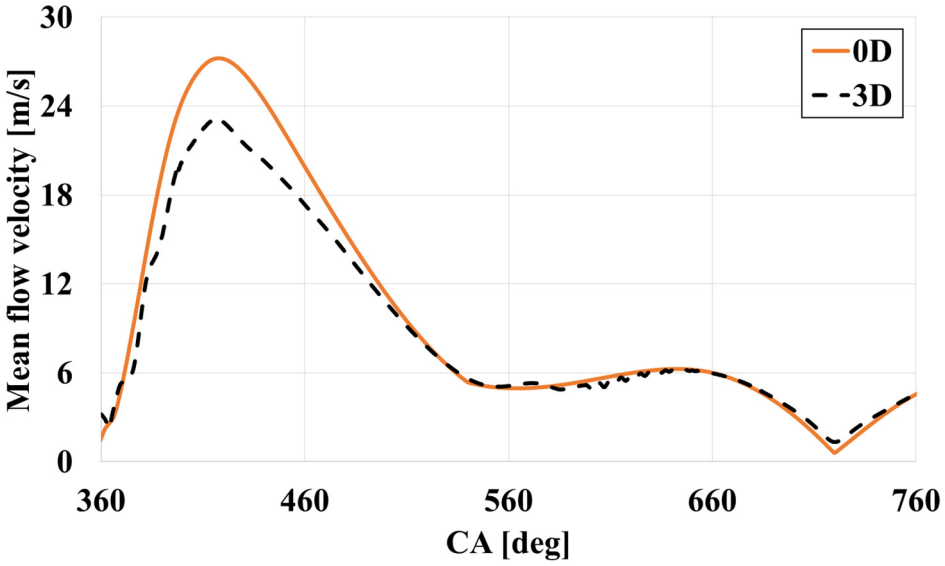

(a)

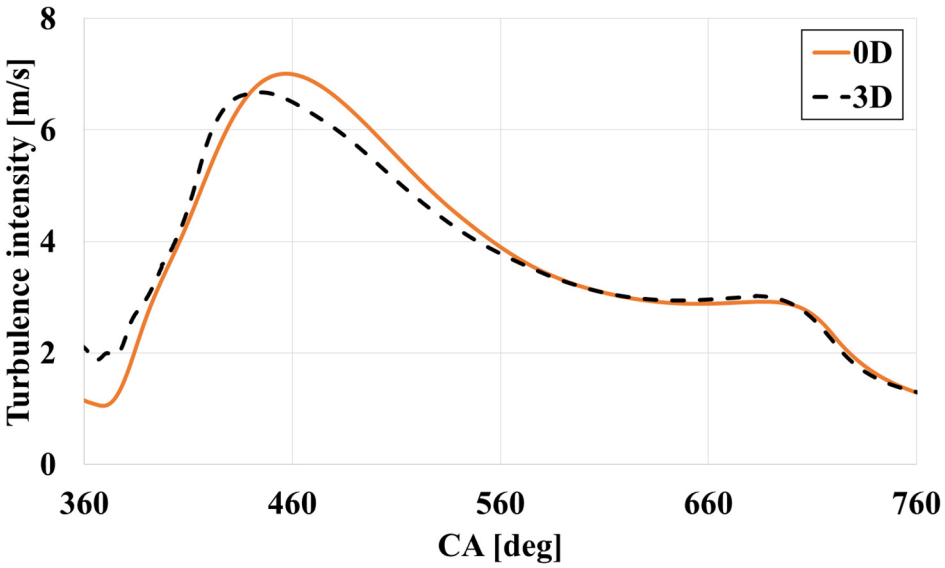

(b)

Figure 2.46 Comparison of (a) mean flow velocity magnitude and (b) turbulence intensity of case 17

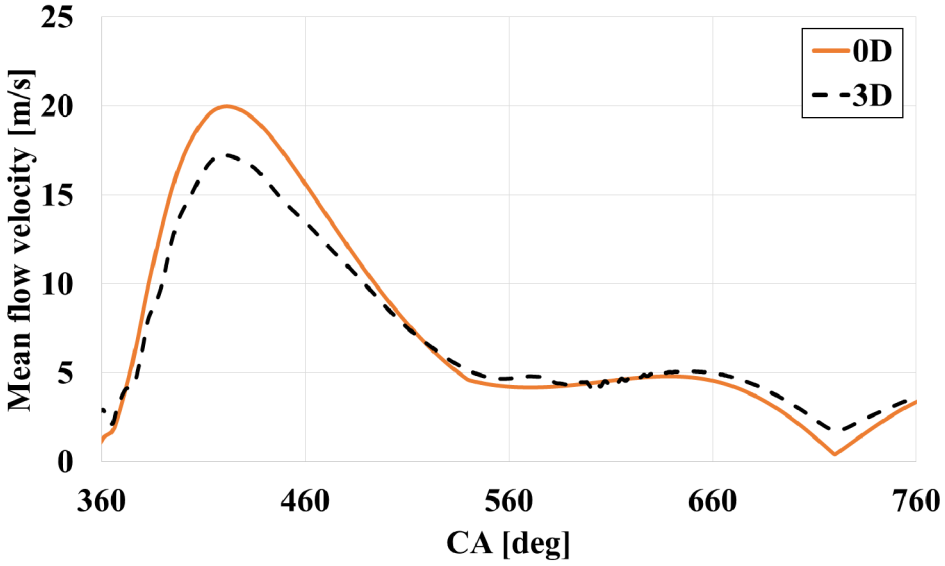

(a)

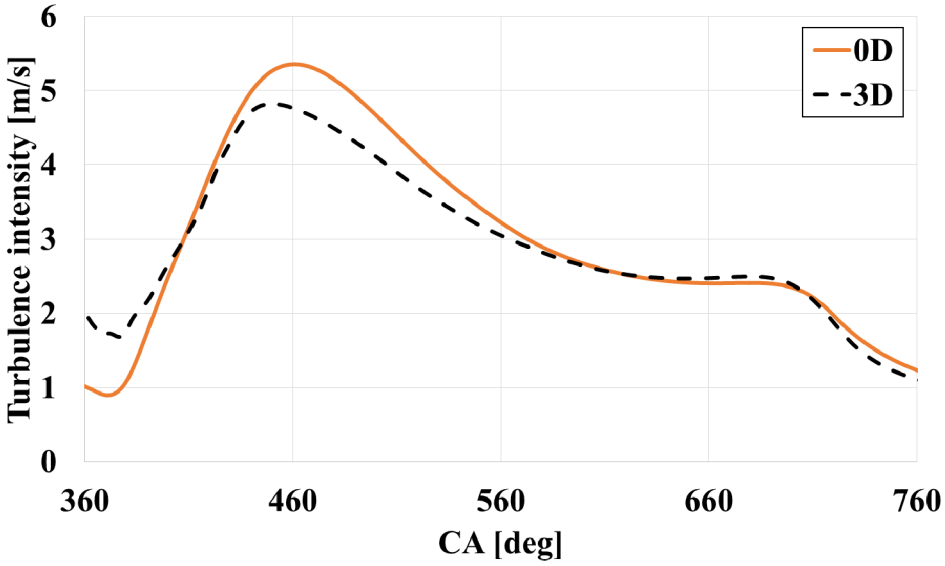

(b)

Figure 2.47 Comparison of (a) mean flow velocity magnitude and (b) turbulence intensity of case 18

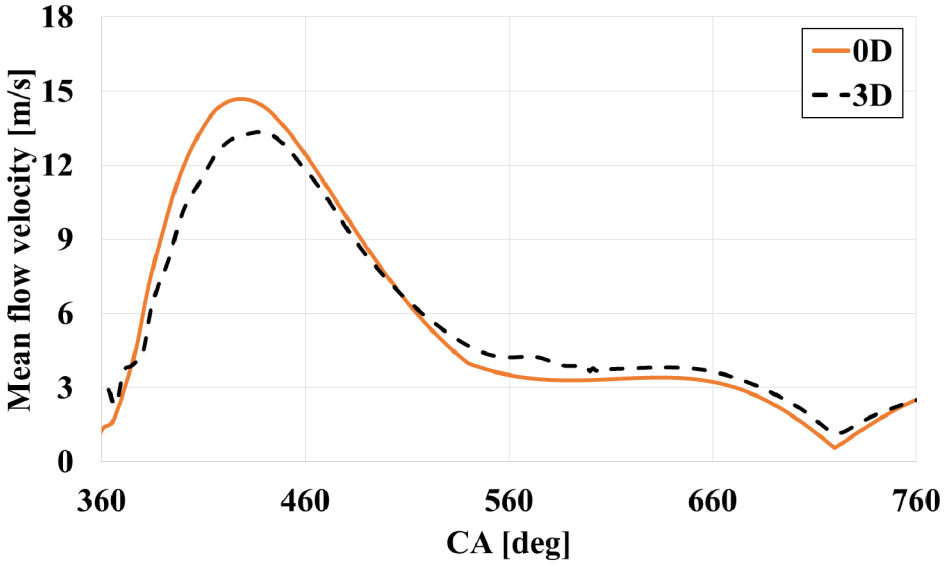

(a)

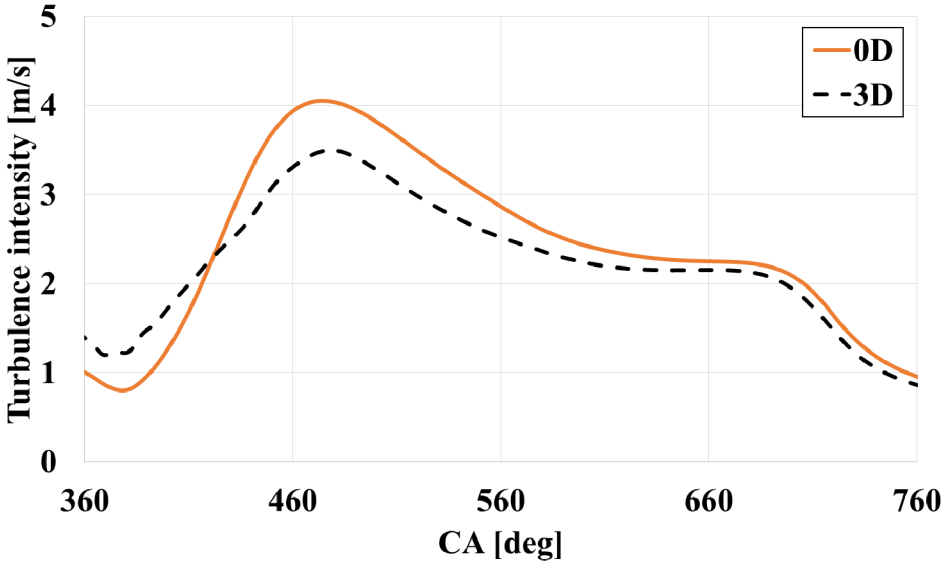

(b)

Figure 2.48 Comparison of (a) mean flow velocity magnitude and (b) turbulence intensity of case 19

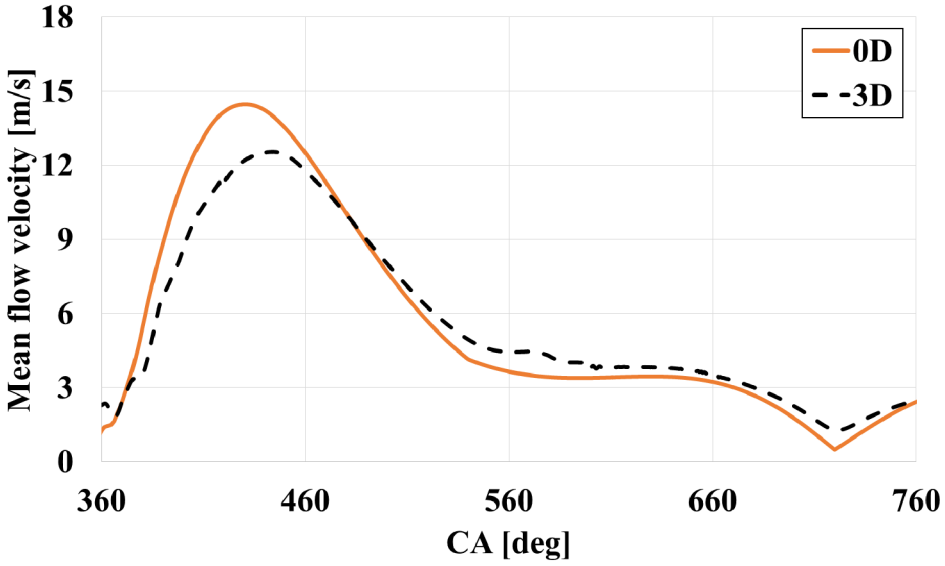

(a)

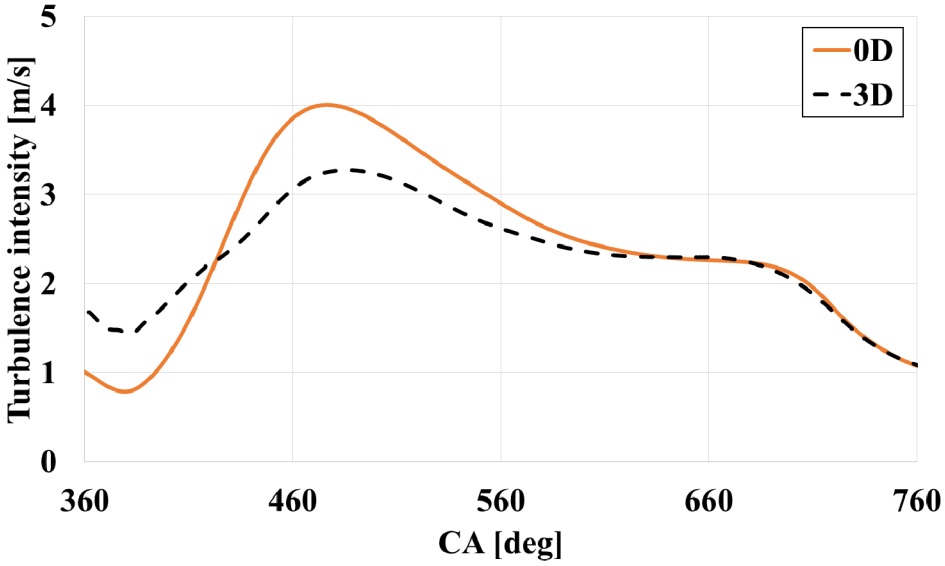

(b)

Figure 2.49 Comparison of (a) mean flow velocity magnitude and (b) turbulence intensity of case 20

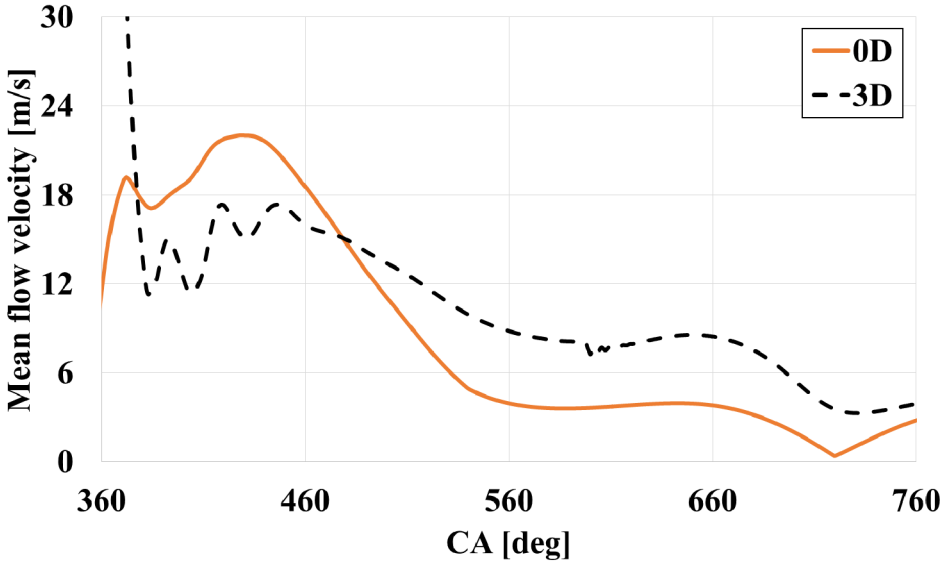

(a)

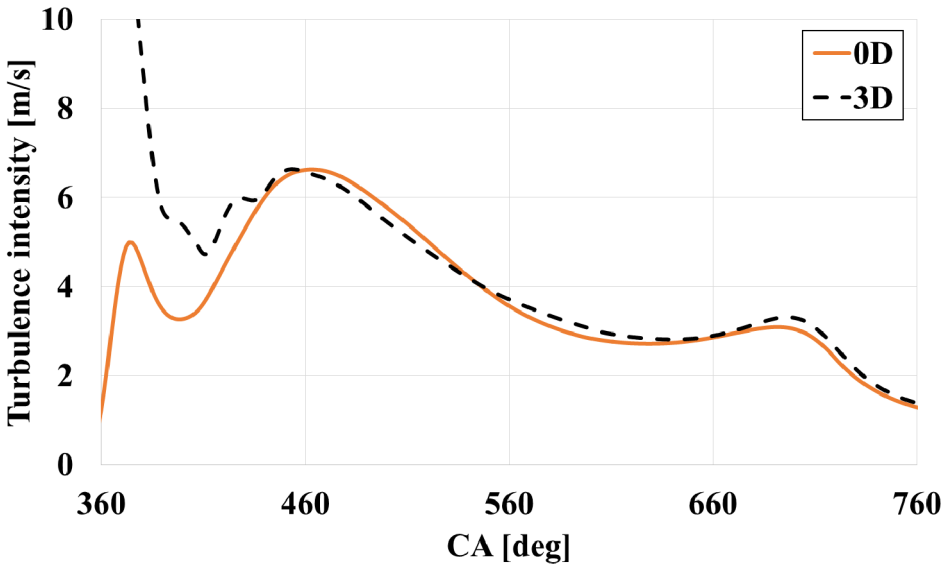

(b)

Figure 2.50 Comparison of (a) mean flow velocity magnitude and (b) turbulence intensity of high tumble engine at 1500 rpm

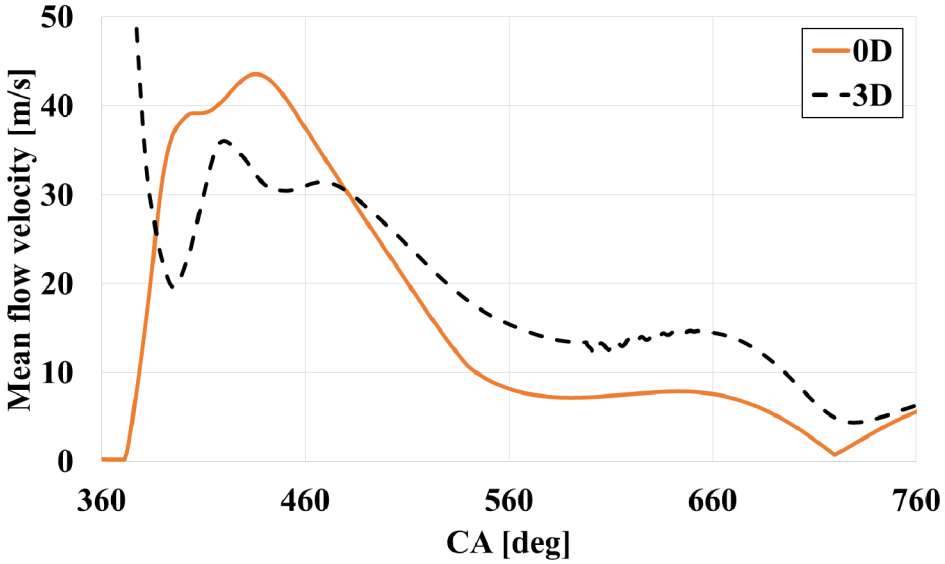

(a)

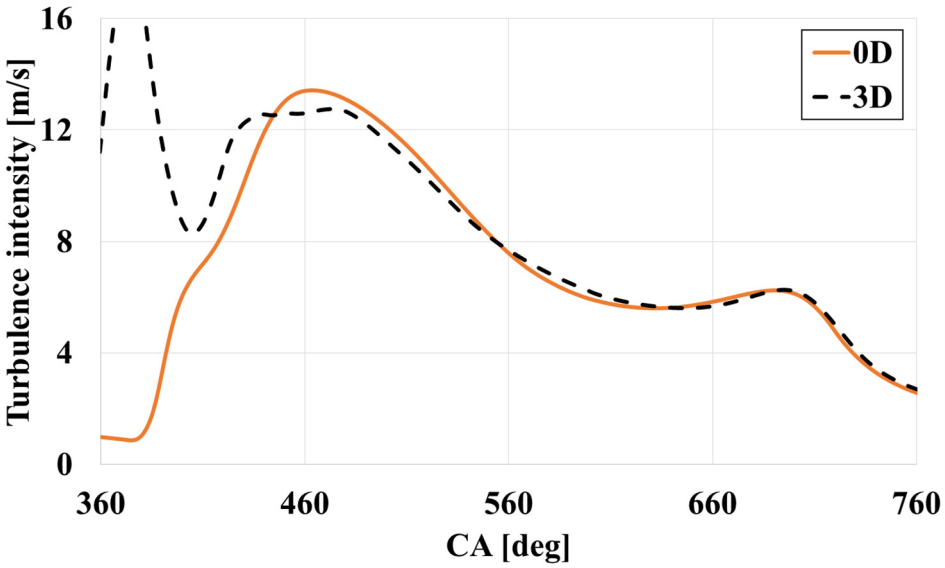

(b)

Figure 2.51 Comparison of (a) mean flow velocity magnitude and (b) turbulence intensity of high tumble engine at 3000 rpm

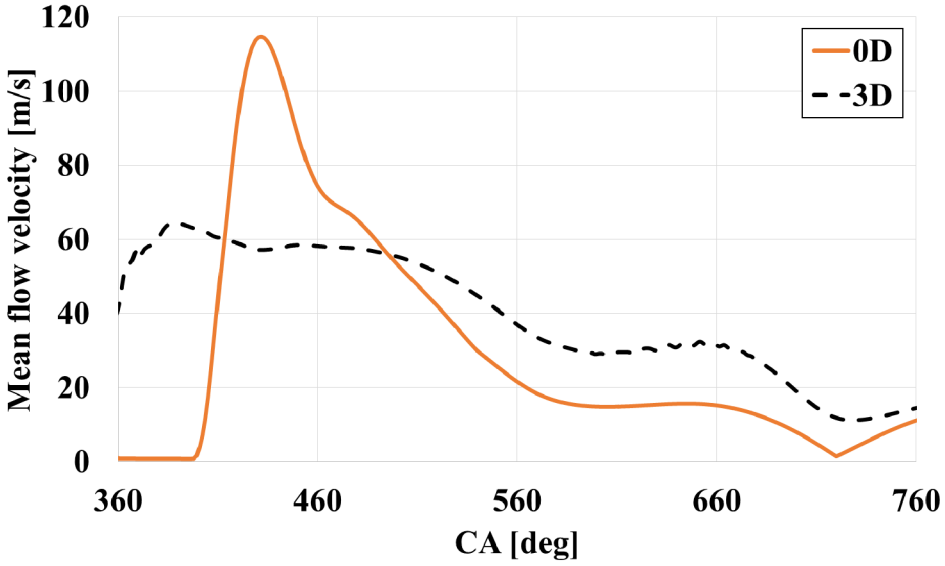

(a)

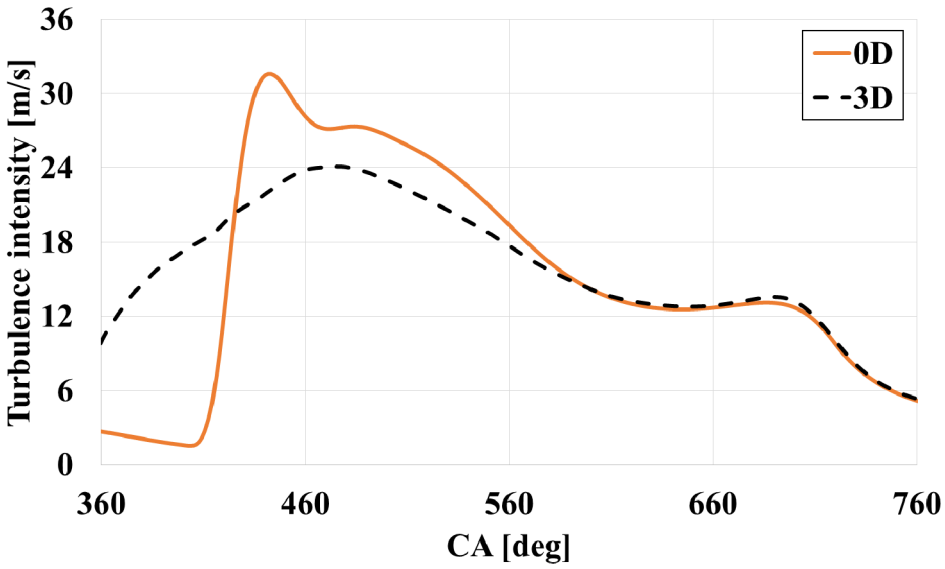

(b)

Figure 2.52 Comparison of (a) mean flow velocity magnitude and (b) turbulence intensity of high tumble engine at 6000 rpm

Chapter 3. Development of phenomenological quasi-dimensional combustion model

3.1 Necessity of model development

The combustion in the engine cylinder is a very sophisticated phenomenon as it incorporates the processes of not only the heat released from chemical energy of the fuel, but also the conversion of the chemical species into harmful emissions. Heat transfer to the wall and changes in temperature due to compression and expansion of the chamber volume occur simultaneously with the combustion processes. To describe the characteristics of combustion processes, QD combustion models have been widely used. Basic assumption of the QD combustion model is that the burned and unburned zones are separated by the flame front, and the thermodynamic state of each zones are computed separately [2]. The thermodynamic state of each zones can be obtained from equations of energy conservation, and the constraints on mass and volume. The relevant equations are well-documented in [96]. The key factor in the QD combustion model is the estimation of rate of mass transfer from unburned zone to burned zone as it determines the burn rate.

Although QD combustion models have been successful in prediction of burn rate obtained from experimental data, the model verification was done for limited range of operating conditions in most of the researches. For QD combustion model to become reliable as much as 3D CFD, the model needs to be able to reproduce the combustion characteristics of 3D CFD. Therefore, a QD combustion model which can predict the combustion characteristics close to those of 3D CFD over wide range of engine operating conditions is necessary.

3.2 Modeling approach

As introduced in the previous chapter, the entrainment model, and the fractal model have been widely used for describing the burn rate. In this study, phenomenological QD combustion model was constructed based on the entrainment model amended by Tabaczynski et al. [71]. This choice was made as the mechanism of the entrainment model is similar to the processes of the combustion simulated in 3D CFD. In 3D CFD, level-set approach using G-equation is utilized to predict the position of the flame front. The engulfed unburned mass by the flame, however, is not converted into fully burned species immediately. Instead, the species are converted according to the evolution of the progress variable within the turbulent flame brush. Similarly, the entrainment model assumes that a portion of unburned mixture is engulfed by the flame front, and the entrained mass is converted into products.

To obtain the burn rate using the entrainment model, the information on turbulence intensity during combustion is required as it determines the entrainment speed, and characteristic burn time [71]. The simplest way to calculate the turbulence intensity during combustion is to utilize the RDT [78]. The equation can be expressed as below:

$$u' = u'_0 \left(\frac{\rho}{\rho_0}\right)^{1/3} \tag{3.1}$$

where u' is the turbulence intensity, and ρ is the in-cylinder gas density. The subscript 0 indicates that properties are from a reference state.

To confirm whether Eq. 3.1 is sufficient to resolve the characteristics of the evolution of turbulence intensity during combustion, it was compared with that of 3D

CFD. Fig. 3.1 shows large difference in the evolution of turbulence intensity, and it can be concluded that Eq. 3.1 is insufficient. Thus, a new model to estimate the turbulence intensity during combustion is necessary.

In addition to the turbulence intensity during combustion, the information on flame area and turbulent flame speed are needed for prediction of entrainment rate and burn rate. The flame area can be obtained from the method introduced by Poulos [78]. For the calculation of the turbulent flame speed, precise calculation of the laminar flame speed must be augmented since the turbulent flame speed is dependent on the laminar flame speed, and turbulence intensity. Also, as the laminar flame speed is heavily dependent upon the gas temperature, the in-cylinder temperature must be predicted precisely. Thus, an appropriate selection of correlation of laminar flame speed, and a model for accurate prediction of heat transfer rate are required. Therefore, in this study, development of a model for prediction of turbulence intensity during combustion, and modification of original models of flame propagation speed, and heat transfer were conducted.

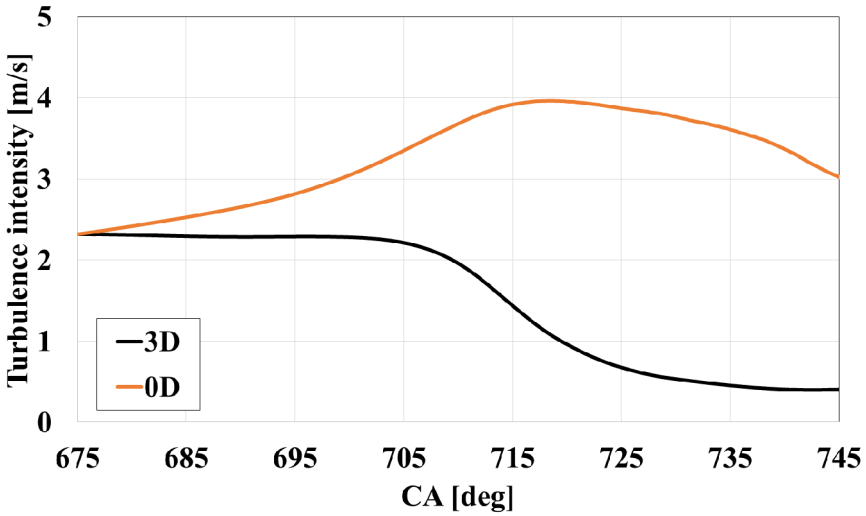

Figure 3.1 Comparison of the turbulence intensity of unburned zone calculated with 0D model and 3D CFD

3.3 Standard for dividing zones in 3D CFD

To utilize the 3D CFD results for model development, and compare the predicted results with those of the developed model, it is necessary to define a standard for dividing zones in 3D CFD. As mentioned previously, in 3D CFD combustion simulation of SI engine applications, G-equation is generally solved to predict the location of the flame front. The G values obtained from solving G-equation indicate the distance from the flame front, so iso-surface of an appropriate value of G may be chosen for diving zones. From the definition, iso-surface of G = 0 can be a good standard. Before proceeding with this definition for dividing zones, burned mass fraction was compared with the progress variable which indicates the degree of the conversion of reactants into products. Fig. 3.2 shows differences in evolution of mass fractions. The reason for such discrepancies can be attributed to that the iso-surface of G = 0 includes only a small portion of the intermediate zone where reactants and products coexist, while progress variable accounts the information of the intermediate zone. From testing various values of G, it was found that G = 1 works well for representing a boundary for dividing zone. Thus, for the rest of the study, the properties of burned, and unburned zone from 3D CFD were calculated by dividing zones with G = 1 iso-surface.

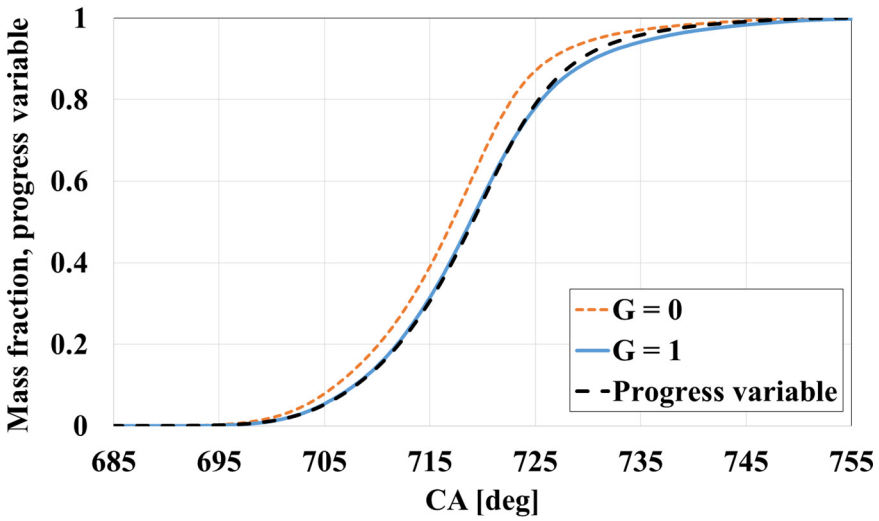

Figure 3.2 Comparison of the burned zone mass fraction according to the zoning strategy under the condition of 1500 rpm, P_i 0.6 bar, and spark timing of 35º bTDC

3.4 Turbulence intensity prediction during combustion

To describe the evolution of turbulence intensity during combustion, basic governing equation has been reviewed. The total amount of the turbulent kinetic energy in cylinder can be written as:

$$k_{cyl}m_{cyl} = k_u m_u + k_b m_b \tag{3.2}$$

where the subscript u and b denote that the properties belong to unburned and burned zone, respectively. The change in turbulent kinetic energy in unburned zone is then expressed as:

$$\frac{d}{dt}(m_u k_u) = k_u \frac{dm_u}{dt} + m_u \frac{dk_u}{dt} \tag{3.3}$$

Using the Eq. 1.1 with variable $a = 0$, and a production term in addition, the above equation can be expanded as:

$$\frac{d}{dt}(m_u k_u) = k_u \dot{m}_u + m_u \left(\Psi_u + \frac{2}{3} RDT_u - \varepsilon_u\right) + F_{k,u} \tag{3.4}$$

The RDT term must be modified from the former expressions in the previous chapter. Although the mass in the control volume of each zone is changing, the convective mass transfer across the control surface is zero as the control surface is attached to the flame front. Therefore, the change in mass of each zone must be included using source or sink term.

$$RDT_u = -k_u \left(\frac{\partial U_j}{\partial x_j}\right) = k_u \left(\frac{1}{\rho_u}\frac{d\rho_u}{dt} - \frac{1}{m_u}\frac{dm_u}{dt}\right) \tag{3.5}$$

$F_{k,u}$ in Eq. 3.4 represents the flux of the turbulent kinetic energy from unburned zone to burned zone due to mass transfer. This term can be expressed as in Eq. 3.6,

which assumes that the turbulent kinetic energy is transported in a same way as the enthalpy of the unburned zone is transferred due to combustion. This is also identical with the flux term expressed in previous research [73].

$$F_{k,u} = k_u \frac{dm_u}{dt} \tag{3.6}$$

The expression for the flux term can be interpreted as the sink of the turbulent kinetic energy in unburned zone and, source in burned zone, respectively. The final form of the Eq. 3.4 becomes:

$$\frac{d}{dt}(m_u k_u) = k_u \dot{m}_u + m_u \left(\Psi_u + \frac{2}{3} k_u \left(\frac{1}{\rho_u} \frac{d\rho_u}{dt} - \frac{1}{m_u} \frac{dm_u}{dt} \right) - \varepsilon_u \right) + k_u \dot{m}_u \tag{3.7a}$$

$$= \left(m_u \Psi_u + \frac{2}{3} \frac{m_u k_u}{\rho_u} \frac{d\rho_u}{dt} - m_u \varepsilon_u + \frac{1}{3} k_u \dot{m}_u \right) + k_u \dot{m}_u \tag{3.7b}$$

Similarly, the rate of change of turbulent kinetic energy in burned zone can be expressed as in Eqs. 3.8.

$$\frac{d}{dt}(m_b k_b) = k_b \dot{m}_b + m_b \left(\Psi_b + \frac{2}{3} k_b \left(\frac{1}{\rho_b} \frac{d\rho_b}{dt} - \frac{1}{m_b} \frac{dm_b}{dt} \right) - \varepsilon_b \right) - k_u \dot{m}_u \tag{3.8a}$$

$$= \left(m_b \Psi_b + \frac{2}{3} \frac{m_b k_b}{\rho_b} \frac{d\rho_b}{dt} - m_b \varepsilon_b + \frac{1}{3} k_b \dot{m}_b \right) + k_u \dot{m}_b \tag{3.8b}$$

The equation above has a similar form with that of Eq. 2.26 with a term related to change in mass of each zone. Some former studies assumed that the turbulent kinetic energy transferred from unburned zone to burned zone would be changed according to RDT right after it is transported. If this assumption were used, the sum of the flux terms expressed by source and sink in each zone would not become zero.

However, since the source or sink of the turbulent kinetic energy does not exist, the sum of the flux terms must become zero. In this sense, it is postulated that the change in turbulent kinetic energy during transport should be kept independent of density change.

The verification of the above expression was carried out for various spark timing using the information obtained from 3D CFD. Figs. 3.3 to 3.6 show some discrepancies in the evolution of the turbulent kinetic energy of each zones predicted by QD model compared to those of 3D CFD. The reason for the differences may be attributed to the assumption that the turbulent field is perfectly isotropic, and uniform so that spatial distribution in turbulent kinetic energy, and its diffusion transport are neglected. Nevertheless, it can be postulated that the Eqs. 3.7 and 3.8 can capture the evolution of the turbulent kinetic energy in each zone closer to 3D CFD.

When verifying the validity of the Eqs. 3.7 and 3.8, the dissipation was calculated using the turbulent kinetic energy and the integral length scale obtained from 3D CFD result. For Eqs. 3.7 and 3.8 to be applied in the QD model, however, the integral length scale of each zone must be prescribed for the calculation of the dissipation rate. During combustion, however, the correlation of the integral length scale developed in the previous chapter cannot be utilized as it is suitable for motored condition only. Thus, an appropriate correlation for integral length scale was found using available thermodynamic. The newly proposed phenomenological expression for unburned and burned zone integral length scale can be written as in Eqs. 3.9 and 3.10.

$$l_u = l_{0D}\left(\frac{\rho_{cyl}}{\rho_u}\right)^{0.16}\left(\frac{V_u}{V_{cyl}}\right)^{0.33} \tag{3.9}$$

$$l_b = 0.8\, l_{0D}\left(\frac{\rho_{cyl}}{\rho_b}\right)^{0.5} \tag{3.10}$$

From Figs. 3.7 and 3.8, it can be confirmed that the above expression can reproduce the evolution of the integral length scale of each zones during combustion. Notable difference in the integral length scale of burned zone at the early part of the combustion is thought to be arising from the non-uniform spatial distribution of the integral length scale which cannot be captured with 0D model.

The production rate in Eqs. 3.7 and 3.8 may be obtained using the Eq. 2.16 derived in previous chapter. However, the magnitude of the production rate calculated using Eq. 2.16 deviated significantly from those of 3D CFD results. It is thought that the in-cylinder flow field during combustion would be different from that of the motoring condition, and difficult to be mimicked by the simple QD model which cannot consider the spatial distribution of the velocity field. Thus, instead of using Eq. 2.16, the production rate during combustion processes was assumed to be proportional to the dissipation term as the production and dissipation rate are closely related [97]. Also, an adjustable constant used in the 0D turbulence model introduced in previous chapter was added for the conjunction between the 0D and QD turbulent intensity prediction models. Rearranging the Eqs. 3.7 and 3.8 with modifications,

$$\frac{d}{dt}(m_u k_u) = \left(\left(\frac{2}{3} + C_{engine}\right)\frac{m_u k_u}{\rho_u}\frac{d\rho_u}{dt} - (1 - C_\Psi)m_u\varepsilon_u + \frac{1}{3}k_u\dot{m}_u\right) + k_u\dot{m}_u \quad (3.11)$$

$$\frac{d}{dt}(m_b k_b) = \left(\left(\frac{2}{3} + C_{engine}\right)\frac{m_b k_b}{\rho_b}\frac{d\rho_b}{dt} - (1 - C_\Psi)m_b\varepsilon_b + \frac{1}{3}k_b\dot{m}_b\right) - k_u\dot{m}_u \quad (3.12)$$

$$\varepsilon_u = C_{dissipation}\frac{{u_u}'^3}{l_{t,u}} \quad (3.13)$$

$$\varepsilon_b = C_{dissipation}\frac{{u_b}'^3}{l_{t,b}} \quad (3.14)$$

Validity of the QD integral length scale correlation and simplified production rate was examined by comparing the rate of change of turbulent kinetic energy in each zone for the same conditions as before. The same value for the constants C_{engine}, and $C_{dissipation}$ were used, and newly introduced constant C_{Ψ} was chosen to be 0.073. From the results shown in Figs. 3.9 to 3.12, it can be confirmed that the correlation of integral length scale and assumption on the production rate are reasonable.

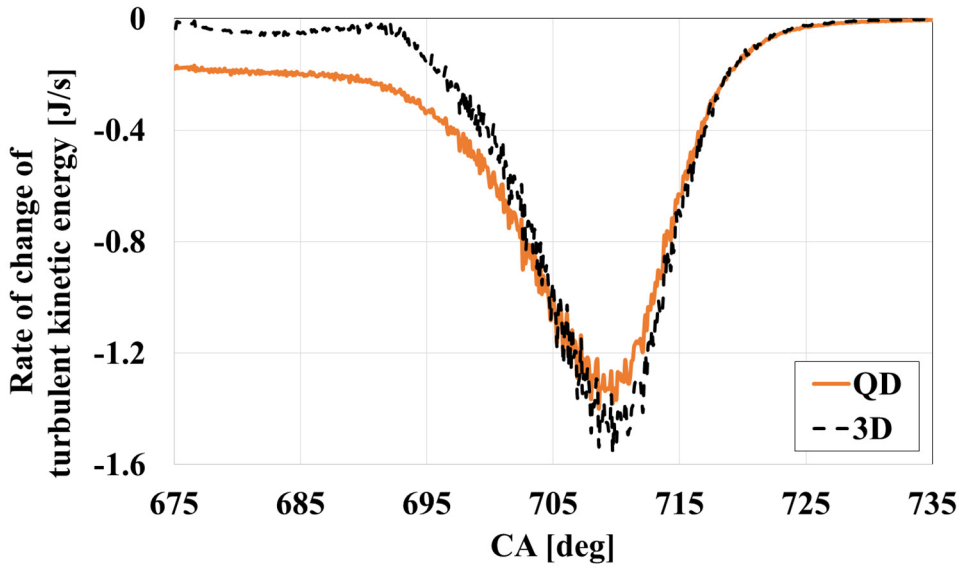

(a)

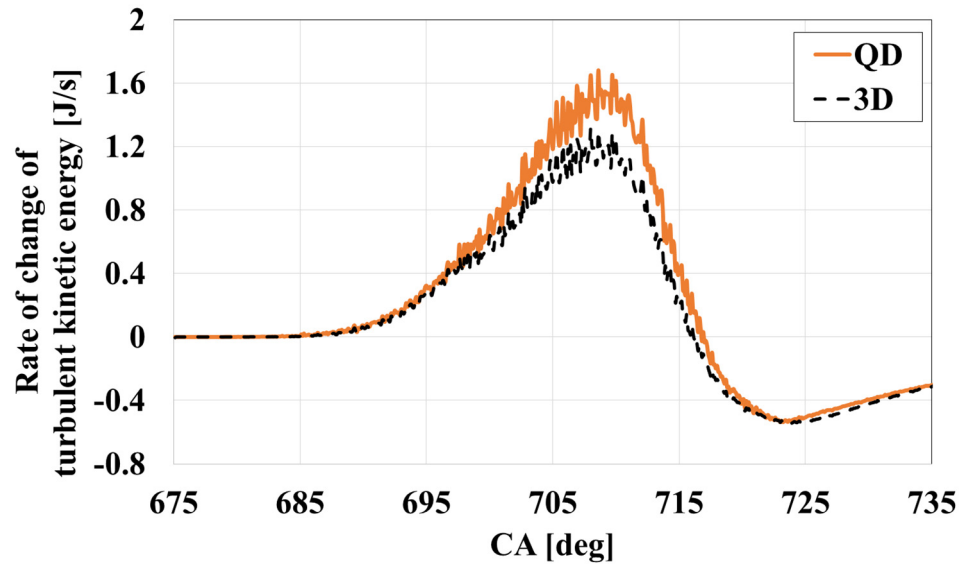

(b)

Figure 3.3 Rate of change of turbulent kinetic energy in (a) unburned, and (b) burned zone under 1500 rpm, P_i = 0.6 bar, and spark timing of 45º bTDC

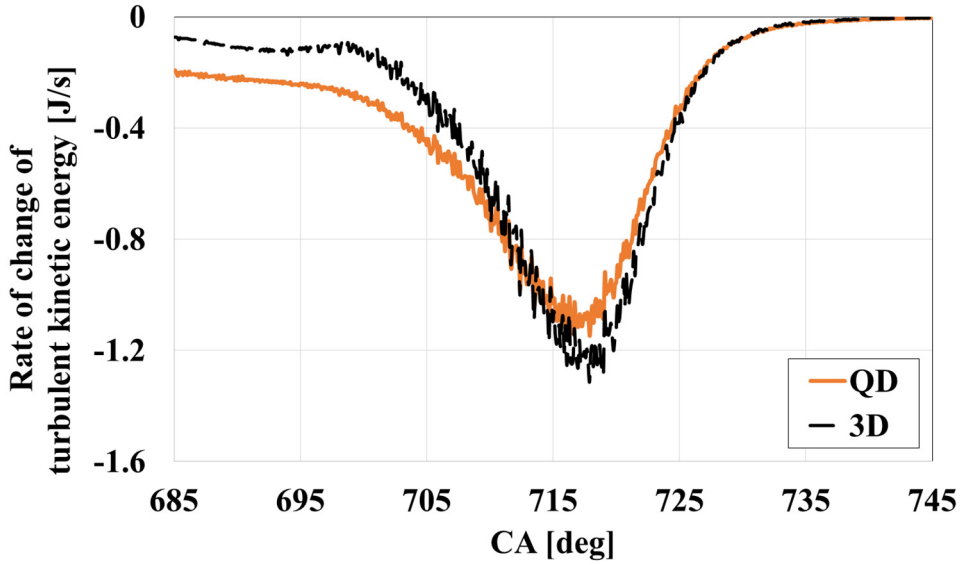

(a)

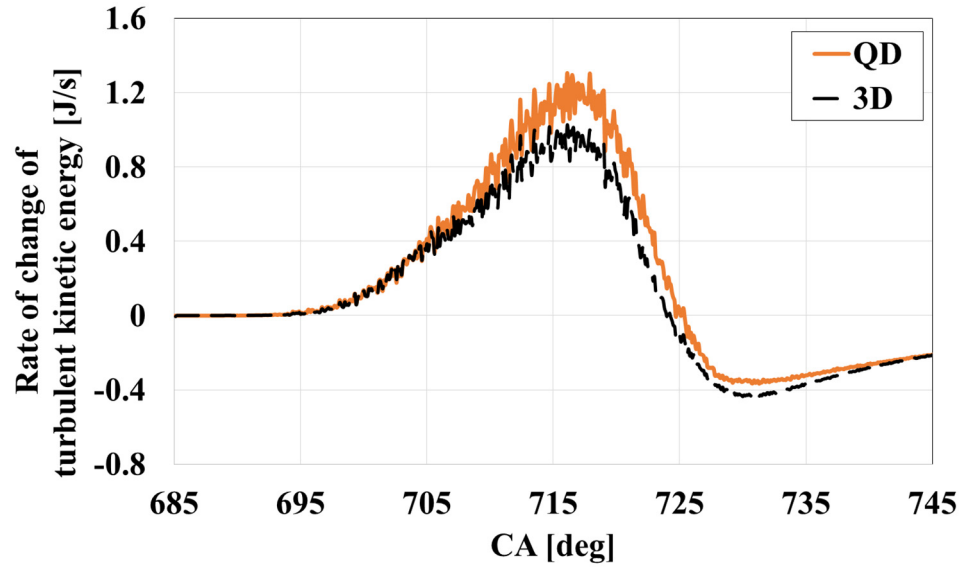

(b)

Figure 3.4 Rate of change of turbulent kinetic energy in (a) unburned, and (b) burned zone under 1500 rpm, P_i = 0.6 bar, and spark timing of 35º bTDC

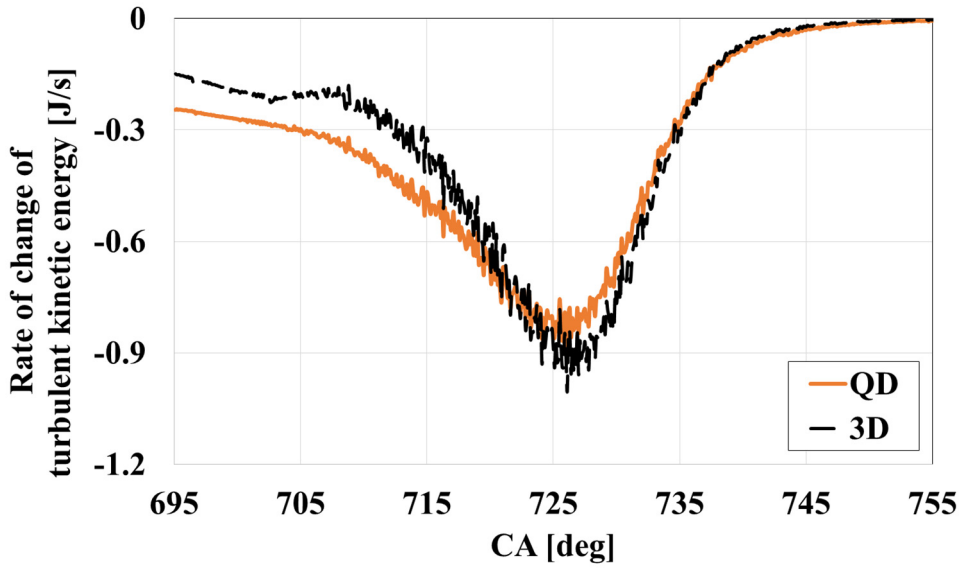

(a)

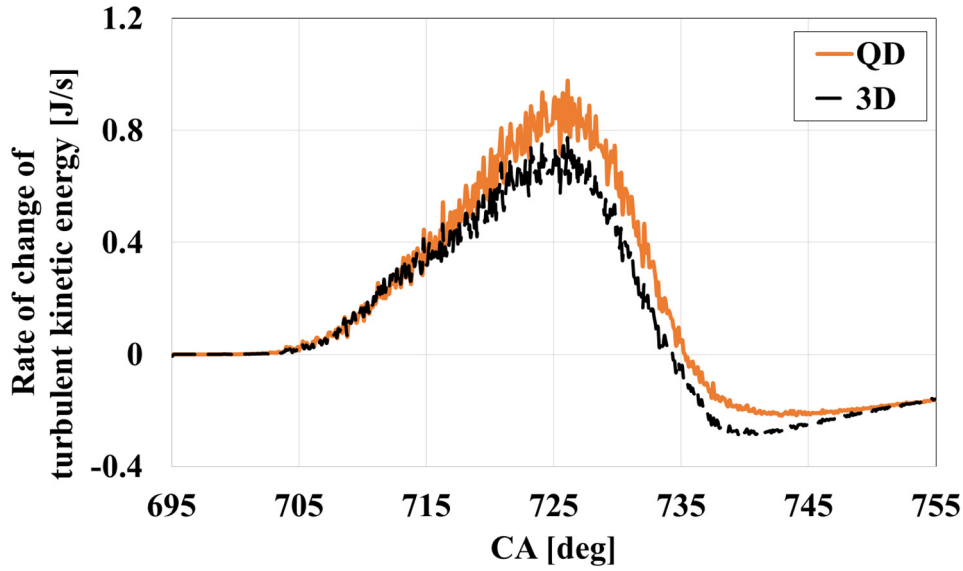

(b)

Figure 3.5 Rate of change of turbulent kinetic energy in (a) unburned, and (b) burned zone under 1500 rpm, P_i = 0.6 bar, and spark timing of 25º bTDC

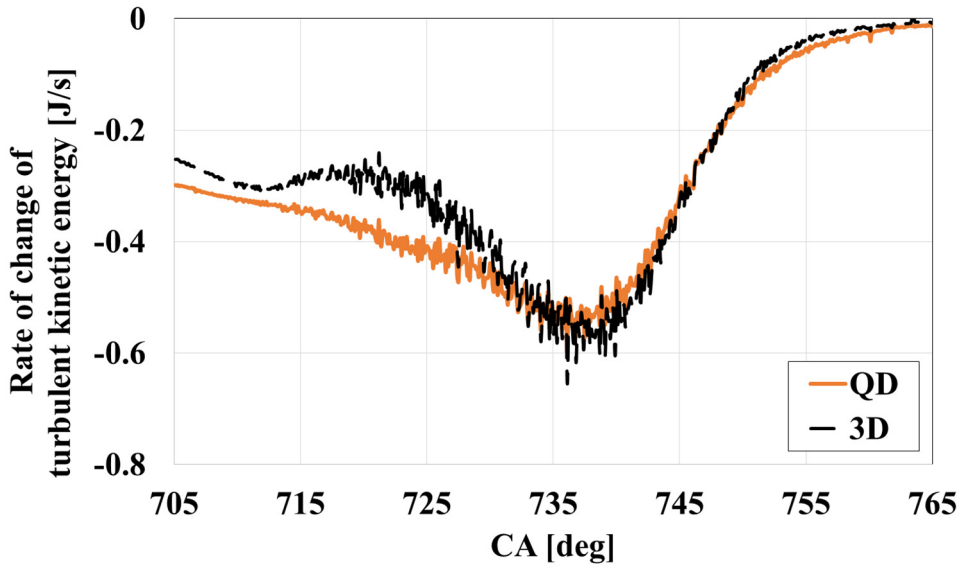

(a)

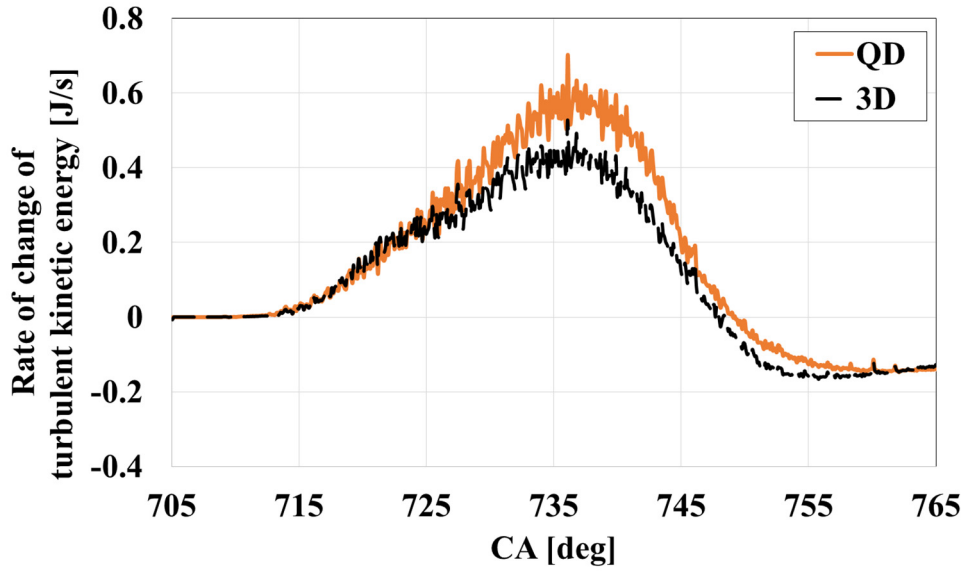

(b)

Figure 3.6 Rate of change of turbulent kinetic energy in (a) unburned, and (b) burned zone under 1500 rpm, P_i = 0.6 bar, and spark timing of 15º bTDC

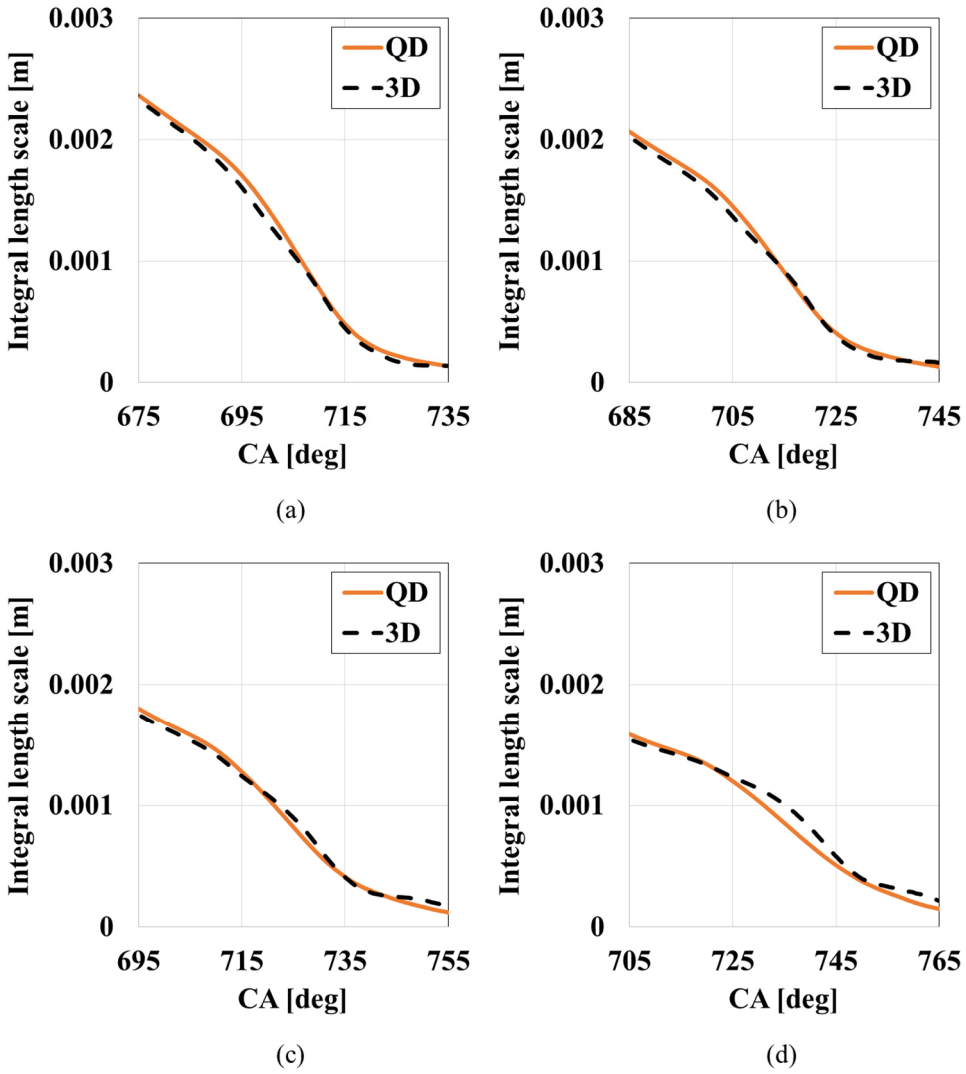

Figure 3.7 Comparison of integral length scale of unburned zone predicted by QD model and 3D CFD for spark timing of (a) 45º bTDC, (b) 35º bTDC, (c) 25º bTDC, and (d) 15º bTDC

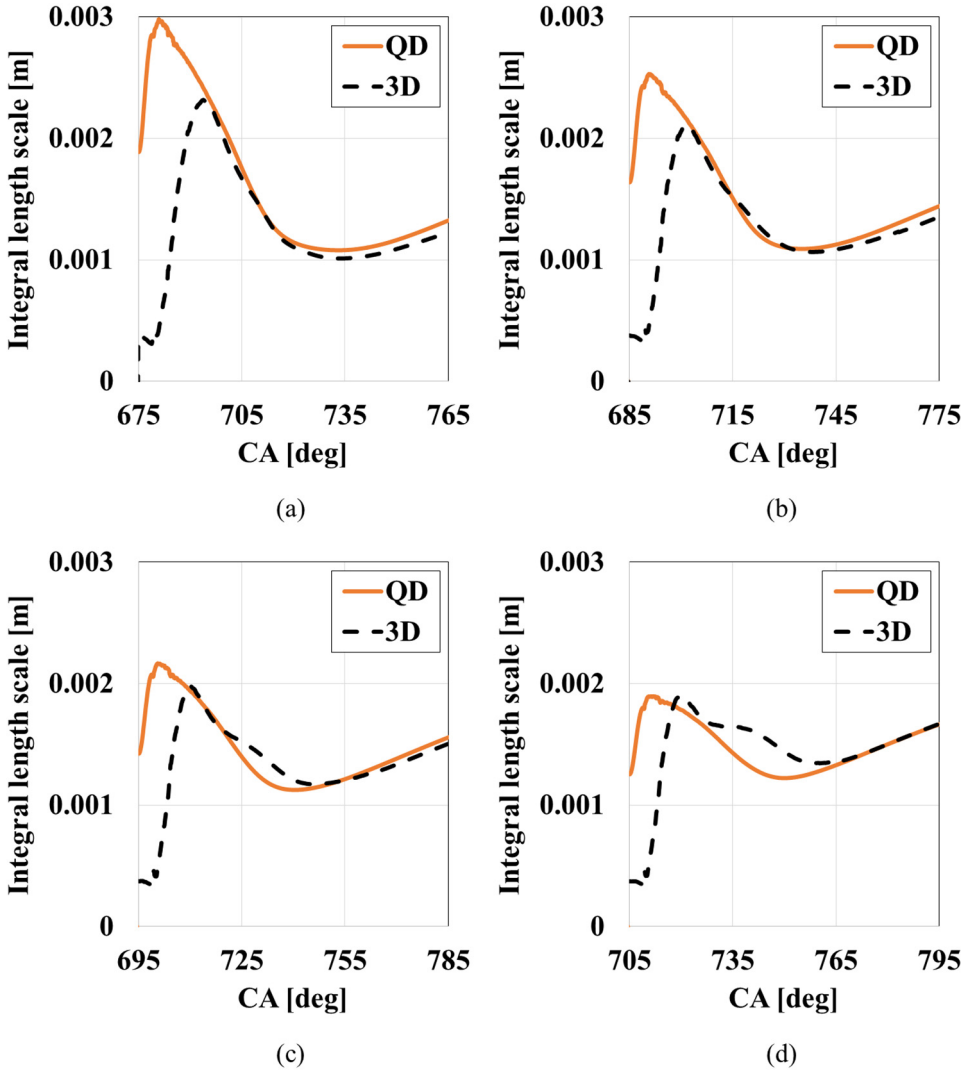

Figure 3.8 Comparison of integral length scale of burned zone predicted by QD model and 3D CFD for spark timing of (a) 45º bTDC, (b) 35º bTDC, (c) 25º bTDC, and (d) 15º bTDC

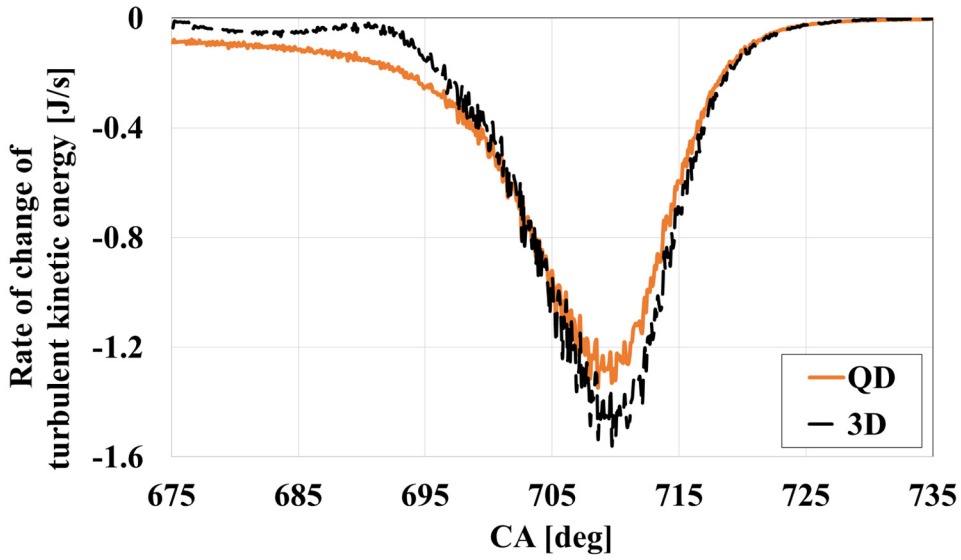

(a)

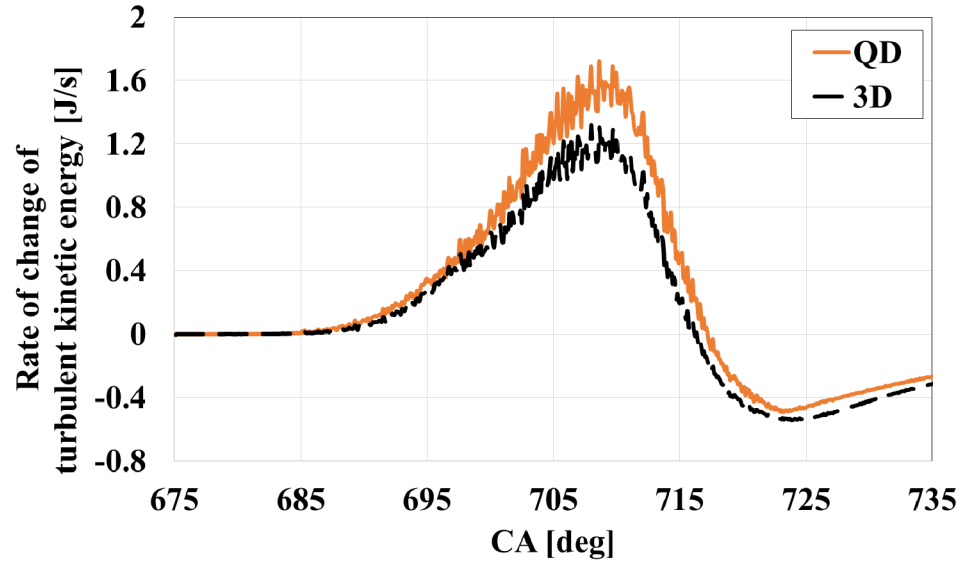

(b)

Figure 3.9 Rate of change of turbulent kinetic energy in (a) unburned, and (b) burned zone calculated with modified governing equations under 1500 rpm, P_i = 0.6 bar, and spark timing of 45º bTDC

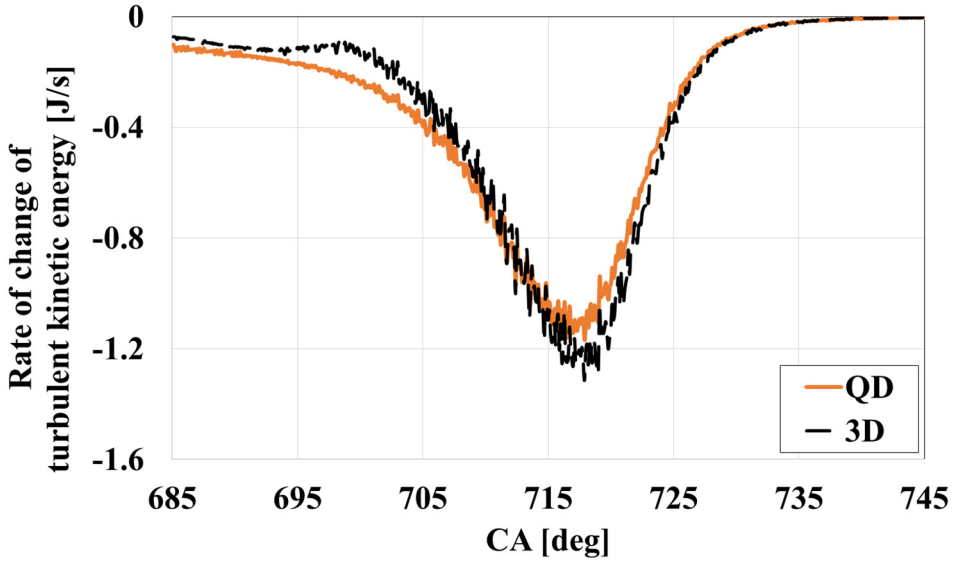

(a)

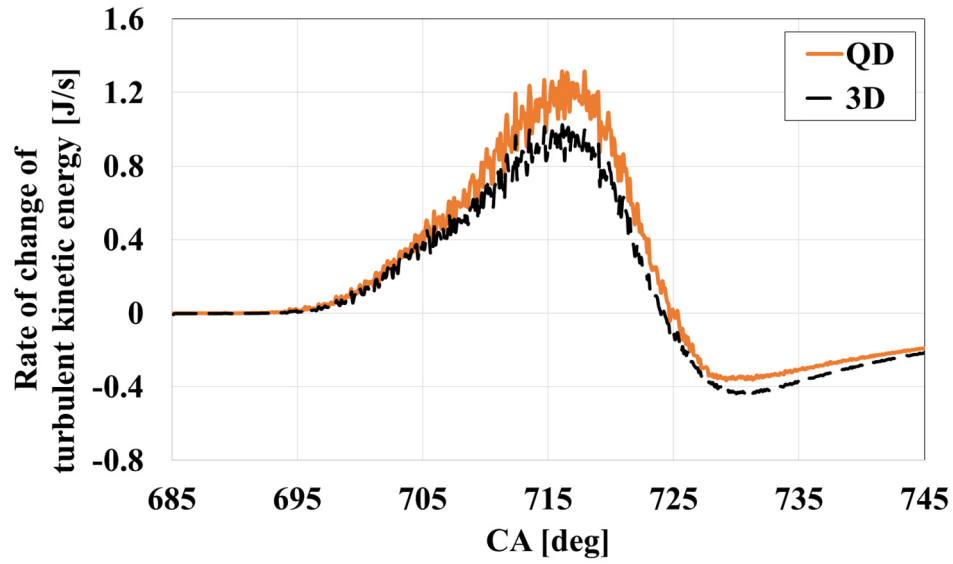

(b)

Figure 3.10 Rate of change of turbulent kinetic energy in (a) unburned, and (b) burned zone with modified governing equations under 1500 rpm, P_i = 0.6 bar, and spark timing of 35º bTDC

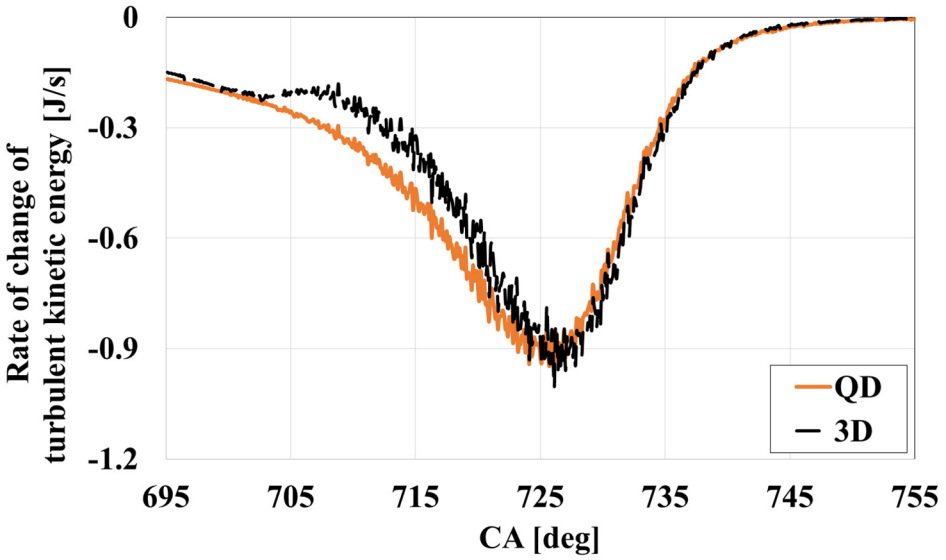

(a)

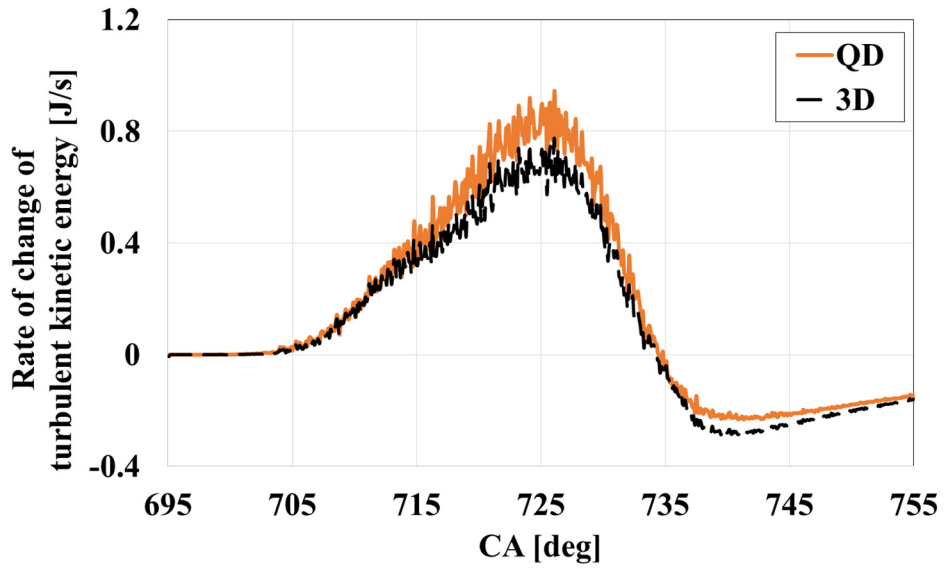

(b)

Figure 3.11 Rate of change of turbulent kinetic energy in (a) unburned, and (b) burned zone with modified governing equations under 1500 rpm, P_i = 0.6 bar, and spark timing of 25º bTDC

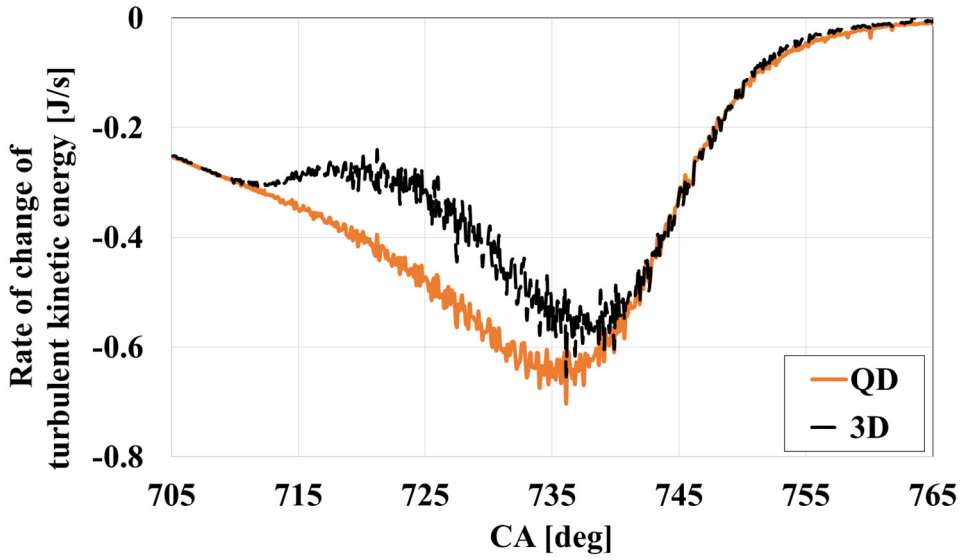

(a)

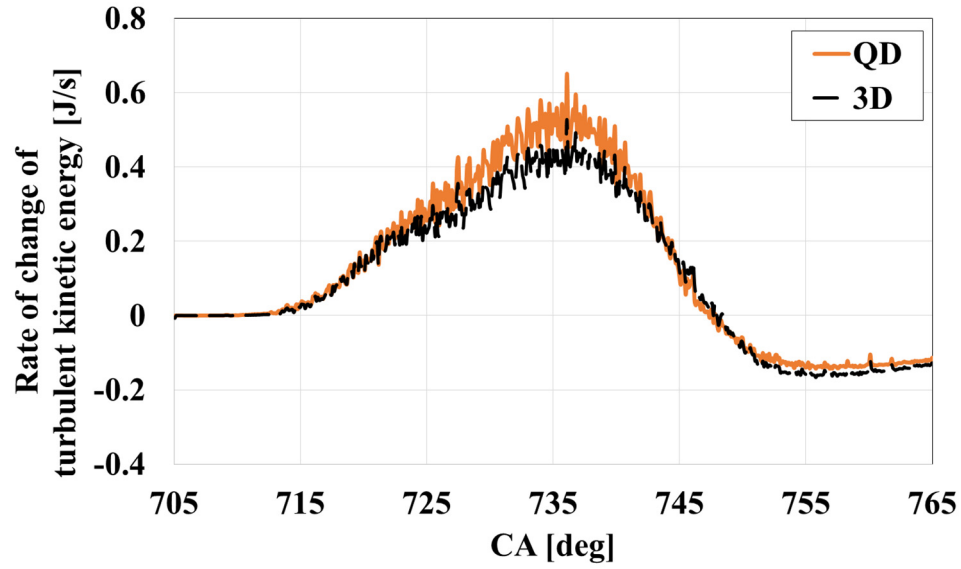

(b)

Figure 3.12 Rate of change of turbulent kinetic energy in (a) unburned, and (b) burned zone with modified governing equations under 1500 rpm, P_i = 0.6 bar, and spark timing of 15º bTDC

3.5 Flame propagation mode during combustion processes

There has been numerous works in attempt to describe the effect of turbulence on the amplification of reactive area of flame front. Damkhöler proposed the correlation between the wrinkled flame area to the projected flame area with the ratio of turbulence intensity and laminar flame speed [98]. Later, Schelkin incorporated a conical geometry formed due to the interaction between turbulence and incoming reactive flow [99]. More correlations have been derived after the preceding studies shortly introduced above. These correlations were derived from the experiment with fully developed turbulent flame. The combustion phenomena in SI engine, however, is interpreted as hybrid of laminar and turbulent flame propagation. This is attributable to the size of the flame kernel produced at the very beginning of the combustion due to plasma formed at the spark plug is relatively small compared to the integral length scale of turbulence. As a result, flame surface cannot be wrinkled by the turbulence effect. As the size of the flame kernel grows, and the size of flame surface relative to the integral length scale becomes comparable, wrinkling of the flame surface would begin to accelerate. This stage is considered to be the transition from laminar to turbulent flame propagation. After transition is over, the flame propagates at the speed of fully-developed turbulent flame speed.

In the subsequent sections, the correlations on flame propagation speed according to flame propagation mode will be explained in more detail

3.5.1 Initial flame kernel development

In QD combustion models, combustion simulation is initiated by imposing a predefined volume or mass converted from reactant to product at the spark timing [72].

In this research, instead of prescribing the identical size for initially combusted volume, the size was varied according to the amount of residual gas content within cylinder as the larger quantity of residual gas increases ignition delay. The correlation of the initially combusted volume was found during the model calibration with experimental results.

After the formation of the flame kernel, the flame surface was assumed to be propagating at the laminar flame speed until the turbulent eddies begin to wrinkle the flame surface. In this study, a model proposed by Kim and Min [100] was used which was developed using Chemkin software, and chemical mechanism for iso-octane, normal heptane, and toluene developed in Lawrence Livermore National Laboratory. This model has been validated over wide range of temperature (600 K ~ 900 K), pressure (5 bar ~ 25 bar), and equivalence ratio (0.5 ~ 2.0).

The laminar flame speed is affected greatly by the presence of residual gas or EGR. Several correlations have been introduced to describe the effect of diluent to the laminar flame speed. The correlations of correction factors developed by Metghalchi and Keck, and Rhodes and Keck are shown below:

$$\text{correction factor} = \begin{cases} 1 - 2.1x_b \\ 1 - 2.06{y_b}^{0.77} \end{cases} \tag{3.15}$$

where x_b is the mass fraction of the diluent, and y_b is the mole fraction of the diluent [101, 102]. The correlation for correction factor will be assessed and selected when model calibration with experimental data is conducted.

The purely laminar flame propagation was assumed to last until the radius of the flame kernel becomes larger than one half of the integral length scale as in the former studies [103, 104].

3.5.2 Transition from laminar to turbulent flame propagation

The transient behavior of the transition from laminar to turbulent flame propagation is explained by the diffusion of the turbulent eddies from the unburned zone to the flame front [86, 105, 106]. There are two models widely utilized in QD combustion models which describe the turbulent eddy diffusion relevant to the turbulent flame propagation [105, 106]. In this study, a correlation derived by Herweg and Maly was selected as this correlation is also used in 3D CFD. The equation for this model is given below:

$$\frac{S_T}{S_L} = 1 + A\left(1 - \exp\left(-\frac{r_f}{L}\right)\right)^{0.5}\left(1 - \exp\left(-\frac{t}{\tau_f}\right)\right)^{0.5}\left(\frac{u'}{u'+S_L}\right)^{0.5}\left[\left(\frac{u'}{S_L}\right)\left(\frac{4.4}{1+3.919(u'/S_L)}\right)^{0.5}\right] \tag{3.16}$$

Where A is the adjustable constant, L is the integral length scale, r_f is the flame radius, t is the time elapsed after spark discharge, and τ_f is the characteristic time constant. The constant A needs to be adjusted according to the engine of interest. The characteristic time constant can be obtained from the following equation:

$$\tau_f = \frac{L}{u'+S_L} \tag{3.17}$$

The correlation derived by Herweg and Maly [105] contains two damping terms, namely time effect and effective length scale effect (size effect), which determine the transient behavior of the transition of flame propagation mode. From the preliminary assessment of this correlation, it was found that the size effect converges to 1 faster than time effect as shown in Fig. 3.13. When compared with the burned mass fraction, it was found that the time effect tends to lag longer than MFB 40 timing. However, the size of the flame radius and its projected surface area at this time is sufficiently

large compared to the integral length scale, and it would be more reasonable to consider that the transition from laminar to turbulent flame propagation is already completed. Thus, in this study, the original correlation is modified so that the time effect would be turned off once the size effect converges to 1.

3.5.3 Fully-developed turbulent flame propagation

Once the transition from the laminar flame propagation mode to turbulent flame propagation mode was complete, the flame propagation speed was calculated using the equation below:

$$\frac{S_T}{S_L} = 1 + A\left(\frac{u'}{u'+S_L}\right)^{0.5}\left[\left(\frac{u'}{S_L}\right)\left(\frac{4.4}{1+3.919(u'/S_L)}\right)^{0.5}\right] \quad (3.18)$$

The Eq. 3.18 is the form which can be obtained from removing the transient terms in the Eq. 3.16.

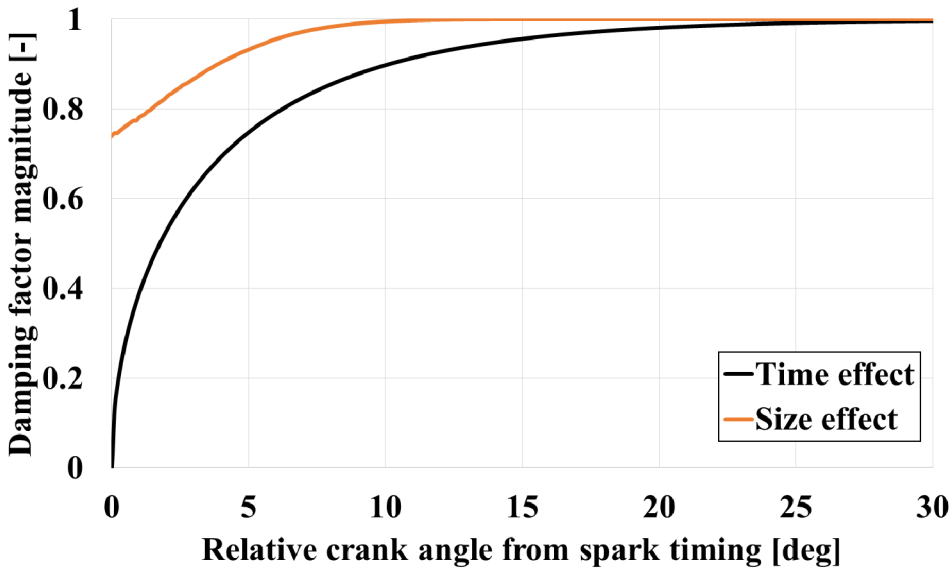

Figure 3.13 Comparison of damping factors in correlation of turbulent flame speed

3.6 Modifications of the heat transfer model

The heat transfer mode in the SI engine is considered to be mainly driven by turbulent convective heat transfer. The basic correlation for turbulent convective heat transfer can be expressed as Eq. 3.19 [107].

$$\mathrm{Nu} = \mathrm{aRe}^{\mathrm{m}}\, Pr^{n} \tag{3.19}$$

where m, and n are model constants with values 0.8, and 0.3, respectively. Numerous models for describing the convective heat transfer coefficient for internal combustion engine have been developed based on this equation. Among the models, the most widely used correlation is the one developed by Woschni [108]. The equation for this correlation is given below:

$$h = 3.26B^{-0.2}\, P^{0.8}\, T^{-0.53} \left(C_1 \overline{S_p} + C_2 \, \frac{V_d T_r}{P_r V_r} (P - P_m) \right)^{0.8} \tag{3.20}$$

where B is the cylinder bore, P is the in-cylinder pressure, P_m is the motored pressure, T is the in-cylinder temperature, V_d is the displaced volume, $\overline{S_p}$ is the mean piston speed, and $\mathrm{P_r}, V_r,$ and T_r are pressure, volume, and temperature at reference state such as IVC timing.

Although not introduced in detail, other models share similar form to that of Woschni's correlation as the correlations are basically derived from the Eq. 3.19. The major differences in the models are the characteristic length scale, characteristic velocity scale, and exponent of the temperature term. Therefore, the three key parameters were reviewed, and modified if necessary.

In this study, $\sqrt[3]{volume}$ of each zone was used for characteristic length scale instead of the cylinder bore of given engine as the volume of each zone during combustion is unlikely to be scaled with the cylinder bore.

For the characteristic velocity scale, the mean piston speed term was replaced by the geometric mean of the mean flow velocity, and the turbulence intensity of each zone. The mean flow velocity of each zone was assumed to be proportional to the mass fraction of each zone, and the mean flow velocity. Here, the mean flow velocity without piston motion effect was utilized. The flow due to piston motion is in normal direction with respect to head, and piston while the tangential velocity is of interest for forced convective heat transfer. The direction of the flow due to piston motion would be tangential with respect to liner. However, if the flow due to piston motion is superimposed with the tumble motion of the mean flow, one side of the liner would be exposed to the mean flow velocity reinforced by the flow due to piston motion while the other side would be exposed to the mean flow velocity counterbalanced by the flow due to piston motion. By averaging the flow velocity over the liner, the effect of the flow due to piston motion would be canceled out. Thus, the flow due to piston motion was neglected.

Lastly, the exponent of the temperature term was investigated. The exponent of the temperature is determined from the correlation of dynamic viscosity, and thermal conductivity. The transport properties of reactant and products were found in various references and fitted to find the correlation in power law [109-111]. The exponent found from fitting are summarized in Table 3.1. The result shows that the exponent of the temperature varies depending on which reference data were used. To observe the impact of the exponent of the temperature, a sample data of burned, and unburned zone temperature were utilized, and the evolution of the temperature effect were plotted in Fig. 3.14. Fig. 3.14 shows that that the impact of the exponent of

temperature is significantly large. However, when the temperature effect is normalized to a reference value and compared, it can be seen that the differences in temperature effect arising from different values of exponent is relatively small as shown in Fig. 3.15. From this result, it is postulated that the influence of the exponent of temperature can be overcome by the adjustable constant multiplied to the convective heat transfer coefficient. Thus, in this study, the same value used in Woschni's correlation is utilized for the exponent of temperature term.

The equations for heat transfer coefficient of burned and unburned zone modified from the original Woschni's correlation in this study can be expressed as the following:

$$\mathrm{h_{c,u}} = \mathrm{C_u}\,\mathrm{V_u}^{-0.066}\,\mathrm{P}^{0.8}\mathrm{T_u}^{-0.53}\left(5.5\sqrt{{u_u}'^2 + \left((1-x_b)\overline{U_{flow}}\right)^2} + C_2\,\frac{V_d T_r}{P_r V_r}(P - P_m)\right)^{0.8} \tag{3.21}$$

$$\mathrm{h_{c,b}} = \mathrm{C}_b\,\mathrm{V}_b^{-0.066}\,\mathrm{P}^{0.8}\mathrm{T}_b^{-0.53}\left(5.5\sqrt{{u_b}'^2 + \left(x_b\overline{U_{flow}}\right)^2} + C_2\,\frac{V_d T_r}{P_r V_r}(P - P_m)\right)^{0.8} \tag{3.22}$$

where x_b is the burned mass fraction.

The constants C_u, and C_b in Eqs. 3.21, and 3.22 are to be determined when the heat transfer rate is compared with the 3D CFD results. Combined with the wetted area of head, piston, and liner in burned and unburned zone, the QD calculation of the heat transfer rate can be realized with the equations below:

$$\dot{Q}_u = h_{c,u}\left[A_{u,head}(T_u - T_{head}) + A_{u,piston}\left(T_u - T_{piston}\right) + A_{u,liner}(T_u - T_{liner})\right] \tag{3.23}$$

$$\dot{Q}_b = h_{c,b}\left[A_{b,head}(T_b - T_{head}) + A_{b,piston}\left(T_b - T_{piston}\right) + A_{b,liner}(T_b - T_{liner})\right] \tag{3.24}$$

where A_u, and A_b are the area wetted by unburned and burned gas, respectively. The subscript head, piston, and liner indicating that the properties belong to head, piston, and liner, respectively. The area of head, liner, and piston wetted by unburned and burned gas were obtained using the method developed by Poulos [78].

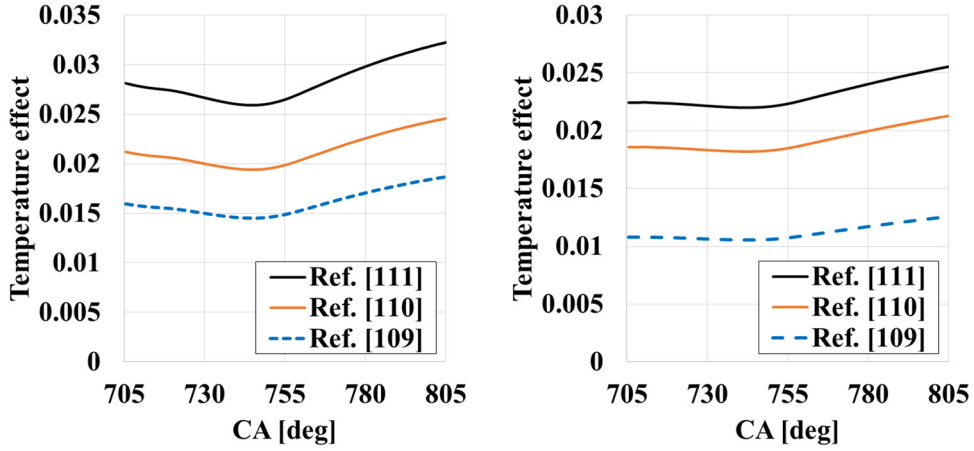

(a) (b)

Figure 3.14 Comparison of the effect of exponent of temperature term in the correlation of heat transfer rate for (a) unburned and (b) burned zones

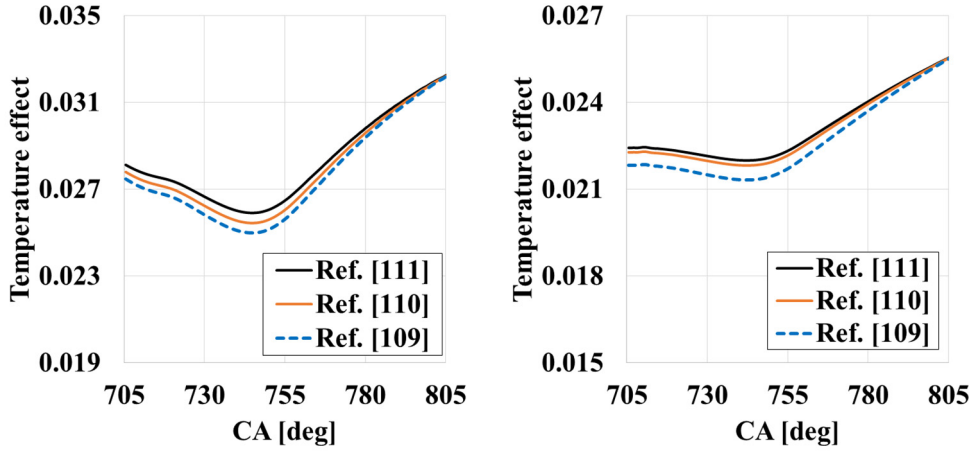

(a) (b)

Figure 3.15 Comparison of the effect of exponent of temperature term in the correlation of heat transfer rate for (a) unburned and (b) burned zones after normalization

Table 3.1 Exponent of the temperature term for convective heat transfer coefficient

Reference	Air	Product
[109]	- 0.6243	- 0.5823
[110]	- 0.5814	- 0.5123
[111]	- 0.5387	- 0.4880

3.7 Verification of the developed model

The verification of the phenomenological QD combustion model was done by comparing the combustion characteristics calculated with 3D CFD. The simulation was conducted using the base engine geometry used in development of the 0D turbulence intensity model in the previous chapter. The simulation conditions for verification of the model are listed in Table 3.2. Such simulation conditions are chosen to cover the wide operating range of the actual engine.

The 3D CFD simulation was carried out using the simple flame kernel development calculation method called numerically imposed ignition model. This ignition model assumes that the unburned mixture confined within a volume of specified flame radius is converted into burned species over a specified time. In this study, it was assumed that the reactant confined in a sphere of 2 mm radius is converted into product over 4 CA. To reproduce the burn rate of 3D CFD results, a similar method was used for flame kernel development.

The reference case for model calibration was selected to be the simulation condition with the engine speed of 3000 rpm under the intake pressure of 0.6 bar. The reason for this choice is because 3000 rpm is the intermediate engine speed among the simulation conditions. The main task of the calibration procedure is to find the values for the constants for turbulent flame speed correlation, and heat transfer coefficients shown in Eqs. 3.16, 3.23, and 3.24. Once the calibration at this condition was done, the value of this constant was kept as invariant.

Fig. 3.16 shows the burned mass fraction, in-cylinder pressure, and turbulence intensity of unburned and burned zone predicted by the developed model under the spark timing of 35 º bTDC. The constant for turbulent flame speed correlation was set

as 2.7. The burned mass fraction is overestimated compared with the 3D CFD result when its value becomes greater than 0.85. This can be attributed to the overestimation of the turbulence intensity of unburned zone as shown in Fig. 3.16 (c). Yet, it had minor impact on the predicted in-cylinder pressure as the degree of overestimation was relatively small.

The evolution of total heat transfer rate predicted using QD heat transfer model modified from the original Woschni's correlation is compared with that of the original Woschni's correlation, and 3D CFD result as shown in Fig. 3.17. The constants for unburned and burned zone heat transfer coefficients were chosen as 3.68, and 5.34, respectively. The difference in the total heat transfer rate can be attributed to the difference in evolution of wetted area computed with the QD model when compared with 3D CFD results as the shape of the flame is assumed to be spherical even though it is not truly spherical when observing one example of flame shape obtained from 3D CFD simulation. The QD heat transfer model, however, was successful in improving predictability of the heat transfer rate when compared with that of the original Woschni's correlation.

Keeping the values of the adjustable constants unchanged, the burn rate of various spark timing were calculated, and the evolution of burned mass fractions were compared with those of 3D CFD in Fig. 3.18. The qualitative comparison shows that the QD model is capable of estimating the evolution of burned mass fractions very close to the 3D CFD results. To quantify the simulation results, combustion phase, and combustion duration of each cases were compared in addition. Here, the definition for the combustion phase and combustion duration were referred to the literature [2] which defines that the combustion phase is the point at which the 50% of the air-fuel mixture is combusted, and the combustion duration is the time between 10% and 90% of the air-fuel mixture is combusted. From Fig. 3.19, it can be seen that the combustion

phase predicted by QD model agrees well with the 3D CFD results. However, slight differences in combustion duration were observed, and the difference in predicted combustion duration tended to increase as the spark timing is retarded. Referring to the evolution of burned mass fraction in Fig 3.18, the increase in the difference in burned mass fraction is observed after MFB 50 point. Such phenomenon is attributable to slower turbulent flame propagation at the latter part of combustion. To understand the cause of such phenomenon, the turbulent flame speed correlation was reviewed.

The correlation used in this study contains three auxiliary terms to describe the transient characteristics of flame propagation speed transition from laminar to fully turbulent flame speed. Among the three auxiliary terms, size and time effect terms do not have any influence in the latter part of the combustion. Thus, characteristics of the third term which is denoted as the turbulence effect term was investigated. The turbulence effect term in Eq. 3.16 becomes smaller with smaller turbulence intensity. As the turbulence intensity becomes smaller drastically after MBF 50 point, the turbulence effect term is thought to be responsible for slower combustion rate for latter part of combustion. Since the Eq. 3.16 was derived for the initial turbulent flame development period, it is reasonable to neglect the turbulence effect term in the turbulent flame speed correlation at the latter part of combustion. Unlike the other transient terms, the magnitude of the turbulence effect term is close to 1 at the beginning of combustion, and have little importance. Thus, the turbulent flame speed correlation was modified by removing the turbulence effect term in Eq. 3.16. The calibration of the turbulent flame speed correlation was conducted again after the modification of the correlation, and the recalculated combustion phase and combustion duration are shown in Fig. 3.20. The new value for the constant in

turbulent flame speed correlation was changed to 2.5. It can be confirmed that the accuracy of combustion duration prediction has been improved.

The total heat transfer rate predicted by modified heat transfer model was compared after revision of the turbulent flame speed correlation. Fig. 3.21 shows that the predicted heat transfer rate closely resembles those of 3D CFD except for the case with the spark timing of 15º bTDC. The main source of the error in the heat transfer rate prediction is thought to be the difference in the wetted area as the QD combustion model assumes that the burned zone has spherical shape while the shape of the burned zone is not truly spherical in 3D CFD. Another reason for the error can be attributed to the assumption on the characteristic velocity scale. In this study, the effect of flow due to piston movement was disregarded. However, in the actual engine, the flow in the vicinity of the surface of cylinder liner may be affected by the flow due to piston movement.

After the final calibration, the combustion phase, and duration under various conditions were simulated and compared with the 3D CFD results. Figs. 3.22 to 3. 25 show the combustion phase, and duration over various engine speed, engine load, and spark timing. The combustion phase predicted by the QD model agreed well with those of 3D CFD under various conditions. However, some discrepancies in combustion duration were found. Referring to the evolution of burned mass fraction shown in Fig. 3.18, the main source of the difference can be attributed to the latter part of the combustion. Figs. 3.26 and 3.27 indicate that if the latter part of the combustion is excluded by observing the combustion duration between MFB 10 to 80, the predictability of the QD model is enhanced. Although two cases under 6000 rpm with late spark timing still show relatively large differences, other cases differed by less than 2 degrees. Thus, it can be concluded that the phenomenological QD combustion model developed in this study can successfully reproduce the combustion

characteristics close to 3D CFD over wide range of operating conditions without case-dependent adjustment of tunable constants.

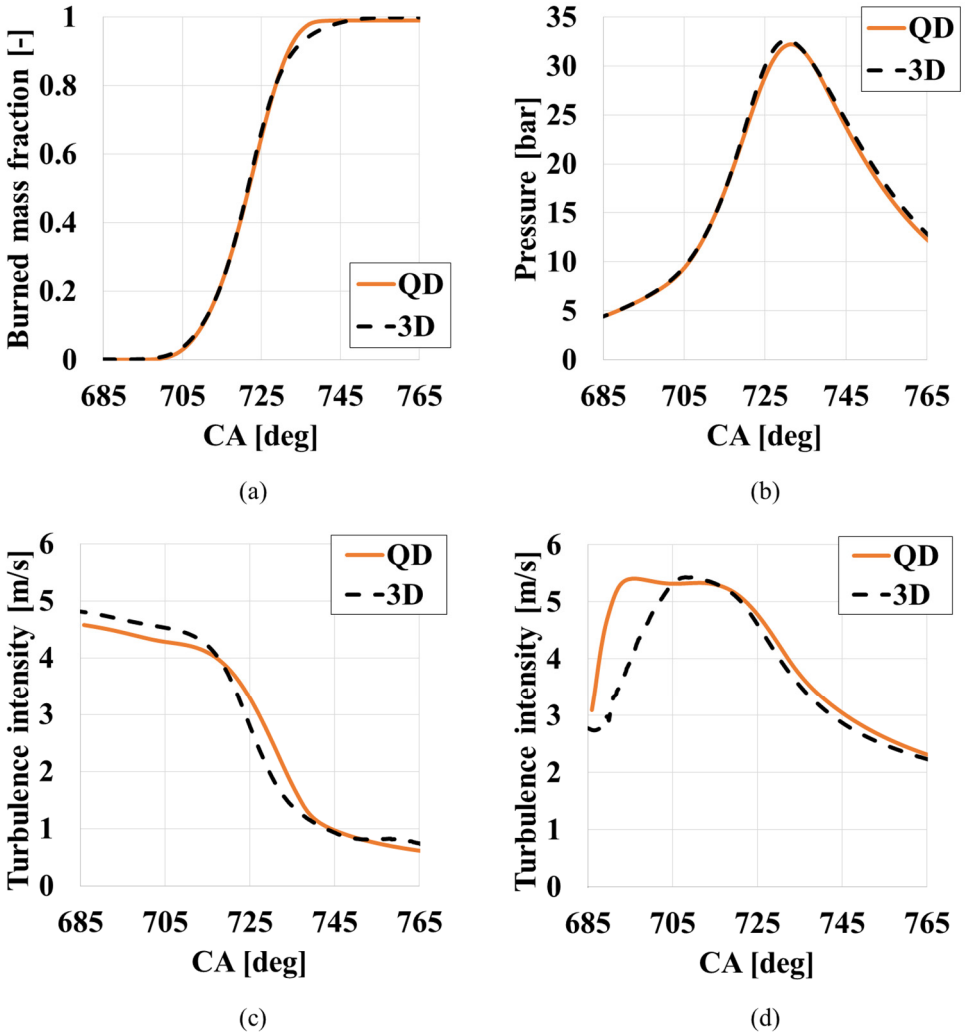

Figure 3.16 Comparison of (a) burned mass fraction profile, (b) in-cylinder pressure, (c) unburned zone turbulence intensity, and (d) burned zone turbulence intensity of QD model and 3D CFD results under 3000 rpm, P_i = 0.6 bar condition at spark timing of 35° bTDC

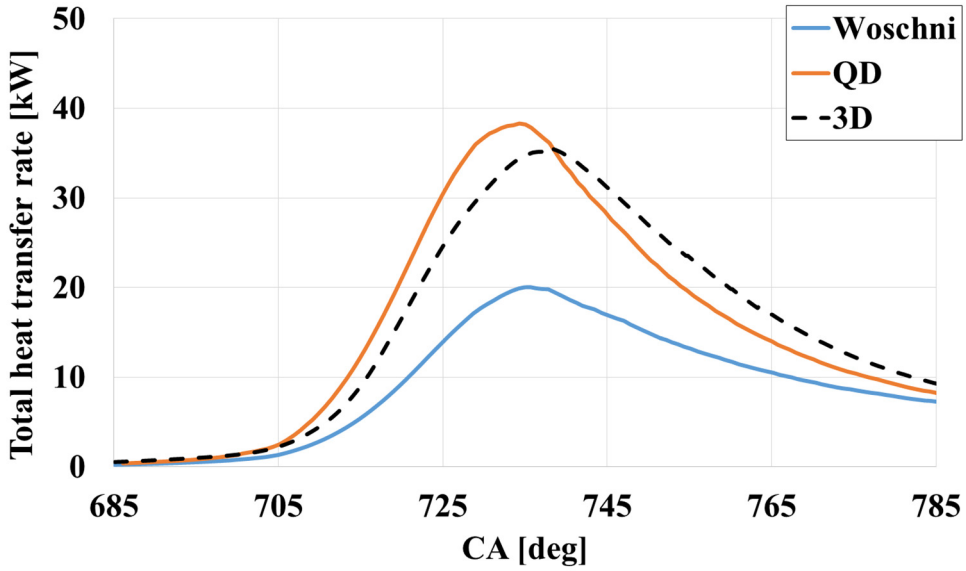

Figure 3.17 Comparison of total heat transfer rate under 3000 rpm, P_i = 0.6 bar condition at spark timing of 35º bTDC

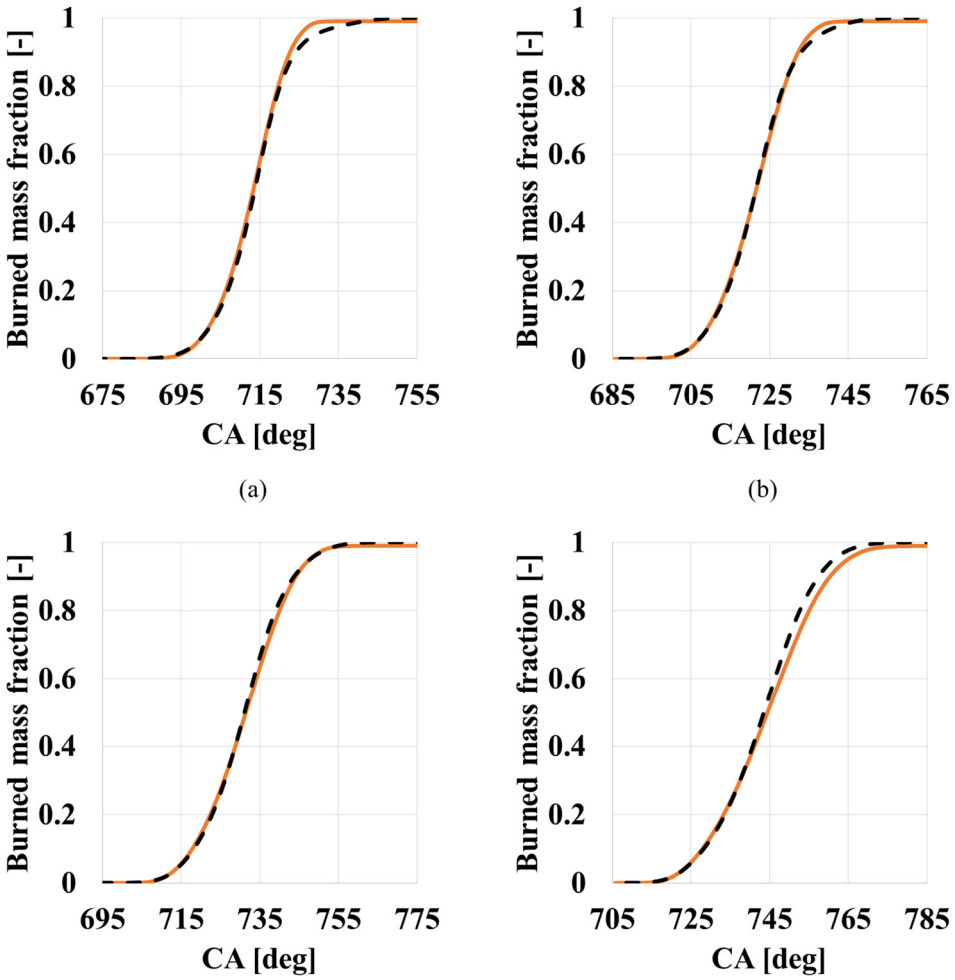

Figure 3.18 Comparison of burned mass fraction profile with spark timing of (a) 45º bTDC, (b) 35º bTDC, (c) 25º bTDC, and (d) 15º bTDC under 3000 rpm, P_i = 0.6 bar

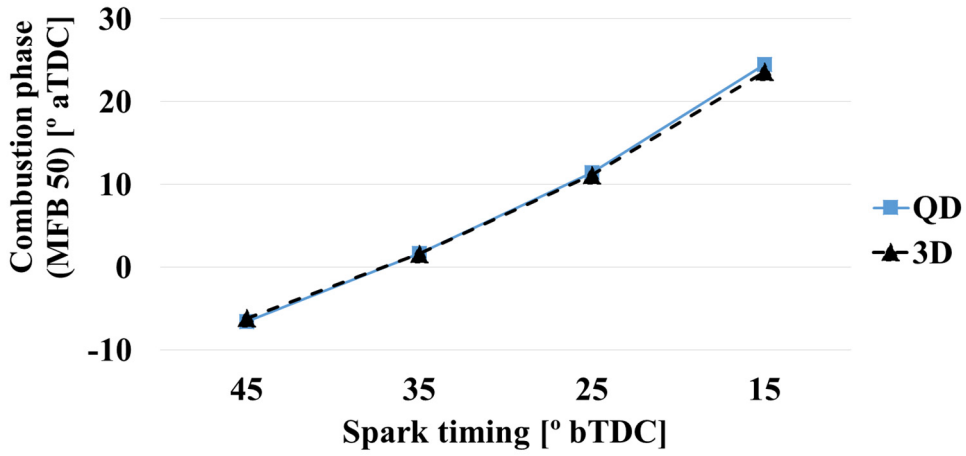

(a)

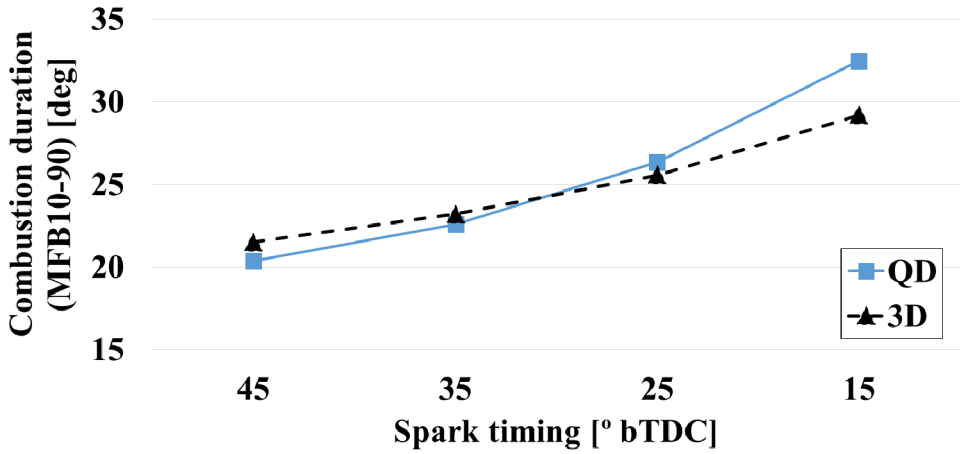

(b)

Figure 3.19 Comparison of (a) combustion phase (MFB 50), and (b) combustion duration (MFB 10-90) for various spark timing under 3000 rpm, P_i = 0.6 bar condition

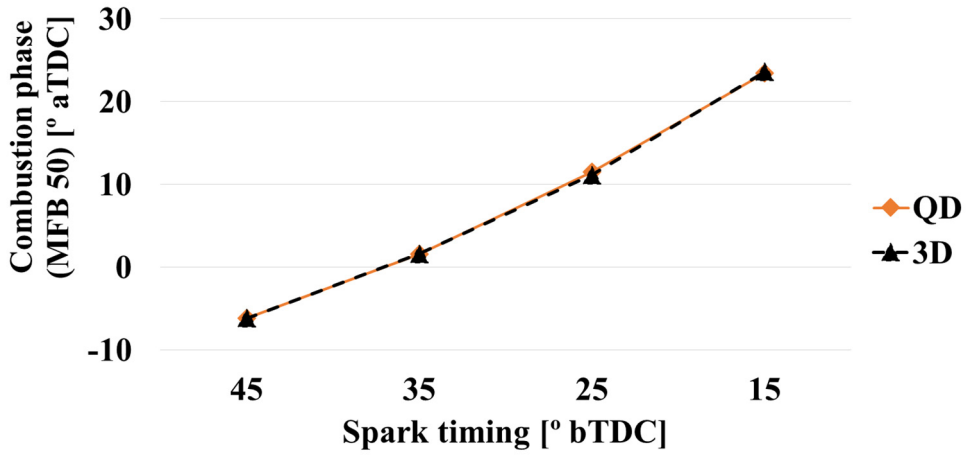

(a)

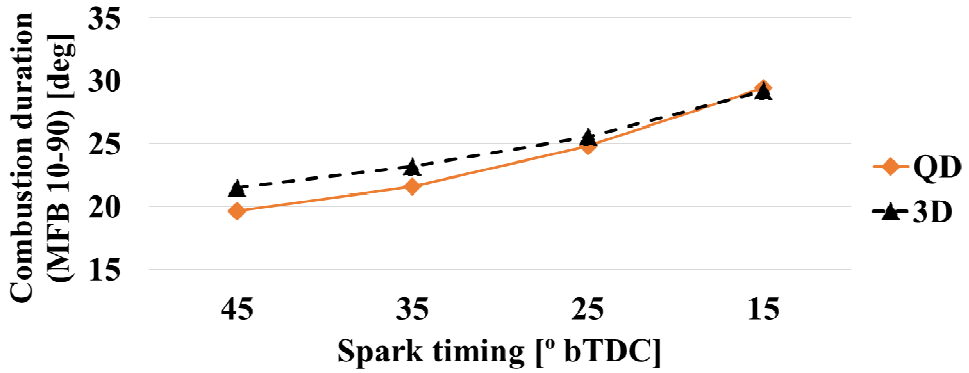

(b)

Figure 3.20 Comparison of (a) combustion phase (MFB 50) , and (b) combustion duration (MFB 10-90) for various spark timing under 3000 rpm, P_i = 0.6 bar after modification of turbulent flame speed correlation

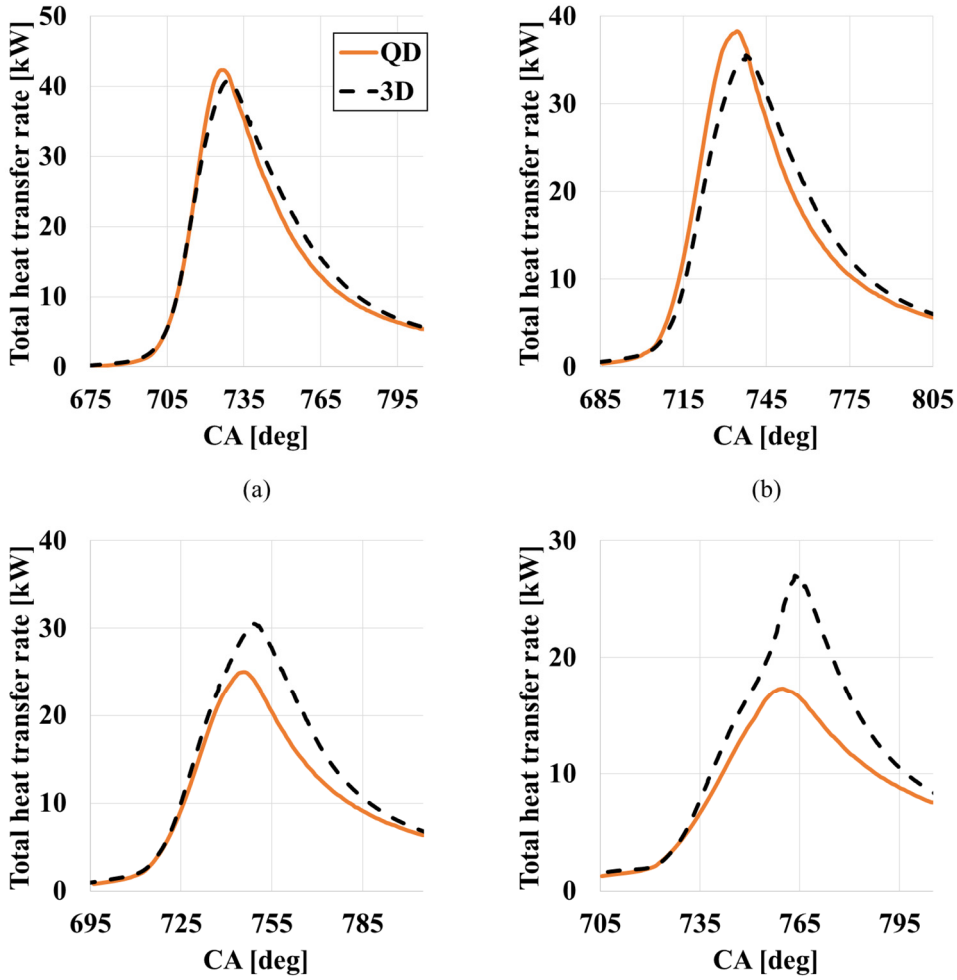

Figure 3.21 Comparison of total heat transfer rate with spark timing of (a) 45º bTDC, (b) 35º bTDC, (c) 25º bTDC, and (d) 15º bTDC under 3000 rpm, P_i = 0.6 bar after modification of turbulent flame speed correlation

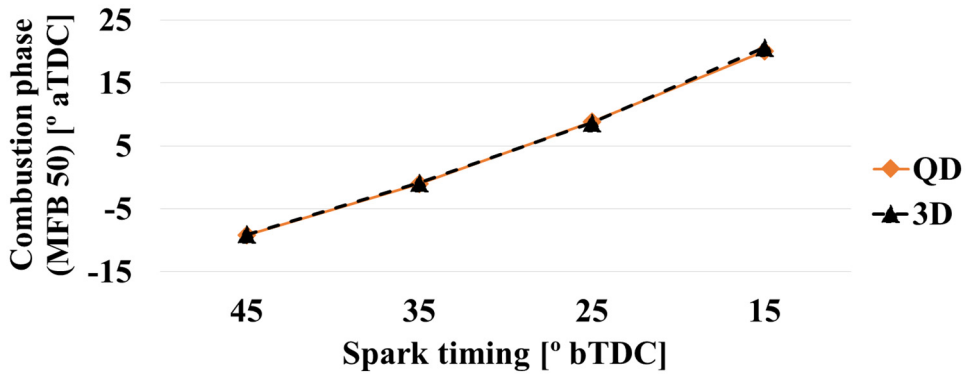

(a)

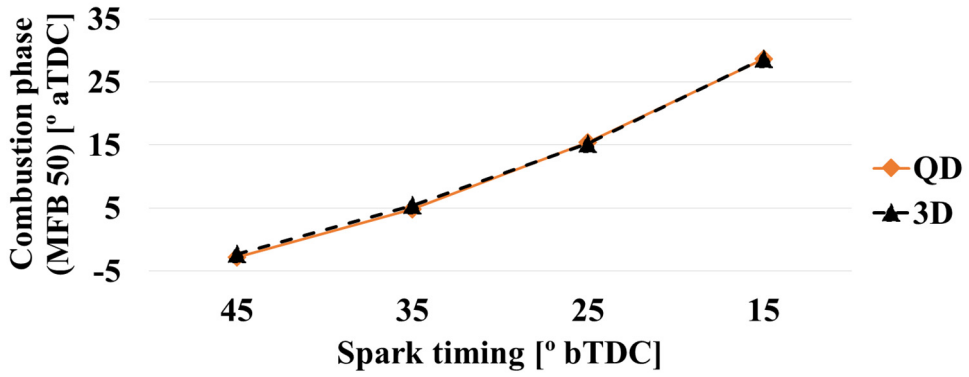

(b)

Figure 3.22 Comparison of combustion phase (MFB 50) for various spark timing under P_i = 0.6 bar, (a) 1500 rpm, and (b) 6000 rpm

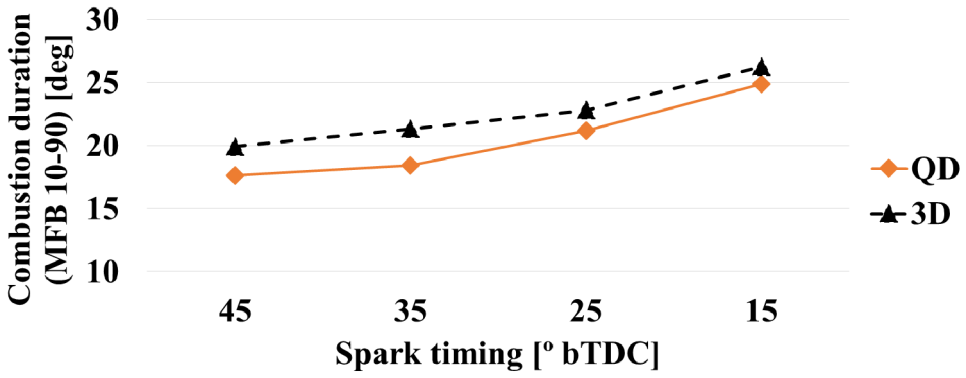

(a)

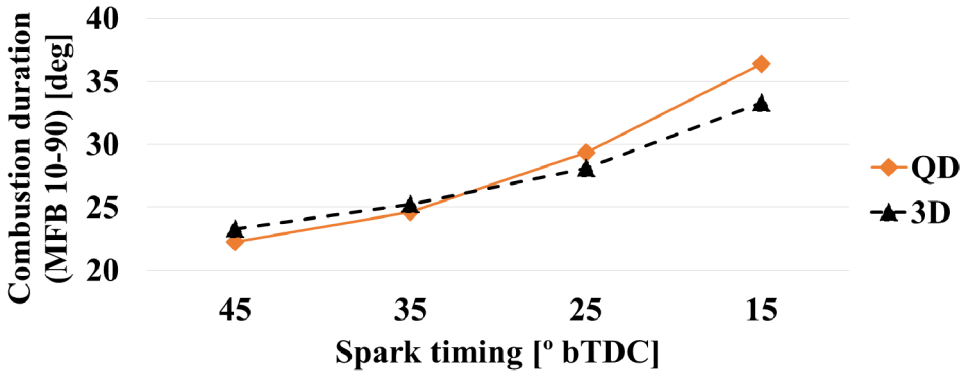

(b)

Figure 3.23 Comparison of combustion duration (MFB 10-90) for various spark timing under P_i = 0.6 bar, (a) 1500 rpm, and (b) 6000 rpm

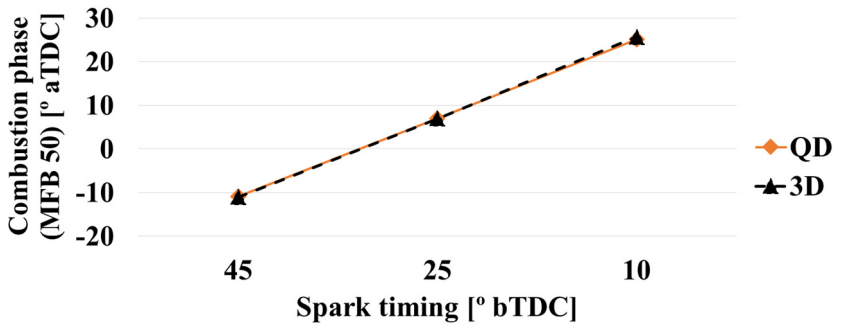

(a)

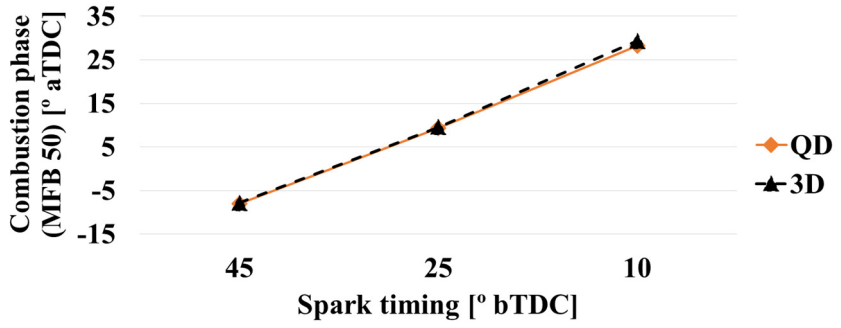

(b)

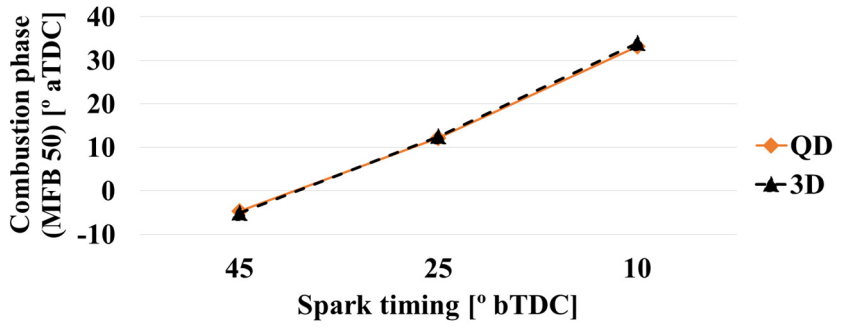

(c)

Figure 3.24 Comparison of combustion phase (MFB 50) for various spark timing under P_i = 1.0 bar, (a) 1500 rpm, (b) 3000 rpm and (c) 6000 rpm

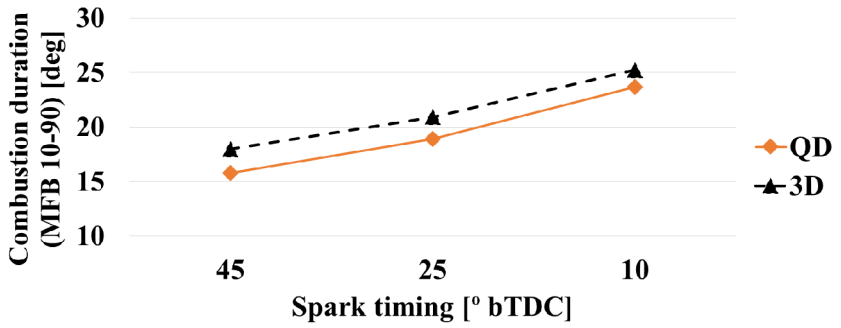

(a)

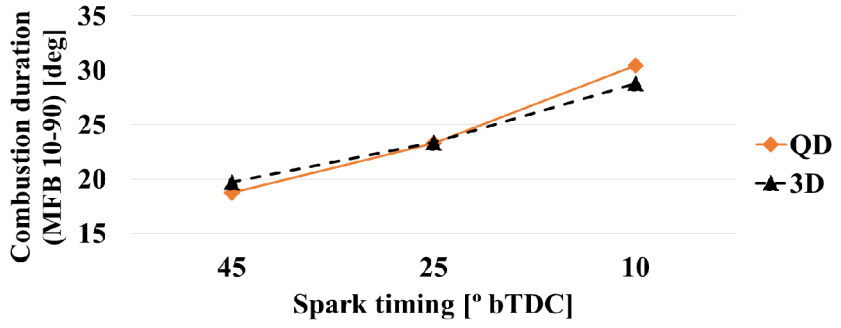

(b)

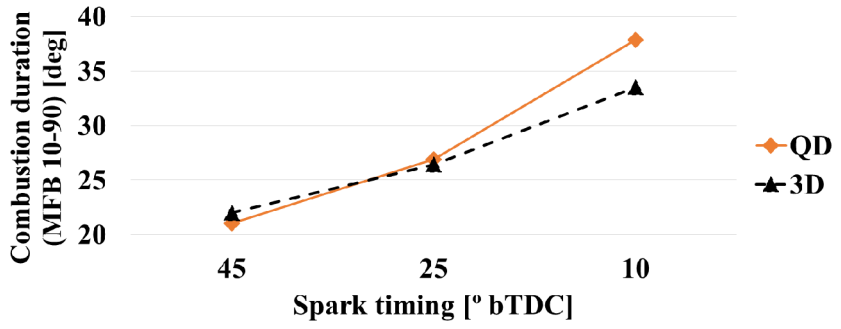

(c)

Figure 3.25 Comparison of combustion duration (MFB 10-90) for various spark timing under P_i = 1.0 bar, (a) 1500 rpm, (b) 3000 rpm and (c) 6000 rpm

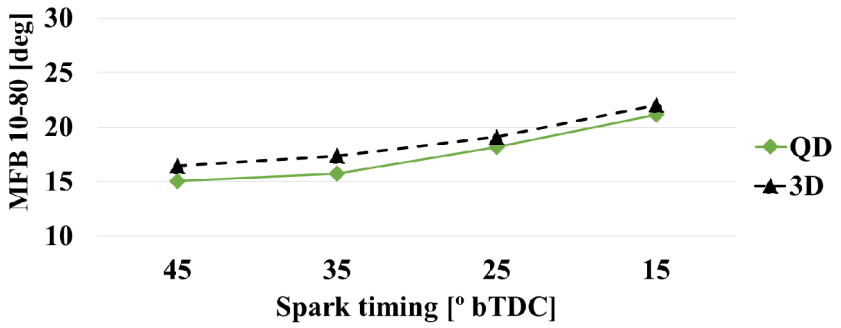

(a)

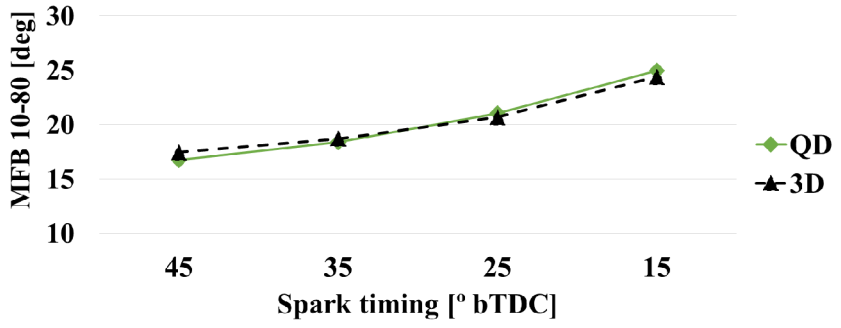

(b)

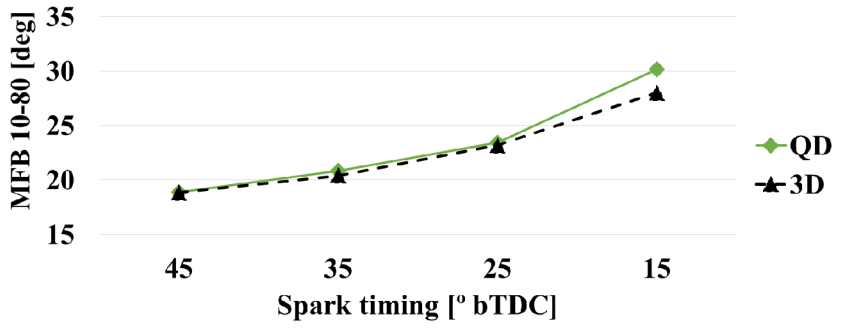

(c)

Figure 3.26 Comparison of burn duration (MFB 10-80) for various spark timing under P_i = 0.6 bar, (a) 1500 rpm, (b) 3000 rpm and (c) 6000 rpm

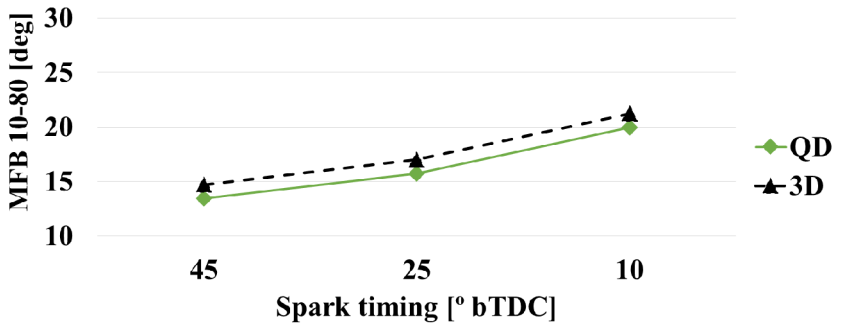

(a)

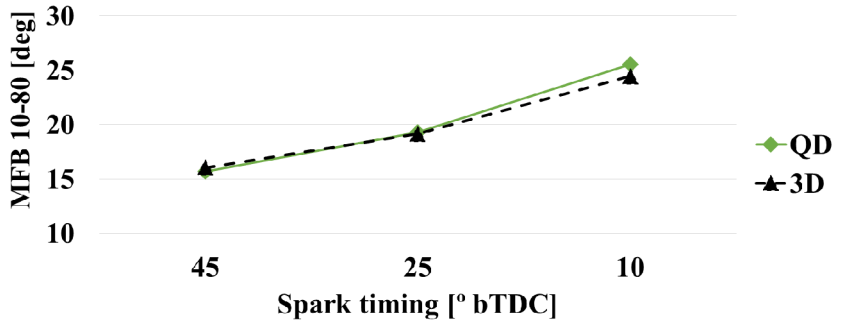

(b)

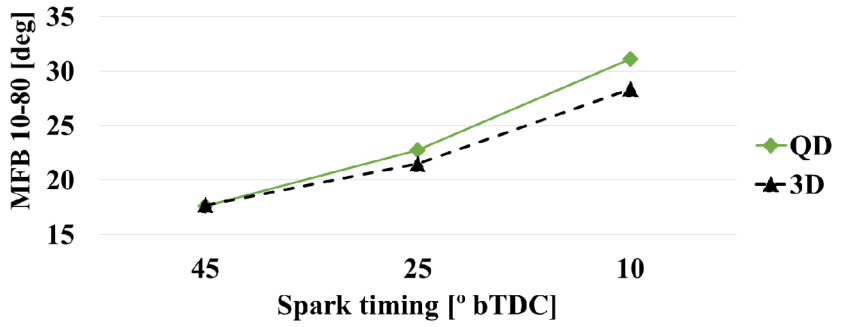

(c)

Figure 3.27 Comparison of burn duration (MFB 10-80) for various spark timing under P_i = 1.0 bar, (a) 1500 rpm, (b) 3000 rpm and (c) 6000 rpm conditions

Table 3.2 Simulation conditions

Parameter	Specification
Engine speed	1500, 3000, 6000 rpm
Intake pressure	0.6 bar (part load) 1.0 bar (full load)
Spark timing	45, 35, 25, 15º bTDC (part load) 45, 25, 10º bTDC (full load)
Lambda	1.00
Intake valve timing	IVO = 358 CA IVC = 598 CA
Exhaust valve timing	EVO = 166 CA EVC = 390 CA

3.8 Sensitivity analysis of the developed model

Sensitivity analysis of the developed model was carried out after the model verification. The model contains three adjustable constants: C_{engine}, and C_{Ψ} from QD turbulence intensity prediction model, and A from turbulent flame speed correlation. The range of the values varied for each adjustable constants are summarized in the Table 3.3.

C_{engine} was varied up to 9 times the original value as it was found that the value of C_{engine} for matching the turbulence intensity of the engine with intensified tumble design was almost 9 times the original value. The change in C_{engine} would show the influence of tumble strength on the combustion characteristics. C_{Ψ} in the QD turbulence intensity prediction model was utilized for modeling turbulent kinetic energy production rate during combustion. The introduction of C_{Ψ} in the QD turbulence intensity prediction model is, however, simply an approximation of the complex phenomenon, and hence C_{Ψ} contains the uncertainty in the estimation of production rate during combustion. Thus, C_{Ψ} was varied up to 4 times the original value to investigate the effect of uncertainty in the simplified modeling of the turbulent kinetic energy production rate during combustion. Although an appropriate value for A was found in the course of model verification, it is not a universal constant. Thus, the value of A was varied up to 10% of the original value to investigate the effect of variance in A.

The simulation was conducted under 3000 rpm, part load condition with various spark timings. This is the same simulation condition selected for the preliminary calibration of the developed model. The simulation results are summarized into combustion phase, and duration, and shown in Figs. 3.28, 3.29, and 3.30. From the results, it can be seen that the increase in C_{engine} advances the combustion phase,

and shortens combustion duration as larger value of C_{engine} increases the turbulence intensity during combustion. The effect of change in C_{engine} on combustion duration was more pronounced compared to that on combustion phase. Change in C_{Ψ} had relatively small effect on combustion phase compared to that on combustion duration. It can be deduced that the increase in turbulent kinetic energy production rate during combustion speeds up the latter part of the combustion. When constant A was varied, the combustion phase, and duration changed linearly with the values of A. Similar to the other adjustable constants, the effect of A on combustion duration was greater.

The result of sensitivity analysis can be utilized when the calibration of the developed model is needed. Since the value of C_{engine} is determined from the 0D turbulence intensity prediction model, the adjustable constants which can be tuned are C_{Ψ} and A. If both the combustion phase, and duration needs to be shifted, adjustment of A is required. If the combustion duration needs to be adjusted, value of C_{Ψ} should be tuned.

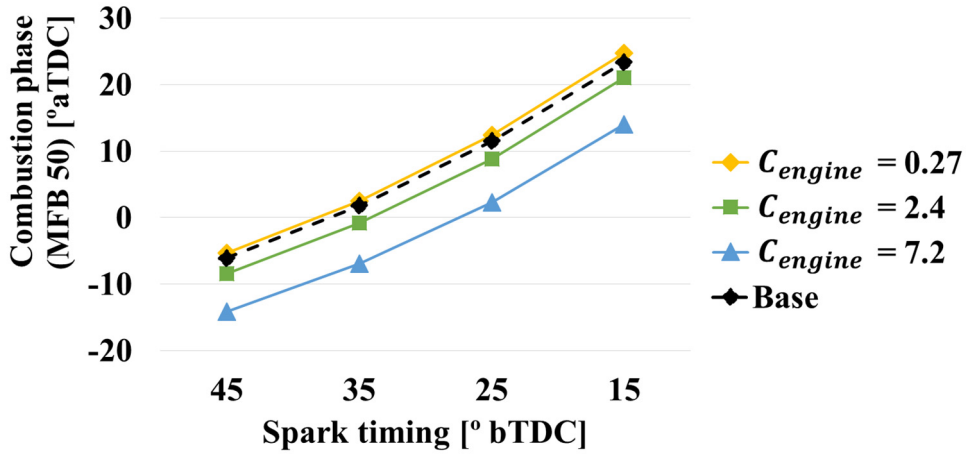

(a)

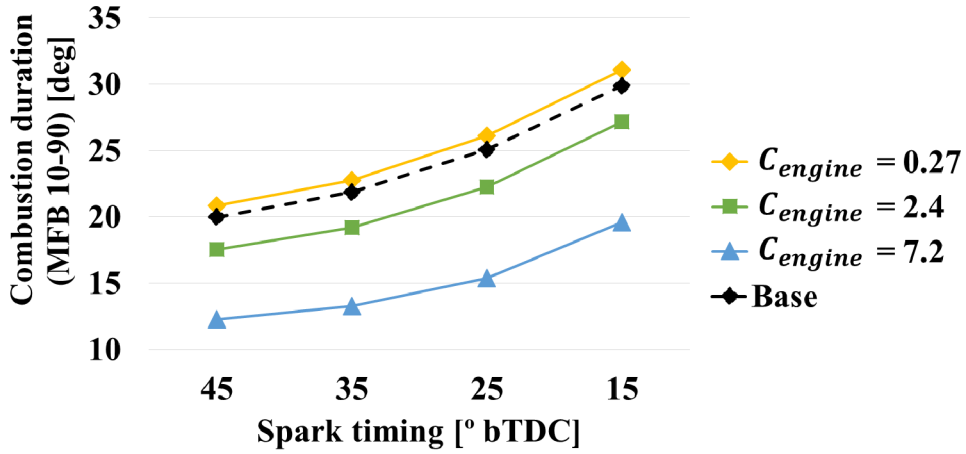

(b)

Figure 3.28 Comparison of (a) combustion phase (MFB 50) , and (b) combustion duration (MFB 10-90) for various spark timing under 3000 rpm, P_i = 0.6 bar according to the variation in constant C_{engine}

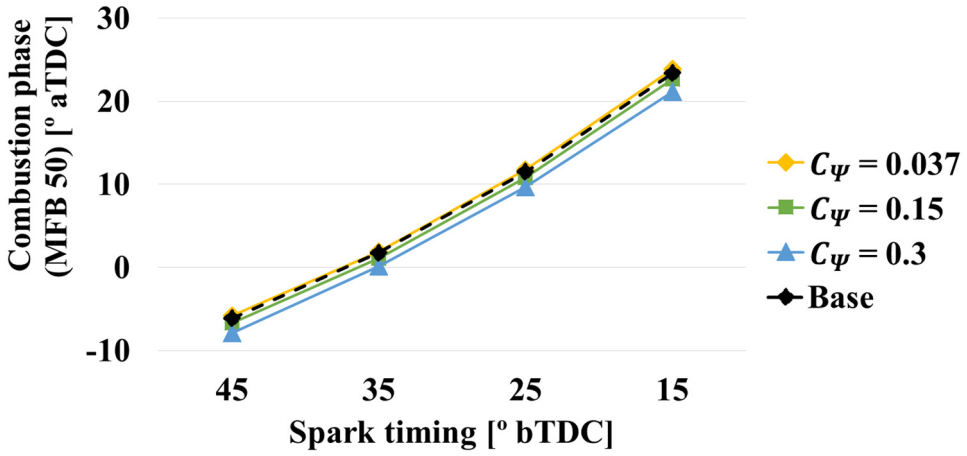

(a)

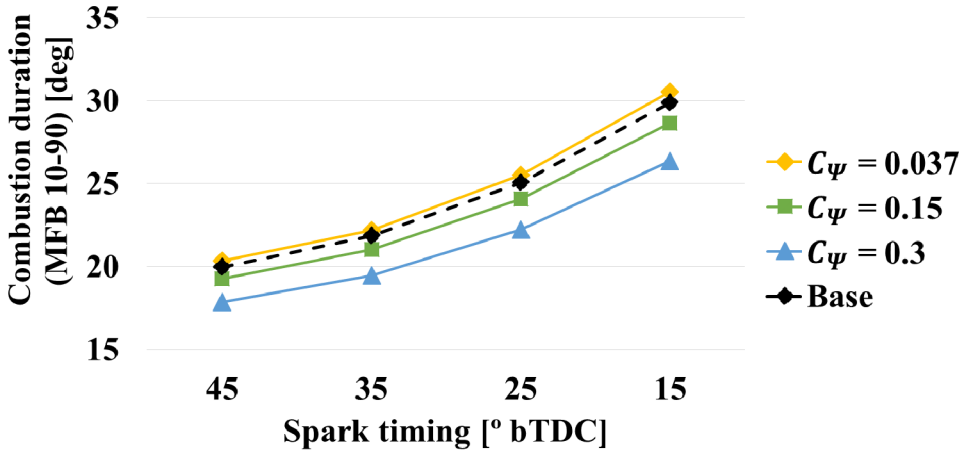

(b)

Figure 3.29 Comparison of (a) combustion phase (MFB 50) , and (b) combustion duration (MFB 10-90) for various spark timing under 3000 rpm, P_i = 0.6 bar according to the variation in constant C_ψ

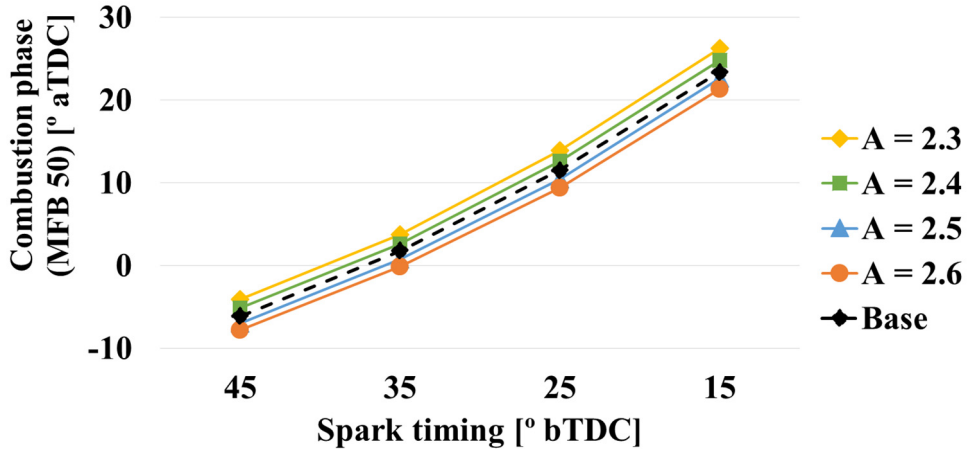

(a)

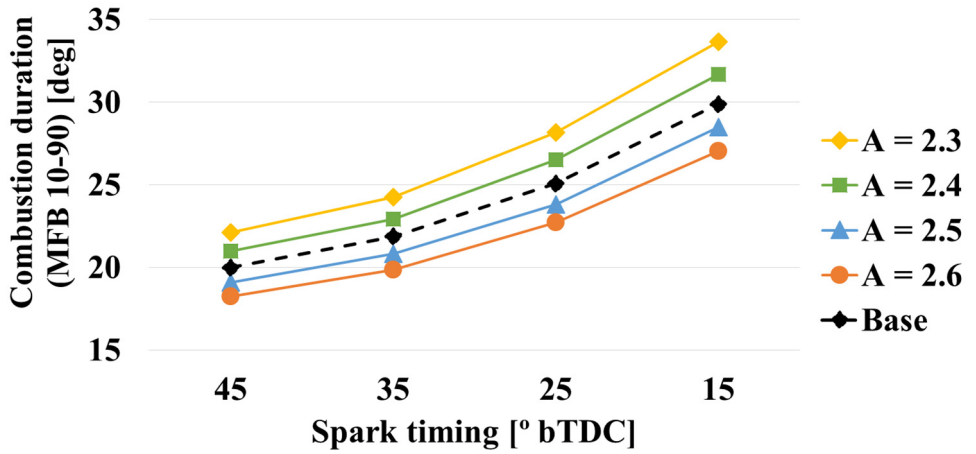

(b)

Figure 3.30 Comparison of (a) combustion phase (MFB 50) , and (b) combustion duration (MFB 10-90) for various spark timing under 3000 rpm, P_i = 0.6 bar according to the variation in constant *A*

Table 3.3 Values of adjustable constants used in sensitivity analysis

Adjustable constant	Values
C_{engine}	0.27, 0.8 (base), 2.4, 7.2
C_{ψ}	0.037, 0.073 (base), 0.15, 0.3
A	2.3, 2.4, 2.5 (base), 2.6, 2.7

Chapter 4. Verification of the developed model with experimental results

The verification of the developed model was conducted by comparing the combustion characteristics predicted by QD combustion model and 3D CFD in the previous chapter. However, the burn rate prediction was done using a simplified method for initial flame kernel development after spark discharge. For the QD combustion model to be able to predict the actual combustion characteristics of the engine, the characteristics of the initial flame kernel development needs to be described, and verified with the experimental results. Therefore, the correlation to predict the size of the initial flame kernel was derived based on the experimental results, and the predictability of the QD combustion model was observed.

4.1 Experimental setup

The schematic diagram of the experimental apparatus is shown in Fig. 4.1. The experiment was conducted using single cylinder test engine. The specification of the test engine is shown in Table 4.1. The test engine was connected to the 37kW DC dynamometer. Basic control of the test engine such as fuel injection timing, spark timing, and fuel injection duration was done by using MOTEC M800 ECU. The intake pressure was controlled using throttle connected to the linear motor with wire. The test fuel used in the experiment is the domestic gasoline sold in Korea with RON 91. The fuel was injected using multi-hole GDI injector. The injection pressure was achieved using the high pressure nitrogen gas to maintain stable pressure. The AF ratio of the air-fuel mixture was measured using Horiba MEXA 110-λ. HC ratio, and OC ratio was set to the values obtained from test fuel assessment according to KS M 2963:2008 method. The intake manifold pressure was measured using piezoresistive

sensor, Kistler 4043A2, and amplifier, Kistler 5019A. The in-cylinder pressure was measured using piezoelectric sensor, Kistler 6052A, and charge amplifier, AVL micro IFEM. For the pressure data acquisition, AVL Indi-module combustion analyzer was utilized. The acquisition was done over 100 consecutive cycles with 0.1 CA resolution.

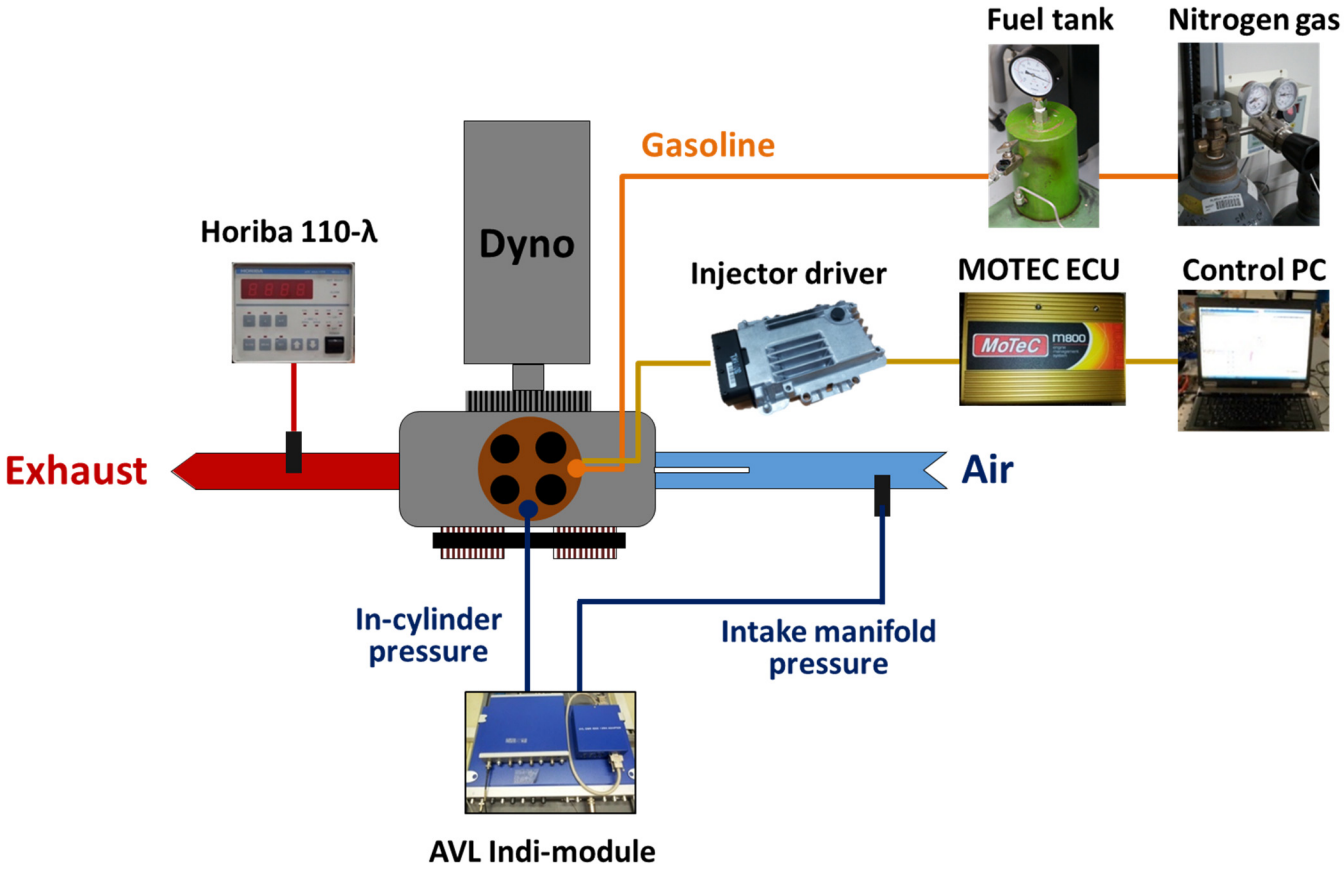

Figure 4.1 Schematic diagram of experimental apparatus

Table 4.1 Specifications of the test engine

Parameter	Specification
Type	4 valve DOCH, GDI
Displacement	500 cc
Bore	86 mm
Stroke	86 mm
Connecting rod	146.25 mm
Compression ratio	9.5
Intake valve open	3.8º bTDC
Intake valve close	56.2º aBDC
Exhaust valve open	14.4º bBDC
Exhaust valve close	29.6º aTDC

Table 4.2 Specifications of the piezoresistive sensor

Parameter	Specification
Measuring range	0 ~ 2 bar
Sensitivity	250 mV/bar
Operating temperature range	20 ~ 120 ºC
Calibration current	3.390 mA
Signal output at 0 bar	-1.7 mV

Table 4.3 Specifications of the piezoelectric sensor

Parameter	Specification
Measuring range	0 ~ 250 bar
Sensitivity	-20 pC/bar
Natural frequency	~ 70 kHz
Non-linearity	< ± 0.5 % (FSO)
Operating temperature range	-50 ~ 350 ºC
Cooling	Water cooled

4.2 Experimental conditions

The experimental conditions are shown in Table 4.4. The temperature of the coolant and oil was maintained at 90 ºC, and 85 ºC, respectively to conduct experiment at fully warmed-up conditions. The engine speed was varied from 1500 rpm to 2500 rpm. The excess air ratio, lambda, was maintained at 1.00. The injection pressure was set to 100 bar, and maintained over the experiment. The intake manifold pressure was varied from 0.6 bar to 1.0 bar to alter engine load. For the part load condition, the spark timing was varied from 45º bTDC to 25º bTDC with 5 CA interval. For the full load condition, however, spark timing advancement was limited due to abnormal combustion. Thus, spark timing was advanced only up to knock-free conditions.

Table 4.4 Experimental conditions

Parameter	Specification	
Engine oil temperature	85 ºC	
Coolant temperature	90 ºC	
Intake air temperature	30 ± 1 ºC	
Engine speed	1500, 2000, 2500 rpm	
Intake manifold pressure	0.6 bar (part load), 1.0 bar (full load)	
Lambda	1.00	
Injection timing	305º bTDC	
Injection pressure	100 bar	
Spark timing	Part load	45, 40, 35, 30, 25º bTDC
	Full load	10, 5, 0º bTDC (1500 rpm) 15, 10, 5º bTDC (2000 rpm) 25, 20, 15º bTDC (2500 rpm)

4.3 Verification of the developed model

4.3.1 GT-Power model verification

Before proceeding with the verification of the developed model, it is important to check whether the GT-Power model is properly constructed as the volumetric efficiency at the WOT condition must agree well with the experimental data. The assessment of the GT-Power model can be done by comparing the intake manifold pressure trace with that of the experimental results under WOT at motored conditions. Fig. 4.2 shows the comparison of the intake manifold pressure of GT-Power model and the experimental results. The results confirm that the GT-Power model is properly constructed to simulate the test engine.

4.3.2 Calibration of the developed model at reference conditions

The developed model needs to be calibrated under reference conditions before comparing the in-cylinder pressure under various operating conditions. The reference cases for model calibration were selected as the 1500 rpm, part load with MBT spark timing which is 35º bTDC, and full load with spark timing of 5º bTDC.

The traces in-cylinder pressure estimated after the calibration are shown in Figs. 4.3 and 4.4. With the proper adjustment of the initial flame kernel size, it was possible to closely reproduce in-cylinder pressure obtained from experiment. The radius of the initial flame kernel under part load and full load conditions were adjusted to 0.01 mm, and 0.5 mm, respectively when the correlation $1 - 2.1x_b$ was used. On the other hand, the radius of the initial flame kernel under part load and full load conditions were adjusted to 0.13 mm, and 0.5 mm, respectively when the correlation

$1 - 2.06\ {y_b}^{0.77}$ was used. Comparing the size of the initial flame kernel for part load condition, radius of 0.01 mm seems to be extremely small, and less likely to be physically feasible. Therefore, the correlation $1 - 2.06\ {y_b}^{0.77}$ was chosen for the correction factor for rest of the simulation.

Based upon the results above, the correlation between the RGF and initial flame kernel size was derived. It was assumed that the initial flame kernel size and RGF has linear relationship as shown below:

$$\mathrm{r_{f,init}} = (0.5\ \times spark\ plug\ gap) \times (e \times\ RGF + f) \qquad (4.1)$$

where *e* and *f* are model constants.

4.3.3 Comparison of the in-cylinder pressure at various test conditions

The cycle simulation under the various experimental conditions were conducted and the predicted in-cylinder pressure were compared with the experimental data. The value of the constant *A* in correlation of turbulent flame speed was kept unchanged from 2.5.

From the comparison of in-cylinder pressure from simulation and experimental data, it can be confirmed that the developed model can reproduce the experimental data accurately for most of the cases. To compare the simulation results with experimental data quantitatively, combustion phases were compared in addition. Except for 4 cases out of 24 cases, predicted values of the combustion phase differed less than 1 CA when compared with the experimental data. The discrepancy can be attributed to the error in the estimation of the initial flame kernel size as the sensitivity in-cylinder pressure to the initial flame kernel size was significantly high, and the simple ignition model was not able to capture the actual flame development

phenomena perfectly. Another possibility is that the flow characteristics near the spark plug in the actual engine may differ for various spark timing, which would result in different evolution of the initial flame development. Such phenomenon would not be possible to be captured by the QD model. Nevertheless, the developed model was capable of predicting the in-cylinder pressure and combustion phase from 1500 rpm to 2500 rpm, part and full load conditions with various spark timing without changing the tunable constants.

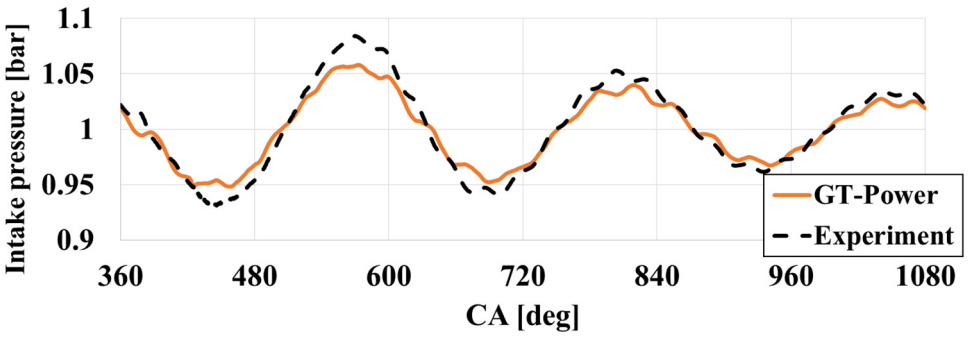

(a)

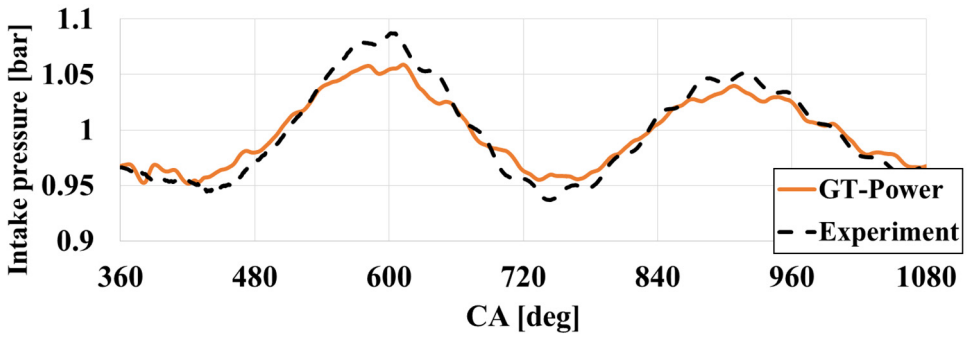

(b)

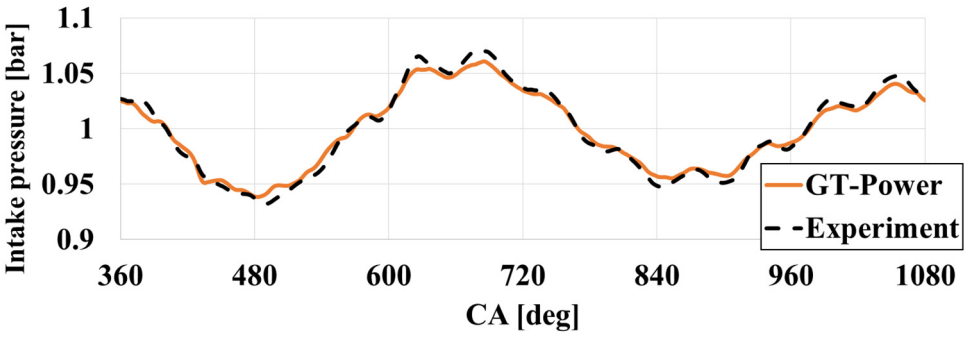

(c)

Figure 4.2 Comparison of intake manifold pressure at WOT condition at (a) 1500 rpm, (b) 2000 rpm, and (c) 2500 rpm

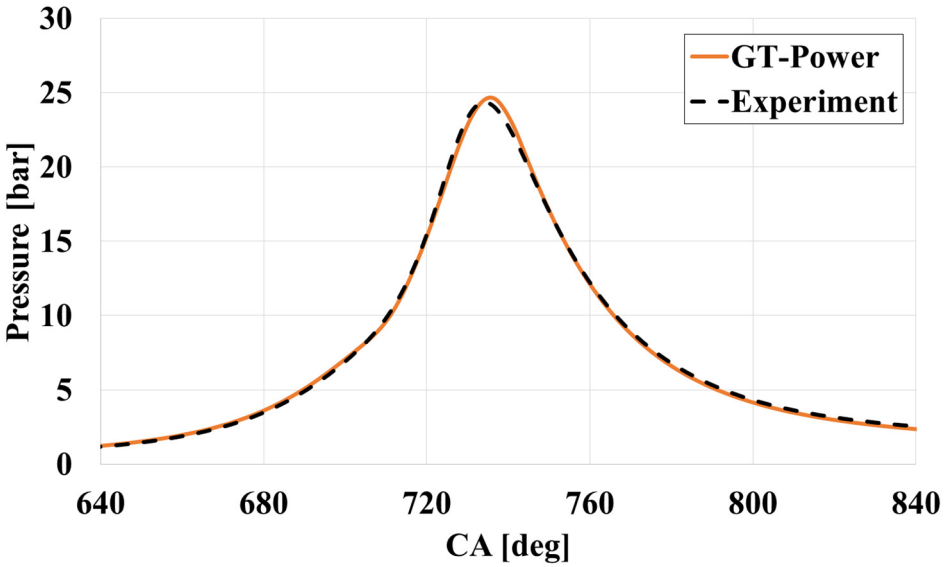

(a)

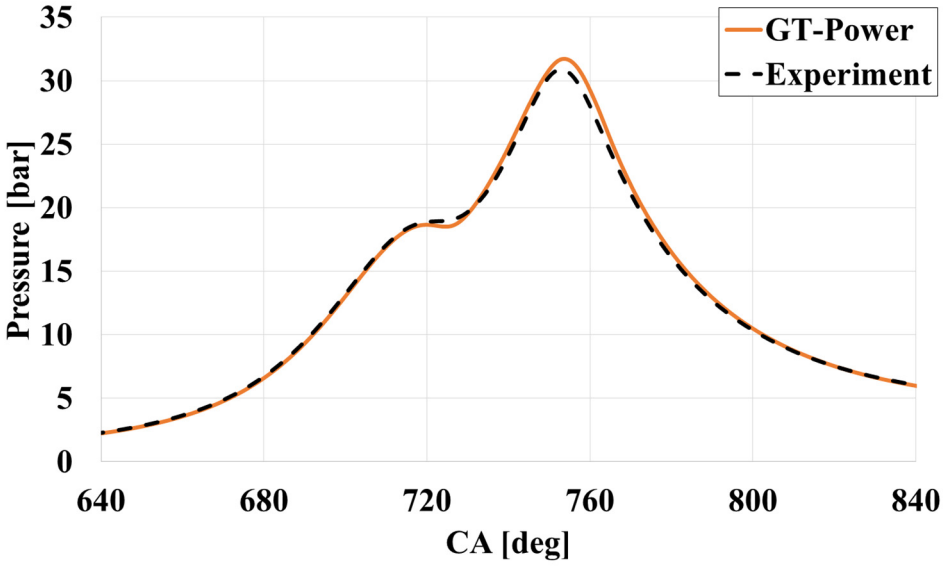

(b)

Figure 4.3 Comparison of in-cylinder pressure curve at 1500 rpm (a) P_i = 0.6 bar, and (b) P_i = 1.0 bar predicted with the correlation 1-2.1x_b for laminar flame speed correction factor

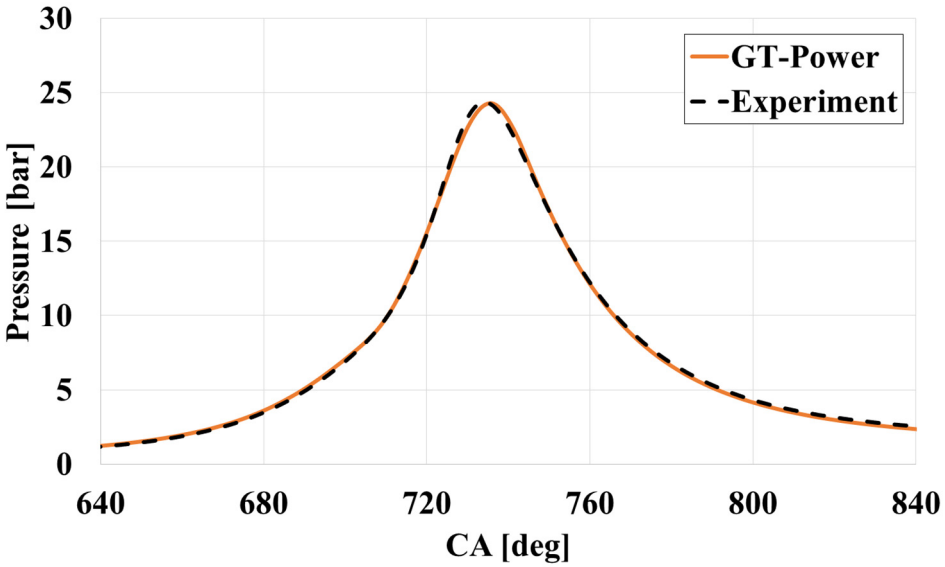

(a)

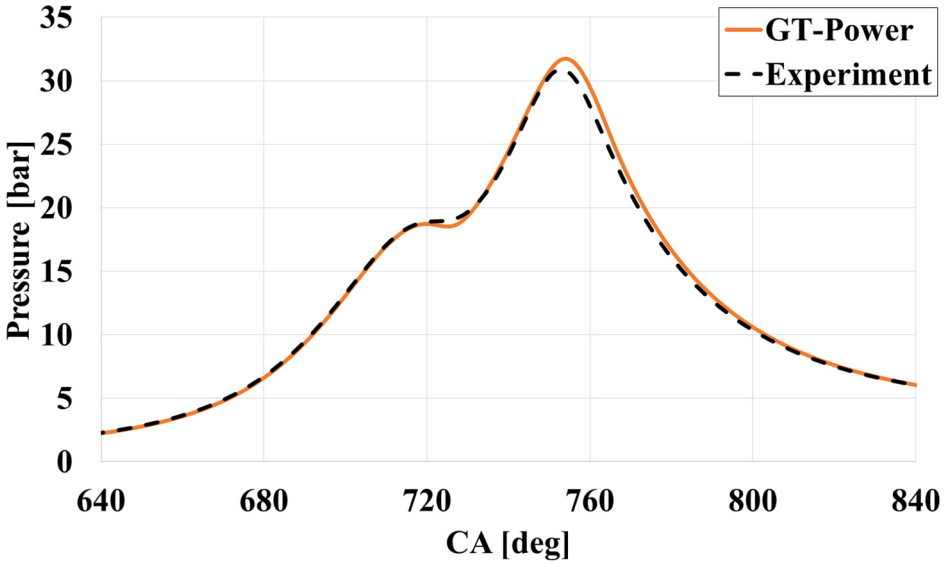

(b)

Figure 4.4 Comparison of in-cylinder pressure curve at 1500 rpm (a) P_i = 0.6 bar, and (b) P_i = 1.0 bar predicted with the correlation $1\text{-}2.06y_b^{0.77}$ for laminar flame speed correction factor

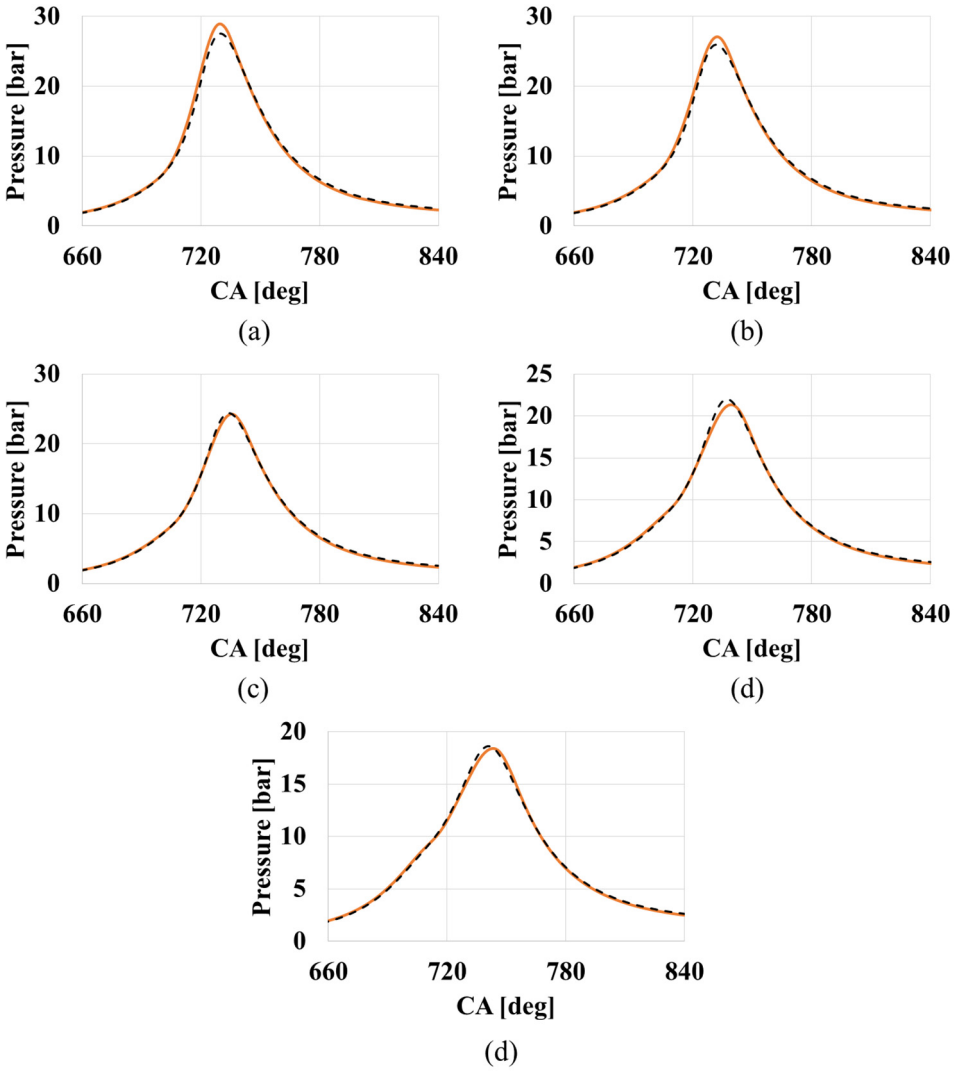

Figure 4.5 Comparison of in-cylinder pressure curve at 1500 rpm, P_i = 0.6 bar with spark timing of (a) 45º bTDC, (b) 40º bTDC, (c) 35º bTDC, (d) 30º bTDC, and (e) 25º bTDC

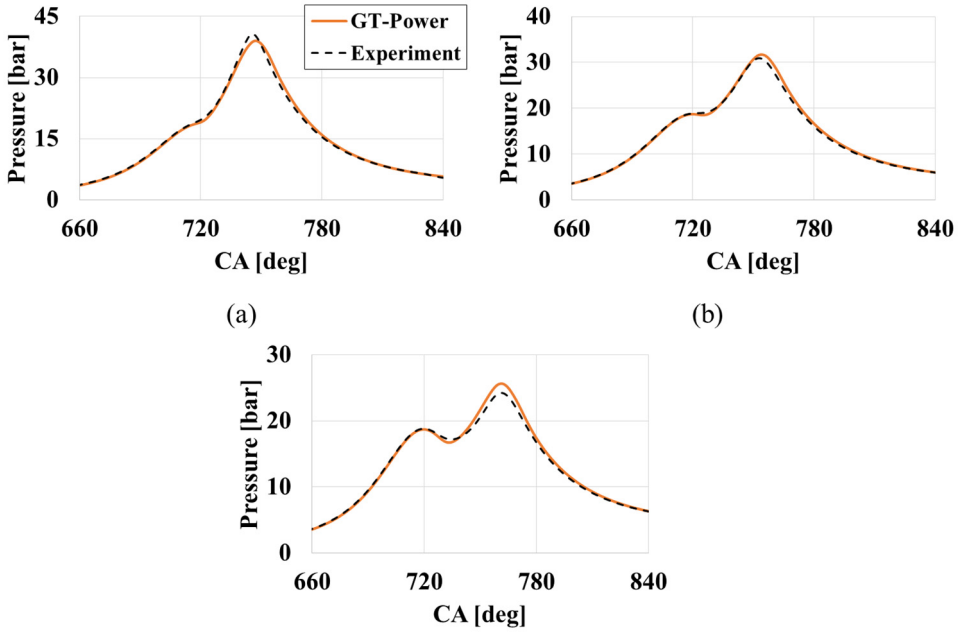

Figure 4.6 Comparison of in-cylinder pressure curve at 1500 rpm, P_i = 1.0 bar with spark timing of (a) 10º bTDC, (b) 5º bTDC, and (c) 0º bTDC

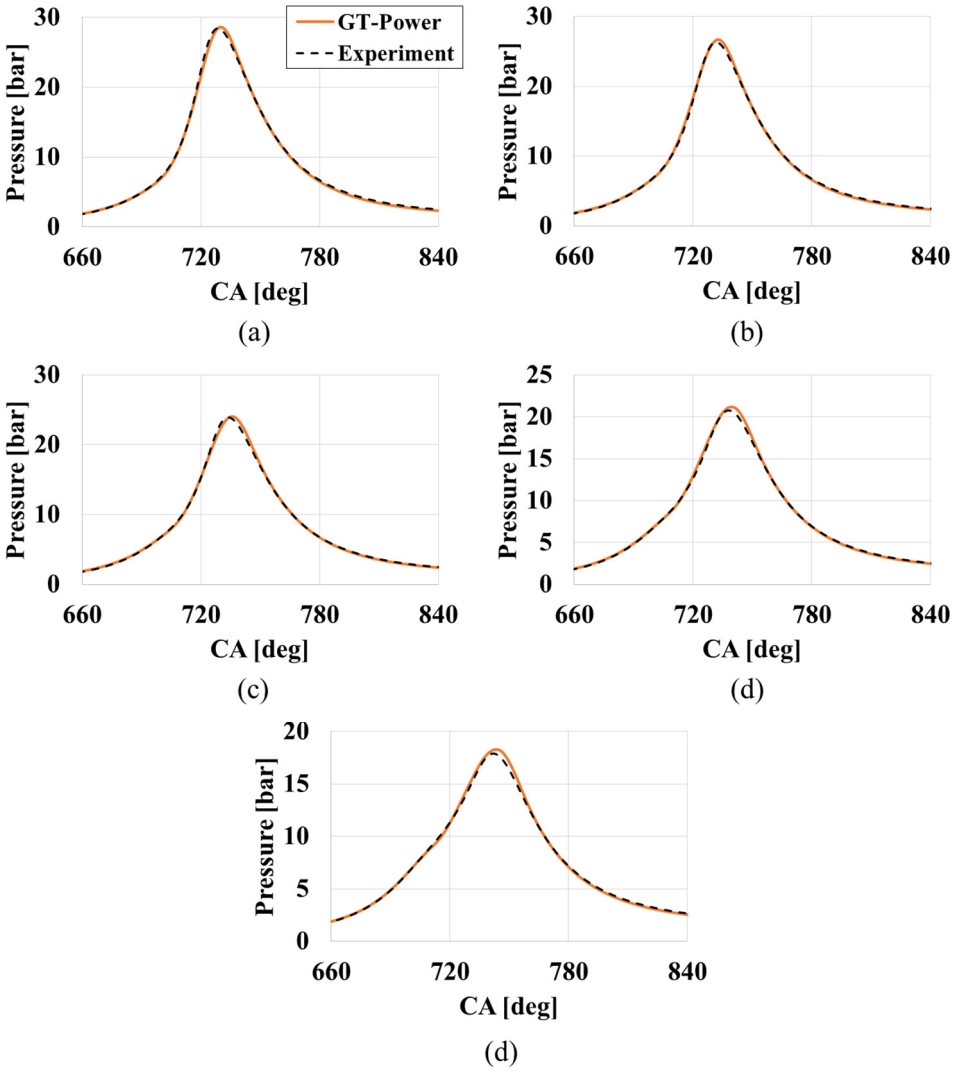

Figure 4.7 Comparison of in-cylinder pressure curve at 2000 rpm, P_i = 0.6 bar with spark timing of (a) 45º bTDC, (b) 40º bTDC, (c) 35º bTDC, (d) 30º bTDC, and (e) 25º bTDC

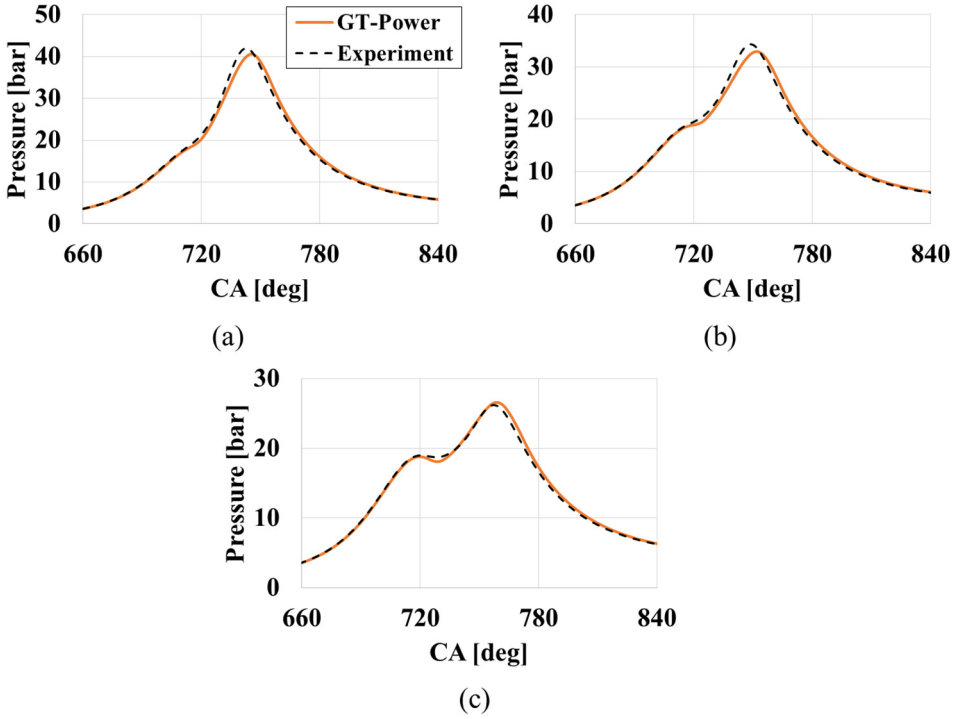

Figure 4.8 Comparison of in-cylinder pressure curve at 2000 rpm, P_i = 1.0 bar with spark timing of (a) 15º bTDC, (b) 10º bTDC, and (c) 5º bTDC

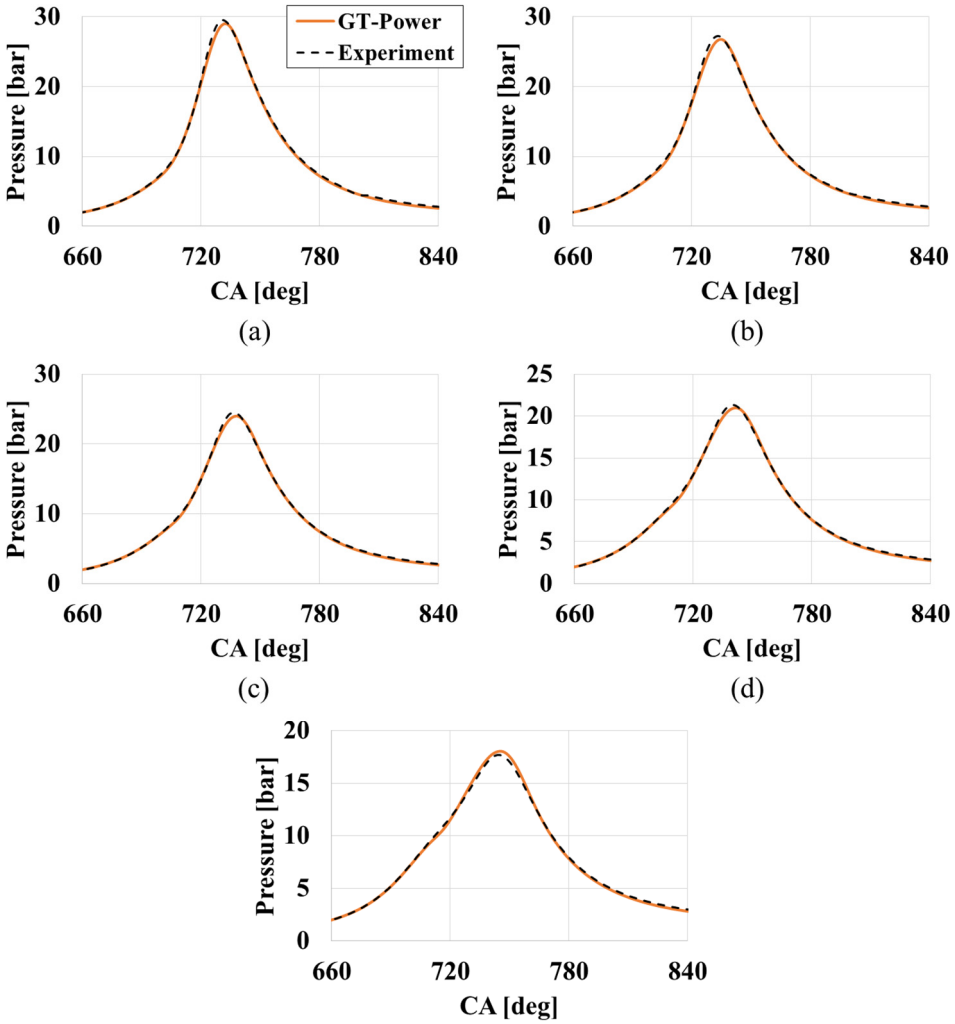

Figure 4.9 Comparison of in-cylinder pressure curve at 2500 rpm, P_i = 0.6 bar with spark timing of (a) 45º bTDC, (b) 40º bTDC, (c) 35º bTDC, (d) 30º bTDC, and (e) 25º bTDC

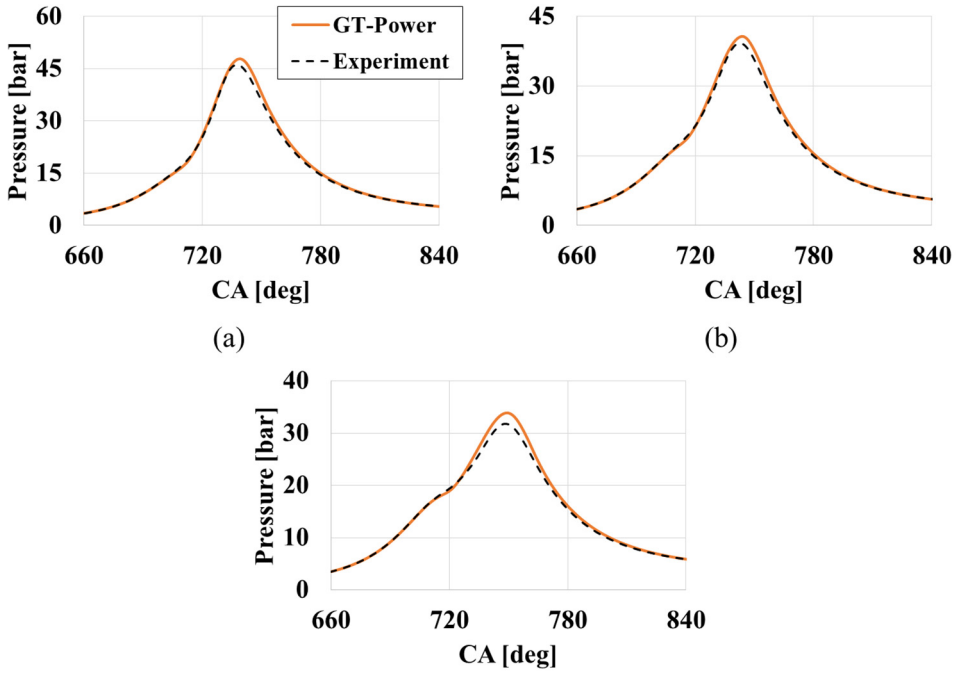

Figure 4.10 Comparison of in-cylinder pressure curve at 2500 rpm, P_i = 1.0 bar with spark timing of (a) 25º bTDC, (b) 20º bTDC, and (c) 15º bTDC

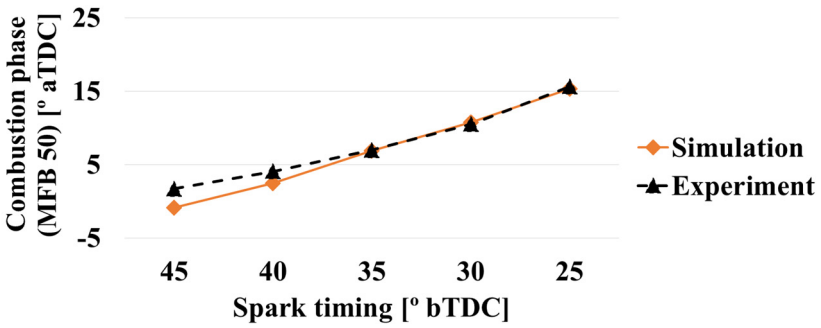

(a)

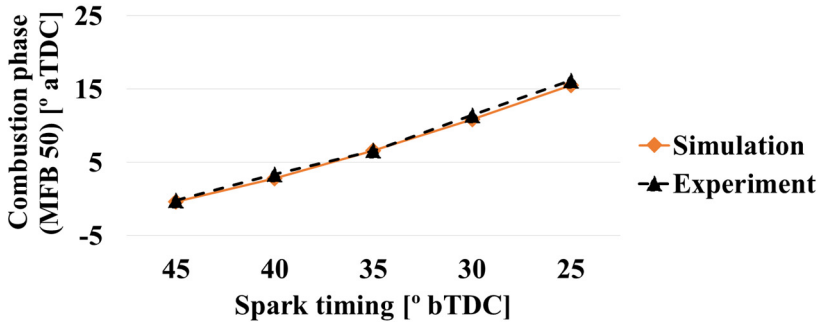

(b)

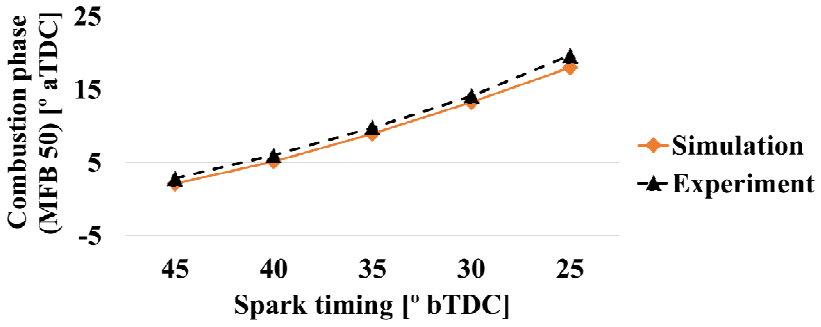

(c)

Figure 4.11 Comparison of combustion phase (MFB 50) for various spark timing under P_i = 0.6 bar, (a) 1500 rpm, (b) 2000 rpm and (c) 2500 rpm

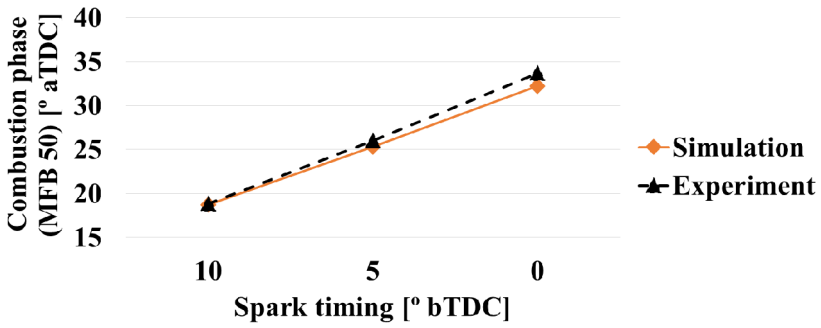

(a)

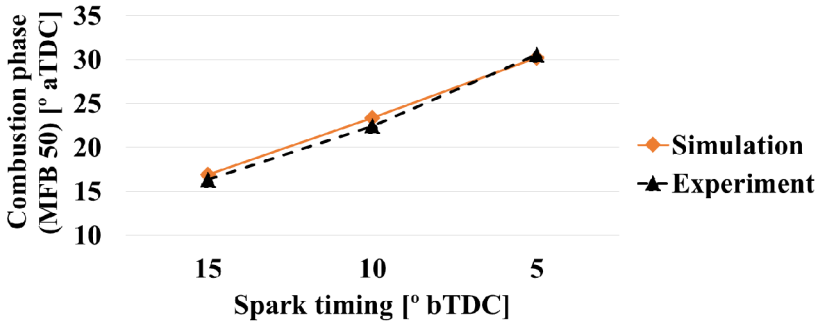

(b)

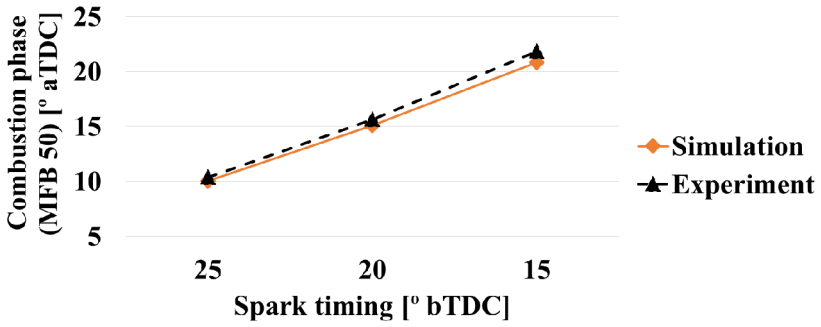

(c)

Figure 4.12 Comparison of combustion phase (MFB 50) for various spark timing under P_i = 1.0 bar, (a) 1500 rpm, (b) 2000 rpm and (c) 2500 rpm

Chapter 5. Application of the developed model for engine performance prediction

5.1 Energy flow analysis within engine cylinder

Since the phenomenological QD combustion model provides information on the convective heat loss to head, piston, and liner, and in-cylinder pressure over a cycle, it is possible to conduct the analysis on the energy flow in the engine. As an example, the usage of fuel energy was observed by comparing the heat balance under 1500 rpm, part load condition. Fig. 5.1 shows the how the heat loss, exhaust loss, pumping loss, and useful work changes according to the spark timing. As the spark timing is retarded, amount of overall heat loss decreases, but the heat loss to the cylinder liner tends to increases. When the spark timing is retarded, the area of the cylinder liner in contact with burned gas would increase as the timing at which the flame front reaches the cylinder liner would be delayed. In addition, the in-cylinder temperature during expansion stage also increases when spark timing is retarded. It is thought that these two factors are main reasons for such tendency.

As the phenomenological QD combustion model developed in this study was confirmed to be able to estimate in-cylinder pressure, and heat transfer rate closer to 3D CFD results, it is expected that the developed model would be able to provide more accurate information on the energy flow in the engine.

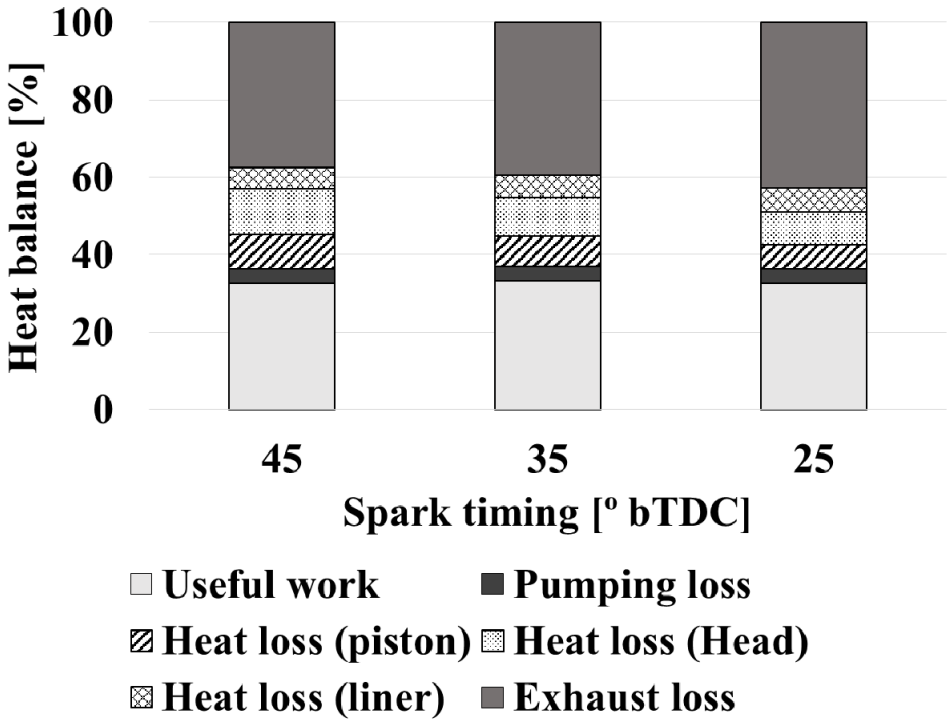

Figure 5.1 Comparison of the heat balance for various spark timings under 1500 rpm, and P_i = 0.6 bar condition

5.2 Effect of VVA function on engine performance

As explained in chapter 1, one of the major factor causing loss in SI engine under part load condition is the pumping loss. Adoption of VVA function is one of the solution to reduce the pumping loss as the air mass control can be achieved without use of throttle valve. To observe the potential of the VVA function, the developed model was utilized. The simulation conditions and valve profile used for simulation is given in Table 5.1, and Fig. 5.2. The simulation was conducted in two steps in order to maintain the air and fuel mass trapped in the cylinder constant. First, the cycle simulation was performed using a short-duration valve profile without throttle so that the trapped air mass is solely controlled with the valve profile. Then, the cycle simulation was conducted using the nominal valve profile, and the throttle opening was controlled to achieve the same amount of air mass as in the former simulation case.

The cycle simulation results and PV diagram are shown in Table 5.2, and Fig. 5.3. The PV diagram shows that the negative work pressure loop has been reduced significantly. As a result, PMEP was reduced by 27.8% while IMEP increased by 2.5%. Although the gain in IMEP may seem small, absolute value of increase in IMEP is larger than the reduction in PMEP. This indicates that the efficiency gain was greater than the reduction of PMEP. Such result can be attributed to two factors. First contributing factor is that the effective compression ratio decreased when short duration valve profile was used, and work done to the system during compression stage decreased. Second contributing factor is the faster combustion. Although the turbulence intensity decreased when VVA function was applied, weaker turbulence intensity was compensated by lower quantity of RGF, and MBT timing was retarded

by 2 CA. This would result in lower in-cylinder pressure during compression stage, and contribute in reduction of negative work done by piston.

From the simulation result, it is evident that the VVA function has positive effect on pumping loss reduction and efficiency improvement. However, PMEP is less significant factor when compared to the heat and exhaust losses. Therefore, it is thought that strategies to reduce another losses such as heat loss is necessary to maximize the merit of the VVA system on efficiency improvement.

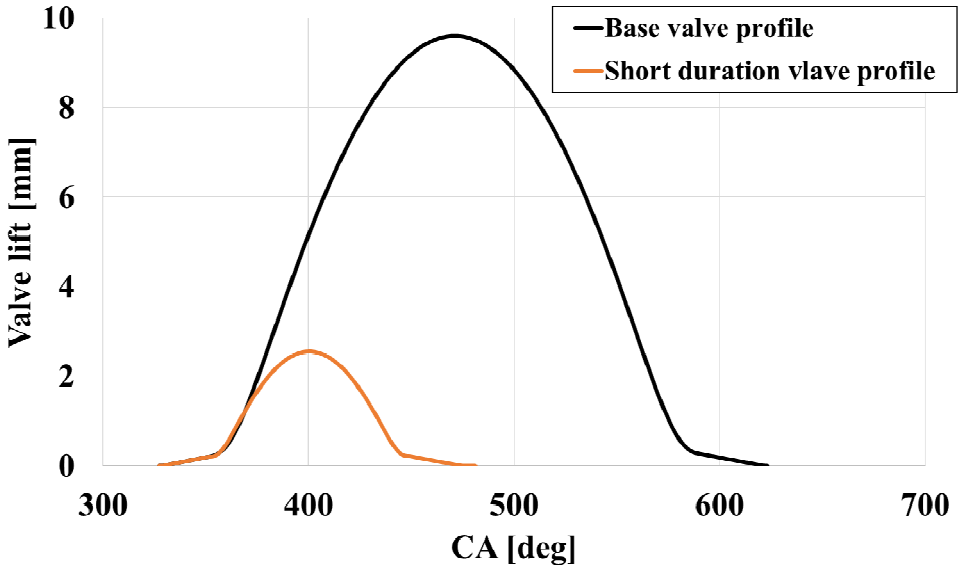

Figure 5.2 Valve profiles used for cycle simulation

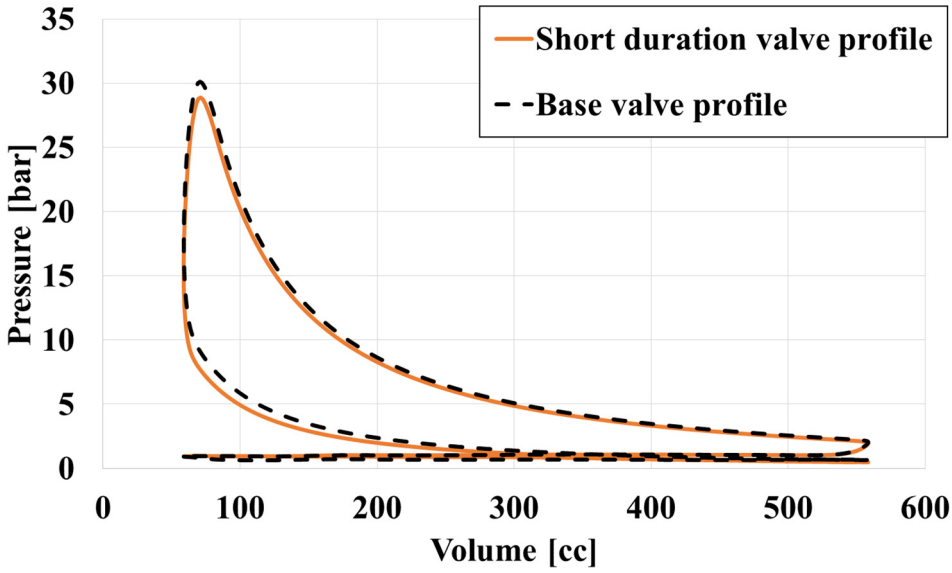

Figure 5.3 Comparison of the PV diagram of base and short duration valve profile

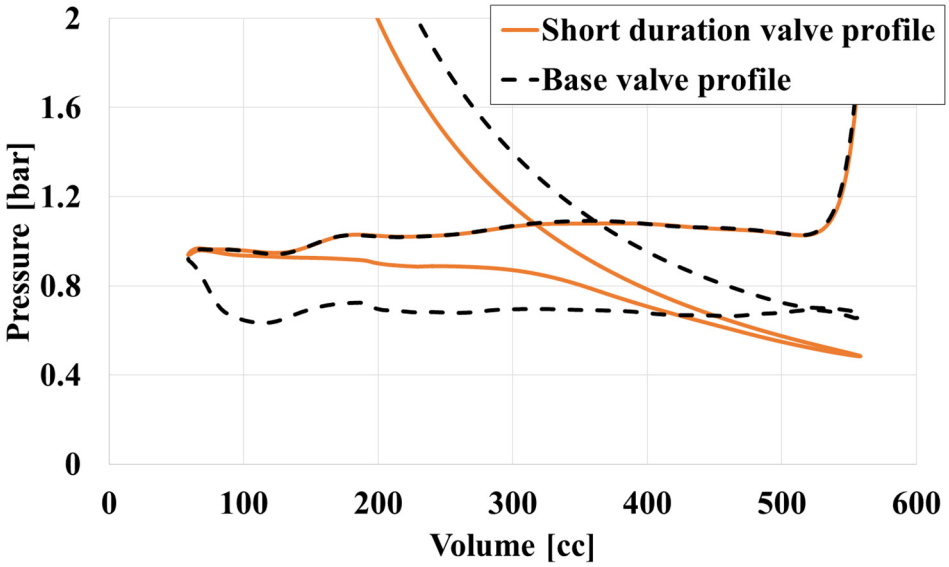

Figure 5.4 Comparison of the pressure loop of negative work of base and short duration valve profile

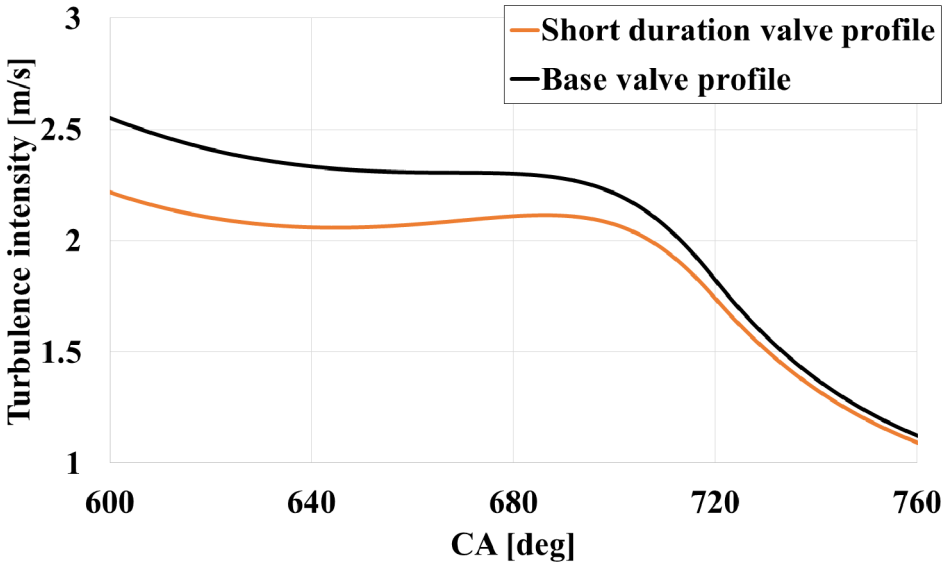

Figure 5.5 Comparison of the turbulence intensity of base and short duration valve profile

Table 5.1 Simulation conditions for VVA function assessment

Parameter	Specification
Engine speed	1500 rpm
Intake pressure	< 1.0 bar (Base valve profile) 1.0 bar (Short duration valve profile)
Spark timing	MBT
Lambda	1.00

Table 5.2 Cycle simulation results

	Base valve profile	Short duration valve profile
Intake pressure	~0.68 bar	1 bar
Fuel mass	17.55 mg	
RGF	12.4%	7.24%
MBT	27º bTDC	25º bTDC
IMEP	5.23 bar	5.36 bar
PMEP	0.36 bar	0.26 bar

Chapter 6. Conclusions

In this study, 0D turbulence model and phenomenological QD combustion model were developed to improve the predictability of the 1D simulation tool for engine performance prediction.

The 0D turbulence model was constructed based on the energy cascade model. To improve the base model, reference data were firstly obtained from the 3D CFD for various engine designs and operating conditions. Three main amendments to the base model were made by introducing new correlations for integral length scale, loss in kinetic energy during intake stroke, and production rate of turbulent kinetic energy. Firstly, the main factors which affect the characteristics of the profile of the integral length scale were identified from the sensitivity analysis, and formulated into correlations to reproduce the profile of the integral length scale for variety of conditions. Secondly, based on the observation of the flow characteristics during the intake stroke with the aid of 3D CFD, a correlation for loss in kinetic energy was derived using the characteristics of the intake and exhaust ports of the engine. Lastly, the equation for production rate of turbulent kinetic energy was revised. A new geometric length scale was introduced which is needed for calculating the production rate of turbulent kinetic energy. An adjustable constant was added to the RDT term to incorporate the effect of engine design which determines the tumble strength. The preliminary verification of the 0D turbulence model was conducted by implementing the model to a 1D simulation tool, GT-Power, and comparing the results obtained from 3D CFD. The mean flow velocity and turbulence intensity predicted by GT-Power agreed well with those of 3D CFD under various engine operating conditions, and designs without case-dependent tuning of model constants. It was also confirmed that

the model can predict the turbulence intensity of the engine designed for stronger tumble strength by tuning only one adjustable constant.

The phenomenological QD combustion model was developed based on the QD turbulence model. The QD turbulence model is an extended version of the 0D turbulence model which can estimate the turbulence intensity of burned and unburned zones during combustion. The equation for the rate of change of turbulent kinetic energy obtained in 0D turbulence model was supplemented with a flux term which accounted for the transport of turbulent kinetic energy during combustion. The production rate of the turbulent kinetic energy was assumed to be proportional to the dissipation rate. Lastly, correlations of the integral length scale of burned and unburned zone were derived. The combustion process was assumed to be divided into three steps: initial flame kernel development, transition from laminar to turbulent flame propagation, and fully-developed turbulent flame propagation. The transition phase and fully-developed turbulent flame propagation phase were described using a correlation derived in former study with several modifications. For heat transfer rate calculation, Woschni's correlation was modified by changing the velocity scale from mean piston speed to the geometric mean of the mean flow velocity and turbulence intensity of unburned and burned zones.

After calibrating the correlation of turbulent flame speed and modified heat transfer model, the phenomenological QD combustion model was successful in reproducing the burn rate, in-cylinder pressure, turbulence intensity of burned and unburned zone, and heat transfer rate obtained from 3D CFD. Except for the cases with late spark timing at 6000 rpm, the combustion phase (MFB 50), and burn duration (MFB 10-80) were predicted with the error less than 0.5 CA, and 2 CA, respectively under part load, and full load with the engine speed varied from 1500 rpm to 6000

rpm. The developed model, however, was not able to predict the latter part of the combustion precisely, and combustion duration (MFB 10-90) was underestimated.

The phenomenological QD combustion model was then verified with the experimental data. The verification of the model was conducted from 1500 rpm to 2500 rpm, part and full load under various spark timing. By introducing the correlation of initial flame kernel size with RGF quantity, the model was able to predict the in-cylinder pressure sufficiently accurate without changing the adjustable constants in the model. The combustion phase (MFB 50) was predicted with the error less than 1 CA for 20 simulation cases out of 24 cases. The accuracy of the model, however, was worsen especially for the conditions with late spark timing at full load. It is thought that this problem is attributable to the limit of the simple ignition model introduced in this study. It is also suspected that the flow characteristics near spark plug differ over various spark timings in actual engine. Such phenomena, however, is very difficult to be predicted in the QD model.

Lastly, the GT-Power model augmented with phenomenological QD combustion model was utilized to observe energy flow in the engine. As an example of energy flow analysis, the energy balance was observed for various spark timing at 1500 rpm, part load condition. From the result, it was possible to understand how the heat loss to head, piston, and liner changed according to the spark timing. The developed model was also utilized to observe the effect of VVA function on engine performance. The cycle simulation was conducted for cases with base valve profile with throttle, and short-duration valve profile without throttle. From the cycle simulation, it was found that the VVA function has notable merits in reduction of pumping loss as PMEP was reduced by 27.8% compared to the base condition without VVA function. The simulation result also showed that the absolute value of increase in IMEP is larger than the reduction in PMEP. It can be attributed to the reduction in negative work done

during compression stroke as the effective compression ratio was lower, and MBT spark timing was retarded due to the faster combustion.

The 0D turbulence model, and the phenomenological QD combustion model developed in this study contain very small number of the adjustable constants including a constant to incorporate the effect of engine design related to tumble strength, and do not require changes to the values of the constants over wide range of engine operating conditions. Thus, it is expected that the developed models would contribute to the assessment of various engine designs, and system configurations at the initial phase of the engine development with better accuracy.

Bibliography

[1] Pulkrabek WW. *Engineering Fundamentals of the Internal Combustion Engine*. New Jersey: Pearson Prentice-Hall; 1997.

[2] Heywood JB. *Internal Combustion Engine Fundamentals*. New York: McGraw-Hill; 1988.

[3] Automotive World Car Industry Forecast Report. Global Insight. 2004.

[4] Heywood JB. On the Road towards 2050. 11th Concawe Symposium Brussels; 2015.

[5] Hoeven MVD. Energy and Climate Change International Energy Agency; 2015.

[6] The Internaltional Council on Clean Transportation. Global passenger vehicle standards. http://www.theicct.org/info-tools/global-passenger-vehicle-standards. [*access date:* September 28th, 2015].

[7] Nissan Motor Corporation. HR12DDR Engine. http://www.nissan-global.com/EN/TECHNOLOGY/OVERVIEW/hr12ddr.html. [*access date:* March 15, 2016].

[8] Szybist J, Foster M, Moore WR, Confer K, Youngquist A, Wagner R. Investigation of knock limited compression ratio of ethanol gasoline blends. SAE Technical Paper 2010-01-0619; 2010.

[9] Ikeya K, Takazawa M, Yamada T, Park S, Tagishi R. Thermal Efficiency Enhancement of a Gasoline Engine. SAE International Journal of Engines. 2015;8:1579-86.

[10] Hara S, Hidaka A, Tomisawa N, Nakamura M, Todo T, Takemura S, et al. Application of a variable valve event and timing system to automotive engines. SAE Technical Paper 2000-01-1224; 2000.

[11] Brüstle C, Schwarzenthal D. Variocam plus-a highlight of the porsche 911 turbo engine. SAE Technical Paper 2001-01-0245; 2001.

[12] Parvate-Patil G, Hong H, Gordon B. An Assessment of Intake and Exhaust Philosophies for Variable Valve Timing SAE Technical Paper 2003-32-0078; 2003.

[13] Fontana G, Galloni E, Palmaccio R, Torella E. The influence of variable valve timing on the combustion process of a small spark-ignition engine. SAE Technical Paper 2006-01-0445; 2006.

[14] Hara S, Nakajma Y, Nagumo S-I. Effects of intake-valve closing timing on spark-ignition engine combustion. SAE Technical Paper 850074; 1985.

[15] Sugiyama T, Hiyoshi R, Takemura S, Aoyama S. Technology for improving engine performance using variable mechanisms. SAE Technical Paper 2007-01-1290; 2007.

[16] Fontana G, Galloni E. Variable valve timing for fuel economy improvement in a small spark-ignition engine. Applied Energy. 2009;86:96-105.

[17] Moore W, Foster M, Lai M-C, Xie X-B, Zheng Y, Matsumoto A. Charge Motion Benefits of Valve Deactivation to Reduce Fuel Consumption and Emissions in a GDi, VVA Engine SAE Technical Paper 2011-01-1221; 2011.

[18] Sellnau M, Rask E. Two-step variable valve actuation for fuel economy, emissions, and performance. SAE Technical Paper 2003-01-0029; 2003.

[19] Sellnau M, Kunz T, Sinnamon J, Burkhard J. 2-step variable valve actuation: System optimization and integration on an SI engine. SAE Technical Paper 2006-01-0040; 2006.

[20] Cleary D, Silvas G. Unthrottled engine operation with variable intake valve lift, duration, and timing. SAE Technical Paper 2007-01-1282; 2007.

[21] De Bellis V, Bozza F, Siano D, Gimelli A. Fuel consumption optimization and noise reduction in a spark-ignition turbocharged VVA engine. SAE International Journal of Engines. 2013;6:1262-74.

[22] Akima K, Seko K, Taga W, Torii K, Nakamura S. Development of new low fuel consumption 1.8 L i-VTEC gasoline engine with delayed intake valve closing. SAE Technical Paper 2006-01-0192; 2006.

[23] Fukuo K, Iwata T, Sakamoto Y, Imai Y, Nakahara K, Lantz KA. Honda 3.0 Liter, New V6 Engine SAE Technical Paper 970916; 1997.

[24] Ha K. Development of Nu 2.0 L CVVL Engine. SAE Technical Paper 2014-01-1635; 2014.

[25] Luttermann C, Schünemann E, Klauer N. Enhanced Valvetronic technology for meeting SULEV emission requirements. SAE Technical Paper 2006-01-0849; 2006.

[26] Rebbert M, Kreusen G, Lauer S. A new cylinder deactivation by FEV and Mahle. SAE Technical Paper 2008-01-1354; 2008.

[27] Hoffmann D, Widmann D, Kreusen D, Meehsen D. Cylinder deactivation for valve trains with roller finger follower. MTZ worldwide. 2009;70:26-30.

[28] Boretti A, Scalzo J. A Novel Mechanism for Piston Deactivation Improving the Part Load Performances of Multi Cylinder Engines. Proceedings of the FISITA 2012 World Automotive Congress: Springer; 2013. p. 3-17.

[29] Scheidt M. Static and transient cylinder deactivation at 4- and 3-cylinder engines. HKIPC2015.

[30] Flierl R, Lauer F, Breuer M, Hannibal W. Cylinder deactivation with mechanically fully variable valve train. SAE International Journal of Engines. 2012;5:207-15.

[31] Feldmann D, Kazmeier B. Compact Electrohydraulic Actuator Powerpacks for Distributed Drives–Configuration, Controls and System Performance. SAE Technical Paper 2002-01-1457; 2002.

[32] Schwaderlapp M, Habermann K, Yapici KI. Variable compression ratio-A design solution for fuel economy concepts. SAE Technical Paper 2002-01-1103; 2002.

[33] Cassiani MDB, Bittencourt ML, Galli LA, Villalva SG. Variable Compression Ratio Engines. SAE Technical Paper 2009-36-0245; 2009.

[34] Kleeberg H, Tomazic D, Dohmen J, Wittek K, Balazs A. Increasing Efficiency in Gasoline Powertrains with a Two-Stage Variable Compression Ratio (VCR) System. SAE Technical Paper 2013-01-0288; 2013.

[35] Pischinger IS, Wittek IK, Tiemann D-IC. Two-stage Variable Compression Ratio with Eccentric Piston Pin. MTZ worldwide. 2009;70:20-7.

[36] Baretzky U, Andor T, Diel H, Ullrich W. The direct injection system of the 2001 audi turbo V8 le mans engines. SAE Technical Paper 2002-01-3357; 2002.

[37] Lippert AM, El Tahry S, Huebler MS, Parrish SE, Inoue H, Noyori T, et al. Development and optimization of a small-displacement spark-ignition direct-injection engine-stratified operation. SAE Transactions. 2004;113:42-66.

[38] Ikoma T, Abe S, Sonoda Y, Suzuki H, Suzuki Y, Basaki M. Development of V-6 3.5-liter engine adopting new direct injection system. SAE Technical Paper 2006-01-1259; 2006.

[39] Schwarz C, Schünemann E, Durst B, Fischer J, Witt A. Potentials of the spray-guided BMW DI combustion system. SAE Technical Paper 2006-01-1265; 2006.

[40] Schmidt L, Seabrook J, Stokes J, Zuhdi MFA, Begg S, Heikal M, et al. Multiple injection strategies for improved combustion stability under stratified part load conditions in a Spray Guided Gasoline Direct Injection (SGDI) engine. SAE Technical Paper 2011-01-1228; 2011.

[41] Han D, Han S-K, Han B-H, Kim W-T. Development of 2.0 L Turbocharged DISI engine for downsizing application. SAE Technical Paper 2007-01-0259; 2007.

[42] Tang Q, Liu J, Zhan Z, Hu T. Influences on combustion characteristics and performances of EGR vs. lean burn in a gasoline engine. SAE Technical Paper 2013-01-1125; 2013.

[43] Kumano K, Yamaoka S. Analysis of Knocking Suppression Effect of Cooled EGR in Turbo-Charged Gasoline Engine. SAE Technical Paper 2014-01-1217; 2014.

[44] Siokos K, Koli R, Prucka R, Schwanke J, Miersch J. Assessment of Cooled Low Pressure EGR in a Turbocharged Direct Injection Gasoline Engine. SAE International Journal of Engines. 2015;8:1535-43.

[45] Alger T, Gingrich J, Roberts C, Mangold B. Cooled exhaust-gas recirculation for fuel economy and emissions improvement in gasoline engines. International Journal of Engine Research. 2011;12:252-64.

[46] Alger T, Mangold B. Dedicated EGR: A new concept in high efficiency engines. SAE International Journal of Engines. 2009;2:620-31.

[47] Ma T, Zhao H, Li J, Ladommatos N. Experimental Investigation of Controlled Auto-ignition (CAI) Combustion in a 4-stroke multi-cylinder gasoline engine and drive cycle simulations. A new generation of engine combustion processes for the future, IFP International Congress, Paris, pp 115-124; 2001.

[48] Zhao H, Peng Z, Williams J, Ladommatos N. Understanding the effects of recycled burnt gases on the controlled autoignition (CAI) combustion in four-stroke gasoline engines. SAE Technical Paper 2001-01-3607; 2001.

[49] Koopmans L, Ogink R, Denbratt I. Direct gasoline injection in the negative valve overlap of a homogeneous charge compression ignition engine. SAE Transactions. 2003;112:1365-76.

[50] Attard WP, Parsons P. A Normally Aspirated Spark Initiated Combustion System Capable of High Load, High Efficiency and Near Zero NOx Emissions in a Modern Vehicle Powertrain. SAE International Journal of Engines. 2010;3:269-87.

[51] Attard WP, Bassett M, Parsons P, Blaxill H. A new combustion system achieving high drive cycle fuel economy improvements in a modern vehicle powertrain. SAE Technical Paper 2011-01-0664; 2011.

[52] Attard WP, Blaxill H. A lean burn gasoline fueled pre-chamber jet ignition combustion system achieving high efficiency and low nox at part load. SAE Technical Paper 2012-01-1146; 2012.

[53] Stein RA, House CJ, Leone TG. Optimal use of E85 in a turbocharged direct injection engine. SAE International Journal of Fuels and Lubricants. 2009;2:670-82.

[54] Jung HH, Leone TG, Shelby MH, Anderson JE, Collings T. Fuel economy and CO2 emissions of ethanol-gasoline blends in a turbocharged DI engine. SAE International Journal of Engines. 2013;6:422-34.

[55] Kim N, Cho S, Min K. A study on the combustion and emission characteristics of an SI engine under full load conditions with ethanol port injection and gasoline direct injection. Fuel. 2015;158:725-32.

[56] Sadakane S, Sugiyama M, Kishi H, Abe S, Harada J, Sonoda Y. Development of a new V-6 high performance stoichiometric gasoline direct injection engine. SAE Technical Paper 2005-01-1152; 2005.

[57] Takahashi D, Nakaa K, Hyoshihara Y, Ohta Y, Nishiura H. Combustion technology to achieve engine thermal efficiency of 40% for HVs engine. SIA Powertrain; 2015.

[58] Castagné M, Cheve E, Dumas J, Henriot S. Advanced tools for analysis of gasoline direct injection engines. SAE Technical Paper 2000-01-1903; 2000.

[59] Laget O, Kleemann A, Jay S, Reveille B, Henriot S. Gasoline engine development using CFD. SAE Technical Paper 2005-01-3814; 2005.

[60] Ge H-W, Shi Y, Reitz RD, Wickman D, Willems W. Engine development using multi-dimensional CFD and computer optimization. SAE Technical Paper 2010-01-0360; 2010.

[61] Enaux B, Granet V, Vermorel O, Lacour C, Thobois L, Dugué V, et al. Large eddy simulation of a motored single-cylinder piston engine: numerical strategies and validation. Flow, turbulence and combustion. 2011;86:153-77.

[62] Fontanesi S, D'adamo A, Rutland CJ. Large-Eddy simulation analysis of spark configuration effect on cycle-to-cycle variability of combustion and knock. International Journal of Engine Research. 2015;16:403-18.

[63] Fontanesi S, Paltrinieri S, Cantore G. LES Analysis of Cyclic Variability in a GDI Engine. SAE Technical Paper 2014-01-1148; 2014.

[64] Fontanesi S, Paltrinieri S, D'adamo A, Duranti S. Investigation of boundary condition and field distribution effects on the cycle-to-cycle variability of a turbocharged GDI engine using LES. Oil & Gas Science and Technology–Revue d'IFP Energies nouvelles. 2014;69:107-28.

[65] Granet V, Vermorel O, Lacour C, Enaux Bı, Dugué V, Poinsot T. Large-Eddy Simulation and experimental study of cycle-to-cycle variations of stable and unstable operating points in a spark ignition engine. Combustion and Flame. 2012;159:1562-75.

[66] Lee T-K. Optimal calibration and transient control of high degree of freedom internal combustion engines [Dissertation]: University of Michigan; 2009.

[67] Blizard NC, Keck JC. Experimental and theoretical investigation of turbulent burning model for internal combustion engines. SAE Technical Paper 740191; 1974.

[68] Nefischer A, Neumann J, Stanciu A, Wimmer A. Quasi-dimensional modelling of turbulence-driven phenomena in SI engines. International Journal of Vehicle Design. 2014;66:297-316.

[69] Tabaczynski RJ, Ferguson CR, Radhakrishnan K. Turbulent entrainment model for spark-ignition engine combustion. SAE Technical Paper 770647; 1977.

[70] Tennekes H. Simple model for the small-scale structure of turbulence. Physics of Fluids. 1968;11:669-71.

[71] Tabaczynski RJ, Trinker FH, Shannon BA. Further refinement and validation of a turbulent flame propagation model for spark-ignition engines. Combustion and Flame. 1980;39:111-21.

[72] Verhelst S, Sheppard C. Multi-zone thermodynamic modelling of spark-ignition engine combustion–an overview. Energy Conversion and Management. 2009;50:1326-35.

[73] Borgnakke C, Arpaci VS, Tabaczynski RJ. A model for the instantaneous heat transfer and turbulence in a spark ignition engine. SAE Technical Paper 800287; 1980.

[74] Borgnakke C, Davis G, Tabaczynski R. Predictions of in-cylinder swirl velocity and turbulence intensity for an open chamber cup in piston engine. SAE Technical Paper 810224; 1981.

[75] Davis G, Borgnakke C. The effect of in-cylinder flow processes (swirl, squish and turbulence intensity) on engine efficiency—model predictions. SAE Technical Paper 820045; 1982.

[76] Pasternak M, Mauss F, Xavier F, Rieß M, Sens M, Benz A. 0D/3D Simulations of Combustion in Gasoline Engines Operated with Multiple Spark Plug Technology. SAE Technical Paper 2015-01-1243; 2015.

[77] Mansouri SH, Heywood JB, Radhakrishnan K. Divided-Chamber Diesel Engine, Part I: A Cycle-Simulation which Predicts Performance and Emissions. SAE Technical Paper 820273; 1982.

[78] Poulos SG. The effect of combustion chamber geometry on SI engine combustion rates: a modeling study [Master's thesis]: Massachusetts Institute of Technology; 1982.

[79] Santavicca DA, Liou D, North GL. A fractal model of turbulent flame kernel growth. SAE Technical Paper 900024; 1990.

[80] Gouldin F. An application of fractals to modeling premixed turbulent flames. Combustion and flame. 1987;68:249-66.

[81] Wu C, Roberts C, Matthews RD, Hall M. Effects of engine speed on combustion in SI engines: comparisons of predictions of a fractal burning model with experimental data. SAE Technical Paper 932714; 1993.

[82] Lafossas F-A, Colin O, Le Berr F, Menegazzi P. Application of a new 1D combustion model to gasoline transient engine operation. SAE Technical Paper 2005-01-2107; 2005.

[83] Richard S, Bougrine S, Font G, Lafossas F-A, Le Berr F. On the reduction of a 3D CFD combustion model to build a physical 0D model for simulating heat release, knock and pollutants in SI engines. Oil & Gas Science and Technology-Revue de l'IFP. 2009;64:223-42.

[84] Bozza F, Fontana G, Galloni E, Torella E. 3D-1D analyses of the turbulent flow field, burning speed and knock occurrence in a turbocharged SI engine. SAE Technical Paper 2007-24-0029; 2007.

[85] Sjeric M, Kozarac D, Bogensperger M. Implementation of a Single Zone k-ε Turbulence Model in a Multi Zone Combustion Model. SAE Technical Paper 2003-01-0722; 2012.

[86] Grasreiner S. Combustion modeling for virtual SI engine calibration with the help of 0D/3D methods [Dissertation]2012.

[87] De Bellis V, Severi E, Fontanesi S, Bozza F. Hierarchical 1D/3D Approach for the Development of a Turbulent Combustion Model applied to a VVA Turbocharged Engine. Part I: Turbulence Model. Energy Procedia. 2014;45:829-38.

[88] De Bellis V, Severi E, Fontanesi S, Bozza F. Hierarchical 1D/3D approach for the development of a turbulent combustion model applied to a VVA turbocharged engine. Part II: Combustion model. Energy Procedia. 2014;45:1027-36.

[89] De Bellis V, Bozza F, Fontanesi S, Severi E, Berni F. Development of a Phenomenological Turbulence Model through a Hierarchical 1D/3D Approach Applied to a VVA Turbocharged Engine. SAE International Journal of Engines. 2016;9:506-19.

[90] Dai W, Newman CE, Davis GC. Predictions of in-cylinder tumble flow and combustion in SI engines with a quasi-dimensional model. SAE Technical Paper 961962; 1996.

[91] Achuth M, Mehta PS. Predictions of tumble and turbulence in four-valve pentroof spark ignition engines. International Journal of Engine Research. 2001;2:209-27.

[92] Falfari S, Forte C, Brusiani F, Bianchi GM, Cazzoli G, Catellani C. Development of a 0D Model Starting from Different RANS CFD Tumble Flow Fields in Order to Predict the Turbulence Evolution at Ignition Timing. SAE Technical Paper 2014-32-0048; 2014.

[93] Han S. Design and demonstration of a spark ignition engine operating in a stratified-EGR mode [Dissertation]: Massachusetts Institute of Technology; 1997.

[94] White FM. *Fluid Mechanics*. 6th ed. New York, USA: McGraw-Hill; 2008.

[95] Wong VW, Hoult DP. Rapid distortion theory applied to turbulent combustion. SAE Technical Paper 790357; 1979.

[96] Lumley JL. *Engines: an introduction*: Cambridge University Press; 1999.

[97] Tennekes H, Lumley JL. *A first course in turbulence*: MIT press; 1972.

[98] Andrews G, Bradley D, Lwakabamba S. Turbulence and turbulent flame propagation—a critical appraisal. Combustion and Flame. 1975;24:285-304.

[99] Kuo KK-Y, Acharya R. *Fundamentals of Turbulent and Multi-Phase Combustion*: John Wiley & Sons; 2012.

[100] Kim J, Min K. Applied Thermal Engineering. 2016. (submitted).

[101] Rhodes DB, Keck JC. Laminar burning speed measurements of indolene-air-diluent mixtures at high pressures and temperatures. SAE Technical Paper 850047; 1985.

[102] Metghalchi M, Keck JC. Burning velocities of mixtures of air with methanol, isooctane, and indolene at high pressure and temperature. Combustion and flame. 1982;48:191-210.

[103] Tan Z, Reitz RD. An ignition and combustion model based on the level-set method for spark ignition engine multidimensional modeling. Combustion and flame. 2006;145:1-15.

[104] Tan Z, Reitz RD. Modeling ignition and combustion in spark-ignition engines using a level set method. SAE Technical Paper 2003-01-0722; 2003.

[105] Herweg R, Maly R. A fundamental model for flame kernel formation in SI engines. SAE Technical Paper 92224; 1992.

[106] Lipatnikov AN, Chomiak J. A simple model of unsteady turbulent flame propagation. SAE Technical Paper 972993; 1997.

[107] Bergman TL, Incropera FP. *Introduction to heat transfer*. John Wiley & Sons; 2011.

[108] Woschni G. A universally applicable equation for the instantaneous heat transfer coefficient in the internal combustion engine. SAE Technical paper 670931; 1967.

[109] NASA. NASA Thermo Build. www.grc.nasa.gov/WWW/CEAWeb/ceaThermoBuild.htm. *access date:* March 21, 2016.

[110] Yaws CL. Transport Properties of Chemicals and Hydrocarbons− Viscosity, Thermal Conductivity, and Diffusivity of C1 to C100 Organics. and; 1; Ac to Zr Inorganics. Norwich, New York: William Andrew Inc. 2009.

[111] Kee RJ, Dixon-Lewis G, Warnatz J, Coltrin ME, Miller JA. A Fortran computer code package for the evaluation of gas-phase multicomponent transport properties. Sandia National Laboratories Report SAND86-8246. 1986;13:80401-1887.

국 문 초 록

최근 몇 십 년간 가솔린 엔진의 효율이 크게 향상되었음에도 불구하고, 지속적으로 강화되고 있는 연비 규제를 만족하기 위하여 엔진 효율 향상은 여전히 큰 과제로 남아있다. 추가적인 엔진 효율 향상을 위한 신기술들이 추가적으로 접목되고 있으며, 결과적으로 엔진 시스템은 점점 더 복잡해지고 있는 상황이다. 이에 새로운 엔진 개발을 위해 필수적인 설계 및 운전 전략 최적화에 있어서 1 차원 시뮬레이션의 활용이 필요하다. 그러나 1 차원 시뮬레이션 툴에 내장되어 있는 연소모델은 엔진 성능 예측에 가장 중요한 부분을 차지하고 있음에도 불구하고 다양한 운전 조건 및 신기술 접목에 따른 연소 특성 변화를 정확하게 모사하지 못하는 문제점이 존재한다. 따라서 1 차원 시뮬레이션 툴을 적극적으로 활용하기 위해서는 보다 정확한 연소모델이 필요하다. 따라서 본 연구에서는 3 차원 시뮬레이션 결과에 준하는 결과를 예측할 수 있는 0 차원 난류 강도 예측 모델 및 이에 기반한 형상학적 유사차원 연소모델을 개발하고자 하였다.

본 연구에서는 난류 강도의 변화 추이를 예측하기 위한 모델링을 기존 에너지 캐스케이드 모델 (energy cascade model) 에 기반을 두고 진행하였다. 다양한 엔진 운전 조건 및 설계에 따른 난류강도 특성을 3 차원 시뮬레이션에 준하는 정확도로 예측하기 위하여 적분 길이 척도 (integral length scale) 및 흡기 과정 중 유동 에너지 손실율, 난류 에너지 생성율에 관련된 새로운 관계식을 도출하였으며, 텀블 강도를 결정짓는 엔진 설계의 영향을 고려할 수 있는 보정계수를 도입하였다.

형상학적 유사차원 연소모델은 유사차원 난류 모델을 기반으로 개발되었다. 유사차원 난류 모델은 0차원 난류 모델에서 확장된 모델이며, 연소 기간 중에 기연 영역과 미연 영역에서의 난류강도 변화 추이를

예측할 수 있다. 화염 전파 과정의 경우, 연소 과정이 초기 화염소 생성 구간, 층류에서 난류화염으로의 천이 구간, 그리고 완전 발달 난류 화염 전파구간의 3 단계로 구성되는 것으로 가정하였다. 화염 속도의 천이 구간을 모사하기 위해서 기존 연구에서 발표된 관계식을 수정하여 사용하였다. 또한, 열손실량을 보다 정확하게 예측하기 위하여 Woschni 관계식을 보완하였다.

본 연구에서 개발된 난류 강도 예측 모델 및 이를 기반으로 하는 연소 모델을 1 차원 시뮬레이션 툴인 GT-Power 에 적용하여, 3 차원 시뮬레이션 결과와의 비교를 통하여 모델의 정확도를 평가하였다. 다양한 조건에서의 난류 강도 변화 추이를 높은 정확도로 예측하고 있는 것을 확인할 수 있었으며, 텀블 강도가 다른 엔진에 대하여 1 개의 보정계수를 변화시킴으로써 난류 강도 변화 추이가 예측 가능한 것을 볼 수 있었다. 연소 모델의 경우, 연소율과 연소 압력, 기연 영역 및 미연 영역에서의 난류 강도 변화 추이 예측이 가능한 것으로 나타났다. 6000 rpm 에서 점화시기가 매우 지각된 조건을 제외하였을 때, 연소상과 연소 기간을 각각 0.5 CA, 2 CA 이내로 예측이 가능하였다.

단기통 엔진 실험 결과와의 비교를 통한 연소 모델의 검증을 추가적으로 진행하였다. 초기 화염소의 크기와 잔류가스량 사이의 관계식을 도출함으로써 보정계수의 변경 없이 다양한 운전 조건에서의 연소 압력을 예측할 수 있음을 확인하였으며, 예측 정확도를 정량화하기 위하여 연소상을 비교한 결과, 24 가지 조건 중 20 가지 조건에서 1 CA 이내로 연소상 예측이 가능한 것으로 나타났다.

마지막으로, 본 연구에서 개발된 모델을 활용하여 에너지 흐름 및 가변밸브기술 적용에 따른 엔진 성능의 변화에 대한 평가를 진행하였다. 다양한 점화시기에 따른 에너지 흐름을 비교함으로써 엔진 헤드와 피스톤, 라이너로의 열전달량의 변화추이를 볼 수 있었다. 가변밸브기술을 적용하였을 때의 성능 예측 시뮬레이션 결과를 진행한 결과, 부분 부하

조건에서 가변밸브기술을 적용하여 별도의 쓰로틀 (throttle) 없이 신기량을 제어하는 경우, 쓰로틀을 사용하는 조건 대비 펌핑 손실 (pumping loss) 이 27.8% 가량 저감되는 것으로 예측되었다. 도시평균유효압력 (IMEP) 의 증가는 펌핑평균유효압력 (PMEP) 의 저감량보다 큰 것으로 나타났으며, 이는 유효압축비가 줄어든 것과 잔류가스량의 저감으로 인한 연소 속도의 증대가 원인인 것으로 판단된다.

본 연구에서 개발된 0 차원 난류강도 모델 및 현상학적 유사차원 연소 모델은 매우 적은 수의 보정계수만을 사용하고 있으며, 다양한 운전 조건에서 별도의 튜닝을 필요하지 않은 것을 확인하였다. 따라서 본 연구에서 개발된 모델은 추후 새로운 엔진 개발 초기 단계에서 엔진 설계 변화 및 시스템 구성 등의 변화에 따른 엔진 성능 변화 예측에 활용될 수 있을 것이다.

주요어 : 가솔린 엔진, 연소 모델, 난류 강도, 0 차원, 유사차원

학번 : 2010-20652